Computational Modeling of Hydro-Electro-Mechanical Flow During CO$_2$ Geosequestration

Mojtaba Talebian

Computational Modeling of Hydro-Electro-Mechanical Flow During CO$_2$ Geosequestration

Proefschrift

ter verkrijging van de graad van doctor
aan de Technische Universtiteit Delft,
op gezag van de Rector Magnificus Prof. ir. K.C.A.M. Luyben,
voorzitter van het College voor Promoties,
in het openbaar te verdedigen
op 9 March 2015 om 10:00 uur door

Mojtaba TALEBIAN

Petroleum Engineer,
University of Calgary, Canada

geboren te Iran

Summary

CO_2 geo-sequestration (CGS) is considered to be a feasible technology for reducing the amount of CO_2 emission into the atmosphere. Selection of an appropriate reservoir is vital and requires appropriate knowledge of the involved phenomena and processes. In a CO_2 geo-sequestration process, carbon dioxide goes through mainly four storage (trapping) mechanisms: structural and stratigraphic trapping, residual trapping, solubility trapping and mineral trapping. In this study, focus is placed on modeling the first trapping mechanism, together with corresponding deformation and electrokinetic flow.

Multiphase fluid flow due to injection of CO_2 in an unsaturated reservoir is accompanied by continuous redistribution of pore pressure and effective stress, causing local and regional deformations and probably major uplifting or subsidence. This flow is also accompanied by electrokinetic flow. In such a system, electrokinetic potentials occur due to the interaction between the formation fluid and the mineral grains. Due to pressure gradients, the flow of the pore fluid produces an advective electric current: such a flow generates an electric field, which produces a counter electric current through the interface, known as the self-potential (SP). Since the electrical conductivity of CO_2 is lower than that of the formation brine, it can be detected by measuring the self-potential. Based on this, the SP can be used for monitoring CO_2 plume movement, a necessary procedure to ensure that geologic sequestration is both safe and effective.

In spite of the versatility of the available numerical tools, attempts to model CO_2 geo-sequestration in a region and considering events occurring in local areas lead to enormous demands for computational power. This makes the development of numerical tools for CO_2 geo-sequestration not only difficult, but rather expensive.

In this study, the governing field equations are derived based on the averaging theory and solved numerically based on a mixed discretization scheme. In this

scheme, variables exhibiting different nature are treated using different numerical discretization techniques. Techniques such as the standard Galerkin finite element method (SG), the extended finite element method (XFEM), the level-set method (LS) and the Petrov-Galerkin method (PG) are integrated in a single numerical scheme. SG is utilized to discretize the deformation and the diffusive dominant field equations, and XFEM, together with LS, are utilized to discretize the advective dominant field equations. The level-set method is employed to trace and locate the CO_2 plume front, and the XFEM is employed to model the associated high gradient in the saturation field front. The use of XFEM for the advective field leads to a computationally efficient, stable and effectively mesh-independent discretization. However, it gives rise to an extra degree of freedom. The use of SG for the deformation and the diffusive fields requires only standard degrees of freedom, limiting the total number of degrees of freedom and making the scheme computationally efficient.

Several verification and numerical examples are presented for both homogenous and fractured reservoirs. The examples demonstrate the capability of the proposed mixed discretization model to simulate challenging, coupled analyses. It has been shown that this model is capable of solving problems, which typically involve several state variables with different transient nature, using relatively coarse meshes.

Samenvatting

CO$_2$-sequestratie (CGS) wordt beschouwd als een uitvoerbare technologie voor het verminderen van de hoeveelheid CO$_2$-uitstoot in de atmosfeer. Het selecteren van een geschikt reservoir is essentieel en vereist passende kennis van de betrokken fenomenen en processen. In CO$_2$-sequestratie wordt koolstof op vier manieren opgeslagen: structurele en stratigrafische opslag, restopslag, opslag door oplossing en opslag in mineralen. In deze studie ligt de focus op het modeleren van het eerstgenoemde opslagmechanisme en de bijbehorende deformatie en elektrokinetisch transport.

Multifase vloeistofstroming door CO$_2$-injectie in een onverzadigd reservoir gaat samen met continue herverdeling van de waterspanning en de effectieve spanning wat locale en regionale deformatie en waarschijnlijk grote bodemstijging of bodemdaling veroorzaakt. Deze stroming gaat ook samen met elektrokinetisch transport. In zo'n systeem ontstaat elektrokinetische spanning door de interactie tussen de vloeistof in het reservoir en de mineralen. Door de spanningsgradiënten produceert de vloeistofstroom een advectieve elektrische stroom: zo'n elektrische stroom genereert een elektrisch veld wat een tegengestelde elektrische stroom door het medium veroorzaakt, beter bekend als de zelfpotentiaal (SP). Omdat de elektrische conductiviteit van CO$_2$ lager is dan die van de vloeistof in het reservoir kan het worden gedetecteerd door het meten van de zelfpotentiaal. De zelfpotentiaal kan dus worden gebruikt voor het monitoren van beweging van de CO$_2$-pluim, een noodzakelijke procedure om te verzekeren dat de geologische sequestratie veilig en effectief is.

Ondanks de veelzijdigheid van de beschikbare numerieke methodes leiden pogingen tot het modelleren van CO$_2$-sequestratie in een gebied samen met het beschouwen van lokale gebeurtenissen tot een enorme vraag naar computerkracht. Dit maakt het ontwikkelen van numerieke methodes voor CO$_2$-sequestratie niet alleen moeilijk maar ook duur.

In deze studie zijn de relevante veldvergelijkingen gebaseerd op de middelingsthe-

orie en numeriek opgelost door gebruik te maken van een gecombineerd discretisatieschema. In dit schema worden variabelen met verschillende karakter behandeld met verschillende numerieke discretisatiemethodes. Technieken zoals de standaard Galerkin eindige-elementenmethode (SG), de uitgebreide eindige-elementenmethode (XFEM), the level-set methode (LS) en de Petrov-Galerkin methode (PG) zijn gecombineerd in één numeriek schema. SG wordt gebruikt om de deformatie en de diffusie dominante veldvergelijkingen te discretiseren, terwijl XFEM en LS samen worden gebruikt om de advectie dominante veldvergelijkingen te discretiseren. De level-set methode wordt toegepast om het front van de CO_2-pluim te traceren en te lokaliseren en de XFEM wordt toegepast om de bijbehorende hoge gradiënt in het saturatiefront te modeleeren. Het gebruikt van XFEM voor het advectieveld leidt tot een efficiënte, stabiele en nagenoeg mesh onafhankelijke discretisatie. Deze aanpak leidt echter tot een extra vrijheidsgraad. Het gebruik van SG voor de deformatie en het diffusieveld vereist standaard vrijheidsgraden wat het totale aantal vrijheidsgraden beperkt en het numerieke schema efficiënt maakt.

Enkele numerieke voorbeelden voor zowel homogene als 'fractured' reservoirs worden gepresenteerd ter verificatie. De voorbeelden tonen de mogelijkheden van het voorgestelde gemixte discretisatiemodel om uitdagende, gekoppelde analyses uit te voeren. Er is aangetoond dat met dit model problemen opgelost kunnen worden met een aantal toestandsvariabelen met verschillend tijdsafhankelijk karakter, terwijl gebruik wordt gemaakt van een grove discretisatie.

Contents

Introduction

1

This chapter addresses the concept, process, and modeling of carbon dioxide (CO_2) geo-sequestration. It provides an overview of trapping mechanisms, types of geological sinks, and risks associated with geological storage. Thereafter, a literature review, current state of the art and challenges in mathematical and numerical modeling and the underlying concepts are presented. Finally, the aims of this work and the thesis outline are summarized.

1.1 Motivation for CO_2 geo-sequestration

Atmospheric levels of CO_2 have increased steadily since the beginning of the industrial revolution and these levels are projected to increase even faster as the global economy grows. Increases in CO_2 concentrations are attributed mainly to burning coal, oil and natural gas for electrical generation, transportation, industrial and domestic uses. Today, globally, significant climate changes are very likely associated with increased atmospheric concentrations of certain gases, most significantly CO_2 (ASME, 2009). The Intergovernmental Panel on Climate Change (IPCC) predicts that the global mean temperature will increase about $3 \pm 1.5°$ Celsius if CO_2 doubles in the atmosphere (IPCC, 2005). The human and ecological cost of climate changes forecast in the absence of mitigation measures is sufficiently large, and the time scales of both intervention and resultant climate change response are sufficiently long, that prudent action is warranted now.

During the past several years, focus has been placed on different solutions that could prevent this by mitigating anthropogenic CO_2 emissions. These solutions are categorized in four main options that can be implemented by using current technology.

1. Use more energy-efficient technologies

2. Use alternative environmentally friendly energy sources

3. Enhance the natural uptake of CO_2 by the terrestrial biosphere through various biochemical processes

4. remove CO_2 from atmosphere and store underground

A variety of factors will need to be considered in any appraisal of these mitigation options. The factors include the potential of each option to deliver emission reductions, the local resources available, the accessibility of each technology for the country concerned, national commitments to reduce emissions, the availability of finances, public acceptance, likely infrastructural changes, environmental side-effects, etc. (IPCC, 2005).

Carbon dioxide capture and storage (CCS) is considered as an effective and viable strategy in the worldwide effort to reduce the human contribution to climate change (Holloway, 1997; IPCC, 2005). This process involves the separation of CO_2 from an emission source (e.g., a fossil fuel power plant), compression to a supercritical fluid condition, transport via pipelines and injection into deep geological formations.

CO_2 sequestration should be done in quantities of gigatonnes of CO_2 per year to be effective for the mitigation of global warming. Effective methods of CO_2 sequestration include enhancement of terrestrial carbon sinks, geological sequestration (CGS), ocean and mineral sequestration. This thesis focuses on the CGS technology.

1.2 Principles of CGS

1.2.1 CGS options

A geological sink for CGS is a system composed of an appropriate porous rock for injection of a large amount of CO_2 and a barrier that will permanently trap the CO_2. Potential targets that fulfill these conditions for CO_2 injection include depleted oil and gas reservoirs, deep unmineable coal seams, salt caverns and deep saline aquifers

CO_2 storage in depleted oil and gas fields

CO_2 can be geologically sequestered in depleted oil and gas reservoirs. The hydro-geological properties that allowed the accumulation of hydrocarbon in the first

place will also permit the trapping of CO_2 in the depleted space in the reservoir. This entails that the sealing condition that prevented the escape of hydrocarbons over geological time can permanently store the injected CO_2.

Depleted oil and gas reservoirs are very attractive candidates for the underground storage of CO_2. This is because these reservoirs have been extensively studied during the oil and gas production period. Moreover, surface and sub-surface facilities (wells, equipment and pipelines) are already available and could be used for CGS. Besides that, the experiences achieved during the injection of miscible and immiscible gases into oil and gas reservoirs as an enhanced oil recovery (EOR) method, including CO_2-EOR can be adapted for CGS projects. Estimates of the world's CO_2 storage capacity in geological formations ranges from 300 to 3200 Gt CO_2 (DOE, 2007). The worldwide capacity of the depleted oil and gas reservoirs is estimated at 100 GtC. Table 1.1 shows the potential volumes of carbon that can be trapped in different formations.

CO_2 storage in active oil and gas reservoirs

CO_2 can be injected into an oil reservoir to increase the production of oil. This technology has long been used in the petroleum industry. This process has mutual benefit to decrease emissions of CO_2 into the atmosphere and enhance oil and gas recovery.

During oil production from a reservoir, a substantial amount of the reserved oil may trap in the reservoir (more than 65%). Enhanced oil recovery processes alter the physical characteristics of the reservoir to increase production. A huge amount of trapped oil can be recovered with CO_2 injection under appropriate conditions. Injected CO_2 has the property of dissolving in the oil to swell it, make it lighter, reduce the viscosity and interfacial tension, increase the reservoir pressure and improves the sweep efficiency, resulting in the recovery of up to 40% of the residual oil.

Table 1.1: An estimate of the volumes of CO_2 that can be sequestered below surface (Herzog, 2001).

geo-sequestration Option	Worldwide Capacity
Oceans	1000 *GtC*
Deep saline formations	$100 - 1000$ *GtC*
Depleted oil and gas reservoirs	100 *GtC*
Coal seams	$10 - 100$ *GtC*

CO_2 storage in coal seams

Coal beds are a possible storage medium for CO_2. Within the microstructure of the coalbed, there is adsorbed methane. Since CO_2 is preferentially adsorbed by coal relative to methane, a large amount of injected CO_2 can be adsorbed in the pore matrix of the coal bed for a long geological time. CO_2 injection can also be used as an enhanced gas recovery (EGR) technique in coal bed methane (CBM) where for every molecule of CH4 desorbed, two molecules of CO_2 will be adsorbed.

CO_2 storage in deep saline aquifers

Saline aquifers are permeable underground formations that contain very salty water (brine) and are considered as one of the most promising options for CO_2 geo-sequestration. Suitable aquifers must be sealed by a regional aquitard (e.g. shale), which is impermeable and should not have any fractures or uncompleted wells (Bachu et al., 1994). Deep saline aquifers provide no economic return for CO_2 injection, but they have the largest potential in volume for CO_2 storage in geological media and are widely distributed in the earth in all sedimentary formations.

Compared to hydrocarbon bearing reservoirs, which usually have broad exploration and characterization study, saline aquifers are mostly uncharacterized in terms of their geological structure. Hence, an appropriate study of the process will be challenging and unexpected problems may come along during operation.

1.2.2 Trapping mechanisms of CGS

Selection of an appropriate reservoir requires appropriate knowledge of the involved phenomena and processes. In general, to reduce costs associated with injection and to reduce the buoyancy forces and increase the mass of CO_2 that can be injected per given pore volume, CO_2 should be injected in a supercritical state (Bachu, 2002). With an average surface temperature of 10 °C, a geothermal gradient of 25°C/km, and a hydrostatic pressure gradient of 10 MPa/km, the critical point for CO_2 (31.1 °C and 7.38 MPa) can be reached at 800 m depth below the surface (Holloway and Savage, 1993). Based on this, the CO_2 injection should take place at a depth of at least 800 m to ensure that the CO_2 enters the formation in a supercritical state.

With time, CGS processes and phenomena go through mainly four storage (trapping) mechanisms, Figure 1.1. During the injection stage, and in the first couple of years after injection, the dominant process is two-phase flow, when the CO_2 systematically displaces the formation brine controlled by gravity, capillary and viscous forces. During this period, structural and stratigraphic trapping occurs, when the low permeability cap-rock prevents the CO_2 from rising upwards. In this

case, an important part of the CO_2 plume resides at the boundary between the reservoir and the cap layer.

The CO_2 plume also leaves a trace of residual saturation that no longer moves (residual trapping). Capillary forces restrict the behavior of the CO_2 flow and CO_2 will be left behind as trapped (residual) saturation. Rock and fluid property distributions, the structure of the porous material, the wettability of the rock and the extent of the displacement process in different regions of an aquifer affect the distribution of residual trapping in different parts. Residual saturation is different for each reservoir and should be measured for each individual rock in the lab.

At a later stage, CO_2 starts to dissolve into the brine by dispersion and diffusion. Diffusion of CO_2 into the brine can set up reverse density gradients that lead to convective mixing and increased rate of CO_2 dissolution. The solubility of CO_2 varies as a function of pressure, temperature, and salinity.

In the long term, chemical reactions between the CO_2-water mixture and the formation and cap rock solid matrices will take place. These geochemical reactions take place slowly within a time frame of decades or centuries. This mechanism is effective and when minerals form, CO_2 is bound for long periods of time in mineral trapping. Incorporating chemical processes may require several additional degrees of freedom per node, depending on the sophistication of the simulation and what processes are deemed important. This will depend on the type of host rock (limestone, granite, sandstone, etc), and the time scale of the simulation.

In this work, focus is placed on the first trapping mechanism, when the CO_2 undergoes stratigraphic trapping by buoyancy due to its density difference with the formation brine water.

A proper selection of underground storage of CO_2 is essential to ensure that CO_2 would stay safely underground for a long geological time. Regions with earthquake or volcanic activity can be dangerous for CO_2 geo-sequestration. Proper storage site selection, comprehensive reservoir characterization, appropriate injection operation, site monitoring, together with the implementation of remedial measures if leakage is identified and also a reliable numerical simulator, assure the safe geo-sequestration of CO_2.

1.2.3   Risks of CGS

CO_2 can remain trapped underground for very long periods, but leakage of CO_2 can lead to serious local environmental consequences. In general, the risks of injecting CO_2 into geological formations can be divided into the following categories:

- CO_2 leakage from the reservoir to the atmosphere
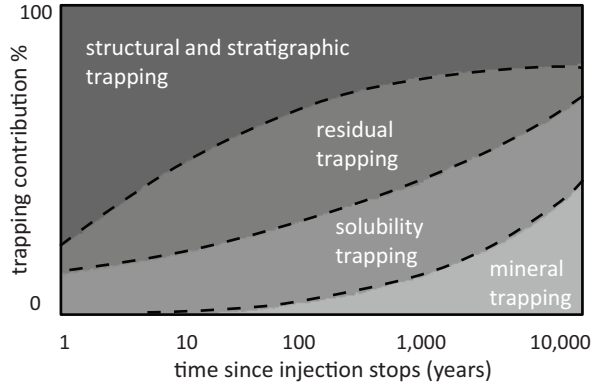
Figure 1.1: CO_2 trapping mechanisms over time (see IPCC (2005)).

- Brine movement and subsequent displacement into shallower drinking water reserves

- Methane displacement and leakage

- Geomechanical uplift or subsidence of earth surface because of underground pressure changes induced by CO_2 injection

- Induced seismicity and small earthquakes

A plume of stored CO_2 can migrate by several mechanisms from the reservoir:

- Escape through low permeability caprocks, if the pressure difference between CO_2 and the water phase exceeds the capillary entry pressure

- Diffusion of CO_2 through the caprock

- Lateral migration along unconformities that end up at the sea bottom

- Escape through openings in the caprock or fractures and faults

- Escape through or along wells, which can be caused by failure in casing or cementation

To ensure safety of large-scale geo-sequestration of CO_2, monitoring of CO_2 migration in the subsurface is needed. Moreover, to assess the long-term fate of injected CO_2 and the effect of CO_2 on the host environment, it is necessary to simulate the process. In this thesis a comprehensive modeling is conducted on simulation of a coupled electrokinetic–hydromechanic process for CGS and the behavior of a well-known CO_2 leakage problem is studied.

1.2.4   Monitoring of CGS

The main purpose of monitoring is to ensure that geologic sequestration is both safe and effective without leakage and to meet the regulation and environmental policy for a long-term period.

Benson and Myer (2000) stated that one of the most important purposes of monitoring is to confirm that the project is performing as expected from the predictive models. This is particularly valuable in the early stages of a project when there is an opportunity to alter the project if it is not performing adequately. Moreover, monitoring data collected early in the project are frequently used to improve and calibrate the predictive model further. The refined model then forms the basis for predicting the longer-term performance of the project.

Existing monitoring methods include geophysical techniques such as surface and borehole seismic and electromagnetic, streaming potential (SP) measurements, geomechanical methods such as tiltmeters, well testing and pressure monitoring, tracers and chemical sampling.

Geophysical techniques are utilized to remotely and economically monitor the distribution and pore-space saturation of CO_2 in underground storage sites. The spatial and temporal resolution of these methods is unlikely to be sufficient for performance evaluation and leakage detection. Of these techniques, in this study the focus is on monitoring by measuring streaming-potential in the reservoir.

Measurements of the streaming potential may be used to monitor subsurface fluid flow in regions where two or more mobile fluid phases occupy the pore space, such as the vadose zone, hydrocarbon reservoirs, contaminated aquifers and CO_2 geo-sequestration (Moore et al., 2004; Sailhac et al., 2004; Saunders et al., 2006, 2008, 2012).

Electrokinetic and electro-magnetic monitoring measures the change in resistivity due to CO_2 injection. The resistivity is expected to increase when CO_2 replaces e.g. the brine. Fracturing can also be detected by this method (Moore and Glaser, 2007).

It is generally considered that the first person to measure a streaming potential was Georg Hermann Quincke in about 1859, which was followed some 20 years later in 1879 by Helmholtz who developed a mathematical expression for that effect. The self-potential has been extensively utilized and modeled for geothermal exploration (Ishido and Pritchett, 1999; Ishido et al., 2010), groundwater flow (Bolève et al., 2007), and oil reservoirs (Saunders et al., 2008; Wurmstich and Morgan, 1994).

The concept of monitoring the streaming potential in hydrocarbon reservoirs was first suggested by Wurmstich and Morgan (1994). They used numerical techniques to simulate the streaming potential measured at monitoring wells and at the surface

during production. Saunders et al. (2006) used numerical techniques to simulate water moving toward a well during oil production and the resulting streaming potential measured at the well.

1.3   Modeling CGS

A model may be defined as a selected simplified version of a real system and phenomena that take place within it. It approximately simulates the system's excitation-response relationships that are of interest (Bear et al., 1993). There are three important steps in the modeling of any physical process: (i) Development of a conceptual model, (ii) mathematical modeling, and (iii) numerical simulation.

The first step is to describe an idealized form of a problem in terms of a set of specific quantities. It is not always feasible to ensure the reliability of the idealized system since, in some cases, the physical process is not totally known.

The second step in the modeling is to characterize the idealization of the physical process by a mathematical model; in other words, the development of the governing equations of the problem. These governing equations are mostly complicated equations that are challenging to solve both analytically and numerically. Therefore, we must introduce simplifying assumptions to decrease the complexity of the model which makes it possible to obtain either an exact or a numerical solution. Because the model is a simplified version of the real system, no unique model exists to describe it.

After the development of a proper mathematical model, with suitable boundary and initial conditions, we need to solve it analytically or numerically.

In the following section, a review of the methodology of constructing models that are required for solving CO_2 geo-sequestration is given.

1.3.1   Conceptual modeling of CGS

The real system of CO_2 geo-sequestration and its behavior may be very complicated, depending on the amount of details we wish, or need to be included in describing it. The art of modeling is to simplify the description of the system and its behavior to a degree that will be useful for the purpose of planning and making management decisions in specific cases. The simplifications are introduced in the form of a set of assumptions that express our understanding of the system and its performance.

The injection of CO_2 into the underground formation and its interaction with the resident fluid as well as with the porous medium domain involves coupled multi-physical processes including multiphase fluid flow (H), geomechanical deformation

(M), heat transfer (T) and geochemical reaction (C), normally denoted as THMC processes. The term coupled THMC indicates that each process affects others, and the overall response of the model cannot be predicted accurately by considering each process.

In recent years, a great deal of attention has been directed towards coupled THMC modeling in petroleum and environmental engineering, geothermal energy utilization and CO_2 geo-sequestration (Gawin and Schrefler, 1996; Gawin et al., 1995; Lewis and Schrefler, 1998; Lewis et al., 1989; Rutqvist et al., 2002). These model frameworks, developed for multiphase flow and reactive transport problems, can be adopted for modeling CO_2 geo-sequestration processes. Different numerical simulation researches determined how the performance evaluation of CO_2 geo-sequestration requires the study of these simultaneously interacting processes (Johnson and Nitao, 2002; Rutqvist et al., 2009; Xu and Pruess, 2001; Xu et al., 2006).

A wide variety of modeling techniques have been reported in literature for HM process in CO_2 geo-sequestration. However, only a few fully coupled THMC models have addressed large-scale numerical simulation of CO_2 injection (Rutqvist et al., 2009; Xu et al., 2007). Since a fully coupled THMC model may be computationally intensive, models that are more manageable may be created by identifying which processes are strongly linked and which processes are weakly linked.

These studies include numerical simulations of CO_2 flow in a homogenous formation (H process) (e.g. Pruess et al., 2002; Weir et al., 1995), a coupled hydromechanical simulation (HM process) to study the potential for tensile and shear failure associated with underground CO_2 injection (e.g. Rutqvist and Tsang, 2002; Rutqvist et al., 2002, 2007, 2009) and a coupling of geochemical reactions with multiphase flow to evaluate long-term caprock integrity considering HC processes during CO_2 geo-sequestration (Johnson and Nitao, 2002; Johnson et al., 2004, 2005; Pruess, 2010). In addition, simulations have been conducted considering mineral precipitation and dissolution reactions in a homogeneous formation (e.g. Xu et al., 2004, 2007). In this thesis a computational model for the simulation of coupled hydromechanical (HM) and electrokinetic flow is introduced. Particular emphasis is placed on modeling CO_2 flow in a deformed, fractured geological formation and the associated electrokinetic flow.

In order to understand and predict a coupled multi-physical process, one must obtain quantitative mathematical models of this process. Therefore, it is necessary to analyze the relationship between the process variables and to obtain a mathematical model.

1.3.2 Mathematical modeling of CGS

The second step in the modeling process is the mathematical modeling. In this step, the conceptual model is expressed in the form of mathematical equations. Mathematical modeling and simulation of CO_2 flow and its propagation in porous media are essential for understanding all THMC processes, designing the injection process and monitoring the geo-sequestration process. A mathematical model consists of:

1. Balance equations describing the conservation of mass, electric charge, momentum and energy in the system.

2. Constitutive equations describing the internal mechanical, thermal, and other properties of the constitutive quantities of the system.

3. Domain geometry describing boundary surfaces of the system.

4. Initial and boundary conditions describing the initial state of the system and the interaction of the system with its surrounding.

The earliest studies of multiphase flows in porous media concern flow in partially saturated soil in ground water hydrology. However, the most intense researches in this field over the past four decades have focused on simulating multiphase flow in petroleum reservoirs. The core of any fluid flow in porous media consists of a partial differential equation (PDE) that represents the physical reality of the subsurface porous medium and flow phenomena that occur there.

The construction of such equations is based on the assumption that the porous medium domains of interest may be described as continua; the models constructed in this way are referred to as 'continuum models'. Continuum models represent the classical engineering approach to describing materials of complex and irregular geometry characterized by several distinct relevant length scales. A spatial domain is said to behave as a continuum if state variables and properties that describe the behavior of the material occupying it can be assigned to every point within it (Bear et al., 1993).

Appropriate models are not based on a physical characterization of the real microstructure, but consider their effects on the physical behavior in a phenomenological manner. For flow in porous medium problems, microscopic modeling is usually impractical, due to the inability to describe the complex configuration of the solid-liquid boundary over large porous medium domains. Moreover, even if the solution of the problem could be obtained in great detail, it would contain much more information than would be useful in any practical sense. To avoid these difficulties, associated with solving problems at the microscopic level, another level of description

is introduced, referred to as the macroscopic level. Therefore, some averaging is necessary to go from the pore scale (micro scale) to the reservoir scale (macro scale).

In the classical model for single phase flows in a porous media (e.g. Bear, 2012; De Marsily), a conservation of mass equation for the fluid phase is combined with an equation of state relating the pressure, temperature and fluid properties; imposing a compressibility model for the solid phase; and invoking Darcy's law to relate macroscopic velocity (volumetric flux density) to the pressure gradient.

For multiphase flow, a similar approach is taken and the governing equations are based on a continuum theory, which consists of two basis elements, the fundamental conservation law and constitutive relations. The equations are written for each fluid phase and fluid saturations are related to the fluid pressures, using empirical correlations. A multiphase extension of the empirical Darcy's law, which typically includes relative permeabilties, is used to relate the flux vector to the pressure gradient of the individual phase.

The classical approach for multiphase flow, based on direct extension of Darcy law, leads to several problems. Limitations are reflected in many aspects, including the hysteresis in capillary pressure and relative permeability relations and interfacial effects. Hysteresis means that capillary pressure and relative permeability have different values between an upper and a lower bound, depending on the history of the system and the path along which the particular state was reached (Dullien, 1991). An example of the interfacial effects would be the effects of the momentum transfer caused by a viscous force across two-phase interface, which is referred to as viscous coupling. Different studies (e.g. Bachmat and Bear, 1986; Ehrlich, 1993; Hassanizadeh and Gray, 1980, 1979b) have shown that viscous coupling effects are important over a broad range of porous media flow problems. The existence of these phenomena indicates that simple extension of Darcy's law for multiphase flow is not capable of capturing microscale physics.

In general there is a lack of a rigorous connection between the microscale and the macroscale in the classical approach. The absence of cross-scale consistency is a result of formulation approaches that by-pass the microscale and instead propose conservation equations and closure relations directly at the macroscale (Gray and Miller, 2005).

In the last three decades, there has been theoretical work attempting to develop a rigorous and consistent framework for formulating macroscale models that better account for microscale physics. In general, there are three major approaches that can be used to transform the microscopic physical laws, e.g., balance equations of extensive quantities, such as mass, momentum and energy, into their macroscopic counterparts for practical application purposes (Bear and Cheng, 2010):

1. The *mixture-theory* approach (Boer, 2000; Whitaker, 1986, 1999), which starts from the macroscopic level and can be viewed as an extension of the classical continuum mechanics theory. Employing the concept of volume fraction allows accounting for the different constituents of the soil.

2. The *averaging approach*, which is characterized by applying the balance laws of classical continuum mechanics to the actual microstructure of the porous medium. based on a thermodynamic framework that provides constraints on system behavior, this approach starts from microscopic balance equations of mass, momentum, and energy for two fluid phases, a solid phase, and the interfaces between the phases and transform them to the macroscale. A number of studies have been devoted to the development of averaging theorem and applying it to multiphase transport problems (e.g. Cushman, 1982; Gray, 1983; Hassanizadeh and Gray, 1979a).

3. The *homogenization approach* (e.g. Hornung, 1997; Sánchez-Palencia, 1980), which is a mathematical technique applied to differential equations that describe physical phenomena associated with a domain exhibiting heterogeneities and geometrical features at two scales or more. This aims at smoothing out the heterogeneity at the pore scale, as well as at other scales. It assumes that the heterogeneity is periodically distributed in the domain. This condition is needed for a rigorous mathematical proof of the existence and uniqueness of the solution. Physically, this means a structure based on a repeated pattern, e.g., a certain form of stacking of grains, or of alternating layers of different materials.

A variety of simplifying assumptions and constraints are introduced in each of these three approaches; hence, the resulting macroscopic laws depend on the selected set of underlying assumptions. It must be pointed out that, under appropriate assumptions, the averaging theory yields the same equations as the classical mixture theory, as shown in Boer et al. (1991).

The averaging theory is one of the most important mathematical models for multiphase flow in porous media. It provides physically sound up-scaling of the microscopic quantities to their corresponding macroscopic quantities. The conservation equations for micro scale variables are transformed to conservation equations for macro scale variables. These theorems essentially transform averages of derivatives to derivatives of averages. Utilization of such a model can effectively be substituted for the use of multiscale techniques, where material properties or system behavior are calculated on one level using information or models from different levels. Concerning

a detailed overview of mathematical modeling of multiphase multicomponent porous media, the reader is referred to Boer (2000).

These different theoretical approaches produce a similar final formulation which is referred as the generalized two-phase flow model. Typically there are a number of different possibilities to select a set of independent variables with which the remaining dependent variables can be eliminated. This results in different mathematical formulations for the same model. The selection of the proper formulation can strongly influence the behavior of the numerical simulation and is, therefore, of primary importance. In the following, an example of this will be briefly discussed

Modeling immiscible two-phase flow in porous media

Darcy's law presents the principle that governs fluid flow in porous media. According to this law the fluid velocity is linearly proportional to the pressure gradient and the gravitational force. In a two-phase flow system, Darcy velocity can be defined as:

$$\mathbf{u}_\alpha = \frac{\mathbf{k} k_{r\alpha}}{\mu_\alpha} \left(-\nabla P_\alpha + \rho_\alpha \, \mathbf{g} \nabla z \right), \quad \alpha = w, n \tag{1.1}$$

where $\mathbf{u}_\alpha$ is the flow velocity, $\mathbf{k}$ is the absolute permeability, the subscript α specifies the fluid phase, w is the wetting phase and n is the non-wetting phase, $k_{r\alpha}$ is relative permeability of phase α (functions of saturation), μ_α is viscosity of phase α, P_α is pressure of phase α, ρ_α is density of phase α and $\mathbf{g}$ is the gravity force vector.

If Darcy's law is inserted into the mass continuity equation, a system of two-phase flow differential equations is obtained,

$$\frac{\partial \left(S_\alpha \phi \rho_\alpha \right)}{\partial t} - div \left(\frac{k_{r\alpha} \rho_\alpha}{\mu_\alpha} \mathbf{k} \left(\nabla P_\alpha - \rho_\alpha \mathbf{g} \right) \right) = \rho_\alpha Q_\alpha \tag{1.2}$$

in which S_α is saturation of phase α, ϕ is porosity and Q_α is a source or sink term.

Note that, in this example, we are concerned with isothermal, immiscible displacement of the incompressible fluids in a rigid porous medium. These assumptions bring certain implications on the equations: the fluid properties of the two-phases are constant, solid matrix is rigid and the temperature is constant.

This set of equations contains four unknowns which are wetting phase pressure, non-wetting phase pressure, wetting phase saturation and non-wetting phase saturation. This system is completed by two further algebraic conditions. The wetting and the non-wetting phases are jointly occupying the voids, implying:

$$S_w + S_n = 1 \tag{1.3}$$

13

and at the interface between the two-phases, the capillary pressure is expressed as:

$$P_c(S_w) = P_n - P_w \tag{1.4}$$

Thus, two of the four unknowns P_w, P_n, S_w and S_n can be eliminated. Due to the non-linear dependencies of the capillary pressure and the relative permeability, the system of equations is non-linear.

Different formulations, describing the primary variables, have been developed. They are briefly explained here; further reading is given in Helmig (1997).

Pressure formulation

Immiscible two-phase flow in porous media includes separate equations for the wetting and nonwetting phases. If a pressure formulation is used, the pressures of the wetting and the non-wetting phases are the primary variables and the resulting system is of mixed parabolic/hyperbolic type. This formulation is based on an inverse function which describes the saturation dependency on the capillary pressure, $S_w = f^{-1}(P_c)$. Substituting Eq.(1.3) into Eq.(1.2), ignoring force sources, using the definition of the capillary pressure, Eq.(1.4), and setting fluid capacity, $C_w = -\phi \frac{\partial S_w}{\partial P_c}$, and phase mobility $\lambda_\alpha = \frac{k_{r\alpha}}{\mu_\alpha}$, results in two PDEs for the wetting and non-wetting phases, as:

$$C_w \left[\frac{\partial P_w}{\partial t} - \frac{\partial P_n}{\partial t} \right] - \nabla \left(\mathbf{k} \lambda_w \nabla P_w \right) = 0 \tag{1.5}$$

$$- C_w \left[\frac{\partial P_w}{\partial t} - \frac{\partial P_n}{\partial t} \right] - \nabla \left(\mathbf{k} \lambda_n \nabla P_n \right) = 0 \tag{1.6}$$

The inverse function only exists if the capillary-pressure gradient is greater than zero. In many practical examples, for instance in the case of discrete fractures or transitions between two heterogeneous medium, the capillary pressure gradient is very small or even zero, so that the pressure formulation cannot be chosen (Hinkelmann, 2005). A regularization approach is needed in this case that can be done by artificially adding capillary diffusion to the system. Consequently, the application range of the pressure formulation is rather limited. For this reason, this formulation is not considered in this work.

Saturation formulation

Darcy's law for a wetting and a non-wetting phase, assuming that both phases are incompressible, can be formulated using Eq.(1.1) combined with Equation Eq.(1.4) as

$$\mathbf{u}_w = -\lambda_w \mathbf{k} \left(\nabla P_w - \rho_w \mathbf{g} \right) \tag{1.7}$$

and

$$\mathbf{u}_n = -\lambda_n \mathbf{k} \left(\nabla P_w + \nabla P_c - \rho_n \mathbf{g} \right) \tag{1.8}$$

Eliminating the wetting phase pressure between Eq.(1.7) and Eq.(1.8) gives

$$\mathbf{u}_w = \frac{\lambda_w}{\lambda_n} \mathbf{u}_n + \lambda_w \mathbf{k} \left[\nabla P_c + \left(\rho_w - \rho_n \right) \mathbf{g} \right] \tag{1.9}$$

By introducing the total velocity of the two-phase system, $\mathbf{u}_t = \mathbf{u}_w + \mathbf{u}_n$ and fractional flow function $f_w = \lambda_w / (\lambda_w + \lambda_n)$ and $\bar{\lambda} = \lambda_w \lambda_n / (\lambda_w + \lambda_n)$ into Eq.(1.9) yields

$$\mathbf{u}_w = f_w \mathbf{u}_t + \bar{\lambda} \mathbf{k} \left[\frac{\partial P_c}{\partial S_w} \nabla S_w + \left(\rho_w - \rho_n \right) \mathbf{g} \right] \tag{1.10}$$

which can be further inserted into the wetting phase mass balance equation, Eq.(1.2). The system is then reduced to one equation with S_w as a primary variable.

$$\phi \frac{\partial S_w}{\partial t} + \nabla \cdot \left[f_w \mathbf{u}_t + \bar{\lambda} \mathbf{K} \frac{\partial P_c}{\partial S_w} \nabla S_w \right] = 0 \tag{1.11}$$

Two major problems in this formulation are that, first; the total velocity must be known in advance, and second; it results into a hyperbolic formulation for small capillary pressure gradients. If the saturation equation is assumed to be advection–dominated, standard methods of finite difference, finite element or finite volume do not perform well. They show nonphysical oscillations and mesh orientation sensitivity. Therefore, this formulation is not considered in this study.

Pressure-Saturation formulation

In a pressure–saturation formulation, one of the phases' pressures and one of the phases' saturations are eliminated, using the constitutive relations. There are two main versions of this formulation: the (P_n, S_w) and the (P_w, S_n). They are directly derived from Eq.(1.2) with the relations:

$$\nabla P_n = \nabla P_c + \nabla P_w \tag{1.12}$$

and

$$\frac{\partial S_w}{\partial t} = -\frac{\partial S_n}{\partial t} \tag{1.13}$$

The differential equations of the wetting and non-wetting phase for (P_n, S_w) formulation read as follows:

$$\nabla \cdot \left(\lambda_w \frac{\partial P_c}{\partial S_w} \mathbf{k} \nabla S_w - \lambda_t \mathbf{k} \nabla P_n \right) = 0 \tag{1.14}$$

$$\phi \frac{\partial S_w}{\partial t} + \nabla \cdot \left(\lambda_w \frac{\partial P_c}{\partial S_w} \mathbf{k} \nabla S_w - \lambda_w \mathbf{k} \nabla P_n \right) = 0 \tag{1.15}$$

15

For many cases, the pressure-saturation formulation represent the most suitable equations. These two equations are a strongly coupled highly non-linear system of equations of a mixed parabolic/hyperbolic type. The degree of advection domination depends on flow conditions and capillary pressure. Eq.(1.14) is a dissipative-convective quasi steady-state equation, and Eq.(1.15) is marching with time. The major advantage lies in the fact that they are not limited to small capillary-pressure gradients, i.e. the pressure-saturation formulation can be applied to discrete fractured systems and heterogeneous media. All equations presented in this study are adopted for a (P_n, S_w) formulation.

Mathematical model in this work

All formulations in this work are based on the averaging theory. Averaging theories offer the possibility of a good understanding of the microscopic scale and its relation to the macroscopic one, which is the natural domain of all continuum mechanical models. For a full development, the reader is referred to Hassanizadeh and Gray (1979a) and Lewis and Schrefler (1998). The averaging theory has also been described by Musivand and Al-Khoury (2014), from whom this outline is derived.

Within the averaging theory we make use of macroscopic variables, which correspond to real measurable quantities directly linked to laboratory measurements. The macroscopic balance equations applied in the model were obtained from balance equations at macroscopic level by use of a local volume/mass averaging of the corresponding microscopic quantities. Some interfacial effects are explicitly accounted for, including the possibility of exchange of mass, momentum and energy between the constituents. The averaging process is conducted by integrating the involved microscopic quantities over a REV of volume dv and area da. At the microscopic level, the conservation equation of phase π of a multiphase system can be described as:

$$\frac{\partial}{\partial t}(\rho\psi) + \text{div}(\rho\psi\dot{\mathbf{r}}) - \text{div}\,\mathbf{i} - \rho b = \rho G \qquad (1.16)$$

in which ψ is a generic conserved variable, which might be mass, linear momentum or energy; ρ is the mass density of phase π; $\dot{\mathbf{r}}$ is the local value of the velocity field at a fixed point in space; $\mathbf{i}$ is the flux vector; b is the external supply of ψ; and G is the net production of ψ. At the interface between two phases, π and α for instance, the following constraint holds:

$$[\rho\psi(\mathbf{w} - \dot{\mathbf{r}}) + \mathbf{i}]|_\pi \cdot \mathbf{n}_{\pi\alpha} + [\rho\psi(\mathbf{w} - \dot{\mathbf{r}}) + \mathbf{i}]|_\alpha \cdot \mathbf{n}_{\alpha\pi} = 0 \qquad (1.17)$$

where $\mathbf{w}$ is the interface velocity, and $\mathbf{n}_{\pi\alpha}$ is the unit normal vector pointing out of phase π and towards phase α, with $\mathbf{n}_{\pi\alpha} = -\mathbf{n}_{\alpha\pi}$. This equation indicates that it is possible to transport mass, momentum and energy between interacting constituents.
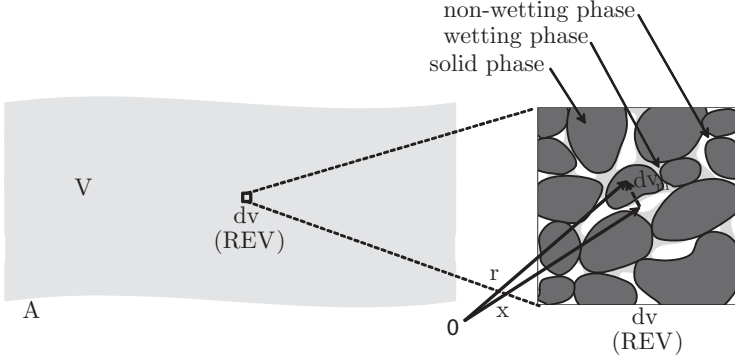
Figure 1.2: REV of a multiphase medium

Consider a multiphase medium occupying a total volume V, and bounded by a surface area A. The constituents, $\pi = 1, 2, \ldots, k$, have the partial volumes V_π. Each point within the total volume V is considered as the centroid of a REV with volume dv, described by a position vector $\mathbf{x}$. The volume of a microscopic element is denoted by dv_m, described by a position vector $\mathbf{r}$ (Figure 1.2). The average volume element of π constituent within REV is defined as:

$$dv_\pi(\mathbf{x}, t) = \int_{dv} \gamma_\pi(\mathbf{r}, t) \, dv_m \tag{1.18}$$

where $\gamma_\pi(\mathbf{r}, t)$ is a phase distribution function, defined as:

$$\gamma_\pi(\mathbf{r}, t) = \begin{cases} 1 & \text{for } \mathbf{r} \in dv_\pi \\ 0 & \text{for } \mathbf{r} \in dv_\alpha, \ \alpha \neq \pi \end{cases} \tag{1.19}$$

This distribution function describes the step discontinuity at the interface between different constituents. The same is valid for the microscopic area element da_m and the average area element da_π. Following these definitions, the concept of volume fraction, η_π, which is an important parameter in multiphase modeling, can be introduced, as

$$\eta_\pi(\mathbf{x}, t) = \frac{dv_\pi}{dv} = \frac{1}{dv} \int_{dv} \gamma_\pi(\mathbf{r}, t) \, dv_m \tag{1.20}$$

with

$$\sum_{\pi=1}^{k} \eta_\pi = 1 \tag{1.21}$$

Volume fractions of a porous material consisting of solid, s, wetting phase (water), w, and non-wetting phase (CO_2), n, are defined as:

- solid phase: $\eta_s = 1 - \phi$, where $\phi = (dv_w + dv_n)/dv$ is the porosity.

- wetting phase: $\eta_w = \phi S_w$, where $S_w = dv_w/(dv_w + dv_n)$ is the degree of wetting phase saturation.

- non-wetting phase: $\eta_n = \phi S_n$, where $S_n = dv_n/(dv_w + dv_n)$ is the degree of non-wetting phase saturation.

Introducing ζ as any microscopic field variable, important averaging operators can be introduced, as:

volume average operator:

$$\langle \zeta \rangle_\pi (\mathbf{x}, t) = \frac{1}{dv} \int_{dv} \zeta(\mathbf{r}, t) \, \gamma_\pi(\mathbf{r}, t) \, dv_m \tag{1.22}$$

intrinsic volume average operator:

$$\langle\langle \zeta \rangle\rangle_\pi (\mathbf{x}, t) = \frac{1}{dv_\pi} \int_{dv} \zeta(\mathbf{r}, t) \, \gamma_\pi(\mathbf{r}, t) \, dv_m \tag{1.23}$$

The relationship between the volume average operator (also known as phase average operator) and the intrinsic operator can then be written as:

$$\langle \zeta \rangle_\pi = \eta_\pi \langle\langle \zeta \rangle\rangle_\pi \tag{1.24}$$

mass average operator::

$$\bar{\zeta}_\pi(\mathbf{x}, t) = \frac{\int_{dv} \rho(\mathbf{r}, t) \, \zeta(\mathbf{r}, t) \gamma_\pi(\mathbf{r}, t) \, dv_m}{\int_{dv} \rho(\mathbf{r}, t) \, \gamma_\pi(\mathbf{r}, t) \, dv_m} \tag{1.25}$$

We also introduce a deviatoric operator, which describes perturbations around the mass average operator, given by:

$$\tilde{\zeta}_\pi(\mathbf{x}, \mathbf{r}, t) = \zeta(\mathbf{r}, t) - \bar{\zeta}_\pi(\mathbf{x}, t) \tag{1.26}$$

Accordingly, by applying a systematic averaging to the microscopic balance equation, Eq.(1.16), the averaged macroscopic conservation equation can be obtained as (Lewis and Schrefler, 1998):

$$\underbrace{\frac{\partial}{\partial t}(\langle \rho \rangle_\pi \bar{\psi}_\pi)}_{\text{storage}} + \underbrace{\text{div}\,(\langle \rho \rangle_\pi \bar{\psi}_\pi \bar{\mathbf{v}}_\pi)}_{\text{advection}} - \underbrace{\text{div}\,\mathbf{i}_\pi}_{\text{diffusion}} - \underbrace{\langle \rho \rangle_\pi \bar{b}_\pi}_{\text{external supply}} - \underbrace{\langle \rho \rangle_\pi e_\pi(\rho\psi)}_{\substack{\text{inter−phase interaction} \\ \text{due to mass exchange}}}$$

$$- \underbrace{\langle \rho \rangle_\pi I_\pi}_{\substack{\text{inter−phase} \\ \text{interaction}}} = \underbrace{\langle \rho \rangle_\pi \bar{G}_\pi}_{\text{net production}}$$

$$\tag{1.27}$$

subjected to:

$$\sum_{\pi} \langle \rho \rangle_{\pi} \left[e_{\pi}(\rho \psi) + I_{\pi} \right] = 0 \qquad (1.28)$$

where $\mathbf{i}_{\pi}$ is the flux vector associated with $\bar{\psi}_{\pi}$, $\bar{b}_{\pi}$ is an external supply associated with $\bar{\psi}_{\pi}$, and $\bar{\mathbf{v}}_{\pi}$ is the mass averaged velocity of phase π. The last two terms on the left-hand side of Equation (1.27) describe possible chemical and physical exchanges between phases, $e_{\pi}(\rho \psi)$ describes an exchange term associated with ψ due to phase changes or mass exchanges between phases, and I_{π} describes the mechanical interaction between phases.

To complete the description of flow and mechanical behavior, we now need to specify the constitutive equations. They express dependent variables of the continuum balance equations as the functions of the state variables. In general, the formulation used in this work relies on the following basic assumptions:

1. The CO_2 phase is modeled as a supercritical fluid with constant properties

2. Isotropic rock mechanical properties

3. Linear elastic deformation under small strain

4. No phase changes

5. No diffusion or dispersion in mass

The resulting field equations represent a coupled, strongly nonlinear set of partial differential equation for an unsaturated two-phase flow in both a homogeneous porous medium and a fractured porous medium. A continuum fracture model, namely the double porosity model, is adopted for the fractured porous medium (see Chapter 4).

The resulting governing equations are then rearranged for a (P_n, S_w) formulation. As it stated before, the pressure-saturation formulation yields the most suitable equations for many cases. Based on the flow conditions and capillary pressure, the equations are parabolic to hyperbolic functions. The advantage of the formulations is that the capillary pressure gradient $\frac{\partial P_c}{\partial S_w}$ is explicitly included, and hence, in contrast to the pressure-pressure formulation, it can be applied to systems with small capillary pressure gradients. This issue will be treated in the next chapters.

The next step in the modeling process is to translate the mathematical model into algorithms that can be treated and solved by computers. In general, the mathematical model of CO_2 geo-sequestration cannot be solved analytically. However, analytical and semi-analytical models do exist for simplified cases and are usually used for gaining physical insight into the phenomenon, to quickly assess potential storage sites and as a relatively simple comparative check on numerical modeling results. Available semi-analytical approaches (Dentz and Tartakovsky, 2009; Nordbotten,

2004; Nordbotten et al., 2004, 2005; Riaz et al., 2006; Saripalli and McGrail, 2002) use significant simplification.

1.3.3 Numerical modeling of CGS

In the mathematical sense, the governing partial differential equations are of a mixed hyperbolic/parabolic type, which has a major impact on the discretization methods. In what follows a brief discussion of the basic concepts in numerical modeling is given and then several numerical methods, used in the simulation of fluid flow in porous media are reviewed. The emphasis is placed on the development of finite element methods.

Numerical model characteristics

The features of the numerical model are typically selected with an effort to minimize the computational demand and also the processing time.

A discretization method must be *consistent*, i.e. the discretization error goes to zero as the temporal and spatial discretization sizes go to zero. The order of consistency is a measure of the speed at which a numerical method converges to the exact solution as the discretization becomes finer.

A discretization method must also be *stable*, this refers to how errors, which are generated during the solution of discretized equations, grow or decay in the solution. The aspect of numerical stabilization plays an important role when it comes to advective dominant flow simulations. There are many well-known stabilization techniques available in the literature, namely upwind schemes and streamline diffusion, as an example. However, the stabilization method may lead to numerical diffusion (smearing of the front), and not representing the exact solution. This emphasizes one major difficulty of numerical methods for advection-diffusion problems.

These important numerical characteristics can quantify how well the mathematics of a partial differential equation is represented, but they cannot identify how well the physics of the system is represented by a particular numerical method. A numerical model that violates the fundamental physics is in many respects just as defective as an unstable solution. Since mathematical models of fluid flow in porous media are based on conservation principles, similar principles should apply to the approximate solution. In a conservative numerical method the temporal change of an entity considered in a domain (mass or entropy for example) should be in equilibrium with the advective and diffusive fluxes across the boundaries plus source or sink terms. A good discretization method should be both locally and globally conservative, thus being in good agreement with the divergence structure of the original PDE. However

for some problems, depending on the nature and severity of the nonlinearity, global mass balance errors may not be totally eliminated even when very small time steps and fine meshes are used.

Classical numerical methods for CGS

Numerical simulations are employed to monitor and model the fate of the injected CO_2 and regional characterization of the reservoir and its caprock. They are also used to investigate the effect of various injection parameters such as injection rate, injection duration, and injection pressure on CO_2 storage efficiency and plume migration in a given reservoir.

The different processes involved in CO_2 injection into underground formation lead to a complicated numerical problem. Any attempt to model a whole region and to consider events happening at local areas will lead to enormous demands for computational power. Parallel computing with tens of computer processors and days of CPU time is not uncommon. This makes the development of numerical tools for CO_2 geo-sequestration difficult and rather expensive.

The first numerical simulators for the computation of multiphase flow in porous media were developed to solve problems in petroleum engineering (see Aziz and Settari, 1979; Peaceman, 1977), followed by solving hydrology and environmental problems, (see Falta et al., 1992; Helmig, 1997). The computational challenges of multiphase flow in oil reservoirs and CO_2 geo-sequestration cause a continuing development of numerical procedures and numerical software. There are several methods to solve time-dependent partial differential equations of multiphase flow in porous media. The three classical choices for the numerical solution of PDEs are: finite difference method (FDM), finite volume method (FVM) and finite element method (FEM). In this thesis, the finite element method is utilized.

Finite difference method

The finite difference method (FDM) is the oldest of the three methods considered here and its main advantage is its conceptual simplicity. Here, a grid with discrete points discretizes the domain of interest. The PDE of the particular field problem is locally transferred into a finite difference equation by using a Taylor expansion.

The finite difference method is the most commonly used numerical method for the simulation of multiphase flow in porous media. This method is straightforward and easy to implement. However, it is difficult to incorporate the high level of detailing of geological models into the flow models, and additionally serious numerical difficulties can arise. These difficulties involve oscillations in advective dominant processes and

near sharp fronts, mesh dependency, convergence problem and instabilities in the iterative and time stepping schemes. The FDM relies on the existence of derivatives and cannot easily satisfy the conservation principles and discontinuity conditions.

Several treatments have been proposed in the literature to avoid these difficulties, including upstream weighting of relative permeabilities and implicit iterative techniques, among others. One of the well-known methods that are employed in this regard is the Implicit Pressure Explicit Saturation (IMPES) (Chen et al., 2004; Coats, 2000; Monteagudo and Firoozabadi, 2007). In this scheme, the pressure equation is evaluated implicitly while the saturation equation is solved explicitly. The IMPES method is more stable than the fully implicit method because it considers the linear terms implicitly and solves the other terms explicitly. A comprehensive review of these techniques has been presented by Aziz and Settari (1979).

Finite volume method

The finite volume method (FVM) is a numerical method for solving PDEs that estimates the values of the conserved field variables averaged through the volume. In this method, volume integrals in a PDE that contain a divergence term are changed to surface integrals, using the divergence theorem. These terms are calculated as fluxes, at the surfaces of each finite volume.

The FVM allows the discrete representation of problems with irregular boundaries. Another advantage of the FVM is that, unlike the node-centered FDM, where the conservation principle is satisfied only if the grid size approaches zero, the FVM conserves the extensive quantity within each local cell.

Godunov (1959) introduced control-volume cell average interpretation in the discretization of the gas dynamics equations by assuming a piecewise constant solution representation in each control-volume with values equal to the cell average. The FVM is also suitable for discontinuity capturing and has been used in obtaining a solution to nonlinear hyperbolic conservation laws (Lax, 1954; LeVeque, 2002). The method is also very popular in the fluid flow in porous media literature, due to their stability and mass conservation. A high order finite volume method has been applied to two-phase flow by Durlofsky (1993) and Michel (2003). The method is used in the cell-centered form on structured meshes in Peaceman (1977) and on unstructured meshes in the TOUGH2 simulator (Pruess, 1991).

Finite element method

The finite element method (FEM) is a numerical method broadly used in different engineering disciplines. It belongs to the family of methods of weighted residual. Here, the residual, which is the difference between the exact solution and the approximate

solution, is weighted and minimized to obtain the best approximation.

FEM is the most flexible numerical method in terms of dealing with complex geometry and complicated boundary conditions. This flexibility is useful not only for irregularly shaped domains, but also for elements in regions where large field variations exist, and where a better accuracy is required. The FEM guarantees global mass and momentum conservation, which is a consequence of the formulation, because it states that the residual should vanish in the whole computational domain.

Another advantage of using FEM in fluid flow in porous media is that FEM provides a more flexible, realistic method to couple geomechanical deformation and transient fluid flow in porous media.

The standard Galerkin method produces accurate solutions to elliptic and parabolic transport equations as long as the Peclet number of the element is relatively small. However it often fails for incompressible Stokes problems and advection-dominated problems. In two-phase flow in porous media, if the saturation equation is advection–dominated, standard methods of FEM do not perform well. They either show nonphysical oscillations or numerical diffusion and mesh orientation sensitivity. Moreover, FEM is known to be accurate on homogeneous domains. Whereas, in the case of a medium involving discontinuities, which is common in CO_2 geo-sequestration, an undesired smearing effect occurs (Klausen and Russell, 2004). This is a direct result of the loss of local conservation property of the method.

The literature available on FEM is vast and the details of the methods and their applications can easily be found in e.g., Meek (1996); Zienkiewicz et al. (2005). Hughes et al. (2000) addressed the conservation issue of continuous finite element methods by showing that local conservation can be achieved by the correct computation of the flux. A complete presentation of the FEM applied to porous medium flow and transport can be found in Huyakorn (1983); Lewis et al. (1989); Pinder and Gray (1977). FEM is becoming more and more popular in implementing fully coupled geomechanics-reservoir simulation (Chin et al., 2002; Lewis and Sukirman, 1993; Noorishad et al., 1982).

Recently, a variety of advanced finite element techniques have been developed for the transport equations.

Advanced finite element methods

A major challenge in reservoir modeling and CO_2 injection processes is raised when the transport process is characterized by low level of physical dispersion and dominance of advection. In these problems with high gradient in the fluid front, the application of standard numerical procedures usually leads to spurious oscillations.

To attain a high level of accuracy and a stable result for the advection-dominant flow process, especially in a large domain, conventional simulators require a large number of finite elements and significant CPU time.

In recent years, a variety of advanced numerical methods have been proposed to overcome the shortcoming of conventional procedures. While finite difference and finite volume approximations are commonly used for solving subsurface flow equations, the focus here is on the finite element method, which is appealing as it is well-suited for unstructured spatial meshes in irregular domains and enables some types of enrichment. Different varieties of finite element methods are introduced in the literature, such as: stabilized finite element, control volume finite element (CVFE), discontinuous Galerkin method (DG), Multi-domain FEM, adaptive FEM, characteristic finite element method, and Extended FEM (XFEM).

Stabilized finite element

The stabilized finite element method is a class of numerical methods for the solutions of advection-dominated flow, which was developed, based on an Eulerian method. The Streamline Upwind Petrov-Galerkin method (SUPG) and Galerkin Least Square method (GLS) are most frequently used techniques in this regard. The SUPG can be considered as the first successful stabilization technique to eliminate oscillations in advection dominant problems. It was proposed by Brooks and Hughes (1982). In upwinding techniques, the node in the upstream direction of flow gives more weight to the solution than the node in the downstream. In the SUPG method, the shape function is perturbated in the direction of the flow. The SUPG has been extended by Hughes et al. (1989), to the Galerkin least-squares (GLS) method by adding residuals of the Euler-Lagrange equations in least-squares form to the standard Galerkin formulation. Hughes et al. (1989) showed similar stabilization by modifying time stepping forms of the associated transient problems. Further elaborations of the stabilized finite element methods for porous medium flow problems can be found in Masud and Hughes (2002) and Brezzi et al. (2005).

Control volume finite element

An attractive numerical method for solving transport equations is the control volume finite element method (CVFEM), which is a hybrid method that combines the advantages of the finite element method and the finite volume method. In this method, the solution of elliptic problems is sought in a finite dimension space of piecewise smooth functions by using a finite set of control volumes defined by the triangles. Control volumes can be created across grid nodes by connecting the midpoints of the edges of a triangle with a point inside the triangle. These types of

discretization were first introduced by Lemonnier et al. (1979) for reservoir simulation. CVFEM with irregular grid has been applied in simulation of the complex geometry reservoir (Forsyth, 1990; Heinemann et al., 1991; Rozon, 1989).

Different types of CVFEM have been developed with a different name like box method, generalized difference method and element based control volume method (EbFVM). As discussed by Cordazzo et al. (2004) in the majority of the CVFEM methods, the approximate equations for multiphase flow are achieved from a single phase flow and then to obtain the multiphase flow equation, the transmissibilities are multiplied by the mobilities. As a result, this method can exhibit non-physical behavior in several situations.

Discontinuous Galerkin method

The discontinuous Galerkin method (DGM) is a special type of finite element method that uses piecewise continuous basis and testing functions that may be discontinuous across element boundaries, consequently obtaining more robustness for a discontinuous process.

DGM was first developed for solving advection problems for which continuous finite element methods lack robustness. Advantages of the discontinuous Galerkin method are supporting non-structured and non-conforming meshes, conserve mass locally and globally, little numerical diffusion and increase the order of accuracy. In general, the discontinuous Galerkin method locally conserves mass, but loses continuity and needs additional stabilization terms in the weak formulation. Moreover, this method introduces further degrees of freedom, which makes it an expensive procedure compared to traditional continuous finite element methods.

Recently, discontinuous Galerkin methods have been applied to a variety of flow and transport problems and due to their flexibility, they have been shown to be competitive to standard methods. The applications of this method in fluid flow in porous media were investigated by different authors (Bastian, 2003; Epshteyn and Riviere, 2007; Riviere, 2004; Sun and Wheeler, 2005).

Multi-domain FEM

In the multi-domain finite element method, instead of a single FE space used in a Galerkin finite element, two or more different approximation spaces are used. Here due to the complexity of the geometry or discontinuity in the solution a multiblock domain structure is used. The computational domain is decomposed into non-overlapping subdomains with meshes constructed independently of each subdomain.

The multi-domain finite element method is well suited for the reservoir simulation

due to its accurate approximation of the velocity, and proper treatment of discontinuities. The method can treat discontinuities in the medium because of inherent flux continuity condition in the formulation.

Douglas et al. (1983) used a multi-domain finite element method for the pressure equation and a Galerkin finite element method for the concentration equation. Wheeler, Yotov and co-workers (Arbogast and Yotov, 1997; Wheeler and Yotov, 2000, 2006) developed a mixed finite element discretization for second order elliptic equations. The continuity of flux is imposed via a mortar finite element space on a coarse grid scale, while the equations in the coarse elements (or sub-domains) are discretized on a fine grid scale

Adaptive FEM

Adaptive methods are other numerical schemes that automatically adjust numerical processes to minimize the discretization errors and improve approximate solutions by a posteriori error estimation. Adaptive techniques try to automatically refine a mesh or adjust the basis to attain a solution with a specified accuracy in an optimal fashion. For example using a dynamic refinement treats localized phenomena such as high gradients and sharp fronts in multiphase flow in porous media.

Although adaptive methods have been studied for several years, little is known about optimal strategies. The main adaptive procedures used in the literature include:

- *h refinement*: local refinement of a mesh

- *r refinement*: relocating a mesh

- *p refinement*: locally varying the polynomial degree of the basis

An h adaptive strategy involves processing the error information, represented by error estimators, to determine the refinement level on which a new mesh can be constructed. In r refinement the nodes of the initial mesh are moved or relocated during multiple passes of mesh relaxation. At each pass, each node of the mesh is moved in a direction that tends to equalize the error of the elements that share the node. The function is then re-evaluated at the new node location. r refinement alone is generally not capable of finding a solution with a specified accuracy, if the mesh is too coarse. This type of refinement is more useful for transient problems, where elements move to follow an evolving phenomenon. With p refinement the mesh is not changed but the order of the finite element basis is varied locally over the domain. Compared to pure h adaptive methods, hp adaptive methods require the choice of h or p type adaption for each element. Conceptually, it is more common to

believe that h refinements near singularities or steep fronts are more appropriate. In practice, it is a popular approach for elliptic problems to choose the order by selecting between p refinement and competitive h refinement. However, this strategy becomes more expensive as the order of approximations increases (Moore, 2001).

Adaptive local mesh refinement approaches in two-phase flow are first considered by Heinemann et al. (1983) and Ewing et al. (1989). In the adaptive mesh refinement methods the computed velocity, obtained from the pressure equation, verifies the location of the sections where local refinement will be needed at the next time step. Different adaptive methods, error estimators and indicators, as well as refinement and coarsening strategies, are explained in Bear and Cheng (2010).

Extended FEM (XFEM)

As it was mentioned, in the classical finite element, mesh refinement is needed near a high gradient region in modeling of evolution problems. This refinement can increase the computational effort. Moreover, mesh-refinement is often not a fully instinctive procedure, and user-controlled modifications are required. As an alternative method, Belytschko's group in 1999 (Belytschko and Black, 1999), utilized the idea of partition of unity enrichment of the finite elements for the simulations of cracks in structures by allowing the discontinuities to be independent of the mesh. The main idea in this method, known also as extended finite element method (XFEM), is to extend a classical approximate solution basis by a set of enrichment functions to capture the discontinuity or high gradient in the problem. For the case of cracks in structures, a Heaviside jump function is used to capture the jump across the crack faces. As a consequence, simple, fixed meshes can be used throughout the simulation and mesh construction and maintenance are reduced to a minimum

In the classical finite element methods, the domain of the problem, Ω is subdivided into elements Ω_e associated with a set of nodes. The approximation of a field variable u is written as:

$$u(x,t) = \sum_{I \in \mathbb{N}} \mathbf{N}_I(x)\mathbf{u}_I(t) \tag{1.29}$$

while in XFEM, the approximation is enriched as:

$$u(x,t) = \underbrace{\sum_{I \in \mathbb{N}} \mathbf{N}_I(x)\mathbf{u}_I(t)}_{\text{standard}} + \underbrace{\sum_{J \in \mathbb{N}_{enr}} \mathbf{N}_J^*(x,t)\mathbf{a}_J(t)}_{\text{enrichement}} \tag{1.30}$$

where

- $\mathbb{N}$ is the set of all nodes in the domain

- $\mathbf{N}_I(x)$ are the standard shape functions associated to the degree of freedom at node I

- $\mathbf{u}_I(t)$ are the nodal values for the standard finite element approximation

- $\mathbb{N}_{enr}$ is the set of all enriched nodes

- $\mathbf{N}_J^*(x,t)$ are the local enrichment shape functions at an enriched node J

- $\mathbf{a}_J(t)$ are additional nodal parameters

One of the main advantages of XFEM is the flexibility it gives in the choice of the enrichment functions for different problems. In general the enrichment shape functions capture the behavior of the solution near the interface. This is particularly useful for problems involving a discontinuity or high gradient. In general, the enrichment shape functions are defined as multiplication of standard shape function and an enrichment function $\psi_J(x,t)$:

$$\mathbf{N}_J^*(x,t) = \mathbf{N}_J(x).\,\psi_J(x,t) \tag{1.31}$$

There are several works in the literature devoted to the selection of the enrichment function. Typical choices for the enrichment functions are the sign function and the Heaviside enrichments. For more details on the history of development of these methods the reader is referred to Fries and Belytschko (2010) and the references therein.

XFEM is a relatively robust and efficient method, which is now used for industrial problems; however, the implementation of it is not straightforward. It has been applied to a wide range of problems, such as fracture mechanics, modeling heterogeneous media (holes, material inclusions), thermal and phase change problems, fluid-structure interaction, high gradient problems and immiscible two-phase flow.

XFEM was successfully applied for crack propagation and other fields in computational physics (e.g. Dolbow and Belytschko, 1999; Sukumar et al., 2001; Wells and Sluys, 2001). The method has been employed to simulate crack growth without remeshing for both two-dimensional and three-dimensional problems (Dolbow et al., 2000; Sukumar and Belytschko, 2000).

XFEM is a promising method to simulate immiscible two-phase flow, which is a coupled problem between velocity and pressure fields. The velocity and pressure fields can show either weak or strong discontinuities in a domain. This method is used by Wagner et al. (2001) and Chessa and Belytschko (2003b) for the simulation of two-fluid flows without surface-tension effects solving the Navier-Stokes equations.

The XFEM framework has also been used for the modeling of fluid-structure interaction (e.g. Legay et al., 2006; Wang et al., 2008). The combined XFEM fluid-

structure-contact interaction method allows computing contact of arbitrarily moving and deforming structures embedded in an arbitrary flow field (Mayer et al., 2009).

Abbas et al. (2010) employed the XFEM with the aim to approximate advection-dominant problems without stabilization or mesh refinement. A regularized enrichment function is proposed that enables the approximation to capture arbitrary high gradients.

Al-Khoury and Sluys (2007) coupled the double porosity model with XFEM and presented a computational model for the fracturing process in a porous medium. In their work XFEM is used for describing the fracturing process, and the double porosity model is used for describing the resulting fluid flow.

Coupling interface-tracking procedures with the XFEM can provide a procedure with accurate results for problems with moving interfaces without remeshing. Sukumar et al. (2001) were the first to combine the XFEM with a level set (LS) method to make the enrichment function related to interfaces. By coupling level set with XFEM, it is not only possible to track where the enrichment function is needed but it also facilitates the assembly of the enrichment.

The level set method was first introduced by Osher and Sethian (1988) for capturing moving fronts. This method makes use of a distance function, referred to as the level-set function, which labels every point with a sign and a value. The sign indicates the fluid domain and the value represents the shortest distance to the interface. As such this function is equal to zero at the interface itself and non-zero in the fluids. The interface is advected with a local flow velocity, using any of the known advection equations. The LS method has found many applications ranging from two-fluid flow simulation, to structure optimization, in the image processing and flame propagation (Osher and Fedkiw, 2001). Chessa and Belytschko (2003a) applied a coupled level set-XFEM technique for modeling a two-phase immiscible flow problem. The level set method was used to track the phase interface and then the enriched basis is constructed directly in terms of the level set function.

In this thesis, XFEM-LS is utilized to develop a computational model for the simulation of coupled hydromechanical and electrokinetic flow in a porous medium.

1.4   Research Objectives

Despite that CO_2 sequestration in geological formations is a relatively new technology, an enormous amount of theoretical and experimental work has already been conducted. Numerical codes at both academic and commercial level, such as CMG, DuMux, Eclipse, FEHM, GeoSys, IPARS-CO_2, MUFTE, RockFlow, SIMUSCOPP, TOUGH and its derivatives, among others, are already in use. Finite difference, finite volume

and, to a lesser extent, finite element methods have been employed. A well-addressed comparison between different commercial and academic codes for simulating a CO_2 leakage problem has been presented by Pruess et al. (2002).

As illustrated earlier, these methods have their own advantages and disadvantages, but in general, the use of standard discretization schemes require fine meshes (or grids) to capture the moving front and to eliminate the possible occurrence of numerical oscillation due to advection. On the other hand, the use of an advanced discretization procedure, such as the discontinuous Galerkin or the multiscale finite element, generates a large system of equations that requires powerful computational capacity.

To tackle the issue of the computational demands associated with modeling CO_2 sequestration in geological formations, in this work, a computationally efficient numerical model based on a mixed discretization scheme is introduced. Focus is placed on the computational aspects of this problem, though maintaining the essential physics. The standard Galerkin finite element method is utilized to discretize the deformation and the diffusive dominant field equations, and the extended finite element method, together with the level-set method, is utilized to discretize the advective dominant field equations. The level set method is employed to trace and locate the CO_2 plume front, and the extended finite element method is employed to model the associated high gradient in the saturation field front. Physically, for such an application, capturing and modeling the front of the CO_2 plume is not very important, but numerically, it is vital that the discretization scheme leads to an accurate and conservative system. The use of XFEM for the advective field leads to locally conservative discretization, giving a stable and convergent scheme. By such a coupling, a numerical scheme that is stable and effectively mesh-independent can be obtained. This technique is utilized in this thesis and applied to different applications involving different fields behavior.

To facilitate the formulation of the computational model and its computer implementation, several assumption were made. The thermodynamic parameters, such as the density and viscosity are made constant. The material behavior under the mechanical forces is assumed to be linear elastic. Also, it is assumed that there is no dissolution or chemical reaction in the reservoir. Though, many other physical and modeling aspects, including the type of balance equations, unsaturated multiphase flow, buoyancy effect, capillary effect, deformation and electrokinetic flow in a CO_2 environment, are carefully considered.

1.5 Thesis outline

This thesis is based on three peer reviewed and published journal papers (Appendix A). It is divided into five chapters, of which Chapters 2, 3 and 4 comprise the main body. The chapters are organized as follows.

In Chapter 2, a computationally efficient finite element model for the simulation of isothermal immiscible two-phase flow in a rigid porous medium with a particular application to CO_2 sequestration in underground formations is presented. Focus is placed on developing a numerical procedure, which is effectively mesh-independent and suitable for problems at regional scales. Chapter 2 is based on an extended version of Paper I (Talebian et al., 2013a).

Chapter 3 deals with the simulation of coupled electrokinetic and hydromechanical flow in a multiphase domain. This chapter extends the model introduced in Chapter 2, to include hydromechanical coupling and the incorporation of flow associated streaming potential. Chapter 3 is based on an extended version of Paper II (Talebian et al., 2013b).

Chapter 4 is an extension of Chapter 3 where the concept of a mixed discretization method is elucidated with application in coupled multiphysics processes of CO_2 sequestration in fractured porous media. The governing field equations are derived based on the averaging theory and the double porosity model. Chapter 4 is based on an extended version of Paper III (Talebian et al., 2013c).

Chapter 5 concludes the thesis with the essential results of this research as well as its implications and potentials.

Two Phase Flow in a rigid porous medium domain

2

This chapter is based on Talebian et al. (2013a), a paper published in the International Journal of Numerical Methods for Heat and Fluid Flow.

2.1   Introduction

In this chapter, a computationally efficient, accurate and consistent model capable of simulating multiphase flow at a regional scale is introduced. The averaging theory, presented in Chapter 1, is utilized to describe the mathematical model, and the coupling between the extended finite element method (XFEM) and the level-set method (LS) is utilized to formulate the numerical model. In the averaging theory, the transport effects at microscopic level are, by definition, taken into consideration, alleviating thus the need for multiscale modeling techniques. The coupling between XFEM and LS is utilized to trace and model the CO_2 plume front. Physically, for such an application, capturing and modeling the front of the CO_2 plume is not very important, but numerically, it is vital that the discretization scheme leads to an accurate and conservative system. By such a coupling, a numerical scheme that is stable and effectively mesh-independent can be obtained.

In what follows, a description of the governing equations and the involved constitutive relationships is given. Based on the averaging theory, the pressure-saturation balance equation of an isothermal two-phase fluid is derived (see Chapter 1) . Then, a detailed formulation of the numerical model and the discretization procedure, including linearization of the system and its time integration, is introduced. Later on, numerical examples illustrating the accuracy, stability, mesh insensitivity and convergence of the model are given.

2.2 Governing Equations

As it was stated in Chapter 1, the macroscopic balance equation can be obtained by applying averaging theory as proposed by, among others, Hassanizadeh and Gray (1979a), to the microscopic balance equation. In the averaging approach, the flow events at the microscopic level are mapped to the macroscopic level on the basis of the thermodynamic principles. The mapping is done by integrating the microscopic fractional volume of each individual constituent over a representative elementary volume (REV), representing a field of macroscopic multiphase medium. The multiphase medium is described as a superposition of all phases involved, but the state of motion of each phase is described independently, leading to a detailed description of their interactions. Based on the averaging theory, the averaged macroscopic conservation equation of phase π in a multiphase medium can be described as

$$\frac{\partial}{\partial t} \left(\langle \rho \rangle_\pi \bar{\psi}_\pi \right) + \mathrm{div} \left(\langle \rho \rangle_\pi \bar{\psi}_\pi \, \bar{\mathbf{v}}_\pi \right) - \mathrm{div} \, \mathbf{J}_\pi - \langle \rho \rangle_\pi \bar{b}_\pi = \langle \rho \rangle_\pi \bar{G}_\pi \qquad (2.1)$$

where the bar $(\bar{\cdot})$ indicates an intrinsic averaged quantity, $\bar{\psi}_\pi$ is a generic thermodynamic variable, which might be mass, linear momentum or energy and $\langle \rho \rangle_\pi$ is the volume-averaged mass density of phase π.

This equation can be specialized to formulate the linear momentum balance and the mass balance equations of a multiphase material. Derivations of these equations are elegantly presented in Lewis and Schrefler (1998). Following this, the governing partial differential equations of a coupled three-phase material constituting soil, water and gas (CO_2) can be presented.

In this chapter, focus is placed on two-phase flow in a rigid porous medium, but for completeness, the equilibrium equations are first introduced, then the governing equations are reduced to describe an incompressible fluid and solid medium.

2.2.1 Equilibrium equations

For a three-phase medium constituting solid, water and gas, the linear momentum balance equation in terms of the total stress tensor, $\boldsymbol{\sigma}$, under a static condition, can be expressed as

$$\nabla \cdot \boldsymbol{\sigma} \, + \, \bar{\rho} \mathbf{g} \, = \, 0 \qquad (2.2)$$

in which $\mathbf{g}$ is the gravity force vector and $\bar{\rho}$ is the average mass density, given by

$$\rho \, = \, (1 - \phi) \, \rho_s \, + \, \phi \, S_w \rho_w + \phi S_g \rho_g \qquad (2.3)$$

where ρ_s is the solid density, ρ_w is the water density, ρ_g is the gas (CO_2) density, S_w is water saturation, S_g is gas saturation and ϕ is the porosity. The total stress is defined as

$$\boldsymbol{\sigma} \;=\; \boldsymbol{\sigma}'' \;-\; \mathbf{m}^T \alpha \left(S_w P_w + S_g P_g \right) \tag{2.4}$$

in which, $\boldsymbol{\sigma}''$ is the effective stress, P_w and P_g are water and gas pressure, $\mathbf{m}^T = [1, 1, 1, 0, 0, 0]^T$ and α is Biot's coefficient, describes the compressibility of the material.

2.2.2 Mass continuity equations

The continuity equations for the water phase and the CO_2 phase, in isothermal condition, and neglecting phase exchanges, can be expressed as (Lewis and Schrefler, 1998):

Water phase:

$$
\begin{aligned}
&\left(\frac{\alpha - \phi}{K_s} S_w^2 + \frac{\phi S_w}{K_w} \right) \frac{\partial P_w}{\partial t} + \frac{\alpha - \phi}{K_s} S_w S_g \frac{\partial P_g}{\partial t} \\
&\quad + \alpha\, S_w \mathbf{m}^T \frac{\partial \boldsymbol{\epsilon}}{\partial t} + \left(\frac{\alpha - \phi}{K_s} P_w S_w - \frac{\alpha - \phi}{K_s} P_g S_w + \phi \right) \frac{\partial S_w}{\partial t} \\
&\quad + \nabla \cdot \left[\frac{\mathbf{k} k_{rw}}{\mu_w} \left(-\nabla P_w + \rho_w\, \mathbf{g} \right) \right] \;=\; Q_w
\end{aligned}
\tag{2.5}
$$

Gas phase:

$$
\begin{aligned}
&\left(\frac{\alpha - \phi}{K_s} S_w S_g \right) \frac{\partial P_w}{\partial t} + \left(\frac{\alpha - \phi}{K_s} S_g^2 + \frac{\phi S_g}{K_g} \right) \frac{\partial P_g}{\partial t} \\
&\quad + \alpha\, S_g \mathbf{m}^T \frac{\partial \boldsymbol{\epsilon}}{\partial t} - \left(\frac{\alpha - \phi}{K_s} S_g \left(P_g - P_w \right) + \phi \right) \frac{\partial S_w}{\partial t} \\
&\quad + \nabla \cdot \left[\frac{\mathbf{k} k_{rg}}{\mu_g} \left(-\nabla P_g + \rho_g\, \mathbf{g} \right) \right] \;=\; Q_g
\end{aligned}
\tag{2.6}
$$

in which K_s, K_w and K_g are the bulk modulus of the solid, water and gas respectively, $\mathbf{k}$ is the absolute permeability, k_{rw} and k_{rg} are water and CO_2 relative permeability (functions of saturation), Q_w and Q_g are source or sink terms and μ_w, μ_g are water and CO_2 viscosities and $\boldsymbol{\epsilon}$ is the strain vector.

The water and the gas are jointly occupying the voids, implying:

$$S_w + S_g = 1 \tag{2.7}$$

and

$$P_c \left(S_w \right) = P_g - P_w \tag{2.8}$$

where $P_c(S_w)$ is the capillary pressure, empirically a function of water saturation.

Equations. (2.2), (2.5) and (2.6), together with the constraints in Eqs. (2.7) and (2.8), represent a strongly coupled system of partial differential equations that is highly nonlinear due to the dependency of the capillary pressure and the relative permeability on the degree of saturation. The strong coupling and the associated non-linearity are known to introduce numerical difficulties, especially at low capillary pressure and/or high advection. In such cases, this set of equations behaves like a hyperbolic function, causing spurious oscillations. To reduce the effects of this coupling, different models have been introduced. Here, we adopt the saturation-pressure formulation, in particular gas pressure-water saturation.

Using Eq. (2.8) and applying the chain rule, the water pressure can be eliminated from Eqs. (2.5) and (2.6) by considering

$$\nabla P_w = \nabla P_g - \frac{\partial P_c}{\partial S_w} \nabla S_w \tag{2.9}$$

$$\frac{\partial P_w}{\partial t} = \frac{\partial P_g}{\partial t} - \frac{\partial P_c}{\partial t} = \frac{\partial P_g}{\partial t} - \frac{\partial S_w}{\partial t} \frac{\partial P_c}{\partial S_w} \tag{2.10}$$

Substituting Eqs. (2.9) and (2.10) into Eq. (2.5), and rearranging, gives

$$\begin{aligned} & d_1 \frac{\partial P_g}{\partial t} + d_2 \frac{\partial S_w}{\partial t} + \alpha\, S_w \mathbf{m}^T \frac{\partial \boldsymbol{\epsilon}}{\partial t} \\ & + \nabla \cdot \left(-\mathbf{k}\lambda_w \nabla P_g + \frac{\partial P_c}{\partial S_w} \mathbf{k}\lambda_w \nabla S_w + \mathbf{k}\lambda_w \rho_w\, \mathbf{g} \right) = Q_w \end{aligned} \tag{2.11}$$

Similarly, substituting Eqs. (2.9) and (2.10) into (2.6), gives:

$$d_3 \frac{\partial P_g}{\partial t} + d_4 \frac{\partial S_w}{\partial t} + \alpha\, S_g \mathbf{m}^T \frac{\partial \boldsymbol{\epsilon}}{\partial t} + \nabla \cdot \left[-\mathbf{k}\lambda_g \nabla P_g + \mathbf{k}\lambda_g\, \rho_g\, \mathbf{g} \right] = Q_g \tag{2.12}$$

where

$$d_1 = \frac{\alpha - \phi}{K_s} S_w + \frac{\phi S_w}{K_w} \tag{2.13}$$

$$d_2 = -\frac{\alpha - \phi}{K_s} P_c S_w + \phi - \frac{\alpha - \phi}{K_s} S_w^2 \frac{\partial P_c}{\partial S_w} - \frac{\phi S_w}{K_w} \frac{\partial P_c}{\partial S_w} \tag{2.14}$$

$$d_3 = \frac{\alpha - \phi}{K_s} - S_w \frac{\alpha - \phi}{K_s} + \frac{\phi(1 - S_w)}{K_g} \tag{2.15}$$

$$d_4 = -\frac{\alpha - \phi}{K_s} P_c + \frac{\alpha - \phi}{K_s} S_w P_c - \phi - \frac{\alpha - \phi}{K_s} S_w \frac{\partial P_c}{\partial S_w} + \frac{\alpha - \phi}{K_s} S_w{}^2 \frac{\partial P_c}{\partial S_w} \tag{2.16}$$

$$\lambda_w = \frac{k_{rw}}{\mu_w} \tag{2.17}$$

$$\lambda_g = \frac{k_{rg}}{\mu_g} \tag{2.18}$$

For an incompressible fluid and solid medium, Eqs. (2.13)-(2.16) reduce to

$$
\begin{aligned}
d_1 &= 0 \\
d_2 &= \phi \\
d_3 &= 0 \\
d_4 &= -\phi
\end{aligned}
\tag{2.19}
$$

Ignoring source/sink terms and substituting Eq. (2.19) into Eqs. (2.11) and (2.12) gives

$$
\phi \frac{\partial S_w}{\partial t} + \nabla \cdot \left(-\mathbf{k}\lambda_w \nabla P_g + \frac{\partial P_c}{\partial S_w} \mathbf{k}\lambda_w \nabla S_w + \mathbf{k}\lambda_w \rho_w \, \mathbf{g} \right) = 0
\tag{2.20}
$$

$$
-\phi \frac{\partial S_w}{\partial t} + \nabla \cdot \left[-\mathbf{k}\lambda_g \nabla P_g + \mathbf{k}\lambda_g \, \rho_g \, \mathbf{g} \right] = 0
\tag{2.21}
$$

Adding Eq. (2.21) to Eq. (2.20), and leaving Eq. (2.20) unmodified, the gas pressure-water saturation formulation can be expressed as

$$
\nabla \cdot \left(\lambda_w \frac{\partial P_c}{\partial S_w} \mathbf{k}\nabla S_w - \lambda_t \mathbf{k}\nabla P_g + (\lambda_w \rho_w + \lambda_g \rho_g) \, \mathbf{k}\,\mathbf{g} \right) = 0
\tag{2.22}
$$

$$
\phi \frac{\partial S_w}{\partial t} + \nabla \left(\lambda_w \mathbf{k} \frac{\partial P_c}{\partial S_w} \nabla S_w + \lambda_w \mathbf{k} \left(\rho_w \mathbf{g} - \nabla P_g \right) \right) = 0
\tag{2.23}
$$

where, $\lambda_t = \lambda_w + \lambda_g$ is the total mobility.

These equations represent a coupled, strongly nonlinear set of partial differential equation for an unsaturated two-phase flow in a rigid porous medium. Eq. (2.22) is a dissipative-convective quasi steady-state equation, and Eq. (2.23) is marching with time. The equations are parabolic to hyperbolic functions, the degree of which depends on flow conditions and capillary pressure. The advantage of this formulation is that the capillary pressure gradient $\partial P_c/\partial S_w$ is explicitly included, and hence, in contrast to the pressure-pressure formulation (Eqs. (2.5) and (2.6)), it can be applied to systems with small capillary pressure gradients (Helmig, 1997). If $\partial P_c/\partial S_w = 0$, Eq. (2.22) becomes elliptic; because the total mobility, λ_t, is always positive (Chen et al., 2006). Thus, this gradient determines the nature of the equations, and consequently the solution behavior. It is therefore vital to formulate a stable and robust numerical procedure capable of solving a wide range of applications, involving a wide-ranging $\partial P_c/\partial S_w$ relationships. This issue will be treated in the next section.

In literature, there are several empirical formulations correlating the capillary pressure and relative permeability to degree of saturation, mainly, the van Genuchten (1980) and Brooks and Corey (1964). Here for an example, the Brook and Corey's

formulation is presented. Accordingly, the capillary pressure-saturation relationship is described as

$$P_c = \frac{P_b}{S_e^{1/\lambda}} \quad P_c \leq P_b \tag{2.24}$$

and the relative permeability-saturation relationships are described as

$$k_{rw} = S_e^{(2+3\lambda)/\lambda} \tag{2.25}$$

$$k_{rg} = (1 - S_e)^2 \left(1 - S_e^{(2+\lambda)/\lambda}\right) \tag{2.26}$$

where $S_e = \frac{S_w - S_{wr}}{1 - S_{wr} - S_{gr}}$ is the effective saturation, S_{wr} is the irreducible water saturation, S_{gr} is the residual gas saturation, λ is the pore size distribution index and p_b is the entry pressure, corresponding to the capillary pressure needed to displace the wetting phase from the largest pore.

2.2.3   Initial and boundary conditions

Initially, at t=0, the gas pressure and water saturation are described as

$$P_g = P_0(\mathbf{x}), \ S_w = S_0(\mathbf{x}) \quad \text{at } t = 0 \tag{2.27}$$

The boundary conditions can be imposed values on Γ_π or fluxes on Γ_π^q, where the boundary $\Gamma = \Gamma_\pi \cup \ \Gamma_\pi^q$. The Dirichlet boundary conditions are prescribed as

$$\begin{aligned} P_g = \hat{P}_g \ \ \text{on } \Gamma_g \\ S_w = \hat{S}_w \ \text{on } \Gamma_w \end{aligned} \tag{2.28}$$

The Neumann boundary conditions are imposed as

$$\frac{\mathbf{k}k_{rg}}{\mu_g} \left(-\nabla P_g + \rho_g \, \mathbf{g}\right) \cdot \mathbf{n} = q_g \quad \text{on } \Gamma_g^q \tag{2.29}$$

$$\frac{\mathbf{k}k_{rw}}{\mu_w} \left(-\nabla P_g + \nabla S_w \frac{\partial P_c}{\partial S_w} + \rho_w \, \mathbf{g}\right) \cdot \mathbf{n} = q_w \quad \text{on } \Gamma_w^q \tag{2.30}$$

where $\mathbf{n}$ is the unit vector, perpendicular to the surface of the medium, q_g and q_w are imposed gas and water fluxes.

2.3   Numerical discretization

Equations (2.22) and (2.23), together with the initial conditions and boundary conditions in Eqs. (2.27)-(2.30), represent an initial and boundary value problem of immiscible CO_2 flow in underground formations. This problem involves injection of

CO_2 flux into a permeable aquifer, creating a plume that travels under the effect of viscous, capillary and gravity forces. At the front of the plume, there is a relatively high gradient in the saturation field and the pressure field. Capturing and modeling this front is usually accompanied by numerical nuisance. A straightforward remedy to this problem is the use of a fine mesh. However, for problems of regional scales this approach is not feasible. CPU time of the order of several days or weeks is then not unusual. Alternatively, in this work, we formulate a numerical technique, which is based on the coupling between the level-set method (Osher and Sethian, 1988) and the extended finite element method (Belytschko and Black, 1999). The level-set method is utilized to trace the propagation of the plume front, and the extended finite element method is utilized to model the front.

2.3.1 Tracing the front

The level-set method makes use of an auxiliary distance function, referred to as the level-set function, which labels every point with a sign and a value. The sign indicates the fluid domain, and the value represents the shortest distance to the interface. This function is equal to zero at the interface and non-zero elsewhere according to

$$\Phi(x) = \begin{cases} \min_{x_i \in \Gamma} \|x - x_i\|, \ x \in \Omega_1 \\ -\min_{x_i \in \Gamma} \|x - x_i\|, \ x \in \Omega_2 \end{cases} \qquad \Phi(x) \in \Re, \ x \in \Omega \qquad (2.31)$$

In each time step, the level-set value is advected by the fluid velocity, such that

$$\frac{\partial \Phi}{\partial t} + \mathbf{v}_{\Gamma_d} \cdot \nabla \Phi = 0 \qquad (2.32)$$

where $\mathbf{v}_{\Gamma_d}$ represents the interface (front, Γ_d) velocity. For a typical multiphase medium, this velocity is difficult to calculate, and is usually treated as a weighted average of the gas velocity and the water velocity. Here, we adopt a formulation suggested by Liu et al. (2010), that reads

$$\mathbf{v}_{\Gamma_d} = \frac{\rho_g (1 - S_w)}{\rho} \mathbf{v}_g + \frac{\rho_w S_w}{\rho} \mathbf{v}_w \qquad (2.33)$$

where $\rho = \rho_w S_w + \rho_g S_g$, $\mathbf{v}_g$ and $\mathbf{v}_w$ are the gas and water Darcy velocities described as

$$\mathbf{v}_\alpha = \frac{\mathbf{k} k_{r\alpha}}{\mu_\alpha} \left(-\nabla P_\alpha + \rho_\alpha \mathbf{g} \nabla z \right), \quad \alpha = g, w \qquad (2.34)$$

To describe the interface motion, the normal component of the interface velocity is considered.

Level-set discretization

The level-set equation, Eq. (2.32), is a first-order hyperbolic equation and its discretization using the standard Galerkin method may result into spurious oscillations. Different techniques have been employed to stabilize this problem, among which the Streamline Upwind Petrov-Galerkin (SUPG) method (Brooks and Hughes, 1982) is known to be effective in many cases. In the SUPG method the weighting function is perturbed in the direction of the flow, as

$$\bar{N} = N + \tau \mathbf{v}_{\Gamma_d} \cdot \nabla N \tag{2.35}$$

where N and $\bar{N}$ are standard and modified finite element weighting functions, respectively, and the parameter τ is a stabilization parameter. In literature, there are several formulations describing τ. In the absence of diffusion, τ can be expressed as

$$\tau = \frac{h_e}{2 \, |\mathbf{v}_{\Gamma_d}|} \tag{2.36}$$

where, h_e is the characteristic length of the element, defined as

$$h_e = 2 \left(\sum_{\alpha}^{n_e} \left| \frac{u_i}{\|\mathbf{v}_{\Gamma_d}\|} \frac{\partial N_\alpha}{\partial x_i} \right| \right)^{-1} \tag{2.37}$$

in which n_e is the number of nodes in the element and N_α is the basis function associated with them.

Applying Eq. (2.35) to Eq. (2.32), the weak formulation of the level-set function can be expressed as

$$\int_\Omega N \left(\frac{\partial \Phi}{\partial t} + \mathbf{v}_{\Gamma_d} \cdot \nabla \Phi \right) d\Omega + \sum_k \int_{\Omega_k} \tau \left(\mathbf{v}_{\Gamma_d} \cdot \nabla N \right) \left(\frac{\partial \Phi}{\partial t} + \mathbf{v}_{\Gamma_d} \cdot \nabla \Phi \right) d\Omega_k = 0 \tag{2.38}$$

Approximating $\Phi = \mathbf{N}\bar{\boldsymbol{\Phi}}$, where $\bar{\boldsymbol{\Phi}}$ is the level-set nodal values, and substituting into Eq. (2.38), yields

$$\int_\Omega \mathbf{N}^T \mathbf{N} \frac{\partial \bar{\boldsymbol{\Phi}}}{\partial t} d\Omega + \int_\Omega \mathbf{N}^T (\mathbf{v}_{\Gamma_d} \cdot \nabla \mathbf{N}) \bar{\boldsymbol{\Phi}} \, d\Omega + \sum_k \int_{\Omega_k} \mathbf{N}_s^T \mathbf{N} \frac{\partial \bar{\boldsymbol{\Phi}}}{\partial t} d\Omega$$
$$+ \sum_k \int_{\Omega_k} \mathbf{N}_s^T (\mathbf{v}_{\Gamma_d} \cdot \nabla \mathbf{N}) \bar{\boldsymbol{\Phi}} \, d\Omega = 0 \tag{2.39}$$

The stabilizing term in Eq. (2.39) is denoted by a subscript k to emphasize that, due to $\nabla \mathbf{N}$, which is discontinuous across the elements, the numerical integration must be carried out on the element interior Ω_k, not at the nodes (Zienkiewicz et al., 2005).
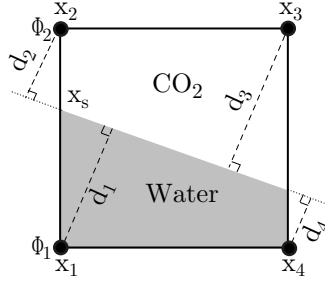
Figure 2.1: Intersection of the interface in the cell face (see Cho et al. (2011)).

Level-set re-initialization

Utilizing the level-set method to trace a moving front requires re-distancing (re-initialization) at every time step. This is necessary because otherwise the distance property of the level-set function is no longer maintained after advection. In literature, several numerical approaches have been employed to treat this problem, including the fast marching method, a distancing direct approach, and a direct solution of the advection hyperbolic partial differential equation (see Choi (2011) for more details). Most of the efforts are spent on maintaining the high gradient curvatures of the boundaries of the involved moving phase, such as the advection of air bubbles in a liquid. In this study, and due to the relatively large size of the CO_2 plume, the gradients of the curvature of the plume front, within an element, are not significant, and thus, a direct distancing approach, proposed by Cho et al. (2011), suffices. In this approach the re-distancing is performed by geometrical updating of the advective front instead of solving a re-initialization equation. The signed distance function from the front, where it intersects the element edges, to each node of the element is calculated as (see Figure 2.1):

$$d = \mathbf{n} \cdot (\mathbf{x} - \mathbf{x}_s) \tag{2.40}$$

where

$$\mathbf{x_s} = \mathbf{x_1} - \frac{\Phi_1}{\Phi_1 - \Phi_2} (\mathbf{x_1} - \mathbf{x}_2) \tag{2.41}$$

Upon locating the plume front, the Φ values of the nodes of the neighboring elements are updated accordingly, and used in the next time step. A detailed procedure can be found in Cho et al. (2011).

2.3.2 Modeling the front

As mentioned earlier, Eqs. (2.22) and (2.23) represent a strongly coupled system of partial differential equations describing a two-phase flow in a rigid porous medium. At the front of the gas plume, the saturation field exhibits a strong jump, but the pore pressure field, due to capillary effects, exhibits a diffusive gradient. Considering this mixed nature of the plume front, we utilize the extended finite element method to discretize the saturation field, and the standard Galerkin method to discretize the pressure field. This approach of a mixed discretization procedure between XFEM and standard Galerkin method has been introduced by Al-Khoury and Sluys (2007) to model fracturing porous media. Using such an approach, a conservative system can be obtained by capturing the field discontinuity, and meanwhile, the number of degrees of freedom are reduced, as compared to a case in which both fields are discretized using XFEM.

XFEM discretization

In XFEM, the finite element space is enhanced by adding a special function necessary to capture physical discontinuities or high gradient fields. Different enhancement functions are utilized and made suitable for different applications. Here, the level-set function is utilized to enhance the water saturation field as

$$S_w(x,t) = \sum_{I \in \mathbb{N}} \mathbf{N}_I(x)\mathbf{S}_{wI}(t) + \sum_{J \in N_{enriched}} \mathbf{N}_J^*(x,t)\mathbf{a}_J \qquad (2.42)$$

where $\mathbf{S_{w}}_I(t)$ is a set of nodal degrees of freedom representing the saturation degree, and $\mathbf{a}_J(t)$ is an additional set of nodal degrees of freedom at the enriched nodes J in the elements where the plume front intersects. As proposed by Chessa and Belytschko (2003a), the enriched shape function is defined as a multiplication between the standard shape function and the level-set function, such that

$$\mathbf{N}_J^*(x,t) = \mathbf{N}_j(x)\left(|\Phi(x,t)| - |\Phi(x_J,t)|\right) \qquad (2.43)$$

Figure 2.2 depicts Eq. (2.43) for a linear two-node element. Note that the enriched shape functions vanish at the nodes. The enrichment functions for a three-node linear triangle and a four-node quadrilateral element are shown in Figures 2.3 and 2.4, receptively.

Using the weighted residual method, the finite element formulation of Eq. (2.22)
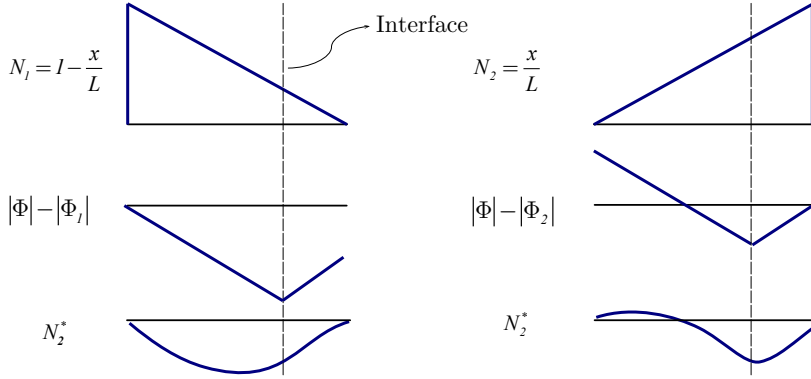
Figure 2.2: Example of the enriched shape functions for a linear two-node element (see also Chessa and Belytschko (2003a))

and its boundry equations Eqs. (2.29) and (2.30) can be described as:

$$
\int_{\Omega} \mathbf{w}^T \left[-\nabla \left(\lambda_t \mathbf{k} \nabla P_g \right) + \nabla \left(\lambda_w \frac{\partial P_c}{\partial S_w} \mathbf{k} \nabla S_w \right) + \nabla \left(\lambda_w \rho_w + \lambda_g \rho_g \right) \mathbf{k} \, \mathbf{g} \right] d\Omega
$$
$$
+ \int_{\Gamma^q} \bar{\mathbf{w}}^T \left[\frac{\mathbf{k} k_{rw}}{\mu_w} \left(-\nabla P_g + \nabla S_w \frac{\partial P_c}{\partial S_w} + \rho_w \, \mathbf{g} \right) \right. \tag{2.44}
$$
$$
\left. + \frac{\mathbf{k} k_{rg}}{\mu_g} \left(-\nabla P_g + \rho_g \, \mathbf{g} \right) \cdot \mathbf{n} - q_g \right] \cdot \mathbf{n} \, d\Gamma = 0
$$

where $\mathbf{w}$ and $\bar{\mathbf{w}}$ are arbitrary weighting functions, limited in such a way that

$$
\mathbf{w} = 0 \quad on \; \Gamma_w \cup \Gamma_g
$$
$$
\bar{\mathbf{w}} = -\mathbf{w} \quad on \; \Gamma_w^q \cup \Gamma_g^q \tag{2.45}
$$

By applying the Galerkin method, the weighting functions $\mathbf{w}$ is replaced by the shape function $\mathbf{N}$. This gives

$$
\int_{\Omega} \mathbf{N}^T \left[-\nabla \left(\lambda_t \mathbf{k} \nabla P_g \right) + \nabla \left(\lambda_w \frac{\partial P_c}{\partial S_w} \mathbf{k} \nabla S_w \right) \right.
$$
$$
\left. + \nabla \left(\lambda_w \rho_w + \lambda_g \rho_g \right) \mathbf{k} \, \mathbf{g} \right] d\Omega = 0 \tag{2.46}
$$

Applying XFEM to Eq. (2.23), and using a weighting function of the form:

$$
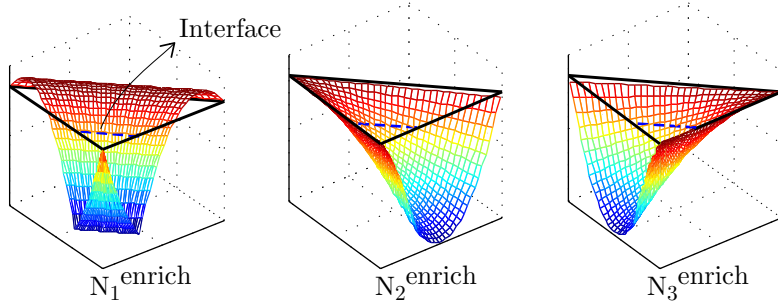\mathbf{w} = \mathbf{N} + \mathbf{N}_{\mathbf{J}}^* \tag{2.47}
$$

43

Figure 2.3: Example of the enriched shape functions for a quadrilateral element.

gives:

$$
\int_{\Omega} \left(\mathbf{N}^T \right) \left[\phi \frac{\partial S_w}{\partial t} + \nabla \cdot \left(-\lambda_w \mathbf{k} \nabla P_g + \lambda_w \mathbf{k} \frac{\partial P_c}{\partial S_w} \nabla S_w + \lambda_w \mathbf{k} \rho_w \mathbf{g} \right) \right] d\Omega
$$
$$
+ \int_{\Omega^+} \left(\mathbf{N}_J^{*T} \right) \left[\phi \frac{\partial S_w}{\partial t} + \nabla \cdot \left(-\lambda_w \mathbf{k} \nabla P_g + \lambda_w \mathbf{k} \frac{\partial P_c}{\partial S_w} \nabla S_w + \lambda_w \mathbf{k} \rho_w \mathbf{g} \right) \right] d\Omega
$$
$$
= 0 \tag{2.48}
$$

where Ω and Ω^+ are the continuous and the discontinuous subdomains, respectively.

As the summation of the residuals of the two subdomains is equal to zero, the residual of each subdomain must also be zero, and Eq. (2.48) can thus be split into two equations, as:

$$
\int_{\Omega} \left(\mathbf{N}^T \right) \left[\phi \frac{\partial S_w}{\partial t} + \nabla \cdot \left(-\lambda_w \mathbf{k} \nabla P_g + \lambda_w \mathbf{k} \frac{\partial P_c}{\partial S_w} \nabla S_w + \lambda_w \mathbf{k} \rho_w \mathbf{g} \right) \right] d\Omega = 0 \tag{2.49}
$$

$$
\int_{\Omega^+} \left(\mathbf{N}_J^{*T} \right) \left[\phi \frac{\partial S_w}{\partial t} + \nabla \cdot \left(-\lambda_w \mathbf{k} \nabla P_g + \lambda_w \mathbf{k} \frac{\partial P_c}{\partial S_w} \nabla S_w + \lambda_w \mathbf{k} \rho_w \mathbf{g} \right) \right] d\Omega = 0
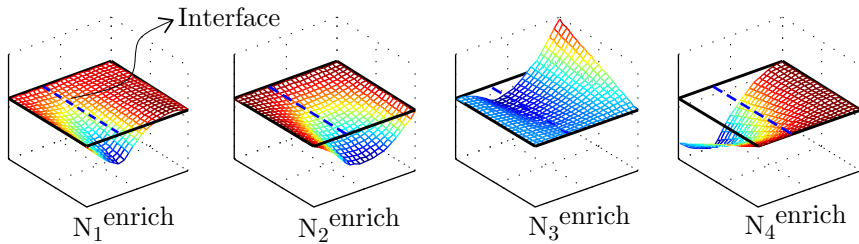$$
$$
\tag{2.50}
$$

Figure 2.4: Example of the enriched shape functions for a quadrilateral element.

Applying Green's theorem and introducing (2.42) into Eq. (2.46) leads to:

$$\int_\Omega (\nabla \mathbf{N})^T (\lambda_t \mathbf{k}) (\nabla \mathbf{N}) \bar{\mathbf{P}}_g \, d\Omega - \int_\Omega (\nabla \mathbf{N})^T \left(\lambda_w \frac{\partial P_c}{\partial S_w} \mathbf{k} \right) (\nabla N) \bar{\mathbf{S}}_w$$

$$- \int_{\Omega^+} (\nabla \mathbf{N})^T \left(\lambda_w \frac{\partial P_c}{\partial S_w} \mathbf{k} \right) (\nabla N^*) \, \mathbf{a}_J \, d\Omega \qquad (2.51)$$

$$= \int_\Omega (\nabla \mathbf{N})^T (\lambda_w \rho_w + \lambda_g \rho_g) \mathbf{k} \mathbf{g} \, d\Omega + \int_{\Gamma^q} \mathbf{N}^T (q_t) \, d\Gamma$$

where $\bar{\mathbf{P}}_g$ and $\bar{\mathbf{S}}_w$ are the nodal vectors of the gas pressure and water saturation. The saturation gradient is calculated from Eq. (2.42) as

$$\nabla \mathbf{S}_w = \sum_{I \in \mathbb{N}} \nabla \mathbf{N}_I \mathbf{S}_{wI} + \sum_{J \in N_{enriched}} \nabla \mathbf{N}_J^* \mathbf{a}_J$$

$$= \sum_{I \in \mathbb{N}} \nabla \mathbf{N}_I \mathbf{S}_{wI} + \sum_{J \in N_{enriched}} (\nabla \mathbf{N}_J \mathbf{\Psi}_J + \mathbf{N}_J \nabla \mathbf{\Psi}_J) \cdot \mathbf{a}_J \qquad (2.52)$$

Similarly, applying Green's theorem and introducing Eqs. (2.42) and (2.47), to Eqs. (2.49) and (2.50) yields

$$\int_\Omega \mathbf{N}^T \phi \mathbf{N} \frac{\partial \bar{\mathbf{S}}_w}{\partial t} \, d\Omega + \int_{\Omega^+} \mathbf{N}^T \phi \mathbf{N}^* \frac{\partial \mathbf{a}_J}{\partial t} d\Omega + \int_\Omega (\nabla \mathbf{N})^T (\lambda_w \mathbf{k}) (\nabla \mathbf{N}) \bar{\mathbf{P}}_g \, d\Omega$$

$$- \int_\Omega (\nabla \mathbf{N})^T \left(\lambda_w \frac{\partial P_c}{\partial S_w} \mathbf{k} \right) (\nabla \mathbf{N}) \bar{\mathbf{S}}_w \, d\Omega - \int_{\Omega^+} (\nabla \mathbf{N})^T \left(\lambda_w \frac{\partial P_c}{\partial S_w} \mathbf{k} \right) (\nabla \mathbf{N}^*) \mathbf{a}_J \, d\Omega$$

$$= \int_\Omega (\nabla \mathbf{N})^T (\lambda_w \rho_w) \mathbf{k} \mathbf{g} \, d\Omega + \int_{\Gamma_w^q} \mathbf{N}^T q_w \, d\Gamma$$

$$\qquad (2.53)$$

and

$$\int_{\Omega^+} \mathbf{N}^{*T} \phi \mathbf{N} \frac{\partial \bar{\mathbf{S}}_w}{\partial t} d\Omega + \int_{\Omega^+} \mathbf{N}^{*T} \phi \mathbf{N}^* \frac{\partial \mathbf{a}_J}{\partial t} d\Omega$$

$$+ \int_{\Omega^+} (\nabla \mathbf{N}^*)^T (\lambda_w \mathbf{k}) (\nabla \mathbf{N}) \bar{\mathbf{P}}_g \, d\Omega - \int_{\Omega^+} (\nabla \mathbf{N}^*)^T \left(\lambda_w \frac{\partial P_c}{\partial S_w} \mathbf{k} \right) (\nabla N^*) \bar{\mathbf{S}}_w \, d\Omega$$

$$- \int_{\Omega^+} (\nabla \mathbf{N}^*)^T \left(\lambda_w \frac{\partial P_c}{\partial S_w} \mathbf{k} \right) (\nabla \mathbf{N}^*) \mathbf{a}_J \, d\Omega$$

$$= \int_{\Omega^+} (\nabla \mathbf{N}^*)^T (\lambda_w \rho_w) \mathbf{k} \mathbf{g} \, d\Omega + \int_{\Gamma_w^q} \mathbf{N}^{*T} q_w \, d\Gamma$$

$$\qquad (2.54)$$

2.3.3 Linearization

The resulting weak formulations, Eqs. (2.51), (2.53) and (2.54), represent a set of semi-discrete nonlinear equations, where the nonlinearity arises from the constitutive

relationships between the relative permeability and water saturation, and between the capillary pressure and water saturation, described in Eqs. (2.24)-(2.26). Since the nonlinearity is due to scalar coefficients (i.e. λ_w, λ_t, $\partial P_c/\partial S_w$, etc.), and as the constitutive relationships are continuous, it is convenient to linearize these equations using Taylor series expansions up to the first order. The Taylor series expansion of a function $f(x)$ around a point $\bar{x}$ is given by

$$f(x) = f(\bar{x}) + \left.\frac{df}{dx}\right|_{x=\bar{x}} (x - \bar{x}) + \text{high order terms} \tag{2.55}$$

For example, the nonlinear mobility parameter λ_w at the current iteration, $r+1$, can be linearized as

$$\lambda_w^{r+1} = \lambda_w(S_w^r) + \frac{\partial \lambda_w(S_w^r)}{\partial S_w}(\delta S_w) \tag{2.56}$$

with

$$\delta S_w = S_w^{r+1} - S_w^r \tag{2.57}$$

Other nonlinear parameters are linearized in the same manner. The unknown variables and their time derivatives can be written as

$$\begin{aligned}
\mathbf{P}_{\mathbf{g}}^{r+1} &= \mathbf{P}_{\mathbf{g}}^r + \delta \mathbf{P}_{\mathbf{g}} & \mathbf{S}_{\mathbf{w}}^{r+1} &= \mathbf{S}_{\mathbf{w}}^r + \delta \mathbf{S}_{\mathbf{w}} & \mathbf{a}_{\mathbf{J}}^{r+1} &= \mathbf{a}_{\mathbf{J}}^r + \delta \mathbf{a}_{\mathbf{J}} \\
\dot{\mathbf{P}}_{\mathbf{g}}^{r+1} &= \dot{\mathbf{P}}_{\mathbf{g}}^r + \delta \dot{\mathbf{P}}_{\mathbf{g}} & \dot{\mathbf{S}}_{\mathbf{w}}^{r+1} &= \dot{\mathbf{S}}_{\mathbf{w}}^r + \delta \dot{\mathbf{S}}_{\mathbf{w}} & \dot{\mathbf{a}}_{\mathbf{J}}^{r+1} &= \dot{\mathbf{a}}_{\mathbf{J}}^r + \delta \dot{\mathbf{a}}_{\mathbf{J}}
\end{aligned} \tag{2.58}$$

where the vectors, $\dot{\mathbf{S}}_{\mathbf{w}}^r$, $\dot{\mathbf{P}}_{\mathbf{g}}^r$, and $\dot{\mathbf{a}}_{\mathbf{J}}^r$ denote the times derivatives of the state vector at iteration r and $\delta \dot{\mathbf{S}}_{\mathbf{w}}$, $\delta \dot{\mathbf{P}}_{\mathbf{g}}$ and $\delta \dot{\mathbf{a}}_{\mathbf{J}}$ are the unknown times derivatives of the incremental state vector.

Using Brook and Corey's model given in Eqs. (2.24)-(2.26), and assuming a constant viscosity, the mobility gradients can be calculated analytically according to

$$\frac{\partial \lambda_w}{\partial S_w} = \frac{1}{\mu_w}\frac{\partial k_{rw}}{\partial S_e}\frac{\partial S_e}{\partial S_w} = \frac{1}{\mu_w\left(1 - S_{wr} - S_{gr}\right)\lambda}\left(3S_e^{(2\lambda+2)/\lambda}\lambda + 2S_e^{(2\lambda+2)/\lambda}\right) \tag{2.59}$$

$$\begin{aligned}
\frac{\partial \lambda_t}{\partial S_w} &= \frac{\partial \lambda_w}{\partial S_w} + \frac{\partial \lambda_g}{\partial S_w} \\
&= \frac{1}{\left(1 - S_{wr} - S_{gr}\right)}\left[\frac{1}{\lambda\mu_w}\left(3S_e^{(2\lambda+2)/\lambda}\lambda + 2S_e^{(2\lambda+2)/\lambda}\right)\right. \\
&\quad \left. - \frac{1}{\lambda\mu_g}\left(S_e^{2/\lambda}\left(3S_e^2 - 4S_e + 1\right) - 2S_e + 2\right)\lambda + S_e^{2/\lambda}\left(2S_e^2 - 4S_e + 2\right)\right]
\end{aligned} \tag{2.60}$$

$$\frac{\partial\left(\lambda_s\right)}{\partial S_w} = \frac{\partial\lambda_w}{\partial S_w}\frac{\partial P_c}{\partial S_w} + \lambda_w\frac{\partial^2 P_c}{\partial S_w{}^2}$$

$$= \frac{-p_b\left(3S_e^{(\lambda+1)/\lambda}\lambda + 2S_e^{(\lambda+1)/\lambda}\right)}{\mu_w(1-S_{wr}-S_{gr})^2\lambda^2} + \frac{\lambda_w p_b\left(1+\lambda\right)}{(1-S_{wr}-S_{gr})^2 S_e^{(2\lambda+1)/\lambda}\lambda^2} \tag{2.61}$$

where $\lambda_s = \lambda_w\frac{\partial P_c}{\partial S_w}$. Inserting Eqs. (2.56)-(2.61), into Eq. (2.51), gives

$$\int_\Omega (\nabla\mathbf{N})^T\left(\mathbf{k}\lambda_t^r\right)(\nabla\mathbf{N})\bar{\mathbf{P}}_{\mathbf{g}}^r\, d\Omega + \int_\Omega (\nabla\mathbf{N})^T\left(\mathbf{k}\lambda_t^r\right)(\nabla\mathbf{N})\delta\bar{\mathbf{P}}_g\, d\Omega$$

$$+ \int_\Omega (\nabla\mathbf{N})^T\left(\mathbf{k}\frac{\partial\lambda_t}{\partial S_w}\bar{\mathbf{P}}_{\mathbf{g}}^r\right)(\nabla\mathbf{N})\delta\bar{\mathbf{S}}_w\, d\Omega - \int_\Omega (\nabla\mathbf{N})^T\left(\mathbf{k}\lambda_s^r\right)(\nabla N)\,\bar{\mathbf{S}}_{\mathbf{w}}^r\, d\Omega$$

$$- \int_\Omega (\nabla\mathbf{N})^T\left(\mathbf{k}\lambda_s^r\right)(\nabla N)\,\delta\bar{\mathbf{S}}_{\mathbf{w}}\, d\Omega - \int_\Omega (\nabla\mathbf{N})^T\left(\mathbf{k}\frac{\partial\lambda_s}{\partial S_w}\bar{\mathbf{S}}_{\mathbf{w}}^r\right)(\nabla N)\,\delta\bar{\mathbf{S}}_{\mathbf{w}}\, d\Omega$$

$$- \int_{\Omega^+} (\nabla\mathbf{N})^T\left(\mathbf{k}\lambda_s^r\right)(\nabla N^*)\,\mathbf{a}_{\mathbf{J}}^r\, d\Omega - \int_{\Omega^+} (\nabla\mathbf{N})^T\left(\mathbf{k}\lambda_s^r\right)(\nabla N^*)\,\delta\mathbf{a}_{\mathbf{J}}\, d\Omega$$

$$- \int_{\Omega^+} (\nabla\mathbf{N})^T\left(\mathbf{k}\frac{\partial\lambda_s}{\partial S_w}\mathbf{a}_{\mathbf{J}}^r\right)(\nabla N^*)\,\delta\bar{\mathbf{S}}_{\mathbf{w}}\, d\Omega$$

$$= \int_\Omega (\nabla\mathbf{N})^T\left(\lambda_w^r\rho_w + \lambda_g^r\rho_g\right)\mathbf{k}\,\mathbf{g}\, d\Omega$$

$$+ \int_\Omega (\nabla\mathbf{N})^T\left(\frac{\partial\lambda_w}{\partial S_w}\rho_w + \frac{\partial\lambda_g}{\partial S_w}\rho_g\right)\mathbf{k}\,\mathbf{g}\,\delta\bar{\mathbf{S}}_{\mathbf{w}}\, d\Omega + \int_{\Gamma^q} \mathbf{N}^T q_t\, d\Gamma \tag{2.62}$$

In a concise form, Eq. (2.62) can be written as

$$\mathbf{K}_{11}\,\delta\bar{\mathbf{P}}_{\mathbf{g}} + \mathbf{K}_{12}\,\delta\bar{\mathbf{S}}_w + \mathbf{K}_{13}\,\delta\mathbf{a}_{\mathbf{J}} = \mathbf{f}^1 - \left(\mathbf{K}_{11}^0\,\bar{\mathbf{P}}_{\mathbf{g}}^r + \mathbf{K}_{12}^0\,\bar{\mathbf{S}}_{\mathbf{w}}^r + \mathbf{K}_{13}^0\,\mathbf{a}_{\mathbf{J}}^r\right) \tag{2.63}$$

Similarly, Eqs. (2.53) and (2.54) can be expressed as

$$\mathbf{C}_{22}\delta\dot{\mathbf{S}}_{\mathbf{w}} + \mathbf{C}_{23}\delta\dot{\mathbf{a}}_{\mathbf{J}} + \mathbf{K}_{21}\,\delta\bar{\mathbf{P}}_g + \mathbf{K}_{22}\,\delta\bar{\mathbf{S}}_w + \mathbf{K}_{23}\,\delta\mathbf{a}_{\mathbf{J}}$$
$$= \mathbf{f}^2 - \left(\mathbf{C}_{22}^0\dot{\mathbf{S}}_{\mathbf{w}}^r + \mathbf{C}_{23}^0\dot{\mathbf{a}}_{\mathbf{J}}^r + \mathbf{K}_{21}^0\,\bar{\mathbf{P}}_{\mathbf{g}}^r + \mathbf{K}_{22}^0\,\bar{\mathbf{S}}_{\mathbf{w}}^r + \mathbf{K}_{23}^0\,\mathbf{a}_{\mathbf{J}}^r\right) \tag{2.64}$$

$$\mathbf{C}_{32}\delta\dot{\mathbf{S}}_{\mathbf{w}} + \mathbf{C}_{33}\delta\dot{\mathbf{a}}_{\mathbf{J}} + \mathbf{K}_{31}\,\delta\bar{\mathbf{P}}_g + \mathbf{K}_{32}\,\delta\bar{\mathbf{S}}_w + \mathbf{K}_{33}\,\delta\mathbf{a}_{\mathbf{J}}$$
$$= \mathbf{f}^3 - \left(\mathbf{C}_{32}^0\dot{\mathbf{S}}_{\mathbf{w}}^r + \mathbf{C}_{33}^0\dot{\mathbf{a}}_{\mathbf{J}}^r + \mathbf{K}_{31}^0\,\bar{\mathbf{P}}_{\mathbf{g}}^r + \mathbf{K}_{32}^0\,\bar{\mathbf{S}}_{\mathbf{w}}^r + \mathbf{K}_{33}^0\,\mathbf{a}_{\mathbf{J}}^r\right) \tag{2.65}$$

Putting Eqs. (2.63), (2.64) and (2.65) in a matrix form, yields

$$
\begin{pmatrix} \mathbf{K}_{11} & \mathbf{K}_{12} & \mathbf{K}_{13} \\ \mathbf{K}_{21} & \mathbf{K}_{22} & \mathbf{K}_{23} \\ \mathbf{K}_{31} & \mathbf{K}_{32} & \mathbf{K}_{33} \end{pmatrix} \begin{Bmatrix} \delta \bar{\mathbf{P}}_{\mathbf{g}} \\ \delta \bar{\mathbf{S}}_{\mathbf{w}} \\ \delta \mathbf{a}_{\mathbf{J}} \end{Bmatrix} + \begin{pmatrix} 0 & 0 & 0 \\ 0 & \mathbf{C}_{22} & \mathbf{C}_{23} \\ 0 & \mathbf{C}_{32} & \mathbf{C}_{32} \end{pmatrix} \begin{Bmatrix} \delta \dot{\mathbf{P}}_{\mathbf{g}} \\ \delta \dot{\mathbf{S}}_{\mathbf{w}} \\ \delta \dot{\mathbf{a}}_{\mathbf{J}} \end{Bmatrix}
$$

$$
= \begin{Bmatrix} \mathbf{f}^1 \\ \mathbf{f}^2 \\ \mathbf{f}^3 \end{Bmatrix} - \begin{pmatrix} \mathbf{K}_{11}^0 & \mathbf{K}_{12}^0 & \mathbf{K}_{13}^0 \\ \mathbf{K}_{21}^0 & \mathbf{K}_{22}^0 & \mathbf{K}_{23}^0 \\ \mathbf{K}_{31}^0 & \mathbf{K}_{32}^0 & \mathbf{K}_{33}^0 \end{pmatrix} \begin{Bmatrix} \bar{\mathbf{P}}_{\mathbf{g}}^r \\ \bar{\mathbf{S}}_{\mathbf{w}}^r \\ \mathbf{a}_{\mathbf{J}}^r \end{Bmatrix} - \begin{pmatrix} 0 & 0 & 0 \\ 0 & \mathbf{C}_{22}^0 & \mathbf{C}_{23}^0 \\ 0 & \mathbf{C}_{32}^0 & \mathbf{C}_{33}^0 \end{pmatrix} \begin{Bmatrix} \dot{\mathbf{P}}_{\mathbf{g}}^r \\ \dot{\mathbf{S}}_{\mathbf{g}}^r \\ \dot{\mathbf{a}}_{\mathbf{g}}^r \end{Bmatrix}
$$
$$(2.66)$$

where
$$
\mathbf{K}_{11} = \mathbf{K}_{11}^0 = \int_\Omega (\nabla \mathbf{N})^T (\mathbf{k} \lambda_t^r)(\nabla \mathbf{N}) \, d\Omega \tag{2.67}
$$

$$
\mathbf{K}_{12} = \int_\Omega (\nabla \mathbf{N})^T \left(\mathbf{k} \frac{\partial \lambda_t}{\partial S_w} \bar{\mathbf{P}}_{\mathbf{g}}^r \right)(\nabla \mathbf{N}) \, d\Omega \; - \int_\Omega (\nabla \mathbf{N})^T (\mathbf{k} \lambda_s^r)(\nabla \mathbf{N}) \, d\Omega
$$
$$
- \int_\Omega (\nabla \mathbf{N})^T \left(\frac{\partial \lambda_w}{\partial S_w} \rho_w + \frac{\partial \lambda_g}{\partial S_w} \rho_g \right) \mathbf{k} \, \mathbf{g} \, \mathbf{N} \, d\Omega
$$
$$
- \int_\Omega (\nabla \mathbf{N})^T \left(\mathbf{k} \frac{\partial \lambda_s}{\partial S_w} \bar{\mathbf{S}}_{\mathbf{w}}^r \right)(\nabla \mathbf{N}) \, d\Omega - \int_{\Omega^+} (\nabla \mathbf{N})^T \left(\mathbf{k} \frac{\partial \lambda_s}{\partial S_w} \mathbf{a}_{\mathbf{J}}^r \right)(\nabla \mathbf{N}^*) \, d\Omega
$$
$$(2.68)$$

$$
\mathbf{K}_{12}^0 = - \int_\Omega (\nabla \mathbf{N})^T (\mathbf{k} \lambda_s^r)(\nabla \mathbf{N}) \, d\Omega \tag{2.69}
$$

$$
\mathbf{K}_{13} = \mathbf{K}_{13}^0 = - \int_{\Omega^+} (\nabla \mathbf{N})^T (\mathbf{k} \lambda_s^r)(\nabla \mathbf{N}^*) \, d\Omega \tag{2.70}
$$

$$
\mathbf{K}_{21} = \mathbf{K}_{21}^0 = \int_\Omega (\nabla \mathbf{N})^T (\mathbf{k} \lambda_w^r)(\nabla \mathbf{N}) \, d\Omega \tag{2.71}
$$

$$
\mathbf{K}_{22} = \int_\Omega (\nabla \mathbf{N})^T \left(\mathbf{k} \frac{\partial \lambda_w}{\partial S_w} \bar{\mathbf{P}}_{\mathbf{g}}^r \right)(\nabla \mathbf{N}) \, d\Omega - \int_\Omega (\nabla \mathbf{N})^T (\mathbf{k} \lambda_s^r)(\nabla \mathbf{N}) \, d\Omega
$$
$$
- \int_\Omega (\nabla \mathbf{N})^T \left(\frac{\partial \lambda_w}{\partial S_w} \rho_w \right) \mathbf{k} \, \mathbf{g} \, \mathbf{N} \, d\Omega - \int_\Omega (\nabla \mathbf{N})^T \left(\mathbf{k} \frac{\partial \lambda_2}{\partial S_w} \bar{\mathbf{S}}_{\mathbf{w}}^r \right)(\nabla \mathbf{N}) \, d\Omega \tag{2.72}
$$
$$
- \int_{\Omega^+} (\nabla \mathbf{N})^T \left(\mathbf{k} \frac{\partial \lambda_s}{\partial S_w} \mathbf{a}_{\mathbf{J}}^r \right)(\nabla \mathbf{N}^*) \, d\Omega
$$

$$
\mathbf{K}_{22}^0 = - \int_\Omega (\nabla \mathbf{N})^T (\mathbf{k} \lambda_s^r)(\nabla \mathbf{N}) \, d\Omega \tag{2.73}
$$

$$
\mathbf{K}_{23} = \mathbf{K}_{23}^0 = - \int_{\Omega^+} (\nabla \mathbf{N})^T (\mathbf{k} \lambda_s^r)(\nabla \mathbf{N}^*) \, d\Omega \tag{2.74}
$$

$$
\mathbf{K}_{31} = \mathbf{K}_{31}^0 = \int_{\Omega^+} (\nabla \mathbf{N}^*)^T (\mathbf{k} \lambda_w^r)(\nabla \mathbf{N}) \, d\Omega \tag{2.75}
$$

$$\mathbf{K}_{32} = \int_{\Omega^+} (\nabla\mathbf{N}^*)^T \left(\mathbf{k}\frac{\partial\lambda_w}{\partial S_w}\bar{\mathbf{P}}_\mathbf{g}^r\right)(\nabla\mathbf{N})\, d\Omega - \int_{\Omega^+} (\nabla\mathbf{N}^*)^T (\mathbf{k}\lambda_s^r)(\nabla\mathbf{N})\, d\Omega$$

$$- \int_{\Omega^+} (\nabla\mathbf{N}^*)^T \left(\frac{\partial\lambda_w}{\partial S_w}\rho_w\right)\mathbf{k}\,\mathbf{g}\,\mathbf{N}\, d\Omega - \int_{\Omega^+} (\nabla\mathbf{N}^*)^T \left(\mathbf{k}\frac{\partial\lambda_s}{\partial S_w}\bar{\mathbf{S}}_\mathbf{w}^r\right)(\nabla\mathbf{N})\, d\Omega$$

$$- \int_{\Omega^+} (\nabla\mathbf{N}^*)^T \left(\mathbf{k}\frac{\partial\lambda_s}{\partial S_w}\mathbf{a}_\mathbf{J}^r\right)(\nabla\mathbf{N}^*)\, d\Omega$$

$$\tag{2.76}$$

$$\mathbf{K}_{32}^0 = -\int_{\Omega^+} (\nabla\mathbf{N}^*)^T (\mathbf{k}\lambda_s^r)(\nabla\mathbf{N})\, d\Omega \tag{2.77}$$

$$\mathbf{K}_{33} = \mathbf{K}_{33}^0 = -\int_{\Omega^+} (\nabla\mathbf{N}^*)^T (\mathbf{k}\lambda_s^r)(\nabla\mathbf{N}^*)\, d\Omega \tag{2.78}$$

$$\mathbf{C}_{22} = \mathbf{C}_{22}^0 = \int_{\Omega} \mathbf{N}^T \phi\,\mathbf{N}\, d\Omega \tag{2.79}$$

$$\mathbf{C}_{23} = \mathbf{C}_{23}^0 = \int_{\Omega^+} \mathbf{N}^T \phi\,\mathbf{N}^*\, d\Omega \tag{2.80}$$

$$\mathbf{C}_{32} = \mathbf{C}_{32}^0 = \int_{\Omega^+} \mathbf{N}^{*T} \phi\,\mathbf{N}\, d\Omega \tag{2.81}$$

$$\mathbf{C}_{33} = \mathbf{C}_{33}^0 = \int_{\Omega^+} \mathbf{N}^{*T} \phi\,\mathbf{N}^*\, d\Omega \tag{2.82}$$

$$\mathbf{f_1} = \int_{\Omega} (\nabla\mathbf{N})^T \left(\lambda_w^r\rho_w + \lambda_g^r\rho_g\right)\mathbf{k}\,\mathbf{g}\, d\Omega + \int_{\Gamma^q} \mathbf{N}^T q_t\, d\Gamma \tag{2.83}$$

$$\mathbf{f_2} = \int_{\Omega} (\nabla\mathbf{N})^T \left(\lambda_w^r\rho_w\right)\mathbf{k}\,\mathbf{g}\, d\Omega + \int_{\Gamma^q} \mathbf{N}^T q_w\, d\Gamma \tag{2.84}$$

$$\mathbf{f_3} = \int_{\Omega^+} (\nabla\mathbf{N}^*)^T \left(\lambda_w^r\rho_w\right)\mathbf{k}\,\mathbf{g}\, d\Omega + \int_{\Gamma^q} \mathbf{N}^{*T} q_w\, d\Gamma \tag{2.85}$$

2.3.4 Time discretization

Finite difference in time is used for solving the semi-discrete equations, Eq. (2.66). Using the theta-method, the time derivatives of the state vector, $\mathbf{X} = [\mathbf{P}_g\ \mathbf{S}_w\ \mathbf{a}_J]^T$ are approximated by

$$\left\{\frac{d\mathbf{X}}{dt}\right\}_{n+1} = \frac{1}{\theta\Delta t}(\mathbf{X}_{n+1} - \mathbf{X}_n) - \frac{1-\theta}{\theta}\left\{\frac{d\mathbf{X}}{dt}\right\}_n \tag{2.86}$$

where, Δt denotes the time step size and θ is a scalar parameter which varies between 0 and 1. Substituting $\delta\mathbf{X}_{n+1} = \mathbf{X}_{n+1}^{r+1} - \mathbf{X}_{n+1}^r$ (see Eq. (2.57)), into Eq. (2.86), and

knowing that $\delta\mathbf{X}_n = d(\delta\mathbf{X}_n)/dt = 0$, gives an expression for the time derivative of the incremental state vector

$$\frac{d(\delta\mathbf{X}_{n+1})}{dt} = \frac{1}{\theta\Delta t}(\delta\mathbf{X}_{n+1}) \tag{2.87}$$

In the first time step, the time derivative $d\mathbf{X}_n/dt$ is not known, and therefore a first-order backward difference scheme is used to approximate the time derivative as

$$\left\{\frac{d\mathbf{X}}{dt}\right\}_1 = \frac{1}{\Delta t}(\mathbf{X}_1 - \mathbf{X}_0) \tag{2.88}$$

where $\mathbf{X}_0$ is the initial condition. For each time step the procedure for updating the results is as follows:

1. Given P_g^n, S_w^n and Φ^n.

2. Compute front velocity $\mathbf{v}_{\Gamma_d}$ from Eq. (2.33).

3. Compute Φ^{n+1} from Eq. (2.32).

4. Reinitialize Φ as explained in section 2.3.1.

5. Locate the plume front and discretize using XFEM.

6. Compute P_g^{n+1} and S_w^{n+1} from Eq. (2.66).

7. $n \leftarrow n + 1$; go to step 1.

2.4 Verifications and numerical examples

In this section, the discretization method described above is examined with respect to its capability to solve three different problems involving multiphase flow in porous media, and the results with those obtained from standard and the upwind finite element methods are compared. Two of the problems have analytical and quasi-analytical solutions, and the other one is a benchmark problem, treated in several literatures: namely, the Buckley-Leverett problem (advection dominant), the McWhorter problem (diffusion dominant), and the CO_2 leakage problem (advection-diffusion). Focus is placed on the accuracy, stability, and the boundedness of the solution (monotonic behavior). In a fourth numerical example, we study the mesh convergence of the proposed model.

2.4.1 Buckley-Leverett example

The Buckely-Leverett problem (Buckley and Leverett, 1942) describes a one-dimensional transient displacement of two immiscible fluids in a porous medium without capillary pressure or gravitational force. The location of the saturation front before

Table 2.1: Parameters for solving Buckley Leverett problem.

Parameter	Value	Unit
Domain length, L	300	m
Absolute permeability, k	1×10^{-13}	m^2
Porosity, ϕ	0.2	
Wetting phase viscosity, μ_w	1×10^{-3}	Pa.s
Non-wetting phase viscosity, μ_{nw}	1×10^{-3}	Pa.s
Residual wetting phase saturation, S_{wr}	0.0	
Residual non-wetting phase saturation, S_{nwr}	0.0	
In-flux velocity, v	4.3×10^{-7}	m/s
pressure, P_w	1×10^7	Pa

breakthrough is described as

$$x_f = \frac{1}{\phi} \left(\frac{\partial f_g}{\partial S_g} \right)_{S_g} \int_0^t v \, dt \tag{2.89}$$

where v is the total velocity, and $f_g = \lambda_g / (\lambda_g + \lambda_w)$ is a fractional flow function. A schematic representation of Eq. (2.89) is shown in Figure 2.5.

A physical domain representing a non-wetting phase saturated one-dimensional porous formation, subjected to a wetting phase flux at its left-hand side boundary, is studied first. The geometry, initial and boundary conditions, and model parameters are given in Table 2.1. The Brooks and Corey model is utilized to describe the relative permeability-saturation relationship, Eqs. (2.24) -(2.26).

Figure 2.6-a shows the relative permeability–saturation relationship for the studied material. Three numerical approaches are utilized to solve the problem: the standard Galerkin method (SG), the upwind method and the proposed XFEM-level set model. Figure 2.7 shows the saturation profiles obtained from these three approaches, together with the analytical solution, after 7 years and 20 years of wetting phase injection. The figure demonstrates that the standard Galerkin method exhibits spurious oscillations, obviously due to advection. The result of the upwind method is rather smooth (monotonic), but highly dissipative. The proposed model, on the other hand, produces a monotonic profile, and is less dissipative.

2.4.2 McWhorter problem

The McWhorter problem (McWhorter and Sunada, 1990) describes a one-dimensional quasi-transient displacement of a non-wetting phase by a wetting phase, driven by the
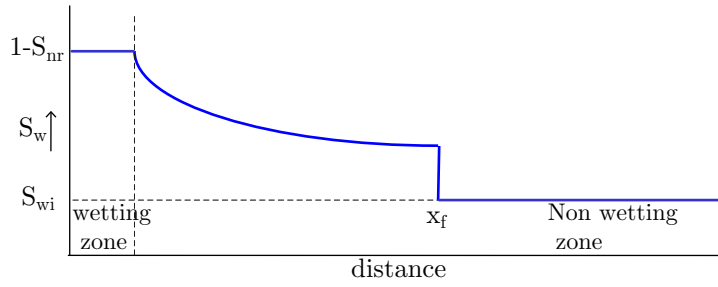
51

Figure 2.5: saturation as a function of distance

(a) Relative permeability curves
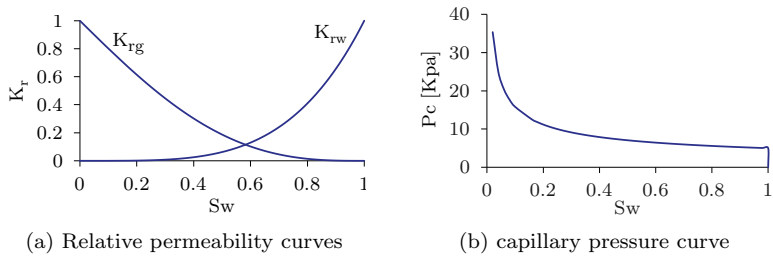
(b) capillary pressure curve
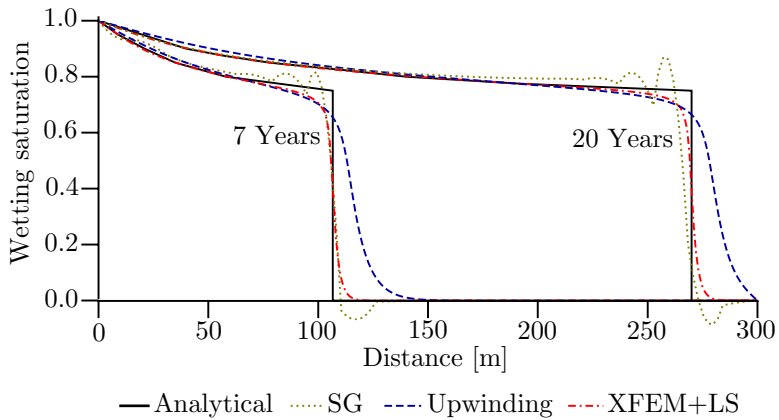
Figure 2.6: Brooks and Corey model

Figure 2.7: Comparison of saturation profile

capillary pressure. It solves an idealized immiscible two-phase flow quasi-analytically. The location of the saturation front, x_f is described as (Helmig, 1997)

$$x_f = \frac{2A\left(1 - f_i R\right)}{\phi} F'\left(S_w\right) t^{-\frac{1}{2}} \tag{2.90}$$

where A is a function of initial saturation, $R = q_t/q_n$ with q_t the total flux and q_n the non-wetting flux, f_i is a fractional flow function at initial effective saturation condition, defined as

$$f_i = \left(1 + \frac{k_{rn}(S_i)\mu_w}{k_{rw}(S_i)\mu_n}\right) \tag{2.91}$$

and

$$F' = \frac{dF}{dS_w} = \frac{\left(\int_{S_w}^{S_n} \frac{D}{F - f_n} d\beta\right)}{\left(\int_{S_i}^{S_n} \frac{(S_w - S_i)D}{F - f_n} dS_w\right)} \tag{2.92}$$

where

$$F\left(x, t\right) = \frac{q_w/q_o - f_i R}{1 - f_i R} \tag{2.93}$$

and

$$f_n = \frac{\left(f_w - f_i\right) R}{1 - f_i R} \tag{2.94}$$

in which D is the capillary diffusion tensor, defined as

$$D = \frac{k_{rn} k f_w}{\mu_n} \frac{dp_c}{dS_w} \tag{2.95}$$

Here, a physical domain for a two phase flow is solved. The initial and boundary conditions are presented in Figure 2.8 and model parameters are given in Table 2.2. The van Genuchten model is utilized to describe the relative permeability-saturation relationship and the capillary pressure-saturation relationship, defined by

$$k_{rw} = \sqrt{S_e}\left[1 - \left(1 - (S_e)^{1/m}\right)^m\right]^2 \tag{2.96}$$

$$k_{rg} = (1 - S_e)^{1/2}\left(1 - S_e^{1/m}\right)^{2m} \tag{2.97}$$

$$p_c = p_b\left(S_e^{-1/m} - 1\right)^{1/n} \tag{2.98}$$

where m and n are fitting parameters, $(m = 1 - 1/n)$, p_b is entry or bubbling pressure, and S_e is the effective saturation.

Figure 2.9 shows numerical results obtained from the proposed model, compared to those obtained from the standard Galerkin method, the upwind method and the quasi-analytical solution of the McWhorter problem, Eq. (2.90). The figure shows that the three discretization procedures are in good agreement with the

Table 2.2: Parameters for solving McWhorter problem.

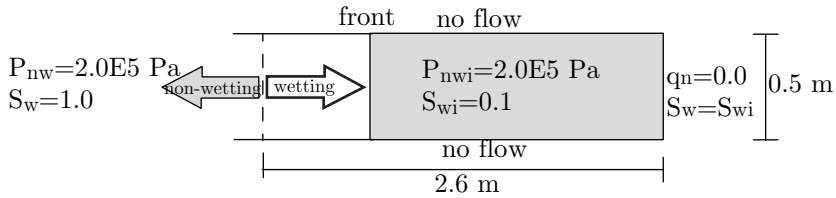| Parameter	Value	Unit
Domain length, L	2.6	m
Absolute permeability, k	1×10^{-10}	m^2
Porosity, ϕ	0.3	
Wetting phase viscosity, μ_w	1×10^{-3}	Pa.s
Non-wetting phase viscosity, μ_{nw}	1×10^{-3}	Pa.s
Residual wetting phase saturation, S_{wr}	0.0	
Residual non-wetting phase saturation, S_{nwr}	0.0	
Van Genuchten parameter, m	2/3	
Entry pressure, P_b	5×10^3	Pa

Figure 2.8: McWhorter problem

quasi-analytical solution, though the proposed model is more accurate at the smaller distance. The reasonably good performance of the standard Galerkin model might be explained by the fact that, unlike the Buckley-Leverett problem, the McWhorter problem exhibits diffusion due to the capillary effect, and hence no sharp front exists.

2.4.3 Leakage problem

This example is a benchmark study utilized in literature to compare the performance of different simulators and models in describing the consequences of CO_2 sequestration in underground formations (Class et al., 2009). It illustrates a leakage scenario of CO_2 from an abandoned well. This problem is physically important since injection of a large amount of CO_2 into underground formations requires careful environmental risk assessment.

The greatest concern is that the injected supercritical CO_2, which is less dense and less viscous than the resident water, is driven by buoyancy forces towards the
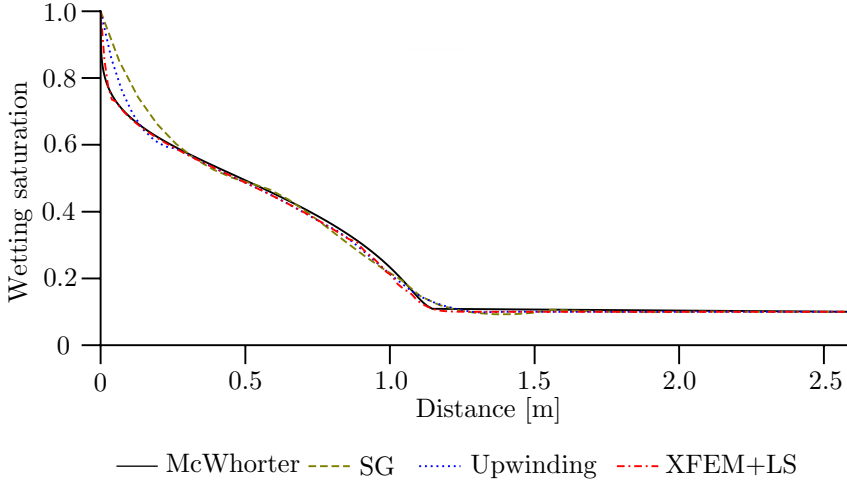
Figure 2.9: Comparison of saturation profile in McWhorter problem

top of the injection formation and the upper layers through cracks or faults.

Here, a 2D benchmark model described by (Nordbotten et al., 2004) and (Ebigbo et al., 2007) is considered, Figure 2.10. It consists of a CO_2 injection well, two aquifers, one aquitard and a leaky well. The physical domain extends 1000 m horizontally, and the upper aquifer is located 2840 m below the ground surface. The thickness of the aquifers is 30 m each, and the aquitard is 100 m. The leaky well is located 100 m from the injection well. The simulation parameters are shown in Table 2.3. Brooks and Corey equations, Eqs. (2.24) -(2.26), are utilized.

Initially, the domain constitutes a fully brine saturated porous material, under a hydrostatic pressure condition. On the horizontal surfaces, a no-flow boundary
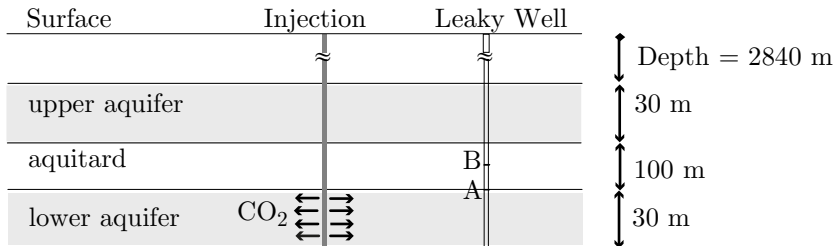

Figure 2.10: CO_2 leakage through an abandoned well

Table 2.3: Simulation parameters

Parameter	Value	Unit
Lateral dimension, L	1000	m
Aquifers thickness, w_1	30	m
Aquitard thickness, w_2	100	m
Distance between wells, d	100	m
Aquifers permeability, k_1	2.0×10^{-14}	m^2
Leaky well permeability, k_2	1×10^{-12}	m^2
Porosity, ϕ	0.15	
Brine viscosity, μ_w	2.535×10^{-4}	Pa.s
CO_2 viscosity, μ_g	3.95×10^{-5}	Pa.s
Brine density, ρ_w	1045	kg/m^3
CO_2 density, ρ_g	479	kg/m^3
Injection rate, q_{inj}	6.26×10^{-5}	m^2/s
Residual water saturation, S_{wr}	0.0	
Residual CO_2 saturation, S_{gr}	0.0	
Brooks and Corey parameter, λ	2	
Bottom pressure, P_{bh}	30.8	MPa

condition is prescribed, and on the vertical surfaces, a constant hydrostatic pressure is imposed. In this simulation, the fluid properties are assumed constant, and the dissolution of CO_2 into the brine is neglected. As for the previous examples, the problem is solved using the standard Galerkin method, the upwind finite element method and the coupled XFEM-level set model. Finite element meshes of different sizes are utilized. The solution results are evaluated at point A, shown in Figure 2.10, at the time when the CO_2 flux reaches 0.005 % of the injected flux. In what follows, we call this moment, the arrival time of the CO_2 plume.

Table 2.4 shows the arrival time of the CO_2 plume to the leaky well. The table shows that, using the coarse mesh (425 elements), the standard Galerkin model failed to converge. Upon refinement, the SG converged, but exhibited mesh sensitivity, i.e. the mesh with 909 elements was still too coarse. For case 2 with 909 elements, the arrival time was 7.2 days, but for case 3, with 2857 elements, the arrival time was 8.45 days. The upwind solution converged for the coarse mesh. However, it exhibited high diffusivity and the CO_2 front arrived in just 6.05 days. Apparently the front is smeared over a wider distance.

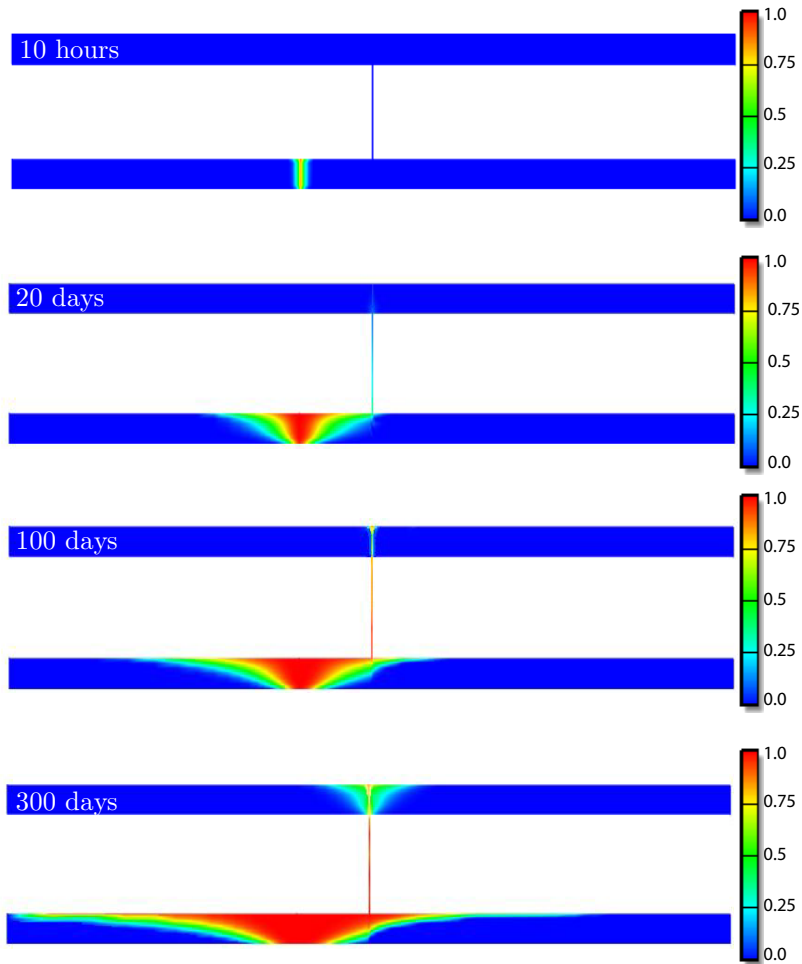On the other hand, the proposed model converged for the coarse mesh and the

Figure 2.11: CO_2 saturation at different times

Table 2.4: different simulation methods and configurations

Case	Elements	Method	Arrival time (day)	CPU time (sec)
1	425	SG	not converged	
2	909	SG	7.20	612
3	2857	SG	8.45	1860
4	425	Upwinding	6.05	265
5	425	XFEM-level set	8.10	365

arrival time of the CO_2 plume was 8.10 days, close to that of the Galerkin solution using the fine mesh.

Figure 2.11 shows CO_2 saturation profile at different time steps during injection (case 5). The CO_2 plume extends radially from the injection well and upon reaching the leakage well, it rises to the upper aquifer.

To examine the stability of the model, we investigate its performance numerically by varying the flow velocity. Three different aquifer permeabilities are utilized (1.5×10^{-14}, 2×10^{-14} and 2.5×10^{-14} m^2) using two different mesh sizes (2857 and 909 elements). The coarser mesh (425 elements) was not considered because the Galerkin model failed to converge for all permeabilities.

Figure 2.12 shows the CO_2 leakage rate, as a function of time for the fine mesh (2857 elements). The CO_2 leakage rate is calculated as the percentage ratio of the CO_2 flux to the injection rate at point B, shown in Figure 2.10. The figure shows that the two models demonstrate similar behavior. Figure 2.13 shows the results of the coarse mesh (909 elements). This figure shows that, for the low permeability, the two models give similar results, while for the higher one (25 mD) the Galerkin model failed to converge. This performance indicates that the proposed model is stable and perturbation in the model parameters results to a physically realistic perturbation in the flow behavior, even for relatively coarse meshes.

Examining Figures 2.12 and 2.13, it can be noticed that, at a certain stage, there is a sharp increase in the CO_2 flux due to the breakthrough in the leakage well. The pressure in the leakage well builds up and, depending on the permeability of the upper aquifer, the pressure might exhibit a peak followed by a drop or a continuous build up. For a high permeability aquifer, there is a pressure build up followed by a fast drop in the pressure due to the relatively fast leakage rate in the upper aquifer. Comparing Figure 2.11 to Figures 2.12 and 2.13, it can be noticed that the pressure build up started after 20 days of injection. For a low permeability aquifer, on the
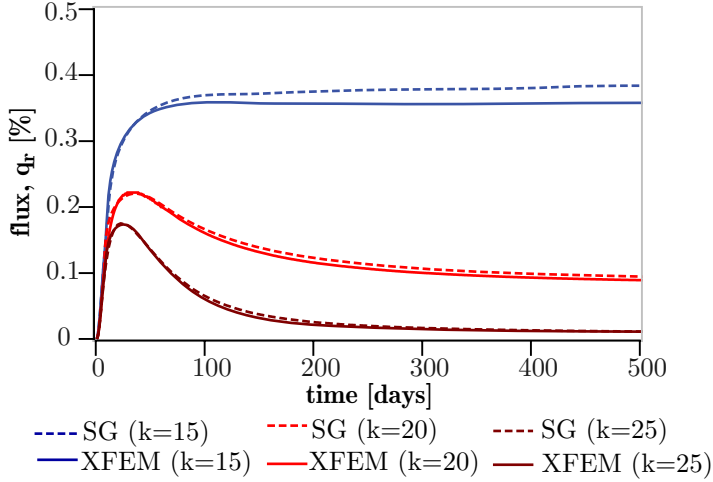
Figure 2.12: Leakage rate at different permeabilities computed with fine mesh simulation (2857 elements)
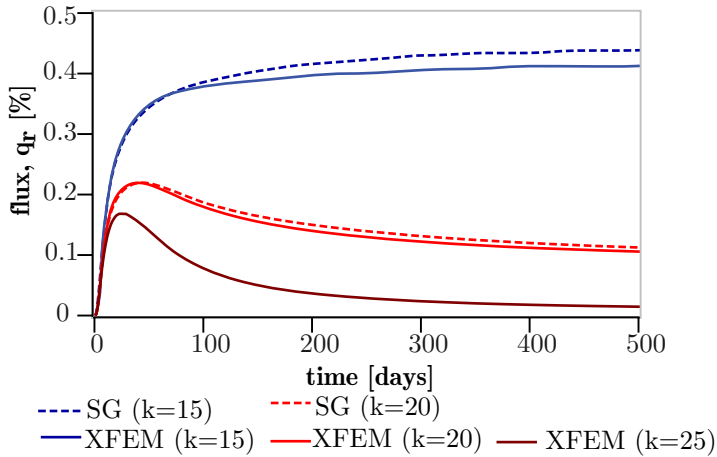

Figure 2.13: Leakage rate at different permeabilities computed with coarse mesh simulation (909 elements)

other hand, the pressure build up will continue for a longer time, though after a certain time limit it will drop (not shown in the figures).

2.4.4   Mesh sensitivity study

Here, we study the mesh sensitivity of the proposed model and compare it to the standard Galerkin model. This example is taken from Ebigbo et al. (2007). Consider a rectangular domain of 30 m × 100 m representing a fully saturated porous medium, see Figure 2.14. Initially, the domain is under hydrostatic pressure, with a top pressure of 10 MPa. At the left boundary, a CO_2 flux with $q_g = 6.263 \times 10^{-5}$ m^2/s is imposed. At the right boundary, a constant hydrostatic pressure and a constant water saturation of $S_w = 1$ are imposed.

The fluid and medium properties are the same as those presented in Table 2.3. Different mesh sizes are utilized and the calculations are carried out for 1000 days. The capillary pressure is ignored, making the problem hyperbolic, i.e. numerically more difficult. The calculation results, indicating the flux percentage q_r, are evaluated at the right boundary. Figure 2.15 shows the calculation results of the standard Galerkin method using 30, 85, 750, 3000 and 12000 quadratic elements. In this example, and because of the advective nature of the problem, we ought to add an artificial diffusion to the standard Galerkin equations to obtain monotonic solutions. The figure shows that the SG model converged after approximately 750 elements. Figure 2.16 shows the calculation results of the proposed model using 30, 85, 120, 480 and 3000 elements. The figure shows that the model converged after 85 elements, almost 9 times coarser than that for the standard Galerkin method.
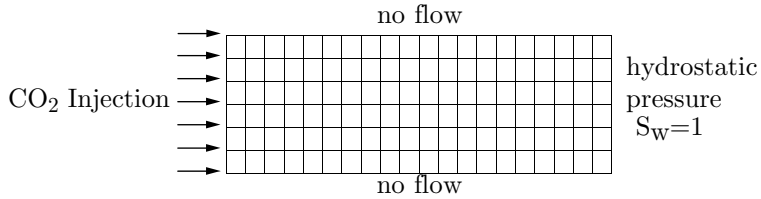
Figure 2.14: Mesh convergence problem
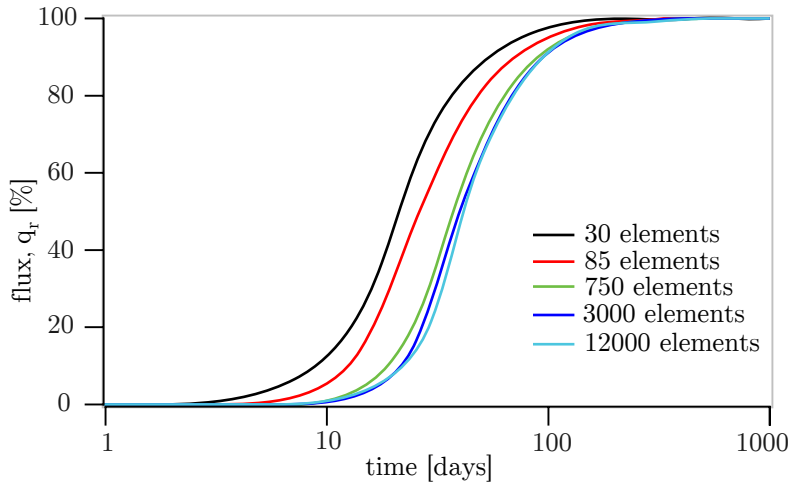
Figure 2.15: Convergence study for standard Galerkin method
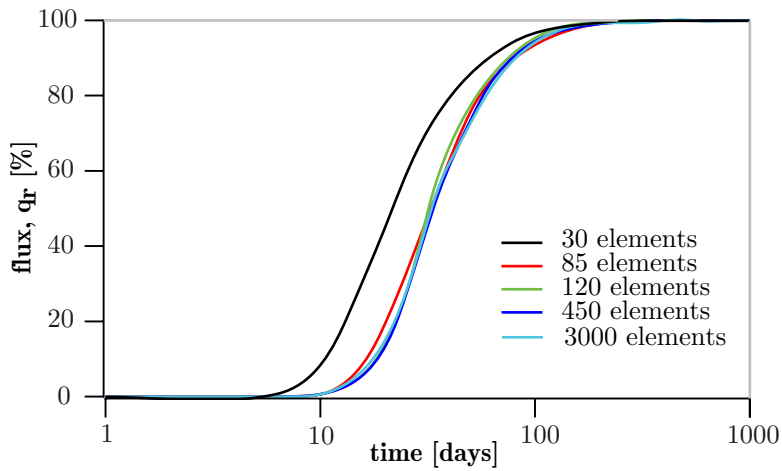
Figure 2.16: Convergence study for XFEM-LS method

2.5   Conclusions

In this chapter a computational model based on the averaging theory, for the mathematical modeling, and the level-set and the extended finite element methods, for the numerical modeling, has been introduced to simulate two-phase flow in an unsaturated porous medium at a regional level. We show that a good combination between a mathematical model and a numerical model enables the simulation of complicated processes occurring in complicated and large geometry using minimal computational efforts. The basic requirements for an accurate, stable, and converging model are met using relatively coarse meshes. Mesh-insensitivity is another important outcome of this combination.

Hydromechanical Modeling of CGS

<div style="text-align:right">**3**</div>

This chapter is based on Talebian et al. (2013b), a paper published in Transport in Porous Media.

3.1 Introduction

Multiphase fluid flow due to injection of CO_2 in an unsaturated reservoir is accompanied by continuous redistribution of pore pressures and effective stresses, causing local and regional deformations and probably a major uplifting or subsidence. Important studies for modeling multiphase flow in rigid, deformable, isothermal, and/or non-isothermal systems have been introduced by, among others, Gawin et al. (1995), Lewis et al. (1989), Schrefler (2001) and Helmig (1997). Modeling CO_2 sequestration in porous media was also covered by, among others, Pruess and García (2002), Rutqvist and Tsang (2002), and Class et al. (2009).

Multiphase fluid flow due to injection of CO_2 in an unsaturated reservoir is also accompanied by electrokinetic flow. Electrokinetic flow is a natural process occurring due to movement of ions in the porous medium electric double layer under the action of fluid flow. The driving hydromechanical force, due to pressure gradient, and the restraining force, due to electrical resistance, give rise to various electrokinetic effects, including the streaming potential, known also as the self-potential (SP). Since the electrical conductivity of CO_2 is lower than that for the formation brine, it can be detected by measuring the self-potential.

Based on this, SP can be used as a monitoring technique, which is necessary to ensure that geologic sequestration is both safe and effective. The self-potential has been extensively utilized and modeled for geothermal exploration (Ishido and Pritchett, 1999; Ishido et al., 2010), groundwater flow (Boleve et al., 2007), and

oil reservoir (Saunders et al., 2008; Wurmstich and Morgan, 1994). However, it seems that so far no study has been introduced on the numerical modeling of the self-potential associated with CO_2 flow in porous media.

In what follows, a description of the governing equations and the involved constitutive relationships is given. Then, a detailed discretization procedure, including linearization of the system and its time integration is introduced. Later, the proposed model is verified by comparing its computational results with analytic solutions of two idealized examples. Finally, numerical examples with parametric analyses are presented.

3.2 Governing Equations

Balance and field equations of a multiphase/multicomponent medium are commonly derived based on multiple overlapping continua with emphasis on the averaged contribution of individual constituents and their interactions. Averaging theories with varying complexities are utilized for formulating the governing balance equations for multiphase flow in porous media. The hybrid mixture theory, known also as the averaging theory, elaborated and effectively employed by Hassanizadeh and Gray (1979a), is considered as one of the most important theories in this field. Based on this theory, general averaged macroscopic balance equations and constitutive relationships for deformed multiphase porous media are derived based on thermodynamic principles. A comprehensive treatment of the averaging theory is given by Lewis and Schrefler (1998) and Bear and Cheng (2010).

Here, an outline of the involved governing equations describing coupled linear momentum, mass balance and electrokinetic balance equations, together with their constitutive laws, are given. It is assumed that the phases are chemically non-reacting, the medium is in isothermal equilibrium, no mutual dissolution between CO_2 and water, CO_2 density and viscosity are constant, and the mechanical properties of the solid phase are not affected by the CO_2 geo-sequestration process.

3.2.1 Equilibrium equations

The linear momentum balance equation of a three-phase medium, under static loading condition, can be expressed as (Lewis and Schrefler, 1998)

$$\text{div}\boldsymbol{\sigma} + \bar{\rho}\mathbf{g} = 0 \tag{3.1}$$

where $\boldsymbol{\sigma}$ is total stress, defined for a multiphase medium constituting solid, s, brine water, w, and CO_2, g, as

$$\boldsymbol{\sigma} = \mathbf{t}_s + \mathbf{t}_w + \mathbf{t}_g \tag{3.2}$$

in which $\mathbf{t}_\pi$ is the intra-phase stress tensor of phase π (s, w, g), $\mathbf{g}$ is the gravity, and $\bar{\rho}$ is an effective density, expressed as

$$\bar{\rho} = \langle \rho \rangle_s + \langle \rho \rangle_w + \langle \rho \rangle_g \tag{3.3}$$

with $\langle \cdots \rangle_\pi$ the volume average quantity of phase π. For simplicity of notation, in what follows, the volume and mass averaged symbol will not be used, though all quantities are volume/mass averaged.

In engineering notation, the total stress is expressed as

$$\boldsymbol{\sigma} = \boldsymbol{\sigma}' - \mathbf{I}\,P \tag{3.4}$$

in which $\boldsymbol{\sigma}'$ is the effective stress, $\mathbf{I}$ is the identity tensor, and

$$P = S_w P_w + S_g P_g \tag{3.5}$$

where P_w and P_g are the water pressure and CO_2 pressure, respectively, and S_w and S_g are their degrees of saturation. Including Eq. (3.5) into Eq. (3.4) gives

$$\boldsymbol{\sigma}' = \boldsymbol{\sigma} + \mathbf{I}(S_w P_w + S_g P_g) \tag{3.6}$$

In the literature, an extended expression incorporating the solid grain compressibility, known as Biot's constant α, is also utilized, as

$$\boldsymbol{\sigma}'' = \boldsymbol{\sigma} + \boldsymbol{I}\alpha(S_w P_w + S_g P_g) \tag{3.7}$$

Substituting Eq. (3.7) into Eq. (3.1) gives

$$\mathrm{div}\,[\boldsymbol{\sigma}'' - \mathbf{I}\alpha(S_w P_w + S_g P_g)] + \bar{\rho}\mathbf{g} = 0 \tag{3.8}$$

The field equilibrium equation of the multiphase domain can be obtained by incorporating appropriate constitutive equations to the linear momentum balance equation, Eq. (3.1). For a linear isotropic solid, the effective stress is described as

$$\boldsymbol{\sigma}'' = \mathbf{D}_e(\boldsymbol{\epsilon} - \boldsymbol{\epsilon}_0) \tag{3.9}$$

in which $\mathbf{D}_e$ is the stiffness tensor of the solid, $\boldsymbol{\epsilon}_0$ is an initial strain, and $\boldsymbol{\epsilon}$ is the total strain of the solid, defined as

$$\boldsymbol{\epsilon} = \hat{\mathbf{L}}\mathbf{u} \tag{3.10}$$

where $\mathbf{u}$ is the displacement vector of the solid phase and $\hat{\mathbf{L}}$ is the displacement-strain operator, defined as

$$\hat{\mathbf{L}}^T = \begin{bmatrix} \frac{\partial}{\partial x} & 0 & 0 & \frac{\partial}{\partial y} & 0 & \frac{\partial}{\partial z} \\ 0 & \frac{\partial}{\partial y} & 0 & \frac{\partial}{\partial x} & \frac{\partial}{\partial z} & 0 \\ 0 & 0 & \frac{\partial}{\partial z} & 0 & \frac{\partial}{\partial y} & \frac{\partial}{\partial x} \end{bmatrix} \tag{3.11}$$

Incorporating Eq. (3.9) into Eq. (3.8), gives the equilibrium field equation (see section 3.2.4).

3.2.2 Mass continuity equations

The continuity equations for the water phase and the CO_2 phase, in isothermal condition with no phase exchange, can be expressed as (Lewis and Schrefler, 1998)
Water phase:

$$\left(\frac{\alpha - \phi}{K_s} S_w^2 + \frac{\phi S_w}{K_w} \right) \frac{\partial P_w}{\partial t} + \frac{\alpha - \phi}{K_s} S_w S_g \frac{\partial P_g}{\partial t}$$
$$+\alpha\, S_w \mathbf{m}^T \frac{\partial \boldsymbol{\epsilon}}{\partial t} + \left(\frac{\alpha - \phi}{K_s} P_w S_w - \frac{\alpha - \phi}{K_s} P_g S_w + \phi \right) \frac{\partial S_w}{\partial t} \tag{3.12}$$
$$+\frac{1}{\rho_w} div\left(\phi S_w \rho_w \mathbf{v}_w \right) = Q_w$$

Gas phase:

$$\left(\frac{\alpha - \phi}{K_s} S_w S_g \right) \frac{\partial P_w}{\partial t} + \left(\frac{\alpha - \phi}{K_s} S_g^2 + \frac{\phi S_g}{K_g} \right) \frac{\partial P_g}{\partial t}$$
$$+\alpha\, S_g \mathbf{m}^T \frac{\partial \boldsymbol{\epsilon}}{\partial t} - \left(\frac{\alpha - \phi}{K_s} S_g \left(P_g - P_w \right) + \phi \right) \frac{\partial S_w}{\partial t} \tag{3.13}$$
$$+\frac{1}{\rho_g} div\left(\phi S_g \rho_g \mathbf{v}_g \right) = Q_g$$

in which K_s, K_w and K_g are the bulk modulus of the solid, water and gas respectively, $\mathbf{v}_w$ and $\mathbf{v}_g$ are water and CO_2 relative velocities to the solid phase, ϕ is porosity, Q_w and Q_g are source or sink terms and $\mathbf{m} = [1, 1, 1, 0, 0, 0]$.

In a multiphase system, the Darcy velocity, $\mathbf{v}_\pi$, is expressed as

$$\phi S_\pi \mathbf{v}_\pi = \frac{\mathbf{k} k_{r\pi}}{\mu_\pi} \left(-\nabla P_\pi + \rho_\pi \mathbf{g} \right) \tag{3.14}$$

where $\mathbf{k}$ is the intrinsic permeability tensor, μ_π and $k_{r\pi}$ are the dynamic viscosity and the relative permeability of phase π respectively.

Eqs. (3.12) and (3.13) contain four unknowns: P_w, P_g, S_w and S_g. However, for a multiphase medium, the water and the CO_2 phases are jointly occupying the voids, implying

$$S_w + S_g = 1 \tag{3.15}$$

Also, the water pressure and the CO_2 pressure are related by the capillary pressure, P_c, as

$$P_c(S_w) = P_g - P_w \tag{3.16}$$

which represents the difference in pressure across the interface between two immiscible fluids. The capillary pressure is a function of water saturation. In literature, there are several empirical formulations correlating the capillary pressure and relative permeability to the degree of saturation, mainly those of van Genuchten (1980) and Brooks and Corey (1964). Using Brooks and Corey (1964) formulation, the capillary pressure-saturation relationship is described as

$$P_c = \frac{P_b}{S_e^{1/\lambda}} \quad P_c \leq P_b \tag{3.17}$$

and the relative permeability-saturation relationships are described as

$$k_{rw} = S_e^{(2+3\lambda)/\lambda} \tag{3.18}$$

$$k_{rg} = (1 - S_e)^2(1 - S_e^{(2+\lambda)/\lambda}) \tag{3.19}$$

where S_e is the effective saturation, defined as

$$S_e = (S_w - S_{wr})/(1 - S_{wr} - S_{gr}) \tag{3.20}$$

in which S_{wr} is the irreducible water saturation, S_{gr} is the residual gas saturation, λ is the pore size distribution index and P_b is an entry pressure, corresponding to the capillary pressure needed to displace the wetting phase from the largest pore.

Spatial and temporal differentiation of Eq. (3.16), using the chain rule, gives

$$\nabla P_w = \nabla P_g - \frac{\partial P_c}{\partial S_w}\nabla S_w \tag{3.21}$$

$$\frac{\partial P_w}{\partial t} = \frac{\partial P_g}{\partial t} - \frac{\partial P_c}{\partial t} = \frac{\partial P_g}{\partial t} - \frac{\partial S_w}{\partial t}\frac{\partial P_c}{\partial S_w} \tag{3.22}$$

Applying these equations to the balance equations, Eqs. (3.12) and (3.13), would eliminate the water pore pressure. Combining Eqs. (3.12) and (3.13) with Eqs. (3.14) and (3.22) gives the general field equations of the mass flow (see section 3.2.4).

3.2.3 Electric current density continuity equation

With no direct electrical current source, there is zero net current flow through the system boundaries, and the conservation of the total current density at quasi-steady state condition implies:

$$\nabla \cdot \mathbf{j} = 0 \tag{3.23}$$

where $\mathbf{j}$ is the total electric current density.

In a multiphase domain, the fluid flow and the electrokinetic flow are coupled. This coupling can be formulated using the theory of coupled flow (Mitchell, 1993), which states that different flow fields can be coupled as

$$\mathbf{q}_i = \sum_{j=1}^{n} L_{ij}.\nabla F_{ij} \tag{3.24}$$

relating a potential gradient, ∇F_{ij}, to a field flux $\mathbf{q}_i$, by a transport coupling coefficient L_{ij} (Revil et al., 1999). In a CO_2 geo-sequestration system, the fluid flow, represented by Darcy's law, Eq. (3.14), can be coupled to the electric flow, represented by Ohm's law, via:

$$\mathbf{v}_w = \mathbf{L}_{11}(-\nabla P_w + \rho_w \mathbf{g}) - \mathbf{L}_{12}\nabla V \tag{3.25}$$

$$\mathbf{j} = \mathbf{L}_{21}(-\nabla P_w + \rho_w \mathbf{g}) - L_{22}\nabla V \tag{3.26}$$

where V is the electrical potential, and $\mathbf{L_{12}}$ and $\mathbf{L_{21}}$ are cross coupling coefficients, which following Onsager reciprocity principle (Onsager, 1931), are equal, giving $\mathbf{L}_{12} = \mathbf{L}_{21} = \mathbf{L}$. Apparently, $\mathbf{L_{11}}$ represents the hydraulic conductivity, and L_{22} represents the electric conductivity, σ_e. Under zero total electrical current condition ($\mathbf{j} = 0$), Eq. (3.26) leads to (Sill, 1983)

$$\left(\frac{\nabla V}{-\nabla P + \rho \mathbf{g}}\right)\Bigg|_{\mathbf{j}=0} = \mathbf{C} = \frac{\mathbf{L}}{\sigma_e} \Rightarrow \quad \mathbf{L} = \sigma_e \mathbf{C} \tag{3.27}$$

in which C is the electrokinetic (voltage) coupling coefficient.

For a partially saturated domain, similar to the permeability coefficient, the electrokinetic coupling coefficient and the electrical conductivity are made function of phase saturation via saturation dependent relative parameters, C_r and σ_r, ranging from 0 to 1. Accordingly, the coupling coefficients in Eqs. (3.25) and (3.26) can be expressed as

$$\mathbf{L}_{11} = \frac{\mathbf{k}\,k_{rw}}{\mu_w}, \quad \mathbf{L}_{12} = \mathbf{L}_{21} = \mathbf{C}C_r\,\sigma_e\sigma_r, \quad L_{22} = \sigma_e\sigma_r \tag{3.28}$$

The electrokinetic coupling coefficient plays a key role in the magnitude of the formation streaming potential. There have been extensive theoretical and empirical

works on this regard, see for example (Bolève et al., 2007; Revil et al., 1999; Saunders et al., 2008).

In a saturated porous medium, the electrokinetic coupling coefficient at a given pressure is a function of temperature, fluid salinity, electrolyte pH, and rock type, expressed as

$$\mathbf{C} = \frac{\zeta \boldsymbol{\epsilon}_w}{\mu_w \sigma_w} \tag{3.29}$$

where ζ is the zeta potential, and $\boldsymbol{\epsilon}_w$, μ_w, σ_w are the brine permittivity (for anisotropic material, a second rank tensor), viscosity and electrical conductivity, respectively. Available data suggests that the effect of temperature changes in the reservoirs conditions is negligible (Reppert and Morgan, 2003).

The electrical conductivity of the bulk formation can be calculated following Glover et al. (2000), as

$$\sigma_e = \phi^m \left[\sigma_g + (S_w)^n (\sigma_w - \sigma_g) \right] \tag{3.30}$$

where n is Archie's saturation exponent (close to 2), m is the cementation exponent (in the range 1.8–2.0 for sandstones, for instance), σ_g and σ_w are the gas and water phase conductivities, respectively. In Eq. (3.30) it is assumed that the electrical conductivity of the non-wetting phase (CO_2) is small compared to that of the wetting (brine), and the electrical conductivity of the sand grains is negligible.

In a partially saturated porous medium, the relative electrical conductivity (inverse of the resistivity index) can simply be calculated using Archie's law, as $\sigma_r = (S_w)^n$. On the other hand, determination of the relative electrokinetic coupling coefficient is more complicated and several models are presented in the literature, see for example (Jackson, 2010; Linde et al., 2007; Revil et al., 1999). Saunders et al. (2008) proposed a power law to describe this parameter, such that

$$C_r = (S_e)^p \tag{3.31}$$

where, exponent p is a function of the excess counter-ions in the diffuse layer and the salinity of the brine. The effect of varying this exponent on the electrokinetic is examined in section 3.4.5.

The salinity of the formation brine significantly affects the conductivity and the electrokinetic coupling coefficients. Electrical conductivity increases with increasing brine salinity. Salinity also affects the zeta potential, permittivity and viscosity (Eq. (3.29)). The effect of salinity on permittivity and viscosity is ignored in this study. According to Worthington et al. (2002), the salt concentration, C_f, is related to the

brine electrical conductivity, σ_w, by

$$
\begin{aligned}
\log(\sigma_w) = \; & 9.42203 \times 10^{-1} + 8.88900 \times 10^{-1} \left[\log(C_f)\right] \\
& -2.72398 \times 10^{-2} [\log(C_f)]^2 - 2.25682 \times 10^{-3} [\log(C_f)]^3 \\
& +1.46605 \times 10^{-5} [\log(C_f)]^4
\end{aligned}
\tag{3.32}
$$

Following Saunders et al. (2008) , the salinity is related to the zeta potential by

$$
\zeta = 16.175 \times \log(C_f) - 16.606
\tag{3.33}
$$

In general, the values of the coupling coefficients decrease as the salinity increases.

Incorporating the constitutive equation for coupled electrokinetic and hydro-dynamic flow, Eq. (3.25), into the mass balance equations, Eqs. (3.12) and (3.13) , and also Eq. (3.26) into the electric current density balance equation, Eq. (3.23), gives the governing field equation for the streaming potential (see section 3.2.4).

3.2.4 General field equations

The governing field equations of a coupled hydromechanical-electrokinetic flow in a CO_2 geo-sequestration process are obtained by incorporating the constitutive equations into the relevant balance equations. In literature, there are three well-known formulations for multiphase flow in porous media: pressure formulation, where phases pressures are the unknown variables; pressure-saturation formulation, where the pressure of a fluid phase and the saturation of the other phases are the unknown variables; and saturation formulation, where phases saturation are the unknown variables (Helmig, 1997). Here we adopt the pressure-saturation formulation, namely P_g-S_w, because it gives a concise set of equations.

Equilibrium field equation
Incorporating Eqs. (3.9), (3.10) and (3.16) into Eq. (3.8), ignoring the initial strain, the equilibrium equation can be obtained as

$$
\mathrm{div}\left[\mathbf{D}_e(\hat{\mathbf{L}}\mathbf{u}) - \mathbf{m}^T \alpha (P_g - P_c S_w) \right] + \bar{\rho}\mathbf{g} = 0
\tag{3.34}
$$

where the effective density is usually described as

$$
\bar{\rho} = (1 - \phi)\rho_s + \phi S_w \rho_w + \phi S_g \rho_g
\tag{3.35}
$$

Mass balance field equations
Incorporating Eqs. (3.21), (3.22) and (3.25) into Eq. (3.12) and rearranging,

70

neglecting the gradient of the water density, the field mass balance equation can be expressed as

$$d_1 \frac{\partial P_g}{\partial t} + d_2 \frac{\partial S_w}{\partial t} + d_3 \mathbf{m}^T \frac{\partial \boldsymbol{\epsilon}}{\partial t} + \nabla \cdot (-\mathbf{c}_1 \nabla P_g - \mathbf{c}_2 \nabla S_w - \mathbf{c}_3 \nabla V + \mathbf{G}_1) = Q_w \quad (3.36)$$

Similarly, substituting Eqs. (3.21) and (3.22) into Eq. (3.13), gives

$$d_4 \frac{\partial P_g}{\partial t} + d_5 \frac{\partial S_w}{\partial t} + d_6 \mathbf{m}^T \frac{\partial \boldsymbol{\epsilon}}{\partial t} + \nabla \cdot (-\mathbf{c}_4 \nabla P_g + \mathbf{G}_2) = Q_g \quad (3.37)$$

where $d_1 \ldots d_6$, $\mathbf{c}_1$-$\mathbf{c}_4$, and $\mathbf{G}_1 \ldots \mathbf{G}_2$ are coefficients described in Table 3.1.

Electric current density balance field equations

Incorporating Eqs. (3.21) and (3.26) into Eq. (3.23) gives

$$\nabla \cdot (-\mathbf{c}_5 \nabla P_g - \mathbf{c}_6 \nabla S_w - c_7 \nabla V + \mathbf{G}_3) = 0 \quad (3.38)$$

where $\mathbf{c}_5$-$\mathbf{c}_7$ and $\mathbf{G}_3$ are coefficients described in Table 3.1.

3.2.5 Initial and boundary conditions

Initially, at t = 0, displacement, CO_2 pressure, water saturation and the electrokinetic potential are described as

$$\mathbf{u} = \mathbf{u}_0; \quad P_g = P_{g0}(\mathbf{x}); \quad S_w = S_{w0}(\mathbf{x}); \quad V = V_0(\mathbf{x}) \quad \text{at } t = 0 \quad (3.39)$$

The Dirichlet boundary conditions for the three fields are prescribed as

$$\begin{aligned}
\mathbf{u} &= \hat{\mathbf{u}} & \text{on } \Gamma_u \\
P_g &= \hat{P}_g & \text{on } \Gamma_g \\
S_w &= \hat{S}_w & \text{on } \Gamma_w \\
V &= \hat{V} & \text{on } \Gamma_V
\end{aligned} \quad (3.40)$$

where $\Gamma = \Gamma_u \cup \Gamma_g = \Gamma_w \cup \Gamma_V = \Gamma_g^q \cup \Gamma_w^q = \Gamma_e^q \cup \Gamma_u^q$ is the boundary surface. The relevant Neumann boundary conditions for the flow are:
CO_2 flux:

$$\frac{\mathbf{k} k_{rg}}{\mu_g} (-\nabla P_g + \rho_g \mathbf{g}) \cdot \mathbf{n} = q_g \quad \text{on } \Gamma_g^q \quad (3.41)$$

Water flux:

$$\frac{\mathbf{k} k_{rw}}{\mu_w} \left(-\nabla P_g + \nabla S_w \frac{\partial P_c}{\partial S_w} + \rho_w \mathbf{g} \right) \cdot \mathbf{n} = q_w \quad \text{on } \Gamma_w^q \quad (3.42)$$

Table 3.1: Coefficients of the general field equations.

C	d	G
$\mathbf{c}_1 = \mathbf{k}\dfrac{k_{rw}}{\mu_w}$	$d_1 = \dfrac{\alpha-\phi}{K_s}\,S_w + \dfrac{\phi S_w}{K_w}$	$\mathbf{G}_1 = \mathbf{k}\dfrac{k_{rw}}{\mu_w}\,\rho_w\,\mathbf{g}$
$\mathbf{c}_2 = -\dfrac{\partial P_c}{\partial S_w}\,\mathbf{k}\dfrac{k_{rw}}{\mu_w}$	$d_2 = -\dfrac{\alpha-\phi}{K_s}\,P_c S_w + \phi - \dfrac{\alpha-\phi}{K_s}\,S_w^2\,\dfrac{\partial P_c}{\partial S_w} - \dfrac{\phi S_w}{K_w}\,\dfrac{\partial P_c}{\partial S_w}$	$\mathbf{G}_2 = \mathbf{k}\dfrac{k_{rg}}{\mu_g}\,\rho_g\,\mathbf{g}$
$\mathbf{c}_3 = \mathbf{C}C_r\,\sigma_e\sigma_r$	$d_3 = \alpha\,S_w$	$\mathbf{G}_3 = \rho_w\mathbf{g}\mathbf{C}C_r\,\sigma_e\sigma_r$
$\mathbf{c}_4 = \mathbf{k}\dfrac{k_{rg}}{\mu_g}$	$d_4 = \dfrac{\alpha-\phi}{K_s} - S_w\,\dfrac{\alpha-\phi}{K_s} + \dfrac{\phi(1-S_w)}{K_g}$	—
$\mathbf{c}_5 = \mathbf{C}C_r\,\sigma_e\sigma_r$	$d_5 = -\dfrac{\alpha-\phi}{K_s}\,P_c + \dfrac{\alpha-\phi}{K_s}\,S_w P_c - \phi - \dfrac{\alpha-\phi}{K_s}\,S_w\,\dfrac{\partial P_c}{\partial S_w} + \dfrac{\alpha-\phi}{K_s}\,S_w^{\,2}\,\dfrac{\partial P_c}{\partial S_w}$	—
$\mathbf{c}_6 = -\mathbf{C}C_r\,\sigma_e\sigma_r\,\dfrac{\partial P_c}{\partial S_w}$	$d_6 = \alpha\,(1 - S_w)$	—
$c_7 = \sigma_e\sigma_r$	—	—

where $\mathbf{n} = \{n_x, n_y, n_z\}^T$ is the unit normal vector. The Neumann boundary condition for the equilibrium field is:

$$\mathbf{I}^T \boldsymbol{\sigma} = \bar{\mathbf{t}} \quad \text{on } \Gamma_u^q \tag{3.43}$$

where the unit matrix $\mathbf{I}$ is defined as

$$\mathbf{I}^T = \begin{bmatrix} n_x & 0 & 0 & n_y & 0 & n_z \\ 0 & n_y & 0 & n_x & n_z & 0 \\ 0 & 0 & n_z & 0 & n_y & n_x \end{bmatrix} \tag{3.44}$$

In a typical CO_2 geo-sequestration system, no Neumann boundary condition for the electrokinetic field is applicable.

3.3   Mixed discretization scheme

Eqs. (3.34)-(3.38) together with the initial and boundary conditions, Eqs. (3.39)-(3.43), represent an initial and boundary value problem of a coupled electrokinetic-multiphase flow in a deformable unsaturated underground formation. It involves the motion of an immiscible CO_2 plume under the combined action of solid deformation and viscous, capillary and gravity forces. At the front of the plume, there is a relatively high gradient in the saturation field and the pressure field. Capturing and modeling this front can lead to spurious oscillations. Using standard finite element discretization schemes requires fine or adaptive meshes, and probably CPU time of the order of several days or weeks to conduct an analysis at a regional level. On the other hand, using advanced discretization schemes, such as the Discontinuous Galerkin or the multiscale finite element, generates a large system of equations, requiring parallel and powerful computational capacity.

To tackle this problem, here, the governing equations are solved using a mixed discretization scheme. The standard Galerkin finite element method (SG) and the extended finite element method (XFEM), coupled to the level-set method (LS), are utilized. Coupling between LS and XFEM is essential for effectively capturing and modeling the CO_2 plume front. Physically, for a typical CO_2 geo-sequestration problem, capturing the front of the CO_2 plume at the exact location is not very important; but numerically, it is vital because it leads to a locally conservative discrete system, making the scheme stable and convergent. For the equilibrium field equation and the diffusive dominant equations, the standard Galerkin method suffices.

3.3.1 Level-set discretization

The level-set method is a numerical technique usually utilized for tracing a moving interface, Γ_d, between two zones, for instance, Ω_1 and Ω_2. A level-set function is defined as a signed distance function $\Phi(x)$, which is positive in Ω_1, negative in Ω_2, and zero at the interface between them. The level-set value is advected by the field motion, as

$$\frac{\partial \Phi}{\partial t} + \mathbf{v}_{\Gamma_d} \cdot \nabla \Phi = 0 \tag{3.45}$$

where $\mathbf{v}_{\Gamma_d}$ represents the interface velocity, the CO_2 plume front velocity. Following Liu et al. (2010), the front velocity can be calculated as

$$\mathbf{v}_{\Gamma_d} = \frac{\rho_g (1 - S_w)}{\bar{\rho}} \mathbf{v}_g + \frac{\rho_w S_w}{\rho} \mathbf{v}_w \tag{3.46}$$

where $\mathbf{v}_g$ and $\mathbf{v}_w$ are CO_2 and water Darcy velocities, calculated by Eq. (3.14) and $\rho = \rho_w S_w + \rho_g S_g$.

The level-set equation, Eq. (3.45), is a first-order hyperbolic and its discretization using the standard Galerkin method may result into spurious oscillations. Different techniques have been employed to stabilize this problem, among which the Streamline Upwind Petrov-Galerkin (SUPG) method is known to be effective in many cases (Brooks and Hughes, 1982). In the SUPG method the shape function is perturbed in the direction of the flow, as

$$\bar{\mathbf{N}} = \mathbf{N} + \mathbf{N_s} \tag{3.47}$$

where $\mathbf{N}$ is the standard finite element shape functions and $\mathbf{N_s}$ is an enhancement function, defined as

$$\mathbf{N}_s = \tau \mathbf{v}_{\Gamma_d} \cdot \nabla \mathbf{N} \tag{3.48}$$

where τ is a stabilization parameter. In literature, there are several formulations describing τ. In the absence of diffusion, it can be expressed as

$$\tau = \frac{h_e}{2 |\mathbf{v}_{\Gamma_d}|} \tag{3.49}$$

where h_e is the characteristic length of the element, defined as

$$h_e = 2 \left(\sum_{\alpha=1}^{n_e} \left| \frac{\mathbf{v}_{\Gamma_d i}}{\|\mathbf{v}_{\Gamma_d}\|} \frac{\partial N_\alpha}{\partial x_i} \right| \right)^{-1} \tag{3.50}$$

in which n_e is the number of nodes in the element and N_α is the basis function associated with node α. Applying the weighted residual finite element discretization procedure to Eq. (3.45), using Eq. (3.47), gives

$$\int_\Omega \mathbf{N} \left(\frac{\partial \Phi}{\partial t} + \mathbf{v}_{\Gamma_d} \cdot \nabla \Phi \right) d\Omega + \sum_k \int_{\Omega_k} \mathbf{N}_s \left(\frac{\partial \Phi}{\partial t} + \mathbf{v}_{\Gamma_d} \cdot \nabla \Phi \right) d\Omega = 0 \tag{3.51}$$

Approximating $\Phi = \boldsymbol{N}\bar{\bar{\boldsymbol{\Phi}}}$, where $\bar{\bar{\boldsymbol{\Phi}}}$ is the level-set nodal values, and substituting into Eq. (3.51), yields

$$
\int_\Omega \mathbf{N}^T \mathbf{N} \frac{\partial \bar{\bar{\boldsymbol{\Phi}}}}{\partial t} d\Omega + \int_\Omega \mathbf{N}^T (\mathbf{v}_{\Gamma_d} \cdot \nabla \mathbf{N}) \bar{\bar{\boldsymbol{\Phi}}} \, d\Omega + \sum_k \int_{\Omega_k} \mathbf{N}_s^T \mathbf{N} \frac{\partial \bar{\bar{\boldsymbol{\Phi}}}}{\partial t} d\Omega
$$
$$
+ \sum_k \int_{\Omega_k} \mathbf{N}_s^T (\mathbf{v}_{\Gamma_d} \cdot \nabla \mathbf{N}) \bar{\bar{\boldsymbol{\Phi}}} \, d\Omega = 0
\tag{3.52}
$$

The stabilizing term in Eq. (3.52) is denoted by a subscript k to emphasize that, due to $\nabla \mathbf{N}$, which is discontinuous across the elements, the numerical integration must be carried out on the element interior Ω_k, not at elements boundaries.

Utilizing the level-set method to trace a moving front requires re-initialization at every time step. This is necessary because otherwise the distance property of the level-set function is no longer maintained after advection. In literature, several numerical approaches have been employed to treat this problem, including the fast marching method, a distancing direct approach, and a direct solution of the advection hyperbolic partial differential equation. Most of the efforts are spent on maintaining the high gradient curvatures of the interface between the involved phases, such as the advection of air bubbles in a liquid. Here, and due to the relatively large size of the CO_2 plume, the gradient of the curvature of the plume front within an element is insignificant, making its contour line within the elements nearly straight (in 2D problems), rather than curves. Thus, a direct distancing approach, proposed by Cho et al. (2011), suffices. In this approach, the re-distancing is performed by geometrical updating of the advective front instead of solving a re-initialization equation. Detailed procedure can be found in Cho et al. (2011).

3.3.2 SG-XFEM discretization

The governing field equations, Eqs. (3.34)-(3.38), involve fields of different nature. The displacement field is continuous but the pressure, saturation and electrokinetic fields at the CO_2 plume front exhibit high gradients. The extended finite element method can be utilized to model these high gradients. However, this implies doubling the degrees of freedom, making the gained stability, computationally inefficient. To reduce the number of degrees of freedom, a mixed discretization scheme, proposed by Al-Khoury and Sluys (2007), is utilized. Equations containing diffusion and/or strong capillary effects can be discretized using SG method, and equations containing advection together with high gradient in the saturation field can be discretized using XFEM method. Following this, Eqs. (3.34), (3.36) and (3.38), and as they contain continuous displacement, capillary effects and diffusive terms including that for

saturation, discretization using SG suffices. Eq. (3.37), on the other hand, describes a marching saturation front with no diffusion, and thus XFEM discretization is more appropriate.

Using the weighted residual method, the finite element formulation of the equilibrium equation, Eq. (3.1), using Eq. (3.43), can be described as

$$\int_\Omega \mathbf{w}^T(\hat{\mathbf{L}}^T\boldsymbol{\sigma} + \bar{\rho}\mathbf{g})d\Omega - \int_{\Gamma_u^q} \mathbf{w}^T(\mathbf{I}^T\boldsymbol{\sigma} - \bar{\mathbf{t}})d\Gamma = 0 \qquad (3.53)$$

in which $\mathbf{w}$ is any arbitrary weighting function. Applying Green's theorem to the first part of Eq. (3.53), gives

$$-\int_\Omega (\hat{\mathbf{L}}\mathbf{w})^T\boldsymbol{\sigma}\ d\Omega + \int_{\Gamma_u^q} \mathbf{w}^T\mathbf{I}^T\boldsymbol{\sigma}\ d\Gamma + \int_\Omega \mathbf{w}^T\bar{\rho}\mathbf{g}\ d\Omega - \int_{\Gamma_u^q} \mathbf{w}^T(\mathbf{I}^T\boldsymbol{\sigma} - \bar{\mathbf{t}})d\Gamma = 0 \qquad (3.54)$$

Simplifying Eq. (3.54) yields

$$-\int_\Omega (\hat{\mathbf{L}}\mathbf{w})^T\boldsymbol{\sigma}\ d\Omega + \int_\Omega \mathbf{w}^T\bar{\rho}\mathbf{g}\ d\Omega + \int_{\Gamma_u^q} \mathbf{w}^T\bar{\mathbf{t}}\ d\Gamma = 0 \qquad (3.55)$$

Introducing Eq. (3.34) gives

$$-\int_\Omega (\hat{\mathbf{L}}\mathbf{w})^T \left[\mathbf{D}_e(\hat{\mathbf{L}}\mathbf{u}) - \mathbf{m}^T\alpha(P_g - P_cS_w)\right]d\Omega + \int_\Omega \mathbf{w}^T\bar{\rho}\mathbf{g}d\Omega + \int_{\Gamma_u^q} \mathbf{w}^T\bar{\mathbf{t}}d\Gamma = 0 \qquad (3.56)$$

Displacement, gas pressure and streaming potential values are expressed in terms of their nodal values as

$$\begin{aligned} \mathbf{u}(x,t) &= \mathbf{N}_u(x)\bar{\mathbf{u}}(t) \\ P_g(x,t) &= \mathbf{N}_p(x)\bar{\mathbf{P}}_g(t) \\ V(x,t) &= \mathbf{N}_V(x)\bar{\mathbf{V}}(t) \end{aligned} \qquad (3.57)$$

where $\bar{\mathbf{u}}$, $\bar{\mathbf{P}}_g$ and $\bar{\mathbf{V}}$ are the nodal vectors for displacement, CO_2 pressure and streaming potential.

The saturation field, on the other hand, exhibits high gradient at the CO_2 plume front that is best described by the XFEM. In XFEM, the finite element spatial discretization is conducted by adding an enhanced function necessary to capture any physical discontinuity or a high gradient field exists within the element. The saturation field can thus be described in terms of its nodal values as

$$S_w(x,t) = \mathbf{N}(x)\bar{\mathbf{S}}_w(t) + \sum_{J \in N_{\text{enriched}}} N_J^*(x,t)a_J(t) \qquad (3.58)$$

where $\bar{\mathbf{S}}_w$ is the nodal water saturation vector and a_J is an additional nodal degree of freedom on node J of an enriched element, N_{enriched}, where the plume front intersects.

As proposed by Chessa and Belytschko (2003a), the level-set function can be utilized for the enriched shape functions, giving

$$N_J^*(x,t) = N_J(x) \left[|\Phi(x,t)| - |\Phi(x_J,t)| \right] \tag{3.59}$$

Based on Eq. (3.58) and Eq. (3.59), the saturation gradient can be calculated, in tensor notation, as

$$
\begin{aligned}
\nabla \mathbf{S}_w &= \sum_{I \in \mathbb{N}} \nabla \mathbf{N}_I \mathbf{S}_{wI} + \sum_{J \in N_{enriched}} \nabla \mathbf{N}_j^* \mathbf{a}_J \\
&= \sum_{I \in \mathbb{N}} \nabla \mathbf{N}_I \mathbf{S}_{wI} + \sum_{J \in N_{enriched}} (\nabla \mathbf{N}_J \mathbf{\Psi}_J + \mathbf{N}_J \nabla \mathbf{\Psi}_J) \cdot \mathbf{a}_J
\end{aligned}
\tag{3.60}
$$

with $\mathbf{\Psi}_J = [|\Phi(x,t)| - |\Phi(x_J,t)|]$.

Using the Galerkin finite element method, the weighting function $\mathbf{w}$ is defined by the shape function, i.e. $\mathbf{w} = \mathbf{N}$. Substituting Eq. (3.57) and Eq. (3.58) into Eq. (3.56) gives

$$
\begin{aligned}
-\int_\Omega \mathbf{B}^T \mathbf{D} \, \mathbf{B} \, \bar{\mathbf{u}} \, d\Omega &+ \int_\Omega \mathbf{B}^T \mathbf{m}^T \alpha \mathbf{N}_p \bar{\mathbf{P}}_g \, d\Omega - \int_\Omega \mathbf{B}^T \mathbf{m}^T \alpha P_c \mathbf{N}_s \bar{\mathbf{S}}_w d\Omega \\
&- \int_{\Omega^+} \mathbf{B}^T \mathbf{m}^T \alpha P_c \, \mathbf{N}^* \mathbf{a}_J \, d\Omega + \int_{\Gamma_u^q} \mathbf{N}_u^T \, \bar{\mathbf{t}} \, d\Gamma + \int_\Omega \mathbf{N}_u^T \bar{\rho} \mathbf{g} \, d\Omega = 0
\end{aligned}
\tag{3.61}
$$

where $\mathbf{B} = \hat{\mathbf{L}}\mathbf{N}$, $\bar{\mathbf{u}}$, $\bar{\mathbf{P}}_g$ and $\bar{\mathbf{S}}_w$ are the nodal vectors for displacement, CO_2 pressure and water saturation; $\bar{\mathbf{t}}$ is the traction force, and Ω and Ω^+ are the continuous and the discontinuous subdomains, representing the formation water zone and the CO_2 zone within an element, respectively. The capillary pressure P_c in Eq. (3.61) is a nonlinear parameter that will be linearized in terms of water saturation (see Eq. (3.70) in section 3.3.3).

In a similar manner applying the Galerkin weighted residual method to Eq. (3.36), employing Green's theorem, applying Eq. (3.42), ignoring source/sink terms, and using the same shape function as for the equilibrium field equation, yields

$$
\begin{aligned}
&\int_\Omega \mathbf{N}^T d_1 \, \mathbf{N} \, \dot{\mathbf{P}}_g \, d\Omega + \int_\Omega \mathbf{N}^T d_2 \mathbf{N} \, \dot{\mathbf{S}}_w d\Omega \; + \int_{\Omega^+} \mathbf{N}^T d_2 \mathbf{N}^* \dot{\mathbf{a}}_J \, d\Omega \\
&+ \int_\Omega \mathbf{N}^T d_3 \, \mathbf{m}^T \mathbf{B} \, \dot{\mathbf{u}} \, d\Omega + \int_\Omega (\nabla \mathbf{N})^T \mathbf{c}_1 \nabla \mathbf{N} \bar{P}_g d\Omega + \int_\Omega (\nabla \mathbf{N})^T \mathbf{c}_2 \nabla \mathbf{N} \bar{\mathbf{S}}_w d\Omega \\
&+ \int_{\Omega^+} (\nabla \mathbf{N})^T \mathbf{c}_2 \nabla \mathbf{N}^* \mathbf{a}_J d\Omega + \int_\Omega (\nabla \mathbf{N})^T \mathbf{c}_3 \nabla \mathbf{N} \bar{\mathbf{V}} \, d\Omega - \int_\Omega (\nabla \mathbf{N})^T \mathbf{G}_1 d\Omega \\
&+ \int_{\Gamma_w^q} \mathbf{N}^T q_w \, d\Gamma = 0
\end{aligned}
\tag{3.62}
$$

where Γ_d represents the interface between the CO_2 plume front and the formation water, and Γ_e^q represents a surface on the system boundary where an electrical flux

can be applied. In a typical geo-sequestration problem, fluxes at these two surfaces are not valid and these two terms vanish.

Applying XFEM to Eq. (3.37), using a weighting function of the form:

$$\mathbf{w} = \mathbf{N} + \mathbf{N}_J^* \tag{3.63}$$

gives gives

$$
\int_\Omega \mathbf{N}^T \left[d_4 \frac{\partial P_g}{\partial t} + d_5 \frac{\partial S_w}{\partial t} + d_6 \, \mathbf{m}^T \frac{\partial \boldsymbol{\epsilon}}{\partial t} + \nabla \cdot (-\mathbf{c}_4 \nabla P_g + \mathbf{G}_2) \right] d\Omega
$$
$$
+ \int_{\Omega+} \mathbf{N}_J^{*T} \left[d_4 \frac{\partial P_g}{\partial t} + d_5 \frac{\partial S_w}{\partial t} + d_6 \mathbf{m}^T \frac{\partial \boldsymbol{\epsilon}}{\partial t} + \nabla \cdot (-\mathbf{c}_4 \nabla P_g + \mathbf{G}_2) \right] d\Omega = 0 \tag{3.64}
$$

As the summation of the residuals of the two subdomains is equal to zero, the residual of each subdomain must also be zero, and thus, Eq. (3.64) can be split into two equations, giving

$$
\int_\Omega \mathbf{N}^T \left[d_4 \frac{\partial P_g}{\partial t} + d_5 \frac{\partial S_w}{\partial t} + d_6 \, \mathbf{m}^T \frac{\partial \boldsymbol{\epsilon}}{\partial t} + \nabla \cdot (-\mathbf{c}_4 \nabla P_g + \mathbf{G}_2) \right] d\Omega = 0 \tag{3.65}
$$

$$
\int_{\Omega+} \mathbf{N}_J^{*T} \left[d_4 \frac{\partial P_g}{\partial t} + d_5 \frac{\partial S_w}{\partial t} + d_6 \, \mathbf{m}^T \frac{\partial \boldsymbol{\epsilon}}{\partial t} + \nabla \cdot (-\mathbf{c}_4 \nabla P_g + \mathbf{G}_2) \right] d\Omega = 0 \tag{3.66}
$$

Employing the Green's theorem, applying Eq.(3.41), and introducing Eq. (3.58) into Eqs. (3.65) and (3.66) leads to

$$
\int_\Omega \mathbf{N}^T d_4 \, \mathbf{N} \dot{\mathbf{P}}_g d\Omega + \int_\Omega \mathbf{N}^T d_5 \mathbf{N} \dot{\mathbf{S}}_w d\Omega + \int_{\Omega+} \mathbf{N}^T d_5 \mathbf{N}^* \dot{\mathbf{a}}_J d\Omega
$$
$$
+ \int_\Omega \mathbf{N}^T d_6 \mathbf{m}^T \mathbf{B} \dot{\mathbf{u}} \, d\Omega + \int_\Omega (\nabla \mathbf{N})^T \mathbf{c}_4 \nabla \mathbf{N} \bar{\mathbf{P}}_g d\Omega \tag{3.67}
$$
$$
+ \int_{\Gamma_g^q} \mathbf{N}^T q_g \, d\Gamma - \int_\Omega (\nabla \mathbf{N})^T \mathbf{G}_2 d\Omega = 0
$$

and

$$
\int_{\Omega+} \mathbf{N}^{*T} d_4 \mathbf{N} \dot{\mathbf{P}}_g d\Omega + \int_{\Omega+} \mathbf{N}^{*T} d_5 \mathbf{N} \, \dot{\mathbf{S}}_w d\Omega + \int_{\Omega+} \mathbf{N}^{*T} d_5 \, \mathbf{N}^* \dot{\mathbf{a}}_J d\Omega
$$
$$
+ \int_{\Omega+} \mathbf{N}^{*T} d_6 \mathbf{m}^T \mathbf{B} \dot{\mathbf{u}} \, d\Omega + \int_{\Omega+} (\nabla \mathbf{N}^*)^T \mathbf{c}_4 \nabla \mathbf{N} \bar{\mathbf{P}}_g d\Omega \tag{3.68}
$$
$$
+ \int_{\Gamma_g^q} \mathbf{N}^{*T} q_g \, d\Gamma - \int_{\Omega+} (\nabla \mathbf{N}^*)^T \mathbf{G}_2 d\Omega = 0
$$

Applying the Galerkin weighted residual method to the streaming potential field balance equation, Eq. (3.38), gives

$$
\int_\Omega (\nabla \mathbf{N})^T \mathbf{c}_5 \nabla \mathbf{N} \bar{\mathbf{P}}_g d\Omega + \int_\Omega (\nabla \mathbf{N})^T \mathbf{c}_6 \nabla \mathbf{N} \bar{\mathbf{S}}_\mathbf{w} d\Omega + \int_{\Omega+} (\nabla \mathbf{N})^T \mathbf{c}_6 \nabla \mathbf{N}^* \mathbf{a}_J d\Omega
$$
$$
+ \int_\Omega (\nabla \mathbf{N})^T \mathbf{c}_7 \nabla \mathbf{N} \bar{\mathbf{V}} d\Omega - \int_\Omega (\nabla \mathbf{N})^T \mathbf{G}_3 d\Omega + \int_{\Gamma_e^q} q_e d\Gamma = 0 \tag{3.69}
$$

where the flux term q_e in a typical self-potential vanishes.

3.3.3 Linearization

The resulting weak formulations, Eqs. (3.61), (3.62), (3.67), (3.68) and (3.69), represent a set of semi-discrete nonlinear equations that need to be solved iteratively. Since the constitutive relationships are continuous, it is convenient to linearize these equations using Taylor series expansions up to the first order. For example, the nonlinear parameter $\mathbf{c}_1$ at iteration $r + 1$, can be linearized as

$$\mathbf{c}_1^{r+1} = \mathbf{c}_1(S_w^r) + \frac{\partial \mathbf{c}_1(S_w^r)}{\partial S_w}(\delta S_w) \tag{3.70}$$

with

$$\delta S_w = S_w^{r+1} - S_w^r \tag{3.71}$$

Using Brook and Corey's model, given in Eqs. (3.17)-(3.19), and assuming a constant viscosity, $\mathbf{c}_1$ variation with saturation can be calculated analytically as

$$\frac{\partial \mathbf{c}_1}{\partial S_w} = \frac{\mathbf{k}}{\mu_w} \frac{\partial k_{rw}}{\partial S_e} \frac{\partial S_e}{\partial S_w} = \frac{\mathbf{k}}{\mu_w(1 - S_{wr} - S_{gr})\lambda}(3S_e^{(2\lambda+2)/\lambda}\lambda + 2S_e^{(2\lambda+2)/\lambda}) \tag{3.72}$$

Derivatives of the other nonlinear parameters, given in Table 3.1, can be calculated in the same way. The primary variables and their time derivatives can be written as

$$\begin{aligned} \mathbf{X}^{r+1} &= \mathbf{X}^r + \delta\mathbf{X} \\ \dot{\mathbf{X}}^{r+1} &= \dot{\mathbf{X}}^r + \delta\dot{\mathbf{X}} \end{aligned} \tag{3.73}$$

where $X^{r+1} = [\mathbf{u}\ \mathbf{P}_g\ \mathbf{S}_w\ \mathbf{a}_J\ \mathbf{V}]^T$ is the unknown state vector at the current iteration $(r + 1)$ and $\delta\mathbf{X}$ is its incremental value. $\dot{\mathbf{X}}^r$ denotes the time derivative of the state vector at iteration r and $\delta\dot{\mathbf{X}}$ is the time derivatives of the incremental state vector.

Linearizing Eq. (3.61) and rearranging gives, in a concise form

$$\begin{aligned} &\mathbf{K}_{11}\,\delta\bar{\mathbf{u}} + \mathbf{K}_{12}\,\delta\bar{\mathbf{P}}_g + \mathbf{K}_{13}\,\delta\bar{\mathbf{S}}_w + \mathbf{K}_{14}\,\delta\mathbf{a}_J \\ &\qquad = \mathbf{f}_1 - (\mathbf{K}_{11}^0\,\bar{\mathbf{u}}^r + \mathbf{K}_{12}^0\,\bar{\mathbf{P}}_g^r + \mathbf{K}_{13}^0\,\bar{\mathbf{S}}_w^r + \mathbf{K}_{14}^0\,\mathbf{a}_J^r) \end{aligned} \tag{3.74}$$

Similarly, Eqs. (3.62), (3.67), (3.68) and (3.69) can be expressed as

$$\begin{aligned} &\mathbf{C}_{21}\delta\dot{\mathbf{u}} + \mathbf{C}_{22}\delta\dot{\mathbf{P}}_g + \mathbf{C}_{23}\delta\dot{\mathbf{S}}_w + \mathbf{C}_{24}\delta\dot{\mathbf{a}}_J + \mathbf{K}_{22}\,\delta\bar{\mathbf{P}}_g + \mathbf{K}_{23}\,\delta\bar{\mathbf{S}}_w \\ &+\mathbf{K}_{24}\,\delta\mathbf{a}_J + \mathbf{K}_{25}\,\delta\bar{\mathbf{V}} = \mathbf{f}_2 - (\mathbf{C}_{21}^0\,\dot{\mathbf{u}}^r + \mathbf{C}_{22}^0\,\dot{\mathbf{P}}_g^r + \mathbf{C}_{23}^0\,\dot{\mathbf{S}}_w^r \\ &+\mathbf{C}_{24}^0\,\dot{\mathbf{a}}_J^r + \mathbf{K}_{22}^0\,\bar{\mathbf{P}}_g^r + \mathbf{K}_{23}^0\,\bar{\mathbf{S}}_w^r + \mathbf{K}_{24}^0\,\mathbf{a}_J^r + \mathbf{K}_{25}^0\,\bar{\mathbf{V}}^r) \end{aligned} \tag{3.75}$$

$$\begin{aligned} &\mathbf{C}_{31}\delta\dot{\mathbf{u}} + \mathbf{C}_{32}\delta\dot{\mathbf{P}}_g + \mathbf{C}_{33}\delta\dot{\mathbf{S}}_w + \mathbf{C}_{34}\delta\dot{\mathbf{a}}_J + \mathbf{K}_{32}\,\delta\bar{\mathbf{P}}_g + \mathbf{K}_{33}\,\delta\bar{\mathbf{S}}_w \\ &\qquad = \mathbf{f}_3 - (\mathbf{C}_{31}^0\,\dot{\mathbf{u}}^r + \mathbf{C}_{32}^0\,\dot{\mathbf{P}}_g^r + \mathbf{C}_{33}^0\,\dot{\mathbf{S}}_w^r + \mathbf{C}_{34}^0\,\dot{\mathbf{a}}_J^r + \mathbf{K}_{32}^0\,\bar{\mathbf{P}}_g^r) \end{aligned} \tag{3.76}$$

$$\mathbf{C}_{41}\delta\dot{\mathbf{u}} + \mathbf{C}_{42}\delta\dot{\mathbf{P}}_g + \mathbf{C}_{43}\delta\dot{\mathbf{S}}_w + \mathbf{C}_{44}\delta\dot{\mathbf{a}}_J + \mathbf{K}_{42}\,\delta\bar{\mathbf{P}}_g + \mathbf{K}_{43}\,\delta\bar{\mathbf{S}}_w$$
$$= \mathbf{f}_4 - (\mathbf{C}_{41}^0\dot{\mathbf{u}}^r + \mathbf{C}_{42}^0\dot{\mathbf{P}}_g^r + \mathbf{C}_{43}^0\dot{\mathbf{S}}_w^r + \mathbf{C}_{44}^0\dot{\mathbf{a}}_J^r + \mathbf{K}_{42}^0\,\bar{\mathbf{P}}_g^r) \tag{3.77}$$

$$\mathbf{K}_{52}\,\delta\bar{\mathbf{P}}_g + \mathbf{K}_{53}\,\delta\bar{\mathbf{S}}_w + \mathbf{K}_{54}\,\delta\mathbf{a}_J + \mathbf{K}_{55}\,\delta\bar{\mathbf{V}}$$
$$= \mathbf{f}_5 - (\mathbf{K}_{52}^0\,\bar{\mathbf{P}}_g^r + \mathbf{K}_{53}^0\,\bar{\mathbf{S}}_w^r + \mathbf{K}_{54}^0\,\mathbf{a}_J^r + \mathbf{K}_{55}^0\,\bar{\mathbf{V}}^r) \tag{3.78}$$

Assembling Eqs. (3.74)-(3.78) in matrix form, yields

$$
\begin{pmatrix}
\mathbf{K}_{11} & \mathbf{K}_{12} & \mathbf{K}_{13} & \mathbf{K}_{14} & 0 \\
0 & \mathbf{K}_{22} & \mathbf{K}_{23} & \mathbf{K}_{24} & \mathbf{K}_{25} \\
0 & \mathbf{K}_{32} & \mathbf{K}_{33} & 0 & 0 \\
0 & \mathbf{K}_{42} & \mathbf{K}_{43} & 0 & 0 \\
0 & \mathbf{K}_{52} & \mathbf{K}_{53} & \mathbf{K}_{54} & \mathbf{K}_{55}
\end{pmatrix}
\begin{Bmatrix}
\delta\bar{\mathbf{u}} \\ \delta\bar{\mathbf{P}}_g \\ \delta\bar{\mathbf{S}}_w \\ \delta\mathbf{a}_J \\ \delta\bar{\mathbf{V}}
\end{Bmatrix}
+
\begin{pmatrix}
0 & 0 & 0 & 0 & 0 \\
\mathbf{C}_{21} & \mathbf{C}_{22} & \mathbf{C}_{23} & \mathbf{C}_{24} & 0 \\
\mathbf{C}_{31} & \mathbf{C}_{32} & \mathbf{C}_{33} & \mathbf{C}_{34} & 0 \\
\mathbf{C}_{41} & \mathbf{C}_{42} & \mathbf{C}_{43} & \mathbf{C}_{44} & 0 \\
0 & 0 & 0 & 0 & 0
\end{pmatrix}
\begin{Bmatrix}
\delta\dot{\mathbf{u}} \\ \delta\dot{\mathbf{P}}_g \\ \delta\dot{\mathbf{S}}_w \\ \delta\dot{\mathbf{a}}_J \\ \delta\dot{\mathbf{V}}
\end{Bmatrix}
$$
$$
=
\begin{Bmatrix}
\mathbf{f}^1 \\ \mathbf{f}^2 \\ \mathbf{f}^3 \\ \mathbf{f}^4 \\ \mathbf{f}^5
\end{Bmatrix}
-
\begin{pmatrix}
\mathbf{K}_{11}^0 & \mathbf{K}_{12}^0 & \mathbf{K}_{13}^0 & \mathbf{K}_{14}^0 & 0 \\
0 & \mathbf{K}_{22}^0 & \mathbf{K}_{23}^0 & \mathbf{K}_{24}^0 & \mathbf{K}_{25}^0 \\
0 & \mathbf{K}_{32}^0 & 0 & 0 & 0 \\
0 & \mathbf{K}_{42}^0 & 0 & 0 & 0 \\
0 & \mathbf{K}_{52}^0 & \mathbf{K}_{53}^0 & \mathbf{K}_{54}^0 & \mathbf{K}_{55}^0
\end{pmatrix}
\begin{Bmatrix}
\bar{\mathbf{u}}^r \\ \bar{\mathbf{P}}_g^r \\ \bar{\mathbf{S}}_w^r \\ \mathbf{a}_J^r \\ \bar{\mathbf{V}}^r
\end{Bmatrix}
+
\begin{pmatrix}
0 & 0 & 0 & 0 & 0 \\
\mathbf{C}_{21}^0 & \mathbf{C}_{22}^0 & \mathbf{C}_{23}^0 & \mathbf{C}_{24}^0 & 0 \\
\mathbf{C}_{31}^0 & \mathbf{C}_{32}^0 & \mathbf{C}_{33}^0 & \mathbf{C}_{34}^0 & 0 \\
\mathbf{C}_{41}^0 & \mathbf{C}_{42}^0 & \mathbf{C}_{43}^0 & \mathbf{C}_{44}^0 & 0 \\
0 & 0 & 0 & 0 & 0
\end{pmatrix}
\begin{Bmatrix}
\dot{\mathbf{u}}^r \\ \dot{\mathbf{P}}_g^r \\ \dot{\mathbf{S}}_w^r \\ \dot{\mathbf{a}}_J^r \\ \dot{\mathbf{V}}^r
\end{Bmatrix}
\tag{3.79}
$$

where
$$\mathbf{K}_{11} = \mathbf{K}_{11}^0 = -\int_\Omega \mathbf{B}^T\mathbf{D}\mathbf{B}\,d\Omega \tag{3.80}$$

$$\mathbf{K}_{12} = \mathbf{K}_{12}^0 = \int_\Omega \mathbf{B}^T\mathbf{m}^T\alpha\mathbf{N}d\Omega \tag{3.81}$$

$$\mathbf{K}_{13} = -\int_\Omega \mathbf{B}^T\mathbf{m}^T\alpha\,P_c^r\mathbf{N}d\Omega - \int_\Omega \mathbf{B}^T\mathbf{m}^T\alpha\frac{\partial P_c}{\partial S_w}\mathbf{S}_w^r\mathbf{N}d\Omega$$
$$- \int_{\Omega^+} \mathbf{B}^T\mathbf{m}^T\alpha\frac{\partial P_c}{\partial S_w}\mathbf{a}_J^r\,\mathbf{N}^*d\Omega + \int_\Omega \mathbf{N}^T\frac{\partial\bar{\rho}}{\partial S_w}\,\mathbf{N}\mathbf{g}\,d\Omega \tag{3.82}$$

$$\mathbf{K}_{13}^0 = -\int_\Omega \mathbf{B}^T\mathbf{m}^T\alpha\,P_c^r\mathbf{N}\,d\Omega \tag{3.83}$$

$$\mathbf{K}_{14} = \mathbf{K}_{14}^0 = -\int_{\Omega^+} \mathbf{B}^T\mathbf{m}^T\alpha\,P_c^r\mathbf{N}^*d\Omega \tag{3.84}$$

$$\mathbf{K}_{22} = \mathbf{K}_{22}^0 = \int_\Omega (\nabla\mathbf{N})^T\mathbf{c}_1^r(\nabla\mathbf{N})\,d\Omega \tag{3.85}$$

$$\mathbf{K}_{23} = \int_{\Omega} \mathbf{N}^T \left(\frac{\partial d_3}{\partial S_w} \dot{\mathbf{u}}^r \mathbf{N} \right) \mathbf{m}^T \mathbf{B} \, d\Omega + \int_{\Omega} \mathbf{N}^T \left(\frac{\partial d_1}{\partial S_w} \mathbf{N} \dot{\mathbf{P}}_g^r \right) \mathbf{N} d\Omega$$

$$+ \int_{\Omega} \mathbf{N}^T \left(\frac{\partial d_2}{\partial S_w} \mathbf{N} \dot{\mathbf{S}}_w^r \right) \mathbf{N} d\Omega + \int_{\Omega} \mathbf{N}^T \left(\frac{\partial d_2}{\partial S_w} \mathbf{N} \dot{\mathbf{a}}_J^r \right) \mathbf{N}^* d\Omega$$

$$+ \int_{\Omega} (\nabla \mathbf{N})^T \left(\frac{\partial \mathbf{c}_1}{\partial S_w} \mathbf{N} \bar{\mathbf{P}}_g^r \right) (\nabla \mathbf{N}) \, d\Omega - \int_{\Omega} (\nabla \mathbf{N})^T \left(\frac{\partial \mathbf{G}_1}{\partial S_w} \mathbf{N} \right) d\Omega$$

$$+ \int_{\Omega} (\nabla \mathbf{N})^T \left(\frac{\partial \mathbf{c}_2}{\partial S_w} \mathbf{N} \bar{\mathbf{S}}_w^r \right) (\nabla \mathbf{N}) \, d\Omega + \int_{\Omega^+} (\nabla \mathbf{N})^T \left(\frac{\partial \mathbf{c}_2}{\partial S_w} \mathbf{N} \mathbf{a}_J^r \right) (\nabla \mathbf{N}^*) d\Omega$$

$$+ \int_{\Omega} (\nabla \mathbf{N})^T (\mathbf{c}_2^r)(\nabla \mathbf{N}) \, d\Omega + \int_{\Omega} (\nabla \mathbf{N})^T \left(\frac{\partial \mathbf{c}_3}{\partial S_w} \mathbf{N} \bar{\mathbf{V}}^r \right) (\nabla \mathbf{N}) \, d\Omega$$

$$(3.86)$$

$$\mathbf{K}_{23}^0 = \int_{\Omega} (\nabla \mathbf{N})^T \mathbf{c}_2^r \, (\nabla \mathbf{N}) \, d\Omega \tag{3.87}$$

$$\mathbf{K}_{24} = \mathbf{K}_{24}^0 = \int_{\Omega^+} (\nabla \mathbf{N})^T \mathbf{c}_2^r \, (\nabla \mathbf{N}^*) d\Omega \tag{3.88}$$

$$\mathbf{K}_{25} = \mathbf{K}_{25}^0 = \int_{\Omega} (\nabla \mathbf{N})^T \mathbf{c}_3^r \, (\nabla \mathbf{N}) \, d\Omega \tag{3.89}$$

$$\mathbf{K}_{32} = \mathbf{K}_{32}^0 = \int_{\Omega} (\nabla \mathbf{N})^T \mathbf{c}_4^r (\nabla \mathbf{N}) \, d\Omega \tag{3.90}$$

$$\mathbf{K}_{33} = \int_{\Omega} \mathbf{N}^T \left(\frac{\partial d_6}{\partial S_w} \mathbf{N} \dot{\mathbf{u}}^r \right) \mathbf{m}^T \mathbf{B} d\Omega + \int_{\Omega} \mathbf{N}^T \left(\frac{\partial d_4}{\partial S_w} \mathbf{N} \dot{\mathbf{P}}_g^r \right) \mathbf{N} d\Omega$$

$$+ \int_{\Omega} \mathbf{N}^T \left(\frac{\partial d_5}{\partial S_w} \mathbf{N} \dot{\mathbf{S}}_w^r \right) \mathbf{N} d\Omega + \int_{\Omega^+} \mathbf{N}^T \left(\frac{\partial d_5}{\partial S_w} \mathbf{N} \dot{\mathbf{a}}_J^r \right) \mathbf{N}^* d\Omega$$

$$+ \int_{\Omega} (\nabla \mathbf{N})^T \left(\frac{\partial \mathbf{c}_4}{\partial S_w} \mathbf{N} \bar{\mathbf{P}}_g^r \right) (\nabla \mathbf{N}) \, d\Omega - \int_{\Omega} (\nabla \mathbf{N})^T \left(\frac{\partial \mathbf{G}_2}{\partial S_w} \mathbf{N} \right) d\Omega$$

$$(3.91)$$

$$\mathbf{K}_{42} = \mathbf{K}_{42}^0 = \int_{\Omega^+} (\nabla \mathbf{N}^*)^T \mathbf{c}_4^r (\nabla \mathbf{N}) d\Omega \tag{3.92}$$

$$\mathbf{K}_{43} = \int_{\Omega^+} \mathbf{N}^{*T} \left(\frac{\partial d_6}{\partial S_w} \mathbf{N} \dot{\mathbf{u}}^r \right) \mathbf{m}^T \mathbf{B} d\Omega + \int_{\Omega^+} \mathbf{N}^{*T} \left(\frac{\partial d_4}{\partial S_w} \mathbf{N} \dot{\mathbf{P}}_g^r \right) \mathbf{N} \, d\Omega$$

$$+ \int_{\Omega^+} \mathbf{N}^{*T} \left(\frac{\partial d_5}{\partial S_w} \mathbf{N} \dot{\mathbf{S}}_w^r \right) \mathbf{N} d\Omega + \int_{\Omega^+} \mathbf{N}^{*T} \left(\frac{\partial d_5}{\partial S_w} \mathbf{N} \dot{\mathbf{a}}_J^r \right) \mathbf{N}^* d\Omega$$

$$+ \int_{\Omega^+} (\nabla \mathbf{N}^*)^T \left(\frac{\partial \mathbf{c}_4}{\partial S_w} \mathbf{N} \bar{\mathbf{P}}_g^r \right) (\nabla \mathbf{N}) \, d\Omega - \int_{\Omega^+} (\nabla \mathbf{N}^*)^T \left(\frac{\partial \mathbf{G}_2}{\partial S_w} \right) \mathbf{N} d\Omega$$

$$(3.93)$$

$$\mathbf{K}_{52} = \mathbf{K}_{52}^0 = \int_{\Omega} (\nabla \mathbf{N})^T \mathbf{c}_5^r (\nabla \mathbf{N}) \, d\Omega \tag{3.94}$$

$$\mathbf{K}_{53} = \int_{\Omega} (\nabla \mathbf{N})^T \left(\frac{\partial c_7}{\partial S_w} \mathbf{N} \bar{\mathbf{V}}^r \right) (\nabla \mathbf{N}) d\Omega + \int_{\Omega} (\nabla \mathbf{N})^T \left(\frac{\partial \mathbf{c}_5}{\partial S_w} \mathbf{N} \bar{\mathbf{P}}_g^r \right) (\nabla \mathbf{N}) d\Omega$$

$$+ \int_{\Omega} (\nabla \mathbf{N})^T \mathbf{c}_6^r (\nabla \mathbf{N}) d\Omega + \int_{\Omega} (\nabla \mathbf{N})^T \left(\frac{\partial \mathbf{c}_6}{\partial S_w} \mathbf{N} \bar{\mathbf{S}}_w^r \right) (\nabla \mathbf{N}) d\Omega$$

$$+ \int_{\Omega^+} (\nabla \mathbf{N})^T \left(\frac{\partial \mathbf{c}_6}{\partial S_w} \mathbf{N} \mathbf{a}_J^r \right) (\nabla \mathbf{N}^*) d\Omega - \int_{\Omega} (\nabla \mathbf{N})^T \left(\frac{\partial \mathbf{G}_3}{\partial S_w} \right) \mathbf{N} \, d\Omega$$

$$\text{(3.95)}$$

$$\mathbf{K}_{53}^0 = \int_{\Omega} (\nabla \mathbf{N})^T \mathbf{c}_6^r (\nabla \mathbf{N}) d\Omega \tag{3.96}$$

$$\mathbf{K}_{54} = \mathbf{K}_{54}^0 = \int_{\Omega^+} (\nabla \mathbf{N})^T \mathbf{c}_6^r (\nabla \mathbf{N}^*) \, d\Omega \tag{3.97}$$

$$\mathbf{K}_{55} = \mathbf{K}_{55}^0 = \int_{\Omega} (\nabla \mathbf{N})^T c_7^r (\nabla \mathbf{N}) \, d\Omega \tag{3.98}$$

$$\mathbf{C}_{21} = \mathbf{C}_{21}^0 = \int_{\Omega} \mathbf{N}^T d_3^r \mathbf{m}^T \mathbf{B} d\Omega \tag{3.99}$$

$$\mathbf{C}_{22} = \mathbf{C}_{22}^0 = \int_{\Omega} \mathbf{N}^T d_1^r \mathbf{N} d\Omega \tag{3.100}$$

$$\mathbf{C}_{23} = \mathbf{C}_{23}^0 = \int_{\Omega} \mathbf{N}^T d_2^r \mathbf{N} d\Omega \tag{3.101}$$

$$\mathbf{C}_{24} = \mathbf{C}_{24}^0 = \int_{\Omega^+} \mathbf{N}^T d_2^r \mathbf{N}^* d\Omega \tag{3.102}$$

$$\mathbf{C}_{31} = \mathbf{C}_{31}^0 = \int_{\Omega} \mathbf{N}^T d_6^r \mathbf{m}^T \mathbf{B} \, d\Omega \tag{3.103}$$

$$\mathbf{C}_{32} = \mathbf{C}_{32}^0 = \int_{\Omega} \mathbf{N}^T d_4^r \mathbf{N} d\Omega \tag{3.104}$$

$$\mathbf{C}_{33} = \mathbf{C}_{33}^0 = \int_{\Omega} \mathbf{N}^T d_5^r \mathbf{N} d\Omega \tag{3.105}$$

$$\mathbf{C}_{34} = \mathbf{C}_{34}^0 = \int_{\Omega} \mathbf{N}^T d_5^r \mathbf{N}^* d\Omega \tag{3.106}$$

$$\mathbf{C}_{41} = \mathbf{C}_{41}^0 = \int_{\Omega^+} \mathbf{N}^{*T} d_6^r \mathbf{m}^T \mathbf{B} d\Omega \tag{3.107}$$

$$\mathbf{C}_{42} = \mathbf{C}_{42}^0 = \int_{\Omega^+} \mathbf{N}^{*T} d_4^r \mathbf{N} d\Omega \tag{3.108}$$

$$\mathbf{C}_{43} = \mathbf{C}_{43}^0 = \int_{\Omega^+} \mathbf{N}^{*T} d_5^r \mathbf{N} d\Omega \tag{3.109}$$

$$\mathbf{C}_{44} = \mathbf{C}_{44}^0 = \int_{\Omega^+} \mathbf{N}^{*T} d_5^r \mathbf{N}^* d\Omega \tag{3.110}$$

$$\mathbf{f}_1 = -\int_{\Omega} \mathbf{N}^T \rho^r \mathbf{g} \; d\Omega - \int_{\Gamma_u^q} \mathbf{N}^T \bar{\mathbf{t}} \; d\Gamma \tag{3.111}$$

$$\mathbf{f}_2 = \int_{\Omega} (\nabla \mathbf{N})^T \mathbf{G}_1{}^r d\Omega - \int_{\Gamma_w^q} \mathbf{N}^T q_w \; d\Gamma \tag{3.112}$$

$$\mathbf{f}_3 = -\int_{\Gamma_g^q} \mathbf{N}^T q_g \; d\Gamma + \int_{\Omega} (\nabla \mathbf{N})^T \mathbf{G}_2^r d\Omega \tag{3.113}$$

$$\mathbf{f}_4 = -\int_{\Gamma_g^q} \mathbf{N}^T q_g \; d\Gamma + \int_{\Omega^+} (\nabla \mathbf{N}^*)^T \mathbf{G}_2^r d\Omega \tag{3.114}$$

$$\mathbf{f}_5 = \int_{\Omega} (\nabla \mathbf{N})^T \mathbf{G}_3^r d\Omega - \int_{\Gamma_e^q} \mathbf{N}^T q_e \; d\Gamma \tag{3.115}$$

3.3.4 Time discretization

A finite difference scheme in time is utilized to solve the semi-discrete system of equations, Eq. (3.79). In a concise form, this equation can be written as

$$\mathbf{C}\frac{d\mathbf{X}}{dt} + \mathbf{K}\mathbf{X} = \mathbf{F} \tag{3.116}$$

Using the theta-method, the dependent state variable and the force vector can be defined as

$$\begin{aligned} \mathbf{X} &= \theta \mathbf{X}_{n+1} + (1-\theta)\mathbf{X}_n \\ \mathbf{F} &= \theta \mathbf{F}_{n+1} + (1-\theta)\mathbf{F}_n \end{aligned} \tag{3.117}$$

in which n is a time step, and $0 \leq \theta \leq 1$ is a time integration parameter, which gives for $\theta \geq 1/2$ an unconditionally stable time scheme.

Using the backward differencing, the time derivative of the state variable is

$$\dot{\mathbf{X}} = \frac{\mathbf{X}_{n+1} - \mathbf{X}_n}{\Delta t} \tag{3.118}$$

Substituting Eqs. (3.117) and (3.118) into Eq. (3.116) gives

$$(\mathbf{C} + \theta \Delta t \mathbf{K})\mathbf{X}_{n+1} = (\mathbf{C} - (1-\theta)\Delta t \mathbf{K})\mathbf{X}_n + \theta \Delta t \mathbf{F}_{n+1} + (1-\theta)\Delta t \mathbf{F}_n \tag{3.119}$$

In all numerical examples presented in next section, the algorithmic time integration parameter θ is assumed 1, fully implicit.

3.3.5 Computer implementation

The above finite element formulation together with the linearization procedure and the time discretization scheme are implemented in a C++ code and included in an object oriented computer environment available at Delft University of Technology. The system of equations is solved using a standard direct solver. The computational algorithm is summarized as the following.

1. Given $\mathbf{X}_0$ and Φ_0.

2. Compute front velocity $\mathbf{v}_{\Gamma_d}$ from Eq. (3.46).

3. Compute Φ_{n+1} from Eq. (3.45).

4. Reinitialize Φ as explained in section 3.3.1.

5. Locate the plume front and discretize using SG-XFEM.

6. Compute $\mathbf{X}_{n+1}$ from Eq. (3.119).

7. $n \leftarrow n + 1$; go to step 2.

3.4 Verifications and numerical examples

In this section, numerical examples illustrating the capability of the proposed model to accurately and efficiently simulate coupled deformation, two-phase flow and electrokinetic flow problems are presented. Currently, there are no analytical solutions capable of solving such coupled problems. Thus, the model is first evaluated by comparing its computational results to those obtained from analytical solutions of two simple cases representing fluid and electrokinetic flow in a saturated porous medium. Then, the performance of the model is studied using complicated examples describing electrokinetic and hydromechanical flows in an unsaturated CO_2 sequestration system.

Analytical verifications
Two examples are discussed. The first example describes a one-dimensional consolidation problem in a linear poroelastic medium (Terzaghi problem). The second example describes an electrokinetic-hydromechanic coupling, where the maximum value of an electro-osmotic head built-up across a block of a saturated porous medium is calculated.

3.4.1 Saturated consolidation

A domain comprising a saturated porous column of height H is simulated. The domain is subjected to load F at the top and fixed at the bottom, with drainage occurring through top and bottom surfaces. The load is applied instantaneously at time $t = 0$, giving a non-zero initial pressure $P_0(z)$. Assuming that the z-axis is positive downwards, the analytical solution gives (Wang, 2000)

$$P(z,t) = \frac{4}{\pi} P_0 \sum_{m=0}^{\infty} \frac{1}{2m+1} \sin\left[(2m+1)\pi \frac{z}{H}\right] \exp\left[-(2m+1)^2 \pi^2 \frac{c_v t}{H^2}\right] \quad (3.120)$$

$$
\begin{aligned}
u(z,t) = c_M P_0 H \frac{4}{\pi^2} \sum_{m=0}^{\infty} \frac{1}{(2m+1)^2} \left\{1 - \cos\left[(2m+1)\pi \frac{z}{H}\right]\right\} \\
\left\{1 - \exp\left[-(2m+1)^2 \pi^2 \frac{c_v t}{H^2}\right]\right\}
\end{aligned}
\quad (3.121)
$$

where
$P_0 = \frac{\alpha M}{c_m^{-1} + \alpha^2 M} F$
$M = \frac{K_w}{\phi}$; Biot modulus
$c_m = \frac{1}{\lambda + 2G}$; vertical uniaxial compressibility
$c_v = \frac{k}{\rho g (M^{-1} + \alpha^2 c_m)}$; consolidation coefficient
and λ and G are Lame's first parameter and shear modulus, respectively. The material parameters are given in Table 3.2. The finite element domain is discretized using 8, 4-node quadrilateral elements.

Figure 3.1 shows the pore pressure and the vertical displacement distribution at different time steps, obtained from the analytical solution and the proposed mixed SG-XFEM-LS model. Apparently, there is a rather good match between the two results.

3.4.2 Electro-osmotic consolidation

In this example, electro-osmotic head build-up in a saturated porous medium is studied. Electro-osmosis (electrokinetic stabilization) is a soil improvement technique used for accelerating the consolidation of saturated fine grained soils. In this process, a direct voltage is applied to the soil by two electrodes to generate electric current. The current induces displacement in the water phase from the positive pole (anode) towards the negative pole (cathode). The model geometry and the boundary conditions are shown in Figure 3.2.

Theoretically, the electro-osmotic consolidation is governed by the ratio of the electrokinetic cross coupling term and the hydraulic conductivity of the soil. The

Table 3.2: Parameters for solving consolidation problem.

Parameter	Value	Unit
Domain height, H	10	m
Absolute permeability, k	1×10^{-12}	m^2
Porosity, ϕ	0.2	
Water viscosity, μ_w	1×10^{-3}	Pa.s
Water density, ρ_w	1000	kg/m^3
Biot's constant, α	1.0	
Young's modulus, E	1.0	MPa
Poisson's ratio, ν	0.3	
Fluid bulk modulus, K_f	100.0	MPa
Load, F	0.1	MN

(a) pore pressures

(b) displacements
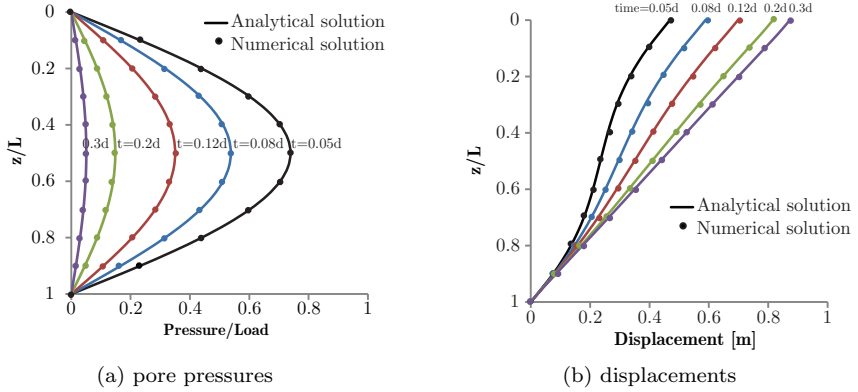
Figure 3.1: Analytical vs. SG-XFEM-LS model

Table 3.3: Parameters for Electro-osmotic consolidation example.

Parameter	Value	Unit
Domain Length, H	2.4	m
Absolute permeability, k	1×10^{-14}	m^2
Electro-osmotic permeability, k_e	1×10^{-9}	m^{2}s^{-1}V
Porosity, ϕ	0.2	
Water viscosity, μ_w	1×10^{-2}	Pa.s
Water density, ρ_w	1000	kg/m^3

analytical solution to this problem is given by Esrig (1967), as

$$
h_p(x) = \frac{k_e}{k_h} E(x) - \frac{2k_e E_{\max}}{k_h \pi^2} \sum_{m=0}^{\infty} \frac{(-1)^m}{(m+1/2)^2} \sin\left[(m+1/2)\pi \frac{x}{L}\right]
$$
$$
\exp\left[-(m+1/2)^2 \pi^2 \frac{c_v t}{L^2}\right]
$$

(3.122)

where h_p is the hydraulic pressure head; k_h and k_e are the hydraulic permeability and the electro-osmotic permeability of the soil, respectively; L is the distance between the anode and the cathode; x is the distance between the anode and any section X-X; and $E(x)$ is the voltage at section X-X. The physical parameters of this problem are presented in Table 3.3. The finite element domain is discretized using 12, 4-node quadrilateral elements.

Figure 3.3. shows the calculation results of the analytical solution and the mixed SG-XFEM-LS model. Obviously, there is a good agreement between the two results.

Numerical examples and parametric analysis
Three examples are discussed. The first example studies consolidation of a partially
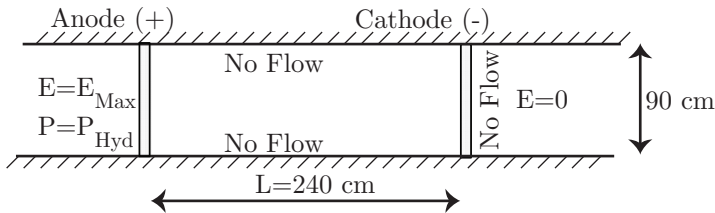

Figure 3.2: Geometry and boundary conditions of the Electro-osmotic consolidation example
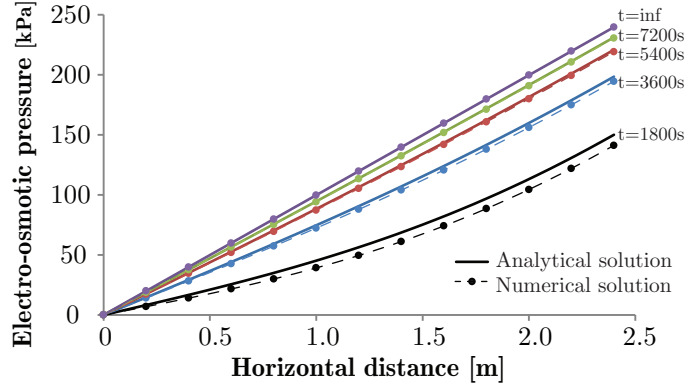
Figure 3.3: Analytical vs. SG-XFEM-LS computational results of Electro-osmotic consolidation

saturated soil column due to a change of pore water pressure at the upper boundary. The simulation results are compared with those presented by Rahman and Lewis (1999). The second example studies the behavior of the well-known CO_2 leakage problem presented by Class et al. (2009), with some modification. The third example studies the electrokinetic response during injection of a fluid into an underground formation: a 2D reservoir model is simulated based on a 3D model presented by Saunders et al. (2008). The effects of different parameters on the electrokinetic response are investigated in this example.

3.4.3 Unsaturated consolidation

Here, the SG-XFEM-LS model is validated based on an example presented by Rahman and Lewis (1999). A vertical soil column, 1 m height and 0.1 m width, is simulated. The soil column is unsaturated, with an initial water saturation of 0.52 and initial water pressure of -280 kN/m^2. The soil column is subjected to an external load of 1000 N/m^2. The top surface is the only drained boundary of the column, and the bottom surface is fixed. At the top boundary, the water pressure is instantaneously changed to -420 kN/m^2, while the air pressure is kept atmospheric. The Brooks and Corey (1964) model is utilized to describe the relative permeability-saturation and the capillary pressure-saturation relationships. Other parameters are summarized in Table 3.4. Figure 3.4 shows the geometry and the finite element mesh of the problem.

Figure 3.5 and 3.6 show the vertical displacement and the water saturation

Table 3.4: Material properties for the unsaturated consolidation example.

Parameter	Value	Unit
Domain height, H	1	m
Absolute permeability, k	0.46×10^{-11}	m^2
Porosity, ϕ	0.3	
Water viscosity, μ_w	1×10^{-3}	Pa.s
Water density, ρ_w	1000	kg/m^3
Dynamic viscosity of air, μ_g	1×10^{-3}	Pa.s
Air density, ρ_g	1.22	kg/m^3
Biot's constant, α	1.0	
Young's modulus, E	6.0	MPa
Poisson's ratio, ν	0.4	
Water bulk modulus, K_w	0.43×10^7	MPa
Bulk modulus of air, K_g	0.1	MPa
Solid phase density, ρ_s	2000	kg/m^3
Bulk modulus of solid, K_s	0.14×10^4	MPa
Gravitational acceleration, g	9.806	ms^-2
Atmospheric pressure, P_{atm}	101.8967	kPa
Residual water saturation, S_{wr}	0.397	
Entry pressure, P_b	225	kPa
Pore size distribution index, λ	3	

distribution at 0.1, 0.5, 0.7, and 0.95 m from the bottom (see Figure 3.4). Figure 3.7 shows the water pressure distribution along the column at different time intervals. The computational results agree with those presented by Rahman and Lewis (1999) and Khoei and Mohammadnejad (2011).

3.4.4 CO_2 Leakage problem

This example examines the capability of the SG-XFEM-LS model to simulate the well-known benchmark case-study utilized in literature to compare the performance of different CO_2 geo-sequestration simulators (Class et al., 2009). The cap rock uplift due to CO_2 injection is examined. This problem is physically important since injection of a large amount of CO_2 into underground formations requires careful environmental risk assessment. The greatest concern is that the injected supercritical CO_2, which is less dense and less viscous than the formation water, is driven by buoyancy forces towards the top of the formation. Thus, the reservoir should be
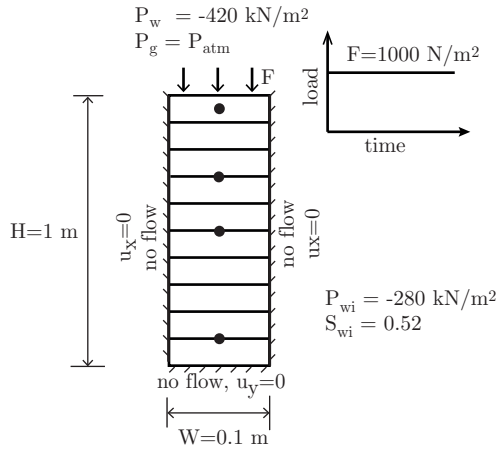
Figure 3.4: Geometry, FE mesh and boundary conditions of the unsaturated consolidation example
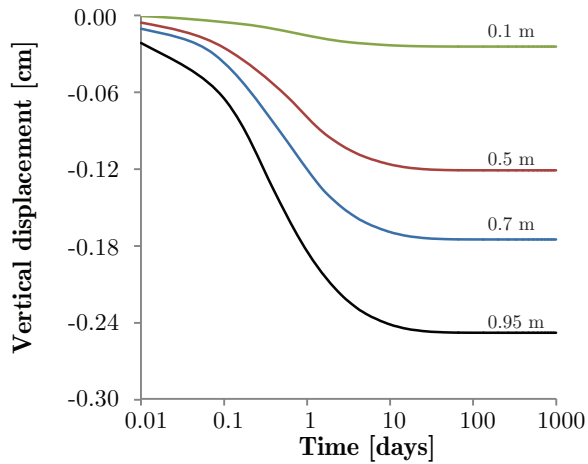

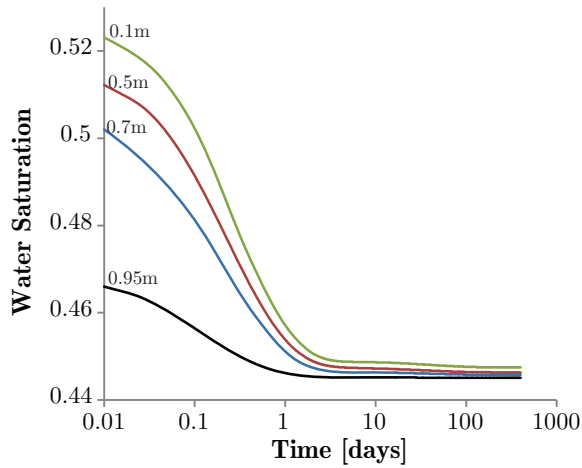Figure 3.5: Vertical displacement along the column

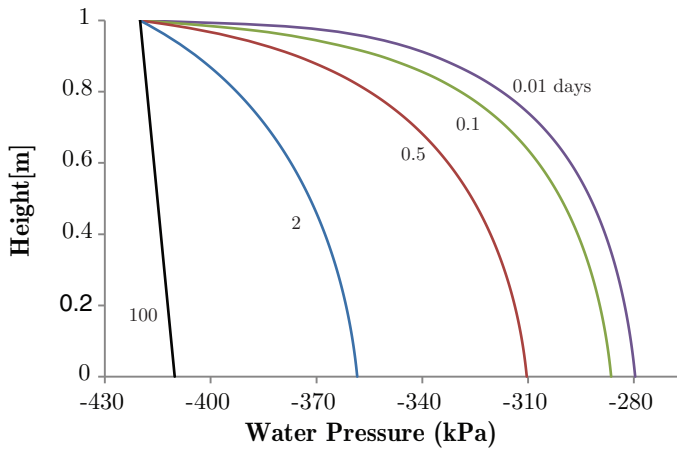Figure 3.6: Water saturation along the column

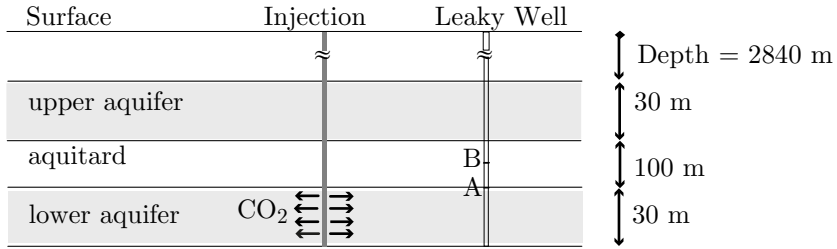Figure 3.7: Water pressure distribution along the column

Figure 3.8: Water pressure distribution along the column

capped by a low-permeability rock to prevent CO_2 movement to upper aquifers or to the ground surface. The mechanical properties of the cap rock play a key role in assessing the risk of long term CO_2 geo-sequestration. Cap rock discontinuities, such as fracture or fault, may promote upwards movement of CO_2. Furthermore, the resulting overpressure due to CO_2 injection affects the stress field and induces deformation in the rock. This may activate closed fractures or create new fractures in the formation.

The domain geometry, shown in Figure 3.8, consists of a CO_2 injection well, two aquifers, one aquitard and a leaky well. Here, the injection well is treated as a Neumann boundary and the leaky well is treated as a porous medium with high permeability compared to the aquifer formation. Initially, the domain is fully saturated with brine, under a hydrostatic pressure condition. The initial stresses in the domain are assumed to be induced by the gravitational force only. CO_2 is injected into the aquifer for a period of time and then stopped.

On the horizontal surfaces, a no-flow boundary condition is prescribed, and on the vertical surfaces, a constant hydrostatic pressure is imposed. In this example, the fluid properties are assumed constant, and the dissolution of CO_2 into the brine is neglected. The simulation parameters are shown in Table 3.5.

To examine the accuracy and the computational efficiency of the proposed model, this example is also analyzed using the standard Galerkin method and the upwind finite element method. Finite element meshes of different sizes are utilized. Since there is no analytical solution available to this problem, the accuracy of the examined schemes and mesh sizes is compared to a "converged" solution using a relatively fine mesh. Galerkin solution using a finite element mesh of 30000 elements is utilized as a reference. The computational results of this simulation gave an arrival time of 8.5 days for the CO_2 plume to reach to the leaky well.

Table 3.6 shows arrival times calculated by the numerical schemes for different

Table 3.5: Simulation parameters of the leakage problem

Parameter	Value	Unit
Lateral dimension, L	1000	m
Aquifers thickness, w_1	30	m
Aquitard thickness, w_2	100	m
Distance between wells, d	100	m
Aquifers permeability, k_1	2.0×10^{-14}	m^2
Leaky well permeability, k_2	1×10^{-12}	m^2
Porosity, ϕ	0.15	
Brine viscosity, μ_w	2.535×10^{-4}	Pa.s
CO_2 viscosity, μ_g	3.95×10^{-5}	Pa.s
Brine density, ρ_w	1045	kg/m^3
CO_2 density, ρ_g	479	kg/m^3
Injection rate, q_{inj}	6.26×10^{-5}	m$^2/s$
Residual water saturation, S_{wr}	0.0	
Residual CO_2 saturation, S_{gr}	0.0	
Brooks and Corey parameter, λ	2	
Bottom pressure, P_{bh}	30.8	MPa
Biot's constant, α	1.0	
Young's modulus, E	6.0	MPa
Poisson's ratio, ν	0.4	
Water bulk modulus, K_w	0.43×10^7	MPa
Bulk modulus of CO_2, K_g	0.1	MPa
Solid phase density, ρ_s	2400	kg/m^3
Bulk modulus of solid, K_s	0.14×10^4	MPa

Table 3.6: SG-XFEM-LS model vs. SG and Upwind finite element models.

	SG				Unwinding				SG-XFEM			
Element size	10	7	4	2	10	7	4	2	10	7	4	2
Elements	300	612	1875	7500	300	612	1875	7500	300	612	1875	7500
Arrival time	−	7.1	8.2	8.4	5.8	6.5	7.4	8.1	7.5	8.2	8.4	8.5

mesh sizes. It shows that the standard Galerkin model exhibits high mesh-dependency, as with mesh refinement, the arrival time decreases. The upwind solution shows a high degree of numerical dissipation, and the CO_2 plume arrives earlier compared to other cases. Apparently, the CO_2 front is smeared to a great extent. In contrast, the proposed model is convergent, as even with a coarse mesh, the results are close to that of the standard Galerkin solution with a fine mesh.

To determine the convergence rate of the different numerical schemes, we compared the CO_2 flux at the leaky well after 100 days of injection to the converged solution, using different mesh sizes. The relative error is calculated using the l^2-norm, defined as

$$\|e_q\|_2 = \left(\frac{\sum_{i=1}^{n} (q_i - q_{Ri})^2}{\sum_{i=1}^{N} q_{Ri}^2} \right)^{1/2} \tag{3.123}$$

in which q_i is the calculated flux at node i on the leaky well boundary, and n is the number of boundary nodes. Figure 3.9 shows the relative error of the different cases compared to the reference case. The figure shows that the convergence rate of the proposed model is almost double those of the Galerkin and the upwind finite element methods.

To study the effect of deformation on the flow fields, numerical analysis illustrating the behavior of a rigid formation and a deformed formation with different stiffness were conducted. Figure 3.10 shows the evolution of saturation at point A (see Figure 3.8). The figure shows that, with more deformation, the CO_2 plume expands further away, though not significant. However, it must be noted that this result is for the linear elastic material proposed in this work. For a nonlinear material, CO_2 expansion might be more pronounced.

Figure 3.11 shows CO_2 saturation profile at different time steps during injection. The CO_2 plume extends radially under buoyancy forces, and upon reaching the leakage well, it rises to the upper aquifer.

Figure 3.12 shows the vertical displacement profile at the top of the aquitard versus distance for different time intervals. As a result of CO_2 injection, the pore
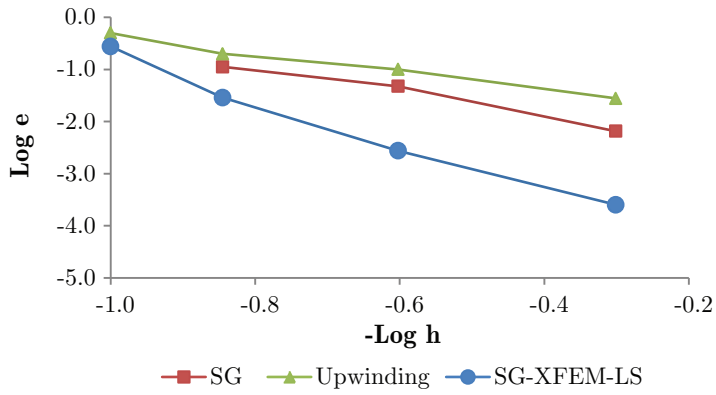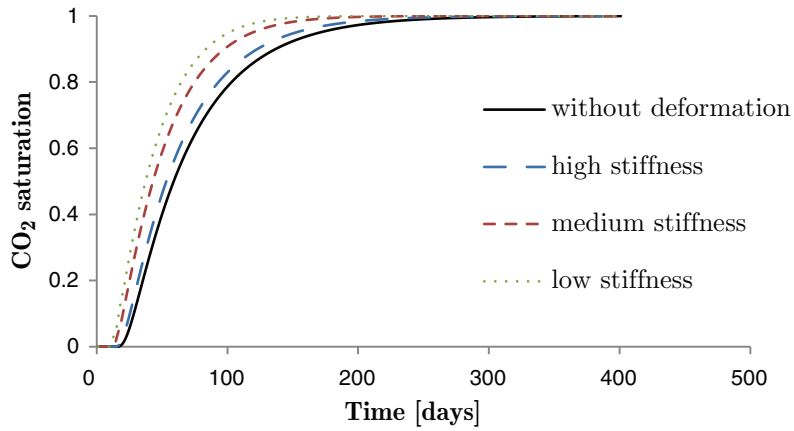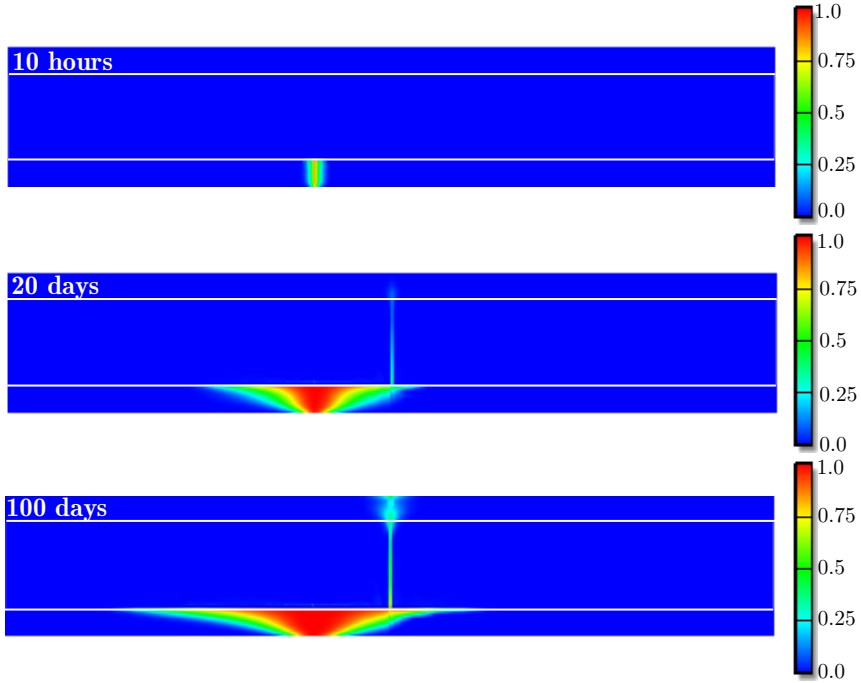
Figure 3.9: Relative error in flux calculation for different mesh sizes

Figure 3.10: Effect of formation stiffness on CO_2 flow

Figure 3.11: CO_2 saturation at different time intervals

pressure increases near the injection well, uplifting the cap rock. Upon seizing injection, the pore pressure dissipates, leading to a gradual decrease of the cap rock uplift.

3.4.5 Front tracking of electrokinetic potential

Electrokinetic measurement has proven to be an efficient technique for monitoring fluid motion in underground formations in response to pumping or injection of fluids or contaminants. For CO_2 injection, the cross coupling coefficient, L in Eq. (3.26), decreases as the CO_2 displaces brine, allowing remote monitoring of the CO_2 plume front. However, it seems that no computational work on monitoring CO_2 movement in underground formations has yet been published. Hence, in order to compare, here, we simulate a numerical example obtained from petroleum engineering, particularly that of Saunders et al. (2008). They simulated water encroachment during oil production towards a well and the resulting electrokinetic potential response.

Based on Saunders et al. (2008) example, a 2D reservoir domain, consisting of
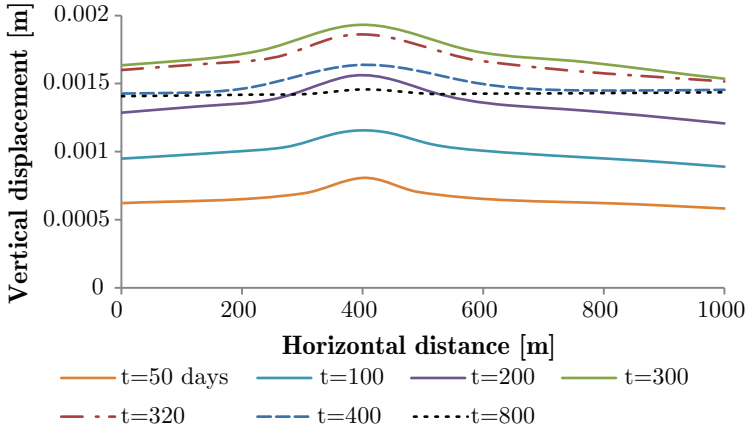
Figure 3.12: Vertical displacement at the top of the aquitard

six layers, is modeled, Figure 3.13. The reservoir is bounded by conductive, low permeability layers, representing reservoir seals. The seal layers are located between two high permeability sandstone layers. At the top of the geometry, a highly resistive weathered layer exists. At the left boundary of the reservoir, a water aquifer exists. As oil is produced, the water in the aquifer expands and moves into the reservoir, displacing oil. The material and other simulation parameters are given in Table 3.7.

A large domain (2000 m × 2000 m) is simulated to allow for setting zero potentials at the boundaries, used as a reference for the electrokinetic measurements. No electrical potential flux is applied on the domain surface. The capillary pressure and the gravitational forces are neglected.

Water and oil relative permeability are calculated using Brook and Corey relationships, Eqs. (3.18) and (3.19). The electrical conductivities of the layers are calculated using Eq. (3.30), with Archie's saturation exponent n=2 and cementation exponent m=1.8.

Figure 3.14 shows the streaming potential versus horizontal distance, along a section in the center of the reservoir, at different time intervals. Salinity of $C_f = 0.01$ mol/L is assumed. Figure 3.15 shows the water saturation front at the same time intervals. Comparing Figures 3.14 and 3.15, reveals that the electric potential peaks follow the water front. Therefore, even though this example is analyzing water-oil front motion, it can be deduced that the electrokinetic potential technique can be utilized for monitoring CO_2 motion in underground formations.

In modeling the streaming potential, it is vital to understand the effects of
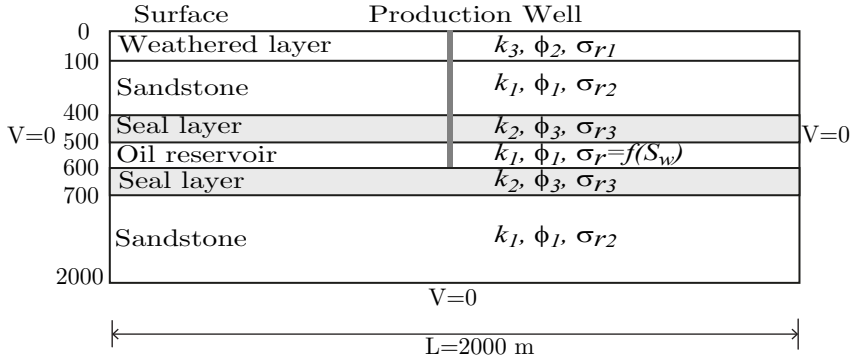
Figure 3.13: Geometry of the electrokinetic potential problem

Table 3.7: Parameters used in the electrokinetic simulation example

| Parameter	Value	Unit
Lateral dimension, L	2000	m
Reservoir thickness, w_1	100	m
Reservoir permeability, k_1	1.0×10^{-13}	m^2
Confining rock permeability, k_2	1×10^{-15}	m^2
Upper layer permeability, k_3	3.3×10^{-13}	m^2
Reservoir porosity, ϕ_1	0.25	
Confining rock Porosity, ϕ_2	0.01	
Upper layer porosity, ϕ_3	0.3	
Upper layer conductivity, σ_{r1}	3.0×10^{-5}	Sm^{-1}
Sandstone conductivity, σ_{r2}	0.0097	Sm^{-1}
Confining rock conductivity, σ_{r3}	0.0135	Sm^{-1}
Brine viscosity, μ_w	1.0×10^{-3}	Pa.s
Oil viscosity, μ_o	1.0×10^{-3}	Pa.s
Oil density, ρ_o	900	kg/m^3
Oil conductivity, σ_{nw}	1.0×10^{-5}	Sm^{-1}
Production rate, q	8.1×10^{-4}	kg/ms
Residual water saturation, S_{wr}	0.2	
Residual oil saturation, S_{nr}	0.2	
Pore size distribution index, λ	2	
Initial pressure, P_i	10.0	MPa
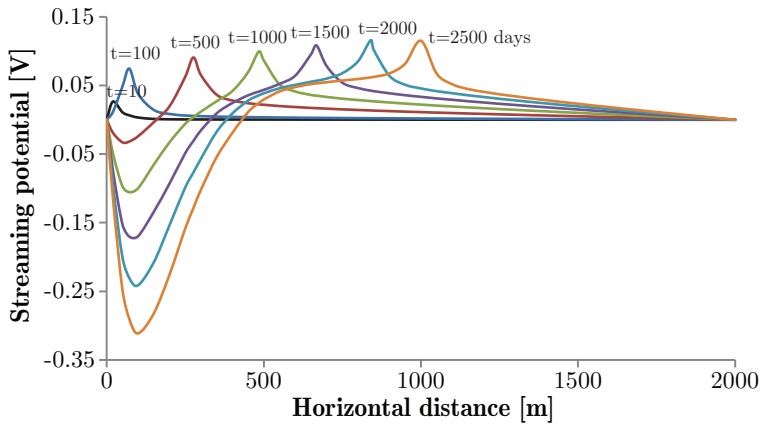
Figure 3.14: Streaming potential along a section in the center of the reservoir at different time intervals
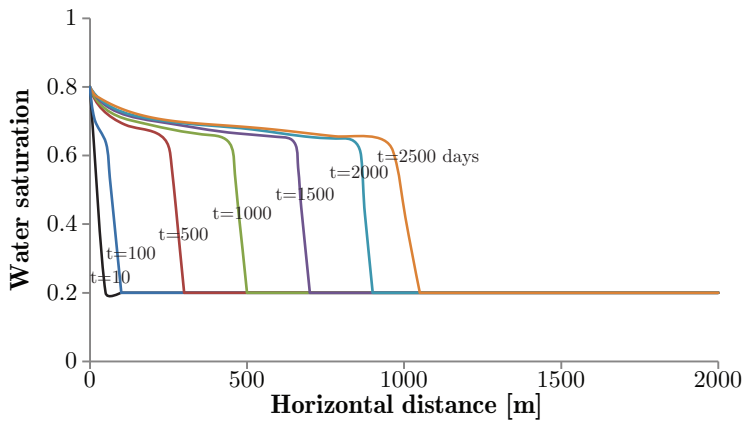

Figure 3.15: Water saturation profile along a section in the center of the reservoir at different time intervals
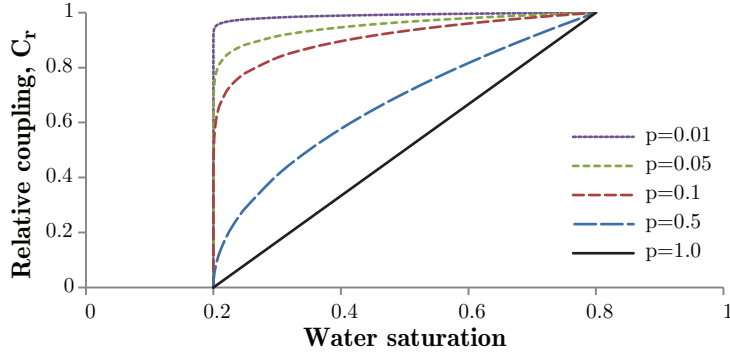
Figure 3.16: Variation of the relative coupling coefficient with p exponent
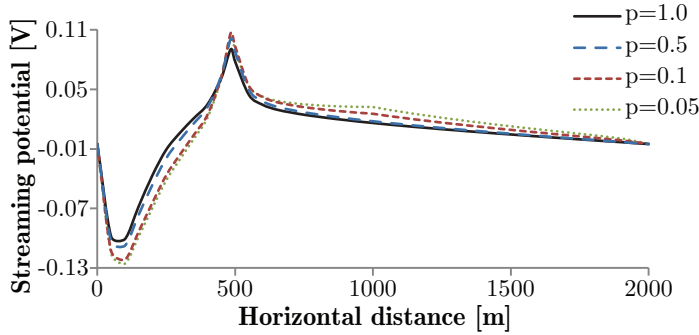
Figure 3.17: Effect of relative coupling coefficient exponent on electrokinetic response

the involved parameters on the electrokinetic flow. Here, the effects of varying the relative coupling coefficient and the salinity on the streaming potential are investigated. Figure 3.16 shows the relationship between the relative coupling coefficient and water saturation, Eq. (3.31), for different exponent values, p. Figure 3.17 shows the streaming potential profiles after 1000 days for different values of 'p'. Apparently, the calculated streaming potentials are not very much affected.

Salinity of the formation brine affects its electrical conductivity and zeta potential and, hence, the electrokinetic coupling coefficient. The brine conductivity and the zeta potential are related to salinity via Eqs. (3.32) and (3.33), respectively. The coupling coefficient for different salinities is shown in Figure 3.18, which illustrates that, as the brine salinity increases, the electrokinetic coupling coefficient reduces to zero. This is attributed to the fact that, at high salinity, the electrical double layers collapses. Hence, it can be deduced that electrokinetic monitoring of CO_2 plume
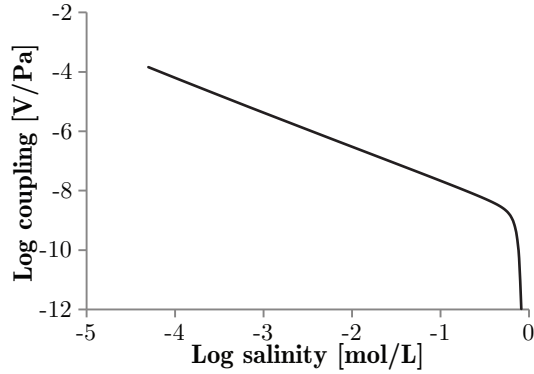
Figure 3.18: Effect of salinity on electrokinetic coupling coefficient
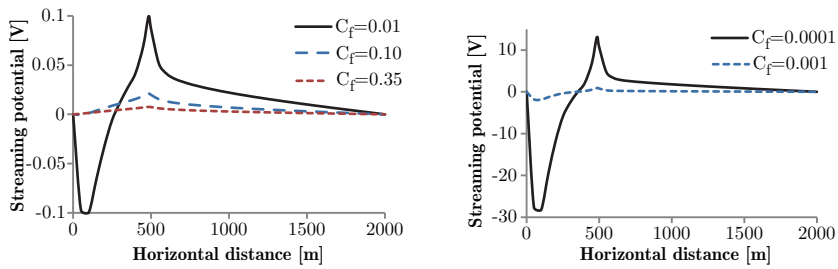
Figure 3.19: Effect of salinity on electrokinetic response

movement can give more accurate results in low salinity reservoirs, compared to high salinity ones.

Several numerical simulations are conducted for different salinity values. The results of the electric potential profile for different salinities, at 1000 days, are compared in Figure 3.19. Figure 3.20 shows that the maximum electrical potential at the fronts decreases significantly as the salinity increases.
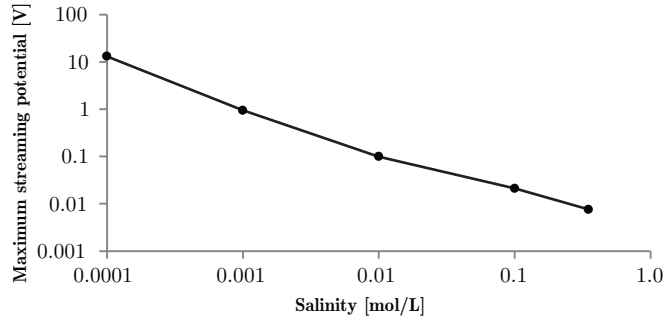
Figure 3.20: Maximum potential at the front vs. brine salinity

3.5   Conclusions

Coupled electrokinetic and hydromechanical flow occurs naturally due to fluids flow in unsaturated porous media, giving rise to various electrokinetic effects, including streaming potential. Remote sensing of the streaming potential is a vital tool for monitoring many geoenvironmental applications, including geothermal systems, groundwater flow, and oil reservoirs. For this, computational models with different complexities have been introduced. However, so far, it seems that no study has been reported for modeling the streaming potential associated with CO_2 plume flow in an unsaturated underground formation. This study focuses on modeling this phenomenon.

In this chapter, a coupled electrokinetic–hydromechanical computational model, based on the averaging theory, for formulating the governing field equations; and a mixed discretization scheme, based on coupling between the standard Galerkin finite element method (SG), the extended finite element method (XFEM), and the level-set method (LS) has been introduced to simulate CO_2 sequestration in geologic formations. SG has been utilized to discretize the deformation and the diffusive dominant field equations, and XFEM, together with LS, has been utilized to discretize the advective dominant field equations. Utilization of XFEM and LS produces a locally conservative discretization scheme, giving a stable and convergent model. However, an extra degree of freedom must be added to describe the discontinuity in the advective field. Nevertheless, utilization of SG limits this increase to the minimum, yielding a computationally efficient numerical scheme.

Several verification and numerical examples with parametric analyzes are presented. The capability of the mixed SG-XFEM-LS numerical scheme has been examined to simulate coupled solid deformation, multiphase flow, and electrokinetic flow in

unsaturated porous media. The coupled deformation-multiphase flow example reveals that the formation deformation, which is a function of stiffness, has little influence on the CO_2 flow. However, this conclusion is valid for the linear elastic material model utilized in this study. For nonlinear materials, with possible occurrence of localization, this conclusion might not be valid.

On the other hand, the coupled electrokinetic-multiphase flow example reveals that the salinity of the formation brine can play a major role in the electrokinetic flow, and hence, measuring the streaming potential can be a useful tool for monitoring CO_2 flow remotely.

Multiphysics Processes of CGS in Fractured Porous Media

<div style="text-align:right">4</div>

This chapter is based on Talebian et al. (2013c), a paper published in Advances in Water Resources.

4.1 Introduction

Many of targeted formations for CO_2 geo-sequestration are to some extent naturally or man-made fractured. The existence of the fractures might significantly influence fluids flow in the formation, depending on their permeability, intensity and length scales.

Fracture models for multiphase porous media can in general be classified into three types: discrete fracture models (Andersson and Dverstorp, 1987; Bear et al., 1993), continuum fracture models (Barenblatt et al., 1960; Royer et al., 2002) and hybrid models (Berkowitz, 2002; Wu and Pruess, 2000). In a discrete fracture model, the fractures represent the flow path geometry and are explicitly modeled. This type of models provides accurate description of fluid flow in the fractures, but for a large scale problem, such as CO_2 geo-sequestration, discretizing the fissure network becomes unrealistic and requires enormous computational power. On the other hand, in a continuum fracture model, no discrete fractures are presented and the formation is divided into two interacting continua: fracture and porous matrix. The two continua vary by their porosities and permeabilities, and interact with each other via leakage occurring, implicitly, at the interfaces between them. The hybrid models are a combination between the discrete models and the continuum models. In this paper, a continuum fracture model, namely the double porosity model, is adopted.

Barenblatt et al. (1960) were the first to formulate the double porosity model for single phase flow in a rigid fractured domain. Later on, this model was extended

and several models with different complexity have been introduced. Aifantis (1977); Khaled et al. (1984); Wilson and Aifantis (1982) extended Barenblatt's model to account for coupled single phase flow to poroelastic deformation. Similarly, Bai et al. (1993); Chen and Teufel (1997); Cho et al. (1991); Ghafouri and Lewis (1996); Valliappan and Khalili (1990) have elaborated on the double porosity model with each considered different aspects of the model. Moreover, Bai et al. (1998); Lewis and Pao (2002); Lewis and Ghafouri (1997) have utilized the double porosity model to simulate multiphase flow in a deformed fractured porous medium domain.

Multiphase fluid flow due to CO_2 injection in an unsaturated porous medium domain generates electrokinetic flow.Since the electrical conductivity of CO_2 is lower than that of the formation brine, it can be detected by measuring the self-potential. Based on this, SP can be used as a monitoring means, which is necessary to ensure that geological sequestration is both safe and effective. Different applications of Electrokinetic in the conventional reservoirs have been presented in the previous chapters. Ishido and Pritchett (2003) seem to be the first to introduce a computational model for the calculation of self-potential in fractured geothermal reservoirs, using the double porosity approach.

In this chapter, a computational model describing coupled electrokinetic– hydromechanic processes in a fractured medium domain is introduced. The mathematical model of two-phase flow in a deformable continuum double porosity domain is formulated based on the averaging theory. The numerical solution is carried out by a mixed discretization technique explained in the previous chapters.This technique is suitable for advective dominant flow, typically exists in fractured domains.

This model is an extension of models presented in the previous chapters. The novel aspect of the proposed model is in the choice of the highly advective balance equation for XFEM discretization, while treating other equations by standard procedures. Here, the CO_2 balance equation of the fractured continuum is chosen for XFEM discretization. This entails introducing an extra degree of freedom for CO_2 saturation, while keeping all other degrees of freedom standard. Employing this technique reduces the number of degrees of freedom in the system as compared to that if all quantities are discretized using XFEM.

In what follows, governing equations describing two-phase flow in a double porosity domain and the involved constitutive relationships are outlined. Then, a detailed finite element discretization is presented. Finally, numerical examples with parametric analyses are given.

4.2 Governing Equations

Fluid flow in an unsaturated porous medium domain is commonly modeled based on a continuum averaging approach, where physical laws describing transport of mass, momentum and energy at the microscopic level are transformed to macroscopic level. The representative elementary volume (REV) averaging approach is one of the most commonly used (Bear and Cheng, 2010; Hassanizadeh and Gray, 1979a). In this approach, the averaging process is conducted by integrating the involved microscopic quantities over the REV, and each spatial point is simultaneously occupied by the material points of all involved phases. The multiphase domain occupying the REV is postulated as a superposition of all involved phases, but the state of motion of each phase is described independently. The averaging theory is elegantly described by Lewis and Schrefler (1998), from whom the governing equations outlined here are derived.

Fluid flow in an unsaturated fractured porous domain can also be modeled based upon the continuum averaging approach. A fractured reservoir can be simulated as a superposition of two distinct continua describing the porous matrix and the fractured zone. As indicated above, this type of models is commonly known as the double porosity model. Here, fluid flow occurs independently in the two continua, but interacting via leakage at their interfaces. The governing equations of such a domain can be derived based on two-phase flow equations in a continuum domain augmented by a leakage term, considering the following assumptions:

- The porous medium domain can be divided into two overlapping but distinct subdomain continua: a porous matrix continuum and a fracture continuum.

- Fluid flow in each subdomain is described independently, but interacting by a leakage term describing the flow of mass between the two subdomains.

- The process of mass transfer between the pores in the porous matrix and the fissures in the fractured zone takes place essentially under a sufficiently smooth change of pressure, and therefore, it can be assumed that this pressure is quasi-stationary (Barenblatt et al., 1960).

- Darcy's law is assumed valid in both subdomains.

- Linear elastic deformation under small strains is assumed to occur only in the porous matrix.

- The involved CO_2, water and solid phases are assumed to be in an isothermal condition, no phase change or exchange and chemically non-reacting.

In the following, governing equations describing coupled linear momentum, mass balance and electrokinetic balance equations for the double porosity model, together with their constitutive laws, are presented.

4.2.1 Momentum balance equation

As mentioned above, linear elastic deformation under small strains is assumed to occur in the porous matrix. Since the volume of the fractures is normally small compared to the total void space, it is assumed that the compressibility of the fracture network does not alter the compressibility of the porous medium significantly and can thus be ignored. However, due to a coupling between the two subdomains, the deformation of the whole domain is affected by the gradients in the pressure field between the porous matrix and fractured zone. It should be noted though, the fracture network compressibility, depending on the geometry and boundary conditions, might play a dominant role in the coupled hydromechanical processes in fractured domains, see Liu et al. (2009).

Using the concept of effective stresses, the total stress can be described as

$$\boldsymbol{\sigma} = \boldsymbol{\sigma}' - \mathbf{I}\,\alpha P_m \tag{4.1}$$

in which $\boldsymbol{\sigma}$ is the total stress, $\boldsymbol{\sigma}'$ is the effective stress, $\mathbf{I}$ is the identity tensor, α is Biot's coefficient, which depends on the compressibility of the constituent, and P_m is the intrinsically averaged pressure of the fluids in the matrix continuum, defined as

$$P_m = S_{wm}P_{wm} + S_{gm}P_{gm} \tag{4.2}$$

where P_{wm} and P_{gm} are the water pressure and CO_2 pressure in the matrix domain, respectively, and S_{wm} and S_{gm} are the corresponding degrees of saturation. The subscripts 'm' refers to the porous matrix domain. Including Eq. (4.2) into Eq. (4.1) gives

$$\boldsymbol{\sigma} = \boldsymbol{\sigma}' - \mathbf{I}\alpha(S_{wm}P_{wm} + S_{gm}P_{gm}) \tag{4.3}$$

The linear momentum balance equation governing the solid phase, under static loading condition, can be expressed as

$$\mathrm{div}\boldsymbol{\sigma} + \bar{\rho}\mathbf{g} = 0 \tag{4.4}$$

where $\mathbf{g}$ is the gravity acceleration and $\bar{\rho}$ is the effective density, described as

$$\bar{\rho} = (1 - \phi_m)\rho_s + \phi_m S_{wm}\rho_w + \phi_m S_{gm}\rho_g \tag{4.5}$$

where ϕ_m is the matrix porosity, ρ_s, ρ_w and ρ_g are the mass density of the solid, water and CO_2 phases, respectively. Substituting Eq. (4.3) into Eq. (4.4) yields

$$\mathrm{div}\left[\boldsymbol{\sigma}' - \mathbf{I}\alpha(S_{wm}P_{wm} + S_{gm}P_{gm})\right] + \bar{\rho}\mathbf{g} = 0 \tag{4.6}$$

4.2.2 Mass continuity equations

Porous matrix continuum

The continuity equations for the water phase and the CO_2 phase in the porous matrix can be expressed as

Water phase:

$$
\left(\frac{\alpha - \phi_m}{K_s} S_{wm}^2 + \frac{\phi_m S_{wm}}{K_w} \right) \frac{\partial P_{wm}}{\partial t} + \frac{\alpha - \phi_m}{K_s} S_{wm} S_{gm} \frac{\partial P_{gm}}{\partial t}
$$
$$
+ \alpha\, S_{wm} \mathbf{m}^T \frac{\partial \boldsymbol{\epsilon}}{\partial t} + \left(\frac{\alpha - \phi_m}{K_s} P_{wm} S_{wm} - \frac{\alpha - \phi_m}{K_s} P_{gm} S_{wm} + \phi_m \right) \frac{\partial S_{wm}}{\partial t} \quad (4.7)
$$
$$
+ \mathbf{q}_w^{leakage} + \frac{1}{\rho_w} \operatorname{div}\left(\phi_m S_{wm} \rho_w \mathbf{v}_{wm} \right) = Q_{wm}
$$

CO_2 phase:

$$
\left(\frac{\alpha - \phi_m}{K_s} S_{wm} S_{gm} \right) \frac{\partial P_{wm}}{\partial t} + \left(\frac{\alpha - \phi_m}{K_s} S_{gm}^2 + \frac{\phi_m S_{gm}}{K_g} \right) \frac{\partial P_{gm}}{\partial t}
$$
$$
+ \alpha\, S_{gm} \mathbf{m}^T \frac{\partial \boldsymbol{\epsilon}}{\partial t} - \left(\frac{\alpha - \phi_m}{K_s} S_{gm} \left(P_{gm} - P_{wm} \right) + \phi_m \right) \frac{\partial S_{wm}}{\partial t} \quad (4.8)
$$
$$
+ \mathbf{q}_g^{leakage} + \frac{1}{\rho_g} \operatorname{div}\left(\phi_m S_{gm} \rho_g \mathbf{v}_{gm} \right) = Q_{gm}
$$

in which K_s, K_w and K_g are the bulk modulus of the solid, water and CO_2 respectively, $\mathbf{v}_{wm}$ and $\mathbf{v}_{gm}$ are water and CO_2 relative velocities to the solid phase, $\mathbf{m} = [1, 1, 1, 0, 0, 0]$ and $\boldsymbol{\epsilon}$ is the strain vector. $\mathbf{q}_w^{leakage}$ and $\mathbf{q}_g^{leakage}$ in Eqs. (4.7) and (4.8) are leakage terms governing water and CO_2 mass transfer between the porous matrix and the fractures, respectively. Several leakage terms have been introduced in literature. According to Warren and Root (1963), the leakage terms can be described as

$$
\mathbf{q}_w^{leakage} = \frac{\bar{\alpha}\, \mathbf{k}_m k_{rwm}}{\mu_w} \left(P_{wm} - P_{wf} \right)
$$
$$
\mathbf{q}_g^{leakage} = \frac{\bar{\alpha}\, \mathbf{k}_m k_{rgm}}{\mu_g} \left(P_{gm} - P_{gf} \right)
$$
$$
(4.9)
$$

where subscript "f" refers to the fractured zone, μ_w and μ_g are water and gas dynamic viscosities, $\mathbf{k}_\alpha$ is the intrinsic permeability tensor for α subdomain (matrix or fracture), $k_{r\pi\alpha}$ is the relative permeability of π phase in α subdomain and the parameter $\bar{\alpha}$ is defined as a shape factor that represents the geometry of the porous matrix and controls flow between the two continua. This parameter has the dimensions of reciprocal area, and, for a cubic matrix block, can be calculated as

$$
\bar{\alpha} = \frac{4n(n+2)}{l^2} \quad (4.10)
$$

in which n is the set of normal fractures and l is a characteristic length given by

$$
\begin{aligned}
l &= a & n &= 1 \\
l &= \frac{2ab}{a+b} & n &= 2 \\
l &= \frac{3abc}{ab+bc+ca} & n &= 3
\end{aligned}
\tag{4.11}
$$

where a, b and c are lengths of the sides of a cubic matrix block.

Fracture continuum

The continuity equations for the water phase and the CO_2 phase in the fracture continuum can be expressed as

Water phase:

$$
\frac{\phi_f S_{wf}}{K_w}\frac{\partial P_{wf}}{\partial t} + \phi_f \frac{\partial S_{wf}}{\partial t} - \mathbf{q}_w^{leakage} + \frac{1}{\rho_w}\text{div}\left(\phi_f S_{wf}\rho_w \mathbf{v}_{wf}\right) = Q_{wf}
\tag{4.12}
$$

CO_2 phase:

$$
\frac{\phi_f S_{gf}}{K_g}\frac{\partial P_{gf}}{\partial t} - \phi_f \frac{\partial S_{wf}}{\partial t} - \mathbf{q}_g^{leakage} + \frac{1}{\rho_g}\text{div}\left(\phi_f S_{gf}\rho_g \mathbf{v}_{gf}\right) = Q_{gf}
\tag{4.13}
$$

where Q_{wf} and Q_{gf} are the source or the sink terms.

4.2.3 Streaming current density continuity equation

Flow of a heterogeneous fluid in a porous medium generates an electrical potential gradient (electrokinetic potential), arising by the interaction of the moving fluid with the electrical double layer at the pore surface. For a saturated porous medium, the relationship between the electrical current density j and the fluid (brine water) velocity $\mathbf{v}_w$ can be obtained by coupling Darcy's law to Ohm's law, as

$$
\mathbf{v}_w = \mathbf{L}_{11}(-\nabla P_w + \rho_w \mathbf{g}) - \mathbf{L}_{12}\nabla V
\tag{4.14}
$$

$$
\mathbf{j} = \mathbf{L}_{21}(-\nabla P_w + \rho_w \mathbf{g}) - L_{22}\nabla V
\tag{4.15}
$$

where V is the electrical potential (self-potential, SP), and $\mathbf{L}_{12}$ and $\mathbf{L}_{21}$ are cross coupling coefficients, which, following Onsager reciprocity principle (Onsager, 1931), are equal, giving $\mathbf{L}_{12} = \mathbf{L}_{21} = \mathbf{L}$. Apparently, $\mathbf{L}_{11}$ represents the hydraulic conductivity, and L_{22} represents the electric conductivity σ_e.

In Eq.(4.15), the first term arises due to the streaming (advection) of the electrical excess charge with fluid flow, while the second term arises due to conduction current

density caused by electric conduction. Under zero total electrical current condition ($\mathbf{j} = \mathbf{0}$), Eq.(4.15) leads to (Sill, 1983)

$$\left(\frac{\nabla V}{-\nabla P + \rho \mathbf{g}} \right)\bigg|_{\mathbf{j}=0} = \mathbf{C} = \frac{\mathbf{L}}{\sigma_e} \Rightarrow \quad \mathbf{L} = \sigma_e \mathbf{C} \tag{4.16}$$

in which $\mathbf{C}$ contains the self-potential coupling coefficients and σ_e is the electrical conductivity.

For a fractured domain, Ishido et al. (2010) suggested that the current density can be volumetrically averaged to calculate the electrokinetic process, as

$$\mathbf{j} = (1 - \psi)\mathbf{j}_m + \psi \mathbf{j}_f \tag{4.17}$$

where ψ is the fractional volume of the fractures.

The conservation of the total current density at quasi-steady state condition in the absence of external current sources implies:

$$\nabla \cdot \mathbf{j} = 0 \tag{4.18}$$

which is the Poisson's equation for the electrical potential V.

4.2.4 Constitutive equations

In a fractured multiphase domain, Darcy's law can be expressed as

$$\phi_\alpha S_{\pi\alpha} \mathbf{v}_{\pi\alpha} = \frac{\mathbf{k}_{\pi\alpha}}{\mu_\pi}(-\nabla P_{\pi\alpha} + \rho_\pi \mathbf{g}) \tag{4.19}$$

where $\alpha = m, f$; $\pi = w, g$, $\mathbf{v}_{\pi\alpha}$ is the velocity of phase π in the α continuum and $\mathbf{k}_{\pi\alpha}$ is the effective phase permeability described as

$$\mathbf{k}_{\pi\alpha} = \mathbf{k}_\alpha k_{r\pi\alpha} \tag{4.20}$$

where $\mathbf{k}_\alpha$ is the intrinsic permeability tensor for α subdomain, and $k_{r\pi\alpha}$ is the relative permeability of phase π in α subdomain. For a multiphase medium, the water and the CO_2 phases are jointly occupying the voids, implying

$$S_{w\alpha} + S_{g\alpha} = 1 \tag{4.21}$$

Also, the water pressure and the CO_2 pressure are related by the capillary pressure, P_c, as

$$P_{c\alpha}(S_{w\alpha}) = P_{g\alpha} - P_{w\alpha} \tag{4.22}$$

111

describing the difference in pressure across the interface between two immiscible fluids. Spatial and temporal differentiation of Eq. (4.22) for the porous matrix and the fracture continuum, using the chain rule, gives

$$\nabla P_{w\alpha} = \nabla P_{g\alpha} - \frac{\partial P_{c\alpha}}{\partial S_{w\alpha}} \nabla S_{w\alpha} \tag{4.23}$$

$$\frac{\partial P_{w\alpha}}{\partial t} = \frac{\partial P_{g\alpha}}{\partial t} - \frac{\partial P_{c\alpha}}{\partial t} = \frac{\partial P_{g\alpha}}{\partial t} - \frac{\partial S_{w\alpha}}{\partial t} \frac{\partial P_{c\alpha}}{\partial S_{w\alpha}} \tag{4.24}$$

In literature, there are several empirical formulations correlating the capillary pressure and relative permeability to saturation. van Genuchten (1980) and Brooks and Corey (1964) are the most commonly used formulations. Using Brooks and Corey, the capillary pressure-saturation relationship for α subdomain is described as

$$P_c = \frac{P_b}{S_e^{1/\lambda}} \quad P_c \leq P_b \tag{4.25}$$

and the relative permeability-saturation relationships are described as

$$k_{rw} = S_e^{(2+3\lambda)/\lambda} \tag{4.26}$$

$$k_{rg} = (1 - S_e)^2(1 - S_e^{(2+\lambda)/\lambda}) \tag{4.27}$$

where S_e is the effective saturation, defined as

$$S_e = (S_w - S_{wr})/(1 - S_{wr} - S_{gr}) \tag{4.28}$$

in which S_{wr} is the irreducible water saturation, S_{gr} is the residual gas saturation, λ is the pore size distribution index and P_b is an entry pressure, corresponding to the capillary pressure needed to displace the wetting phase from the largest pore.

The SP coupling coefficients in the electrokinetic equations, Eqs. (4.14) and (4.15), have been developed for fully saturated conditions (Esrig, 1967; Revil et al., 2007; Sill, 1983).

In a fully saturated condition, at a given pressure, the SP coupling coefficient is a function of temperature, fluid salinity, electrolyte pH, and rock type, expressed as

$$\mathbf{C}_{\text{sat}} = \frac{\zeta \, \boldsymbol{\epsilon}_w}{\mu_w \sigma_w} \tag{4.29}$$

where ζ is the zeta potential, and $\boldsymbol{\epsilon}_w$, μ_w, σ_w are the brine permittivity, viscosity and electrical conductivity, respectively.

For unsaturated conditions, however, determination of the SP coupling coefficient is still debatable. Commonly, they are treated similar to the effective permeability

relation, Eq.(4.20), and they are made function of a phase saturation via saturation-dependent relative parameters, C_r and σ_r. Accordingly, the cross coupling coefficients in Eqs. (4.14) and (4.15) can be expressed as

$$
\begin{aligned}
\mathbf{L}_{11} &= \frac{\mathbf{k}\, k_{rw}}{\mu_w} \\
\mathbf{L} &= \mathbf{C}_{\text{eff}}\sigma_{\text{eff}} = \mathbf{C}_{\text{sat}}C_r\ \sigma_b\sigma_r \\
L_{22} &= \bar{\sigma} = \ \sigma_b\sigma_r
\end{aligned}
\tag{4.30}
$$

where $\mathbf{C}_{\text{eff}}$ is the effective SP coupling coefficient for unsaturated media and $\bar{\sigma}$ is the effective electrical conductivity, $\mathbf{C}_{sat}$ is the SP coupling coefficient for the saturated media and σ_b is the electrical conductivity of the bulk formation.

Incorporating Eqs. (4.17) and (4.30) into Eq. (4.15), the averaged electrical current density for a fractured porous media can be expressed as

$$
\begin{aligned}
\mathbf{j} = (1-\psi)(\mathbf{C}_m C_{rm}\,\sigma_{em}\sigma_{rm}(-\nabla P_{wm}\,+\,\rho_{wm}\,\mathbf{g}) - \sigma_{em}\sigma_{rm}\nabla V) \\
+\psi(\mathbf{C}_f C_{rf}\,\sigma_{ef}\sigma_{rf}(-\nabla P_{wf}\,+\,\rho_{wf}\,\mathbf{g}) - \sigma_{ef}\sigma_{rf}\nabla V)
\end{aligned}
\tag{4.31}
$$

Determination of the relative SP coupling coefficient is not straightforward and several constitutive models have been proposed in the literature (Jackson, 2008; Linde et al., 2007; Revil et al., 2007).

For an unsaturated porous media, the relative SP coupling coefficient (C_r) is a function of a number of parameters, including the wettability of the rock and the distribution of fluids in porous media.

Perrier and Morat (2000) monitored SP signals at an experimental site for one year and proposed a means to explain observed daily variations by considering vadose zone processes. They proposed an empirical expression describing the dependence of relative SP coefficient on water content based on a relative permeability model as:

$$
C_r = \frac{k_{rw}}{\sigma_r}
\tag{4.32}
$$

where k_{rw} is the relative permeability of the wetting phase and σ_r is relative electrical conductivity of the rock matrix, which is a function of saturation.

Guichet et al. (2003) performed the first experimental SP coefficient measurements. They conducted several drainage experiments by injecting an inert gas into a 1-meter long column of water saturated sand, and measured the streaming potentials at the different water saturation. They observed that the coupling coefficient decreases linearly with increasing water saturation as

$$
\mathbf{C}_e = \mathbf{C}_{\text{sat}}C_r = AS_w + B
\tag{4.33}
$$

where A and B are constants. For a dry porous media with no flow and hence no electrokinetic flow, B must be zero. For a fully saturated domain $C_r = S_w = 1$ and $\mathbf{C}_e = \mathbf{C}_{\text{sat}} = A$ and A can thus be calculated from Eq. (4.29). This relation is valid when the surface electrical conductivity of the sample is negligible.

A simple bundle of capillary tubes model has been used by Jackson (2008) to investigate SP coupling during the flow of water and a second immiscible phase such as air or oil. It is shown that the SP coupling coefficient depends on the pore size distribution, the wetting behavior of the capillaries, and the thickness of electrical double layer. The Jackson formulation can be expressed as:

$$C_r = \frac{k_{rw} Q_r}{\sigma_r} \tag{4.34}$$

where, Q_r is the relative excess charge density transported by the flow of water at partial saturation, describing how the charge density of counter ions in the fluid is affected by the saturation of the wetting phase. Jackson (2008) assumed that the excess charge transported by the flow is independent of water saturation, and in this case $Q_r = 1$ and Eq. (4.34) for the relative coupling coefficient becomes

$$C_r = \frac{k_{rw}}{\sigma_r} \tag{4.35}$$

which is the same as Eq. (4.32), presented by Perrier and Morat (2000).

In an alternative approach, Revil and Linde (2006) used the volume averaging of the excess charge within a representative elementary volume (REV) instead of characterization of the excess charge distribution at the pore scale. This approach was then extended by Revil et al. (2007) to consider wetting and non-wetting phases in unsaturated porous media. In this method the excess charge density scales inversely with water saturation ($Q_r = 1/S_w$) and Eq. (4.34) becomes

$$C_r = \frac{k_{rw}}{\sigma_r S_w} \tag{4.36}$$

Lately Saunders et al. (2008) proposed a power law to describe the behavior of the unsaturated relative coupling coefficient during imbibition.

$$C_r = (S_e)^p \tag{4.37}$$

where exponent p is a positive number between 0.01 and 1, which is function of the excess counter-ions in the diffuse layer and the salinity of the brine.

Allègre et al. (2010) presented continuous records of the electrokinetic coefficient as a function of water saturation. Two drainage experiments were performed within a column filled with clean sand. Streaming potential measurements were combined

with water pressure and saturation measurements along the column. They observed that SP coupling coefficient first increases with decreasing saturation, and then decreases up to the residual water saturation. Therefore, they proposed an empirical relation for the relative SP coupling coefficient as,

$$C_r = S_e \left[1 + \beta(1 - S_e)^\gamma\right] \tag{4.38}$$

where β and γ are two fitted parameters (Allègre et al., 2012).

In a work by Saunders et al. (2012) all mentioned models are adjusted for the imbibition process to account for the presence of immobile fractions of both the wetting and non-wetting phases and to have endpoints at 0 and 1. This adjustment was done by substituting the mobile wetting phase volume fraction (effective saturation) S_e with S_w in the Guichet model, Eq. (4.33), and by multiplying the Jackson model, Eq. (4.34), and the Revil model, Eq. (4.36), by the reciprocal of the original function value at $S_w = 1 - S_{nwi}$; where S_{nwi} is initial non-wetting phase saturation. The Guichet model then becomes

$$C_r = S_e \tag{4.39}$$

and the Revil formulation reads

$$C_r = \frac{k_{rw}}{\sigma_r S_w} \frac{\tilde{\sigma}_r (1 - S_{nwr})}{\tilde{k}_{rw}} \tag{4.40}$$

where $\tilde{\sigma}_r$ and $\tilde{k}_{rw}$ are the relative fluid conductivity and permeability calculated at $S_w = 1 - S_{nwi}$, i.e., at the maximum possible brine saturation. The Jackson model is modified as:

$$C_r = \frac{S_e \tilde{\sigma}_r}{\sigma_r} \tag{4.41}$$

All mentioned models for calculating relative SP coupling coefficient are numerically compared in Section 4.4.4.

The relative electrical conductivity (inverse of the resistivity index) can be calculated using Archie's law, as

$$\sigma_r = (S_w)^n \tag{4.42}$$

where n is Archie's saturation exponent (close to 2).

4.2.5 General Field Equations

The governing field equations for a coupled hydromechanical-electrokinetic flow in a double porosity system are obtained by incorporating the constitutive equations into the relevant balance equations. Here, we adopt the pressure-saturation formulation.

Equilibrium field equation

For a linear isotropic solid, the effective stress is described as

$$\boldsymbol{\sigma}'' = \mathbf{D}_e \boldsymbol{\epsilon} = \mathbf{D}_e \hat{\mathbf{L}} \, \mathbf{u} \tag{4.43}$$

in which $\mathbf{D}_e$ is the stiffness tensor of the solid phase, $\mathbf{u}$ is the displacement and $\hat{\mathbf{L}}$ is the displacement-strain operator.

Incorporating Eq. (4.22) for the matrix continuum and Eq. (4.43) into the momentum equation, Eq.(4.6), the equilibrium field equation can be expressed as

$$\mathrm{div}\left[\mathbf{D}_e(\hat{\mathbf{L}}\mathbf{u}) - \mathbf{m}^T \alpha (P_{gm} - P_{cm}S_{wm})\right] + \bar{\rho}\mathbf{g} = 0 \tag{4.44}$$

Mass balance field equations

Substituting Eq. (4.14), together with Eqs (4.23), (4.24) and (4.9), into the mass balance equation, Eqs. (4.7), the field mass balance equations for the water phase can be expressed as

Porous matrix:

$$d_1 \frac{\partial P_{gm}}{\partial t} + d_2 \frac{\partial S_{wm}}{\partial t} + d_3 \mathbf{m}^T \frac{\partial \boldsymbol{\epsilon}}{\partial t} + \nabla \cdot (-\mathbf{c}_1 \nabla P_{gm} - \mathbf{c}_2 \nabla S_{wm} - \mathbf{c}_3 \nabla V + \mathbf{G}_1)$$
$$+ a_1 P_{gm} + a_2 P_{gf} + f_1 = 0 \tag{4.45}$$

Fracture continuum:

$$d_7 \frac{\partial P_{gf}}{\partial t} + d_8 \frac{\partial S_{wf}}{\partial t} + \nabla \cdot (-\mathbf{c}_5 \nabla P_{gf} - \mathbf{c}_6 \nabla S_{wf} - \mathbf{c}_7 \nabla V + \mathbf{G}_3)$$
$$+ a_5 P_{gm} + a_6 P_{gf} + f_2 = 0 \tag{4.46}$$

Similarly, the field mass balance equation for the CO_2 phase can be expressed as

Porous matrix:

$$d_4 \frac{\partial P_{gm}}{\partial t} + d_5 \frac{\partial S_{wm}}{\partial t} + d_6 \mathbf{m}^T \frac{\partial \boldsymbol{\epsilon}}{\partial t} + \nabla \cdot (-\mathbf{c}_4 \nabla P_{gm} + \mathbf{G}_2)$$
$$+ a_3 P_{gm} + a_4 P_{gf} = 0 \tag{4.47}$$

Fracture continuum:

$$d_9 \frac{\partial P_{gf}}{\partial t} + d_{10} \frac{\partial S_{wf}}{\partial t} + \nabla \cdot (-\mathbf{c}_8 \nabla P_{gf} + \mathbf{G}_4) + a_7 P_{gm} + a_8 P_{gf} = 0 \tag{4.48}$$

where $a_1 - a_8$, $d_1 - d_6$, $\mathbf{c}_1 - \mathbf{c}_8$, $\mathbf{G}_1 - \mathbf{G}_4$ and $f_1 \ldots f_2$ are coefficients described in Table 4.1.

Electric current density balance field equation

Incorporating Eqs. (4.15) and (4.23) into Eq. (4.18) gives

$$\nabla \cdot \left(-\mathbf{c}_9 \nabla P_{gm} - \mathbf{c}_{10} \nabla S_{wm} - \mathbf{c}_{11} \nabla P_{gf} - \mathbf{c}_{12} \nabla S_{wf} - c_{13} \nabla V + \mathbf{G}_5 \right) = 0 \quad (4.49)$$

where $c_9 \dots c_{13}$ and G_5 are coefficients described in Table 4.1.

4.2.6   Initial and boundary conditions

Initially, at $t = 0$, solid displacement, CO_2 pressure, water saturation in the porous matrix and the fractured zone, and the electrokinetic potential are described as

$$\begin{array}{lll}
\mathbf{u} = \mathbf{u}_0; & P_{gm} = P_{gm0}(\mathbf{x}); & P_{gf} = P_{gf0}(\mathbf{x}) \\
S_{wm} = S_{wm0}(\mathbf{x}); & S_{wf} = S_{wf0}(\mathbf{x}); & V = V_0(\mathbf{x})
\end{array} \quad \text{at } t = 0 \quad (4.50)$$

The Dirichlet boundary conditions for these fields are prescribed as

$$\begin{array}{llllll}
\mathbf{u} & = & \hat{\mathbf{u}} & \text{on } \Gamma_u & P_{gm} = \hat{P}_{gm} \text{ on } \Gamma_{gm} & P_{gf} = \hat{P}_{gf} \text{ on } \Gamma_{gf} \\
S_{wm} & = & \hat{S}_{wm} & \text{on } \Gamma_{wm} & S_{wf} = \hat{S}_{wf} \text{ on } \Gamma_{wf} & V = \hat{V} \text{ on } \Gamma_V
\end{array} \quad (4.51)$$

The relevant Neumann boundary conditions for the flow fields are: CO_2 flux:

$$\frac{\mathbf{k} k_{rgf}}{\mu_g}(-\nabla P_{gf} + \rho_g \mathbf{g}) \cdot \mathbf{n} = q_g \quad \text{on } \Gamma_{gf}^q \quad (4.52)$$

Water flux:

$$\frac{\mathbf{k} k_{rwf}}{\mu_w} \left(-\nabla P_{gf} + \nabla S_{wf} \frac{\partial P_{cf}}{\partial S_{wf}} + \rho_w \mathbf{g} \right) \cdot \mathbf{n} = q_w \quad \text{on } \Gamma_{wf}^q \quad (4.53)$$

where $\mathbf{n} = \{n_x, n_y, n_z\}^T$ is the unit normal vector.

The Neumann boundary condition for the equilibrium field is:

$$\mathbf{I}^T \boldsymbol{\sigma} = \bar{\mathbf{t}} \quad \text{on } \Gamma_u^q \quad (4.54)$$

where the unit matrix $\mathbf{I}$ is defined as

$$\mathbf{I}^T = \begin{bmatrix}
n_x & 0 & 0 & n_y & 0 & n_z \\
0 & n_y & 0 & n_x & n_z & 0 \\
0 & 0 & n_z & 0 & n_y & n_x
\end{bmatrix} \quad (4.55)$$

Table 4.1: Coefficients of the general field equations.

a	c	d	G,f
$a_1 = \bar{\alpha} \frac{\mathbf{k}_m k_{rwm}}{\mu_w}$	$\mathbf{c}_1 = \mathbf{k}_m \frac{k_{rwm}}{\mu_w}$	$d_1 = \frac{\alpha - \phi_m}{K_s} S_{wm} + \frac{\phi_m S_{wm}}{K_w}$	$\mathbf{G}_1 = \mathbf{k}_m \frac{k_{rwm}}{\mu_w} \rho_w \mathbf{g}$ $\mathbf{f}_1 = -\bar{\alpha} \frac{\mathbf{k}_m k_{rwm}}{\mu_{wm}} (P_{cm} - P_{cf})$
$a_2 = -a_1$	$\mathbf{c}_2 = -\frac{\partial P_{cm}}{\partial S_{wm}} \mathbf{k}_m \frac{k_{rwm}}{\mu_w}$	$d_2 = -\frac{\alpha - \phi_m}{K_s} P_{cm} S_{wm} + \phi_m$ $-\frac{\alpha - \phi_m}{K_s} S_{wm}^2 \frac{\partial P_{cm}}{\partial S_{wm}} - \frac{\phi_m S_{wm}}{K_w} \frac{\partial P_{cm}}{\partial S_{wm}}$	$\mathbf{G}_2 = \mathbf{k}_m \frac{k_{rg}}{\mu_g} \rho_g \mathbf{g}$ $\mathbf{f}_2 = -\bar{\alpha} \frac{\mathbf{k}_m k_{rwm}}{\mu_{wm}} (P_{cm} - P_{cf})$
$a_3 = \bar{\alpha} \frac{\mathbf{k}_m k_{rgm}}{\mu_g}$	$\mathbf{c}_3 = \mathbf{C}_m C_{rm} \sigma_{bm} \sigma_{rm}$	$d_3 = \alpha S_{wm}$	$\mathbf{G}_3 = \frac{\mathbf{k}_f k_{rwf}}{\mu_{wf}} \rho_{wf} \mathbf{g}$
$a_4 = -a_3$	$\mathbf{c}_4 = \mathbf{k}_m \frac{k_{rgm}}{\mu_g}$	$d_4 = \frac{\alpha - \phi_m}{K_s} - S_{wm} \frac{\alpha - \phi_m}{K_s}$ $+ \frac{\phi_m (1 - S_{wm})}{K_g}$	$\mathbf{G}_4 = \frac{\mathbf{k}_f k_{rgf}}{\mu_{gf}} \rho_{gf} \mathbf{g}$
$a_5 = -a_1$	$\mathbf{c}_5 = \frac{k_{rwf}}{\mu_w} \mathbf{k}_f$	$d_5 = -\frac{\alpha - \phi_m}{K_s} P_{cm} + \frac{\alpha - \phi_m}{K_s} S_{wm} P_{cm}$ $-\phi_m - \frac{\alpha - \phi_m}{K_s} S_{wm} \frac{\partial P_{cm}}{\partial S_{wm}}$ $+ \frac{\alpha - \phi_m}{K_s} S_{wm}^2 \frac{\partial P_{cm}}{\partial S_{wm}}$	$\mathbf{G}_5 =$ $\rho_{wm} \mathbf{G} C_m C_{rm} \sigma_{em} \sigma_{rm} (1 - \psi)$ $+ \rho_{wf} \mathbf{g} C_f C_{rf} \sigma_{ef} \sigma_{rf} \psi$
$a_6 = a_1$	$\mathbf{c}_6 = -\frac{\partial P_{cf}}{\partial S_{wf}} \mathbf{k}_f \frac{k_{rwf}}{\mu_w}$	$d_6 = \alpha (1 - S_{wm})$	—
$a_7 = -a_3$	$\mathbf{c}_7 = \mathbf{C}_f C_{rf} \sigma_{bf} \sigma_{rf}$	$d_7 = \frac{\phi_f S_{wf}}{K_w}$	—
$a_8 = a_3$	$\mathbf{c}_8 = \mathbf{k}_f \frac{k_{rgf}}{\mu_g}$	$d_8 = \phi_f - \frac{\phi_f S_{wf}}{K_w} \frac{\partial P_{cf}}{\partial S_{wf}}$	—
—	$\mathbf{c}_9 = \mathbf{C}_m C_{rm} \sigma_{bm} \sigma_{rm} (1 - \psi)$	$d_9 = \frac{\phi_f (1 - S_{wf})}{K_g}$	—
—	$\mathbf{c}_{10} = -\mathbf{C}_m C_{rm} \sigma_{bm} \sigma_{rm}$ $\frac{\partial p_{cm}}{\partial S_{wm}} (1 - \psi)$	$d_{10} = -\phi_f$	—
—	$\mathbf{c}_{11} = \mathbf{C}_f C_{rf} \sigma_{bf} \sigma_{rf} \psi$	—	$\mathbf{G}_{11} = 1$
—	$\mathbf{c}_{12} = -\mathbf{C}_f C_{rf} \sigma_{bf} \sigma_{rf} \frac{\partial p_{cf}}{\partial S_{wf}} \psi$	—	—
—	$\mathbf{c}_{13} = \sigma_{bm} \sigma_{rm} (1 - \psi)$ $+ \sigma_{bf} \sigma_{rf} \psi$	—	—

4.3 Numerical discretization

The governing equations, given in Eqs. (4.44)-(4.49), describe a two-phase flow in a deformable fractured porous medium domain coupled to electrokinetic processes arising from the interaction between the moving phases and the electrical double layer existing on the solid pore surface. These equations consist of six primary variables (u, P_{gm}, P_{gf}, S_{wm}, S_{wf}, V), which are of basically different nature. The displacement field is continuous, but the pressure, saturation and electrokinetic fields exhibit relatively high gradients at the CO_2 plume front. Using standard numerical procedures, it is likely that the solution leads to spurious oscillations unless very fine meshes and/or adaptive meshes are utilized. A better alternative is to utilize the extended finite element method (XFEM), where a discontinuity or a high gradient in a field can be modeled regardless of the mesh. However, this implies doubling the degrees of freedom, making the gained stability, computationally inefficient. To reduce the number of degrees of freedom, a mixed discretization scheme, proposed by Al-Khoury and Sluys (2007) and extended in the previous chapters, is utilized. Equations containing diffusion and/or strong capillary effects can be discretized using the standard Galerkin finite element method (SG), and equations containing advection together with high gradient in the saturation field can be discretized using XFEM, together with the level-set method (LS) and the Petrov-Galerkin method (PG).

A fractured reservoir comprises a porous matrix of a relatively low permeability and a network of fissures of a relatively high permeability. Consequently, under the combined action of solid deformation and viscous, capillary and gravity forces, there exists a relatively high velocity motion of the CO_2 plume in the fractured continuum. This gives rise to an advective dominant fluid flow with a high gradient saturation field at the CO_2 plume front. All other fields exhibit a relatively low velocity motion, giving rise to a diffusive dominant fluid flow. Accordingly, here, SG is utilized to discretize solid deformation $\mathbf{u}$, CO_2 pressure in the porous matrix and the fractured zone, P_{gm} and P_{gf}, water saturation in the porous matrix s_{wm}, and the effective self-potential in the porous matrix and the fractured zone, V. The water saturation field in the fractured zone S_{wf}, on the other hand, is discretized using XFEM-LS-PG. The level-set method is employed to trace and locate the CO_2 plume front, and XFEM, is employed to model the high gradient in the saturation field front. Two advantages can be drawn from this scheme: a) capturing and modeling the front of the advective field gives a locally conservative system, resulting in an accurate and convergent simulation, and b) using XFEM only for the highly advective saturation field in the fractured zone and SG for all other fields reduces drastically the number

of degrees of freedom of the system, compared to that if all fields are simulated using XFEM.

4.3.1 Level-set discretization

The level-set method is a numerical technique usually utilized for tracing a moving interface, Γ_d, between two zones, for instance, Ω_1 and Ω_2. A level-set function is defined as a signed distance function $\Phi(x)$, which is positive in Ω_1, negative in Ω_2, and zero at the interface between them. The level-set value is advected by the field motion, as

$$\frac{\partial \Phi}{\partial t} + \mathbf{v}_{\Gamma_d} \cdot \nabla \Phi = 0 \tag{4.56}$$

where $\mathbf{v}_{\Gamma_d}$ represents the interface velocity, in this case the CO_2 plume front velocity in the fractured zone. Following Liu et al. (2010), the front velocity can be calculated as

$$\mathbf{v}_{\Gamma_d} = \frac{\rho_g(1 - S_{wf})}{\rho}\mathbf{v}_{gf} + \frac{\rho_w S_{wf}}{\rho}\mathbf{v}_{wf} \tag{4.57}$$

where $\mathbf{v}_{gf}$ and $\mathbf{v}_{wf}$ are CO_2 and brine water Darcy velocities in the fractured zone, calculated by Eq. (4.19) and $\rho = \rho_w S_{wf} + \rho_g S_{gf}$.

The level-set equation, Eq.(4.56), is a first-order hyperbolic function and its discretization using the standard Galerkin method may result into spurious oscillations. Different techniques have been employed to stabilize this problem, among which the Streamline Upwind Petrov-Galerkin (SUPG) method is known to be effective in many cases. In the SUPG method the shape function is perturbed in the direction of the flow, as

$$\bar{\mathbf{N}} = \mathbf{N} + \mathbf{N}_s \tag{4.58}$$

where N is the standard finite element shape functions and N_s is an enhancement function, defined as

$$\mathbf{N}_s = \tau \mathbf{v}_{\Gamma_d} \cdot \nabla \mathbf{N} \tag{4.59}$$

where τ is a stabilization parameter, which, in the absence of diffusion, can be expressed as

$$\tau = \frac{h_e}{2\,|\mathbf{v}_{\Gamma_d}|} \tag{4.60}$$

with h_e the characteristic length of the element, defined as

$$h_e = 2\left(\sum_{\alpha=1}^{n_e}\left|\frac{\mathbf{v}_{\Gamma_d i}}{\|\mathbf{v}_{\Gamma_d}\|}\frac{\partial N_\alpha}{\partial x_i}\right|\right)^{-1} \tag{4.61}$$

in which n_e is the number of nodes in the element and N_α is the basis function associated with node α.

Applying the weighted residual finite element discretization procedure to Eq. (4.56), using Eq. (4.58), gives

$$\int_\Omega \mathbf{N} \left(\frac{\partial \Phi}{\partial t} + \mathbf{v}_{\Gamma_d} \cdot \nabla \Phi \right) d\Omega + \sum_k \int_{\Omega_k} \mathbf{N}_s \left(\frac{\partial \Phi}{\partial t} + \mathbf{v}_{\Gamma_d} \cdot \nabla \Phi \right) d\Omega = 0 \qquad (4.62)$$

Approximating $\Phi = \mathbf{N}\bar{\bar{\Phi}}$, where $\bar{\bar{\Phi}}$ are the level-set nodal values, and substituting into Eq. (3.62), yields

$$\int_\Omega \mathbf{N}^T \mathbf{N} \frac{\partial \bar{\bar{\Phi}}}{\partial t} d\Omega + \int_\Omega \mathbf{N}^T (\mathbf{v}_{\Gamma_d} \cdot \nabla \mathbf{N}) \bar{\bar{\Phi}} \, d\Omega + \sum_k \int_{\Omega_k} \mathbf{N}_s^T \mathbf{N} \frac{\partial \bar{\bar{\Phi}}}{\partial t} d\Omega$$
$$+ \sum_k \int_{\Omega_k} \mathbf{N}_s^T (\mathbf{v}_{\Gamma_d} \cdot \nabla \mathbf{N}) \bar{\bar{\Phi}} \, d\Omega = 0 \qquad (4.63)$$

The stabilizing term in Eq. (4.63) is denoted by a subscript k to emphasize that, due to $\nabla \mathbf{N}$, which is discontinuous across the elements, the numerical integration must be carried out on the element interior Ω_k and not at the nodes (Zienkiewicz et al., 2005).

Utilizing the level-set method to trace a moving front requires re-initialization. This is necessary because otherwise the distance property of the level-set function is no longer maintained after advection. Here, we adopt a re-initialization technique proposed by (Cho et al., 2011).

4.3.2 SG-XFEM-LS discretization

Following the above described discretization scheme, Eqs. (4.44)-(4.47) and (4.49) are discretized using SG, and Eq. (4.48) is discretized using XFEM-LS. Using the weighted residual method, the finite element formulation of the equilibrium equation, Eq. (4.4), using Eq. (4.54), can be described as

$$\int_\Omega \mathbf{w}^T (\hat{\mathbf{L}}^T \boldsymbol{\sigma} + \bar{\rho}\mathbf{g}) d\Omega - \int_{\Gamma_u^q} \mathbf{w}^T (\mathbf{I}^T \boldsymbol{\sigma} - \bar{\mathbf{t}}) d\Gamma = 0 \qquad (4.64)$$

in which $\mathbf{w}$ is any arbitrary weighting function. Applying Green's theorem to the first part of Eq. (4.64), gives

$$-\int_\Omega (\hat{\mathbf{L}}\mathbf{w})^T \boldsymbol{\sigma} \, d\Omega + \int_\Omega \mathbf{w}^T \bar{\rho}\mathbf{g} \, d\Omega + \int_{\Gamma_u^q} \mathbf{w}^T \bar{\mathbf{t}} \, d\Gamma = 0 \qquad (4.65)$$

Using standard finite element method, solid displacement, CO_2 pressure in the porous matrix and the fractured zone, water saturation in the porous matrix and

streaming potential values can be approximated in terms of their nodal values, as

$$
\begin{aligned}
\mathbf{u}(x,t) &= \mathbf{N}_u(x)\bar{\mathbf{u}}(t) \\
P_{gm}(x,t) &= \mathbf{N}_{pm}(x)\bar{\mathbf{P}}_{gm}(t) \\
S_{wm}(x,t) &= \mathbf{N}_{sm}(x)\bar{\mathbf{S}}_{wm}(t) \\
P_{gf}(x,t) &= \mathbf{N}_{pf}(x)\bar{\mathbf{P}}_{gf}(t) \\
V(x,t) &= \mathbf{N}_V(x)\bar{\mathbf{V}}(t)
\end{aligned}
\tag{4.66}
$$

where $\bar{\mathbf{u}}, \bar{\mathbf{P}}_{gm}, \bar{\mathbf{S}}_{wm}, \bar{\mathbf{P}}_{gf}$ and $\bar{\mathbf{V}}$ are the nodal vectors for displacement, CO_2 pressure in the porous matrix, water saturation in the porous matrix, CO_2 pressure in the fractured zone and the effective streaming potential in the porous matrix-fracture subdomains.

The saturation field in the fractured zone, on the other hand, is approximated using XFEM. In XFEM, the finite element spatial discretization is conducted by adding an enhanced function necessary to capture any physical discontinuity or a high gradient field exists within the element. The saturation field in the fractured subdomain can thus be described in terms of its nodal values as

$$
S_{wf}(x,t) = \mathbf{N}(x)\bar{\mathbf{S}}_{wf}(t) + \sum_{J \in N_{\text{enriched}}} N_J^*(x,t)\mathbf{a}_J(t)
\tag{4.67}
$$

where $\bar{\mathbf{S}}_{wf}$ is the nodal water saturation vector in the fractured zone, and $\mathbf{a}_J$ is an additional nodal degree of freedom on node J of an enriched element,N_{enriched}, where the plume front intersects. As proposed by Chessa and Belytschko (2003a), the level-set function can be utilized for the enriched shape functions, giving

$$
N_J^*(x,t) = N_J(x)\left[|\Phi(x,t)| - |\Phi(x_J,t)|\right]
\tag{4.68}
$$

Using the Galerkin finite element method, the weighting function $\mathbf{w}$ is taken equal to the shape function, i.e. $\mathbf{w} = \mathbf{N_u}$. Making the shape function of all fields equal, i.e $\mathbf{N}_u = \mathbf{N}_{pm} = \mathbf{N}_{pf} = \mathbf{N}_{sm} = \mathbf{N}_V = \mathbf{N}$, and substituting Eqs. (4.66) and (4.67) into Eq. (4.65) gives

$$
\begin{aligned}
&-\int_{\Omega_m} \mathbf{B}^T \mathbf{D}\, \mathbf{B}\, \bar{\mathbf{u}}\, d\Omega + \int_{\Omega_m} \mathbf{B}^T \mathbf{m}^T \alpha \mathbf{N} \bar{\mathbf{P}}_{gm}\, d\Omega - \int_{\Omega_m} \mathbf{B}^T \mathbf{m}^T \alpha P_{cm} \mathbf{N} \bar{\mathbf{S}}_{wm} d\Omega \\
&+ \int_{\Gamma_u^q} \mathbf{N}^T \bar{\mathbf{t}}\, d\Gamma + \int_{\Omega_m} \mathbf{N}^T \bar{\rho}\mathbf{g}\, d\Omega = 0
\end{aligned}
\tag{4.69}
$$

where $\mathbf{B} = \hat{\mathbf{L}}\mathbf{N}$ and Ω_m is the porous matrix subdomain. In a similar manner applying the Galerkin weighted residual method to Eqs.(4.45)-(4.46), employing Green's theorem, yields

Matrix (water phase)

$$
\begin{aligned}
&\int_{\Omega_m} \mathbf{N}^T d_1 \, \mathbf{N} \, \dot{\mathbf{P}}_{gm} \, d\Omega + \int_{\Omega_m} \mathbf{N}^T d_2 \mathbf{N} \, \dot{\mathbf{S}}_{wm} d\Omega \; + \int_{\Omega_m} \mathbf{N}^T d_3 \, \mathbf{m}^T \mathbf{B} \, \dot{\mathbf{u}} \, d\Omega \\
&+ \int_{\Omega_m} (\nabla \mathbf{N})^T \mathbf{c}_1 \nabla \mathbf{N} \bar{\mathbf{P}}_{gm} d\Omega + \int_{\Omega_m} (\nabla \mathbf{N})^T \mathbf{c}_2 \nabla \mathbf{N} \bar{\mathbf{S}}_{wm} d\Omega \\
&+ \int_{\Omega_m} (\nabla \mathbf{N})^T \mathbf{c}_3 \nabla \mathbf{N} \bar{\mathbf{V}}_m \, d\Omega - \int_{\Omega_m} (\nabla \mathbf{N})^T \mathbf{G}_1 d\Omega \\
&+ \int_{\Omega_m} \mathbf{N}^T a_1 \, \mathbf{N} \, \bar{\mathbf{P}}_{gm} \, d\Omega + \int_{\Omega_m} \mathbf{N}^T a_2 \, \mathbf{N} \, \bar{\mathbf{P}}_{gf} \, d\Omega + \int_{\Omega_m} \mathbf{N}^T \mathbf{f_1} \; d\Omega = 0
\end{aligned}
\tag{4.70}
$$

Matrix (CO_2 phase)

$$
\begin{aligned}
&\int_{\Omega_m} \mathbf{N}^T d_4 \, \mathbf{N} \, \dot{\mathbf{P}}_{gm} \, d\Omega + \int_{\Omega_m} \mathbf{N}^T d_5 \mathbf{N} \, \dot{\mathbf{S}}_{wm} d\Omega \; + \int_{\Omega_m} \mathbf{N}^T d_6 \, \mathbf{m}^T \mathbf{B} \, \dot{\mathbf{u}} \, d\Omega \\
&+ \int_{\Omega_m} (\nabla \mathbf{N})^T \mathbf{c}_4 \nabla \mathbf{N} \bar{\mathbf{P}}_{gm} d\Omega - \int_{\Omega_m} (\nabla \mathbf{N})^T \mathbf{G}_2 d\Omega \\
&+ \int_{\Omega_m} \mathbf{N}^T a_3 \, \mathbf{N} \, \bar{\mathbf{P}}_{gm} \, d\Omega + \int_{\Omega_m} \mathbf{N}^T a_4 \, \mathbf{N} \, \bar{\mathbf{P}}_{gf} \, d\Omega = 0
\end{aligned}
\tag{4.71}
$$

Fracture (water phase)

$$
\begin{aligned}
&\int_{\Omega_f} \mathbf{N}^T d_7 \, \mathbf{N} \, \dot{\mathbf{P}}_{gf} \, d\Omega + \int_{\Omega_f} \mathbf{N}^T d_8 \mathbf{N} \, \dot{\mathbf{S}}_{wf} d\Omega \; + \int_{\Omega_f^+} \mathbf{N}^T d_8 \mathbf{N}^* \dot{\mathbf{a}}_J d\Omega \\
&+ \int_{\Omega_f} (\nabla \mathbf{N})^T \mathbf{c}_5 \nabla \mathbf{N} \bar{\mathbf{P}}_{gf} d\Omega + \int_{\Omega_f} (\nabla \mathbf{N})^T \mathbf{c}_6 \nabla \mathbf{N} \bar{\mathbf{S}}_{wf} d\Omega \\
&+ \int_{\Omega_f^+} (\nabla \mathbf{N})^T \mathbf{c}_6 \nabla \mathbf{N}^* \mathbf{a}_J \, d\Omega + \int_{\Omega_f} (\nabla \mathbf{N})^T \mathbf{c}_7 \nabla \mathbf{N} \bar{\mathbf{V}}_f \, d\Omega \\
&- \int_{\Omega_f} (\nabla \mathbf{N})^T \mathbf{G}_3 d\Omega + \int_{\Omega_m} \mathbf{N}^T a_5 \, \mathbf{N} \, \bar{\mathbf{P}}_{gm} \, d\Omega \\
&+ \int_{\Omega_m} \mathbf{N}^T a_6 \, \mathbf{N} \, \bar{\mathbf{P}}_{gf} \, d\Omega + \int_{\Omega_m} \mathbf{N}^T \mathbf{f_2} \; d\Omega = \int_{\Gamma_{wf}^q} \mathbf{N}^T q_w \, d\Gamma
\end{aligned}
\tag{4.72}
$$

where Ω and Ω^+ are the continuous and the discontinuous subdomains, respectively.

Applying XFEM to Eq. (4.48), using a weighting function of the form: $\mathbf{w} = \mathbf{N} + \mathbf{N}_J^*$ gives

123

Fracture (CO_2 phase)

$$\int_{\Omega_f} \mathbf{N}^T \left[d_9 \frac{\partial P_{gf}}{\partial t} + d_{10} \frac{\partial S_{wf}}{\partial t} + \nabla \cdot (-\mathbf{c}_8 \nabla P_{gf} + \mathbf{G}_4) + a_7 P_{gm} + a_8 P_{gf} \right] d\Omega$$

$$+ \int_{\Omega_f^+} \mathbf{N}_J^{*T} \left[d_9 \frac{\partial P_{gf}}{\partial t} + d_{10} \frac{\partial S_{wf}}{\partial t} + \nabla \cdot (-\mathbf{c}_8 \nabla P_{gf} + \mathbf{G}_4) + a_7 P_{gm} \right.$$
$$\left. + a_8 P_{gf} \right] d\Omega = 0 \tag{4.73}$$

This equation can be split into two equations, giving

$$\int_{\Omega_f} \mathbf{N}^T \left[d_9 \frac{\partial P_{gf}}{\partial t} + d_{10} \frac{\partial S_{wf}}{\partial t} + \nabla \cdot (-\mathbf{c}_8 \nabla P_{gf} + \mathbf{G}_4) + a_7 P_{gm} + a_8 P_{gf} \right] d\Omega = 0 \tag{4.74}$$

$$\int_{\Omega_f^+} \mathbf{N}_J^{*T} \left[d_9 \frac{\partial P_{gf}}{\partial t} + d_{10} \frac{\partial S_{wf}}{\partial t} + \nabla \cdot (-\mathbf{c}_8 \nabla P_{gf} + \mathbf{G}_4) + a_7 P_{gm} \right.$$
$$\left. + a_8 P_{gf} \right] d\Omega = 0 \tag{4.75}$$

Employing the Green's theorem and introducing Eq. (4.67) into Eqs. (4.74) and (4.75) leads to

$$\int_{\Omega_f} \mathbf{N}^T d_9 \, \mathbf{N} \dot{\mathbf{P}}_{gf} d\Omega + \int_{\Omega_f} \mathbf{N}^T d_{10} \mathbf{N} \dot{\mathbf{S}}_{wf} d\Omega + \int_{\Omega_f^+} \mathbf{N}^T d_{10} \mathbf{N}^* \dot{\mathbf{a}}_J d\Omega$$

$$+ \int_{\Omega_f} (\nabla \mathbf{N})^T \mathbf{c}_8 \nabla \mathbf{N} \bar{\mathbf{P}}_{gf} d\Omega - \int_{\Omega_f} (\nabla \mathbf{N})^T \mathbf{G}_4 d\Omega \tag{4.76}$$

$$+ \int_{\Omega_m} \mathbf{N}^T a_7 \, \mathbf{N} \, \bar{\mathbf{P}}_{gm} \, d\Omega_m + \int_{\Omega_f} \mathbf{N}^T a_8 \, \mathbf{N} \, \bar{\mathbf{P}}_{gf} \, d\Omega_f = \int_{\Gamma_{gf}^q} \mathbf{N}^T q_g \, d\Gamma_f$$

and

$$\int_{\Omega_f^+} \mathbf{N}^{*T} d_9 \mathbf{N} \dot{\mathbf{P}}_{gf} d\Omega + \int_{\Omega_f^+} \mathbf{N}^{*T} d_{10} \mathbf{N} \, \dot{\mathbf{S}}_{wf} d\Omega + \int_{\Omega_f^+} \mathbf{N}^{*T} d_{10} \, \mathbf{N}^* \dot{\mathbf{a}}_J d\Omega$$

$$+ \int_{\Omega_f^+} (\nabla \mathbf{N}^*)^T \mathbf{c}_8 \nabla \mathbf{N} \bar{\mathbf{P}}_{gf} d\Omega + \int_{\Omega_m} \mathbf{N}^{*T} a_7 \, \mathbf{N} \, \bar{\mathbf{P}}_{gm} \, d\Omega \tag{4.77}$$

$$+ \int_{\Omega_f} \mathbf{N}^{*T} a_8 \, \mathbf{N} \, \bar{\mathbf{P}}_{gf} \, d\Omega - \int_{\Omega_f^+} (\nabla \mathbf{N}^*)^T \mathbf{G}_4 d\Omega = \int_{\Gamma_{gf}^+} \mathbf{N}^T q_g \, d\Gamma$$

Applying the Galerkin weighted residual method to the streaming potential field balance equation, Eq.(4.49), gives

$$
\begin{aligned}
&\int_{\Omega_m} (\nabla \mathbf{N})^T \mathbf{c}_9 \nabla \mathbf{N} \bar{\mathbf{P}}_{gm} d\Omega + \int_{\Omega_m} (\nabla \mathbf{N})^T \mathbf{c}_{10} \nabla \mathbf{N} \bar{\mathbf{S}}_{\mathbf{w}m} d\Omega \\
&+ \int_{\Omega_f} (\nabla \mathbf{N})^T \mathbf{c}_{11} \nabla \mathbf{N} \bar{\mathbf{P}}_{gf} d\Omega + \int_{\Omega_f} (\nabla \mathbf{N})^T \mathbf{c}_{12} \nabla \mathbf{N} \bar{\mathbf{S}}_{\mathbf{w}f} d\Omega \\
&+ \int_{\Omega_f^+} (\nabla \mathbf{N})^T \mathbf{c}_{12} \nabla \mathbf{N}^* \mathbf{a}_J d\Omega + \int_{\Omega} (\nabla \mathbf{N})^T c_{13} \nabla \mathbf{N} \bar{\mathbf{V}} d\Omega \\
&- \int_{\Omega} (\nabla \mathbf{N})^T \mathbf{G}_5 d\Omega = 0
\end{aligned}
\tag{4.78}
$$

The resulting weak formulations, Eqs. (4.69)-(4.72) and Eqs. (4.76)-(4.78), represent a set of semi-discrete nonlinear equations that need to be solved iteratively. To linearize the problem, Taylor series expansions up to the first order suffices. For example, the nonlinear parameter $\mathbf{c_1}$ at iteration $r + 1$, can be linearized as

$$
\mathbf{c}_1^{r+1} = \mathbf{c}_1(S_w^r) + \frac{\partial \mathbf{c}_1(S_w^r)}{\partial S_w}(\delta S_w)
\tag{4.79}
$$

with

$$
\delta S_w = S_w^{r+1} - S_w^r
\tag{4.80}
$$

and $\mathbf{c_1}$ variation with saturation can be calculated analytically via Brook and Corey's or other constitutive relationships.

Derivatives of all nonlinear parameters, given in Table 4.1, can be calculated in the same way. The primary variables and their time derivatives can be written as

$$
\begin{aligned}
\mathbf{X}^{r+1} &= \mathbf{X}^r + \delta \mathbf{X} \\
\dot{\mathbf{X}}^{r+1} &= \dot{\mathbf{X}}^r + \delta \dot{\mathbf{X}}
\end{aligned}
\tag{4.81}
$$

where $\mathbf{X}^{r+1} = [\mathbf{u} \; \mathbf{P}_{gm} \; \mathbf{S}_{wm} \; \mathbf{P}_{gf} \; \mathbf{S}_{wf} \; \mathbf{V} \; \mathbf{a}_J]^T$ is the unknown state vector at the current iteration $(r + 1)$ and $\delta \mathbf{X}$ is its incremental value. $\dot{\mathbf{X}}^r$ denotes the time derivative of the state vector at iteration r and $\delta \dot{\mathbf{X}}$ is the time derivative of the incremental state vector. Linearizing Eqs. (4.69)-(4.72) and Eqs. (4.76)-(4.78) and rearranging gives

$$
\begin{pmatrix}
\mathbf{K}_{11} & \mathbf{K}_{12} & \mathbf{K}_{13} & 0 & 0 & 0 & 0 \\
0 & \mathbf{K}_{22} & \mathbf{K}_{23} & \mathbf{K}_{24} & \mathbf{K}_{25} & 0 & \mathbf{K}_{27} \\
0 & \mathbf{K}_{32} & \mathbf{K}_{33} & \mathbf{K}_{34} & 0 & 0 & 0 \\
0 & \mathbf{K}_{42} & \mathbf{K}_{43} & \mathbf{K}_{44} & \mathbf{K}_{45} & \mathbf{K}_{46} & \mathbf{K}_{47} \\
0 & \mathbf{K}_{52} & \mathbf{K}_{53} & \mathbf{K}_{54} & \mathbf{K}_{55} & 0 & 0 \\
0 & \mathbf{K}_{62} & \mathbf{K}_{63} & \mathbf{K}_{64} & \mathbf{K}_{65} & 0 & 0 \\
0 & \mathbf{K}_{72} & \mathbf{K}_{73} & \mathbf{K}_{74} & \mathbf{K}_{75} & \mathbf{K}_{76} & \mathbf{K}_{77}
\end{pmatrix}
\begin{Bmatrix}
\delta\bar{\mathbf{u}} \\
\delta\bar{\mathbf{P}}_{gm} \\
\delta\bar{\mathbf{S}}_{wm} \\
\delta\bar{\mathbf{P}}_{gf} \\
\delta\bar{\mathbf{S}}_{wf} \\
\delta\mathbf{a}_J \\
\delta\bar{\mathbf{V}}
\end{Bmatrix}
$$

$$
+
\begin{pmatrix}
0 & 0 & 0 & 0 & 0 & 0 & 0 \\
\mathbf{C}_{21} & \mathbf{C}_{22} & \mathbf{C}_{23} & 0 & 0 & 0 & 0 \\
\mathbf{C}_{31} & \mathbf{C}_{32} & \mathbf{C}_{33} & 0 & 0 & 0 & 0 \\
0 & 0 & 0 & \mathbf{C}_{44} & \mathbf{C}_{45} & \mathbf{C}_{46} & 0 \\
0 & 0 & 0 & \mathbf{C}_{54} & \mathbf{C}_{55} & \mathbf{C}_{56} & 0 \\
0 & 0 & 0 & \mathbf{C}_{64} & \mathbf{C}_{65} & \mathbf{C}_{66} & 0 \\
0 & 0 & 0 & 0 & 0 & 0 & 0
\end{pmatrix}
\begin{Bmatrix}
\delta\dot{\mathbf{u}} \\
\delta\dot{\mathbf{P}}_{gm} \\
\delta\dot{\mathbf{S}}_{wm} \\
\delta\dot{\mathbf{P}}_{gf} \\
\delta\dot{\mathbf{S}}_{wf} \\
\delta\dot{\mathbf{a}}_J \\
\delta\dot{\mathbf{V}}
\end{Bmatrix}
\tag{4.82}
$$

$$
=
\begin{Bmatrix}
\mathbf{f}_1 \\
\mathbf{f}_2 \\
\mathbf{f}_3 \\
\mathbf{f}_4 \\
\mathbf{f}_5 \\
\mathbf{f}_6 \\
\mathbf{f}_7
\end{Bmatrix}
-
\begin{pmatrix}
\mathbf{K}_{11}^0 & \mathbf{K}_{12}^0 & \mathbf{K}_{13}^0 & 0 & 0 & 0 & 0 \\
0 & \mathbf{K}_{22}^0 & \mathbf{K}_{23}^0 & \mathbf{K}_{24}^0 & 0 & 0 & \mathbf{K}_{27}^0 \\
0 & \mathbf{K}_{32}^0 & 0 & \mathbf{K}_{34}^0 & 0 & 0 & 0 \\
0 & \mathbf{K}_{42}^0 & 0 & \mathbf{K}_{44}^0 & \mathbf{K}_{45}^0 & \mathbf{K}_{46}^0 & \mathbf{K}_{47}^0 \\
0 & \mathbf{K}_{52}^0 & 0 & \mathbf{K}_{54}^0 & 0 & 0 & 0 \\
0 & \mathbf{K}_{62}^0 & 0 & \mathbf{K}_{64}^0 & 0 & 0 & 0 \\
0 & \mathbf{K}_{72}^0 & \mathbf{K}_{73}^0 & \mathbf{K}_{74}^0 & \mathbf{K}_{75}^0 & \mathbf{K}_{76}^0 & \mathbf{K}_{77}^0
\end{pmatrix}
\begin{Bmatrix}
\bar{\mathbf{u}}^r \\
\bar{\mathbf{P}}_{gm}^r \\
\bar{\mathbf{S}}_{wm}^r \\
\bar{\mathbf{P}}_{gf}^r \\
\bar{\mathbf{S}}_{wf}^r \\
\mathbf{a}_J^r \\
\bar{\mathbf{V}}^r
\end{Bmatrix}
$$

$$
+
\begin{pmatrix}
0 & 0 & 0 & 0 & 0 & 0 & 0 \\
\mathbf{C}_{21}^0 & \mathbf{C}_{22}^0 & \mathbf{C}_{23}^0 & 0 & 0 & 0 & 0 \\
\mathbf{C}_{31}^0 & \mathbf{C}_{32}^0 & \mathbf{C}_{33}^0 & 0 & 0 & 0 & 0 \\
0 & 0 & 0 & \mathbf{C}_{44}^0 & \mathbf{C}_{45}^0 & \mathbf{C}_{46}^0 & 0 \\
0 & 0 & 0 & \mathbf{C}_{54}^0 & \mathbf{C}_{55}^0 & \mathbf{C}_{56}^0 & 0 \\
0 & 0 & 0 & \mathbf{C}_{64}^0 & \mathbf{C}_{65}^0 & \mathbf{C}_{66}^0 & 0 \\
0 & 0 & 0 & 0 & 0 & 0 & 0
\end{pmatrix}
\begin{Bmatrix}
\dot{\mathbf{u}}^r \\
\dot{\mathbf{P}}_{gm}^r \\
\dot{\mathbf{S}}_{wm}^r \\
\dot{\mathbf{P}}_{gf}^r \\
\dot{\mathbf{S}}_{wf}^r \\
\dot{\mathbf{a}}_J^r \\
\dot{\mathbf{V}}_f^r
\end{Bmatrix}
$$

where

$$
\mathbf{K}_{11} = \mathbf{K}_{11}^0 = -\int_{\Omega_m} \mathbf{B}^T \mathbf{D} \mathbf{B} \, d\Omega \tag{4.83}
$$

$$
\mathbf{K}_{12} = \mathbf{K}_{12}^0 = \int_{\Omega_m} \mathbf{B}^T \mathbf{m}^T \alpha \mathbf{N} d\Omega \tag{4.84}
$$

$$
\mathbf{K}_{13} = -\int_{\Omega_m} \mathbf{B}^T \mathbf{m}^T \alpha \, P_{cm}^r \mathbf{N} d\Omega - \int_{\Omega_m} \mathbf{B}^T \mathbf{m}^T \alpha \frac{dP_{cm}}{dS_{wm}} \mathbf{S}_{wm}^r \mathbf{N} d\Omega
$$
$$
+ \int_{\Omega_m} \mathbf{N}^T \frac{\partial\bar{\rho}}{\partial S_{wm}} \mathbf{Ng} \, d\Omega \tag{4.85}
$$

$$
\mathbf{K}_{13}^0 = -\int_{\Omega_m} \mathbf{B}^T \mathbf{m}^T \alpha \, P_{cm}^r \mathbf{N} \, d\Omega \tag{4.86}
$$

$$\mathbf{K}_{22} = \mathbf{K}_{22}^0 = \int_{\Omega_m} (\nabla\mathbf{N})^T \mathbf{c}_1 \nabla\mathbf{N} d\Omega_m + \int_{\Omega_m} \mathbf{N}^T a_1 \mathbf{N} \ d\Omega_m \tag{4.87}$$

$$\mathbf{K}_{23} = \int_{\Omega_m} (\nabla\mathbf{N})^T \frac{\partial \mathbf{c}_1}{\partial S_{wm}} \bar{\mathbf{P}}_{gm}^r \nabla\mathbf{N}\mathbf{N} d\Omega_m + \int_{\Omega_m} (\nabla\mathbf{N})^T \mathbf{c}_2 \nabla\mathbf{N} d\Omega_m$$

$$+ \int_{\Omega_m} (\nabla\mathbf{N})^T \frac{\partial \mathbf{c}_2}{\partial S_{wm}} \bar{\mathbf{S}}_{wm}^r \nabla\mathbf{N}\mathbf{N} d\Omega_m + \int_{\Omega_m} (\nabla\mathbf{N})^T \frac{\partial \mathbf{c}_3}{\partial S_{wm}} \bar{\mathbf{V}}_m^r \nabla\mathbf{N}\mathbf{N} \ d\Omega_m$$

$$- \int_{\Omega_m} (\nabla\mathbf{N})^T \frac{\partial \mathbf{G}_1}{\partial S_{wm}} \mathbf{N} d\Omega_m + \int_{\Omega_m} \mathbf{N}^T \frac{\partial a_1}{\partial S_{wm}} \bar{\mathbf{P}}_{gm}^r \mathbf{N} \mathbf{N} \ d\Omega_m$$

$$+ \int_{\Omega_m} \mathbf{N}^T \frac{\partial a_2}{\partial S_{wm}} \bar{\mathbf{P}}_{gf}^r \mathbf{N} \mathbf{N} \ d\Omega_m + \int_{\Omega_m} \mathbf{N}^T \frac{\partial f_1}{\partial S_{wm}} \mathbf{N} d\Omega_m$$

$$\tag{4.88}$$

$$\mathbf{K}_{23}^0 = \int_{\Omega_m} (\nabla\mathbf{N})^T \mathbf{c}_2 \nabla\mathbf{N} d\Omega \tag{4.89}$$

$$\mathbf{K}_{24} = \mathbf{K}_{24}^0 = \int_{\Omega_m} \mathbf{N}^T a_2 \mathbf{N} \ d\Omega \tag{4.90}$$

$$\mathbf{K}_{25} = \int_{\Omega_m} \mathbf{N}^T \frac{\partial f_1}{\partial S_{wf}} \mathbf{N} d\Omega \tag{4.91}$$

$$\mathbf{K}_{27} = \mathbf{K}_{27}^0 = \int_{\Omega_m} (\nabla\mathbf{N})^T \mathbf{c}_3 \nabla\mathbf{N} \ d\Omega \tag{4.92}$$

$$\mathbf{K}_{32} = \mathbf{K}_{32}^0 = \int_{\Omega_m} (\nabla\mathbf{N})^T \mathbf{c}_4 \nabla\mathbf{N} d\Omega + \int_{\Omega_m} \mathbf{N}^T a_3 \mathbf{N} \ d\Omega \tag{4.93}$$

$$\mathbf{K}_{33} = \int_{\Omega_m} (\nabla\mathbf{N})^T \frac{\partial \mathbf{c}_4}{\partial S_{wm}} \bar{\mathbf{P}}_{gm}^r \nabla\mathbf{N}\mathbf{N} d\Omega - \int_{\Omega_m} (\nabla\mathbf{N})^T \frac{\partial \mathbf{G}_2}{\partial S_{wm}} \mathbf{N} d\Omega$$

$$+ \int_{\Omega_m} \mathbf{N}^T \frac{\partial a_3}{\partial S_{wm}} \bar{\mathbf{P}}_{gm}^r \mathbf{N} \mathbf{N} \ d\Omega + \int_{\Omega_m} \mathbf{N}^T \frac{\partial a_4}{\partial S_{wm}} \bar{\mathbf{P}}_{gf}^r \mathbf{N}\mathbf{N} \ d\Omega$$

$$\tag{4.94}$$

$$\mathbf{K}_{34} = \mathbf{K}_{34}^0 = \int_{\Omega_m} \mathbf{N}^T a_4 \mathbf{N} \ d\Omega \tag{4.95}$$

$$\mathbf{K}_{42} = \mathbf{K}_{42}^0 = \int_{\Omega_m} \mathbf{N}^T a_5 \mathbf{N} \ d\Omega \tag{4.96}$$

$$\mathbf{K}_{43} = \int_{\Omega_m} \mathbf{N}^T \frac{\partial a_5}{\partial S_{wm}} \bar{\mathbf{P}}_{gm}^r \mathbf{N}\mathbf{N} \ d\Omega + \int_{\Omega_m} \mathbf{N}^T \frac{\partial a_6}{\partial S_{wm}} \bar{\mathbf{P}}_{gf}^r \mathbf{N}\mathbf{N} \ d\Omega$$

$$+ \int_{\Omega_m} \mathbf{N}^T \frac{\partial f_2}{\partial S_{wm}} \mathbf{N} \ d\Omega_m$$

$$\tag{4.97}$$

$$\mathbf{K}_{44} = \mathbf{K}_{44}^0 = \int_{\Omega_m} \mathbf{N}^T a_6 \mathbf{N} \ d\Omega + \int_{\Omega_f} (\nabla\mathbf{N})^T \mathbf{c}_5 \nabla\mathbf{N} d\Omega \tag{4.98}$$

127

$$\mathbf{K}_{45} = \int_{\Omega_f} (\nabla\mathbf{N})^T \frac{\partial \mathbf{c}_5}{\partial S_{wf}} \bar{\mathbf{P}}_{gf}^r \nabla\mathbf{N}\mathbf{N}d\Omega + \int_{\Omega_f} (\nabla\mathbf{N})^T \mathbf{c}_6 \nabla\mathbf{N}d\Omega$$

$$+ \int_{\Omega_f} (\nabla\mathbf{N})^T \frac{\partial \mathbf{c}_6}{\partial S_{wf}} \bar{\mathbf{S}}_{wf}^r \nabla\mathbf{N}\mathbf{N}d\Omega + \int_{\Omega_m} \mathbf{N}^T \frac{\partial f_2}{\partial S_{wf}}\mathbf{N} \, d\Omega_m$$

$$+ \int_{\Omega_f^+} (\nabla\mathbf{N})^T \frac{\partial \mathbf{c}_6}{\partial S_{wf}} \bar{\mathbf{a}}_J^r \nabla\mathbf{N}^*\mathbf{N} \, d\Omega + \int_{\Omega_f} (\nabla\mathbf{N})^T \frac{\partial \mathbf{c}_7}{\partial S_{wf}} \bar{\mathbf{V}}_f^r \nabla\mathbf{N}\mathbf{N} \, d\Omega \tag{4.99}$$

$$- \int_{\Omega_f} (\nabla\mathbf{N})^T \frac{\partial \mathbf{G}_3}{\partial S_{wf}}\mathbf{N}d\Omega$$

$$\mathbf{K}_{45}^0 = \int_{\Omega_f} (\nabla\mathbf{N})^T \mathbf{c}_6 \nabla\mathbf{N}d\Omega \tag{4.100}$$

$$\mathbf{K}_{46} = \mathbf{K}_{46}^0 = \int_{\Omega_f^+} (\nabla\mathbf{N})^T \mathbf{c}_6 \nabla\mathbf{N}^* \, d\Omega \tag{4.101}$$

$$\mathbf{K}_{47} = \mathbf{K}_{47}^0 = \int_{\Omega_f} (\nabla\mathbf{N})^T \mathbf{c}_7 \nabla\mathbf{N} \, d\Omega \tag{4.102}$$

$$\mathbf{K}_{52} = \mathbf{K}_{52}^0 = \int_{\Omega_m} \mathbf{N}^T a_7 \mathbf{N} \, d\Omega \tag{4.103}$$

$$\mathbf{K}_{53} = \int_{\Omega_m} \mathbf{N}^T \frac{\partial a_7}{\partial S_{wm}} \bar{\mathbf{P}}_{gm}^r \mathbf{N}\mathbf{N} \, d\Omega + \int_{\Omega_f} \mathbf{N}^T \frac{\partial a_8}{\partial S_{wm}} \bar{\mathbf{P}}_{gf}^r \mathbf{N}\, \mathbf{N} \, d\Omega \tag{4.104}$$

$$\mathbf{K}_{55} = \int_{\Omega_f} (\nabla\mathbf{N})^T \frac{\partial \mathbf{c}_8}{\partial S_{wf}} \bar{\mathbf{P}}_{gf}^r \nabla\mathbf{N}\mathbf{N}d\Omega - \int_{\Omega_f} (\nabla\mathbf{N})^T \frac{\partial \mathbf{G}_4}{\partial S_{wf}}\mathbf{N}d\Omega \tag{4.105}$$

$$\mathbf{K}_{62} = \mathbf{K}_{62}^0 = \int_{\Omega_m} \mathbf{N}^{*T} a_7 \mathbf{N}d\Omega \tag{4.106}$$

$$\mathbf{K}_{63} = \int_{\Omega_m} \mathbf{N}^{*T} \frac{\partial a_7}{\partial S_{wm}} \bar{\mathbf{P}}_{gm}^r \mathbf{N}\, \mathbf{N} \, d\Omega + \int_{\Omega_f} \mathbf{N}^{*T} \frac{\partial a_8}{\partial S_{wm}} \bar{\mathbf{P}}_{gf}^r \mathbf{N}\, \mathbf{N} \, d\Omega \tag{4.107}$$

$$\mathbf{K}_{64} = \mathbf{K}_{64}^0 = \int_{\Omega_f^+} (\nabla\mathbf{N}^*)^T \mathbf{c}_8 \nabla\mathbf{N} \, d\Omega + \int_{\Omega_f} \mathbf{N}^{*T} a_8 \, \mathbf{N} \, d\Omega \tag{4.108}$$

$$\mathbf{K}_{65} = \int_{\Omega_f^+} (\nabla\mathbf{N}^*)^T \frac{\partial \mathbf{c}_8}{\partial S_{wf}} \bar{\mathbf{P}}_{gf}^r \nabla\mathbf{N}\mathbf{N}d\Omega - \int_{\Omega_f^+} (\nabla\mathbf{N}^*)^T \frac{\partial \mathbf{G}_4}{\partial S_{wf}}\mathbf{N}d\Omega \tag{4.109}$$

$$\mathbf{K}_{72} = \mathbf{K}_{72}^0 = \int_{\Omega} (\nabla\mathbf{N})^T \mathbf{c}_9 \nabla\mathbf{N}d\Omega \tag{4.110}$$

$$\mathbf{K}_{73} = \int_{\Omega} (\nabla\mathbf{N})^T \frac{\partial \mathbf{c}_9}{\partial S_{wm}} \bar{\mathbf{P}}_{gm}^r \nabla\mathbf{N}\mathbf{N}d\Omega + \int_{\Omega} (\nabla\mathbf{N})^T \mathbf{c}_{10} \nabla\mathbf{N}d\Omega$$

$$+ \int_{\Omega} (\nabla\mathbf{N})^T \frac{\partial \mathbf{c}_{10}}{\partial S_{wm}} \bar{\mathbf{S}}_{wm}^r \nabla\mathbf{N}\mathbf{N}d\Omega_m + \int_{\Omega} (\nabla\mathbf{N})^T \frac{\partial \mathbf{c}_{13}}{\partial S_{wm}} \bar{\mathbf{V}}^r \nabla\mathbf{N}\mathbf{N}d\Omega \tag{4.111}$$

$$- \int_{\Omega} (\nabla\mathbf{N})^T \frac{\partial \mathbf{G}_5}{\partial S_{wm}}\mathbf{N}d\Omega$$

$$\mathbf{K}_{73}^0 = \int_\Omega (\nabla \mathbf{N})^T \mathbf{c}_{10} \nabla \mathbf{N} d\Omega \tag{4.112}$$

$$\mathbf{K}_{74} = \mathbf{K}_{74}^0 = \int_\Omega (\nabla \mathbf{N})^T \mathbf{c}_{11} \nabla \mathbf{N} \delta d\Omega \tag{4.113}$$

$$\begin{aligned}
\mathbf{K}_{75} &= \int_\Omega (\nabla \mathbf{N})^T \frac{\partial \mathbf{c}_{11}}{\partial S_{wf}} \bar{\mathbf{P}}_{gf}^r \nabla \mathbf{N} \mathbf{N} d\Omega + \int_\Omega (\nabla \mathbf{N})^T \mathbf{c}_{12} \nabla \mathbf{N} d\Omega \\
&+ \int_\Omega (\nabla \mathbf{N})^T \frac{\partial \mathbf{c}_{12}}{\partial S_{wf}} \bar{\mathbf{S}}_{wf}^r \nabla \mathbf{N} \mathbf{N} d\Omega + \int_{\Omega_f^+} (\nabla \mathbf{N})^T \frac{\partial \mathbf{c}_{12}}{\partial S_{wf}} \bar{\mathbf{a}}_J^r \nabla \mathbf{N}^* \mathbf{N} d\Omega \\
&+ \int_\Omega (\nabla \mathbf{N})^T \frac{\partial c_{13}}{\partial S_{wf}} \bar{\mathbf{V}}_f^r \nabla \mathbf{N} \mathbf{N} d\Omega - \int_{\Omega_f} (\nabla \mathbf{N})^T \frac{\partial \mathbf{G}_5}{\partial S_{wf}} \mathbf{N} d\Omega
\end{aligned} \tag{4.114}$$

$$\mathbf{K}_{75}^0 = \int_\Omega (\nabla \mathbf{N})^T \mathbf{c}_{12} \nabla \mathbf{N} d\Omega \tag{4.115}$$

$$\mathbf{K}_{76} = \mathbf{K}_{76}^0 = \int_{\Omega_f^+} (\nabla \mathbf{N})^T \mathbf{c}_{12} \nabla \mathbf{N}^* d\Omega \tag{4.116}$$

$$\mathbf{K}_{77} = \mathbf{K}_{77}^0 = \int_\Omega (\nabla \mathbf{N})^T \mathbf{c}_{13} \nabla \mathbf{N} d\Omega \tag{4.117}$$

$$\mathbf{C}_{21} = \mathbf{C}_{21}^0 = \int_{\Omega_m} \mathbf{N}^T d_3^r \mathbf{m}^T \mathbf{B} d\Omega \tag{4.118}$$

$$\mathbf{C}_{22} = \mathbf{C}_{22}^0 = \int_{\Omega_m} \mathbf{N}^T d_1^r \mathbf{N} d\Omega \tag{4.119}$$

$$\mathbf{C}_{23} = \mathbf{C}_{23}^0 = \int_{\Omega_m} \mathbf{N}^T d_2 \mathbf{N} d\Omega \tag{4.120}$$

$$\mathbf{C}_{31} = \mathbf{C}_{31}^0 = \int_{\Omega_m} \mathbf{N}^T \mathbf{N}^T d_6 \, \mathbf{m}^T \mathbf{B} \, d\Omega \tag{4.121}$$

$$\mathbf{C}_{32} = \mathbf{C}_{32}^0 = \int_{\Omega_m} \mathbf{N}^T d_4 \mathbf{N} \, d\Omega \tag{4.122}$$

$$\mathbf{C}_{33} = \mathbf{C}_{33}^0 = \int_{\Omega_m} \mathbf{N}^T d_5 \mathbf{N} \, d\Omega \tag{4.123}$$

$$\mathbf{C}_{44} = \mathbf{C}_{44}^0 = \int_{\Omega_f} \mathbf{N}^T d_7 \mathbf{N} \, d\Omega \tag{4.124}$$

$$\mathbf{C}_{45} = \mathbf{C}_{45}^0 = \int_{\Omega_f} \mathbf{N}^T d_8 \mathbf{N} \, d\Omega \tag{4.125}$$

$$\mathbf{C}_{46} = \mathbf{C}_{46}^0 = \int_{\Omega_f^+} \mathbf{N}^T d_8 \mathbf{N}^* d\Omega \tag{4.126}$$

$$\mathbf{C}_{54} = \mathbf{C}_{54}^0 = \int_{\Omega_f} \mathbf{N}^T d_9 \mathbf{N} d\Omega \tag{4.127}$$

$$\mathbf{C}_{55} = \mathbf{C}_{55}^0 = \int_{\Omega_f} \mathbf{N}^T d_{10} \mathbf{N} d\Omega \tag{4.128}$$

$$\mathbf{C}_{56} = \mathbf{C}_{56}^0 = \int_{\Omega_f^+} \mathbf{N}^T d_{10} \mathbf{N}^* d\Omega \tag{4.129}$$

$$\mathbf{C}_{64} = \mathbf{C}_{64}^0 = \int_{\Omega_f^+} \mathbf{N}^{*T} d_9 \mathbf{N} \, d\Omega \tag{4.130}$$

$$\mathbf{C}_{65} = \mathbf{C}_{65}^0 = \int_{\Omega_f^+} \mathbf{N}^{*T} d_{10} \mathbf{N} \, d\Omega \tag{4.131}$$

$$\mathbf{C}_{66} = \mathbf{C}_{66}^0 = \int_{\Omega_f^+} \mathbf{N}^{*T} d_{10} \, \mathbf{N}^* d\Omega \tag{4.132}$$

$$\mathbf{f}_1 = -\int_{\Omega_m} \mathbf{N}^T \rho^r \mathbf{g} \, d\Omega - \int_{\Gamma_u^q} \mathbf{N}^T \bar{\mathbf{t}} \, d\Gamma \tag{4.133}$$

$$\mathbf{f}_2 = \int_{\Omega_m} (\nabla \mathbf{N})^T \mathbf{G}_1 d\Omega - \int_{\Omega_m} \mathbf{N}^T f_1 \, d\Omega \tag{4.134}$$

$$\mathbf{f}_3 = \int_{\Omega_m} (\nabla \mathbf{N})^T \mathbf{G}_2 d\Omega \tag{4.135}$$

$$\mathbf{f}_4 = \int_{\Omega_f} (\nabla \mathbf{N})^T \mathbf{G}_3 d\Omega - \int_{\Omega_m} \mathbf{N}^T f_2 \, d\Omega - \int_{\Gamma_{wf}^q} \mathbf{N}^T q_w \, d\Gamma \tag{4.136}$$

$$\mathbf{f}_5 = \int_{\Omega_f} (\nabla \mathbf{N})^T \mathbf{G}_4 d\Omega - \int_{\Gamma_{gf}^q} \mathbf{N}^T q_g \, d\Gamma \tag{4.137}$$

$$\mathbf{f}_6 = \int_{\Omega_f^+} (\nabla \mathbf{N}^*)^T \mathbf{G}_4 d\Omega \tag{4.138}$$

$$\mathbf{f}_7 = \int_{\Omega_f} (\nabla \mathbf{N})^T \mathbf{G}_5 d\Omega \tag{4.139}$$

Eq. (4.82) is a semi-discrete system of equations that can be written in a concise form as

$$\mathbf{C}\frac{d\mathbf{X}}{dt} + \mathbf{K}\mathbf{X} = \mathbf{F} \tag{4.140}$$

Using the θ finite difference scheme in time, the state variable vector and the force vector can be defined as

$$\mathbf{X} = \theta \mathbf{X}_{n+1} + (1-\theta)\mathbf{X}_n$$
$$\mathbf{F} = \theta \mathbf{F}_{n+1} + (1-\theta)\mathbf{F}_n \tag{4.141}$$

in which n is a time step, and $0 \leq \theta \leq 1$ is time integration parameter. Substituting Eq. (4.141) into Eq. (4.140) gives

$$(\mathbf{C} + \theta\Delta t\mathbf{K})\mathbf{X}_{n+1} = (\mathbf{C} - (1 - \theta)\Delta t\mathbf{K})\mathbf{X}_n + \theta\Delta t\mathbf{F}_{n+1} + (1 - \theta)\Delta t\mathbf{F}_n \quad (4.142)$$

The above finite element formulation together with the linearization procedure and the time discretization scheme are implemented in a C++ code. The system of equations is solved using a standard direct solver.

4.4 Numerical examples

In this section, numerical examples illustrating the capability of the proposed model to simulate coupled deformation, two-phase flow and electrokinetic flow problems in fractured domains are presented. As there are no analytical solutions for this kind of problems, the computational results are compared with those obtained with other numerical models. First, we modeled a case presented by Ghafouri and Lewis (1996) to model saturated flow in a deformable double porosity domain. Then the five-spot and the CO_2 leakage benchmark problems are simulated and discussed. Finally a coupled hydromechanical-electrokinetic problem is simulated.

4.4.1 Consolidation problem

In this example we discuss the computational accuracy of the proposed SG-XFEM-LS model and the effect of fracture spacing and permeability ratio between the porous matrix and the fractured zone on the pore pressure distribution and deformation.

A one-dimensional consolidation problem in a saturated linear poroelastic double porosity medium is considered. A plane strain soil column of height H is simulated. The domain is subjected to a load F at the top and fixed at the bottom. The top surface is open ($P_w = 0$), and the drainage occurs only through the fracture continuum. All other boundaries are close, Figure 4.1. The load is applied instantaneously at time $t = 0$, giving an initial pressure $P_0(z)$. The geometry and material parameters are given in Table 4.2. The finite element domain is discretized using a mesh size of 28 isoparametric 4-node quadrilateral elements. Varying time step sizes for different time intervals are utilized, see Table 4.3.

Analysis for different ratios of fracture permeability to matrix permeability (k_f/k_m), and for different fracture spacing were conducted. In all examples, the matrix permeability $k_m = 4 \times 10^{-9}m^2$ was constant. Figure 4.2 shows surface displacement for different combinations of k_f/k_m, including results obtained from Ghafouri and Lewis (1996) and analytical solution of a single porosity domain,

Table 4.2: Simulation parameters for the consolidation problem.

Parameter	Value	Unit
Domain height, H	7	m
Matrix permeability, k_m	4×10^{-9}	m^2
Fracture permeability, k_f	variable	m^2
Matrix Porosity, ϕ_m	0.1	
Fracture Porosity, ϕ_f	0.05	
Fracture spacing, d	0.1	m
Water viscosity, μ_w	1×10^{-3}	Pa.s
Water density, ρ_w	1000	kg/m^3
Biot's constant, α	1.0	
Young's modulus, E	6000.0	Pa
Poisson's ratio, ν	0.4	
Fluid bulk modulus, K_f	∞	
Load, F	1.0	kN

$k_f/k_m = 1$. Apparently, there is a good match between the results. As it can be seen, the consolidation is significantly affected by the permeability ratio: the higher permeability ratio, the faster consolidation occurs. Figure 4.3 compares the consolidation process for different fracture spacing. Fracture spacing of 0.1, 1.0 and 3.0 were simulated. As fracture spacing is small, the excess pore pressure dissipates rapidly, leading to faster consolidation.

Figure 4.4 shows the pore pressure variation with time in the porous matrix continuum (solid lines) and the fracture continuum (dashed lines), for different permeability ratios. As expected, in the fracture continuum, the dissipation of pore pressure is faster than in the matrix continuum. This amplifies as the permeability ratio increases.

Table 4.3: Time step sizes for different time intervals.

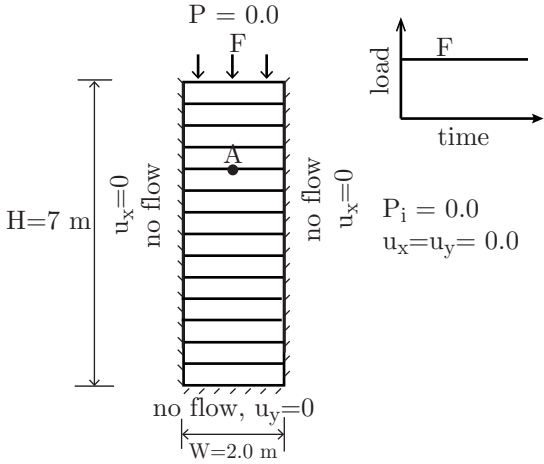| Time interval (s)	Number of time steps
1×10^{-2}	10
1×10^{-1}	10
1×10^{0}	10
1×10^{1}	10
1×10^{2}	10
1×10^{3}	10
1×10^{4}	10

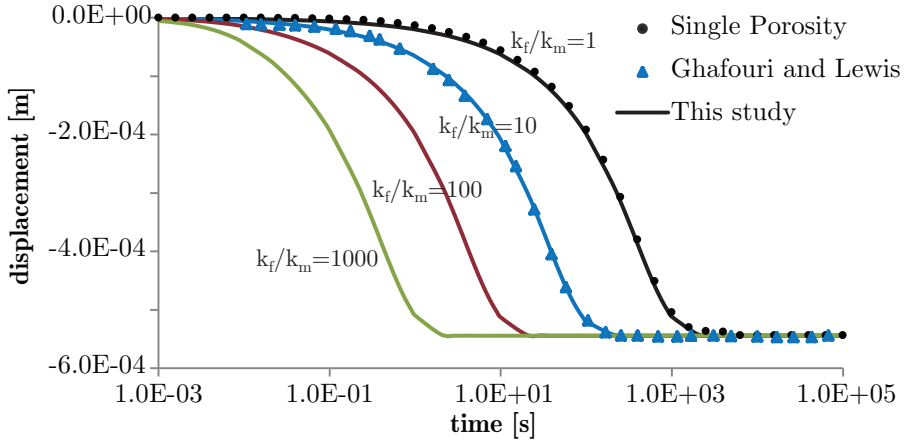Figure 4.1: Geometry and boundary conditions of the consolidation problem

Figure 4.2: Surface displacement for different permeability ratios
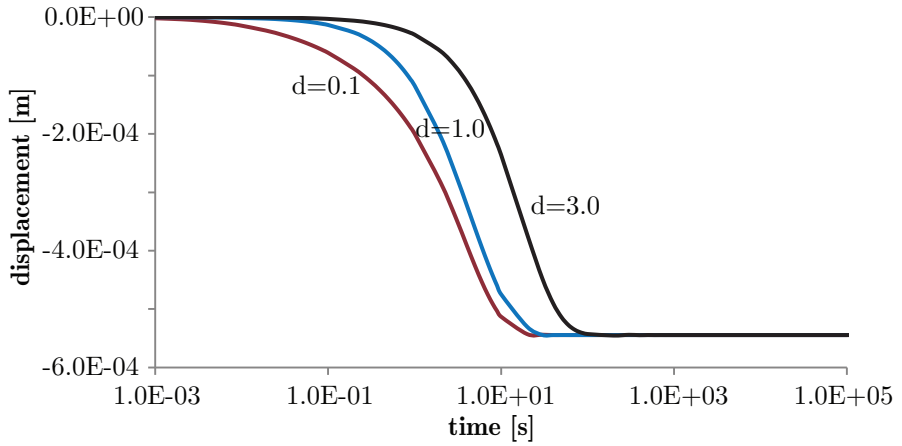

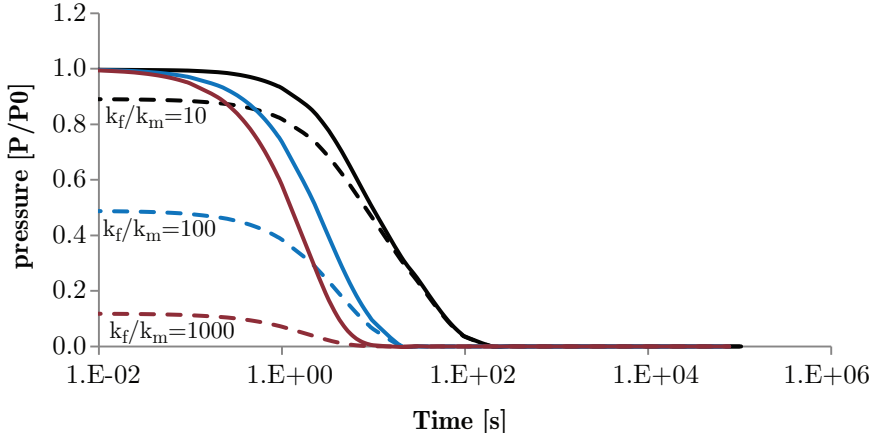Figure 4.3: Surface displacement for different fracture spacings

Figure 4.4: Matrix (solid) and fracture (dashed) pore pressure for different permeability ratios

4.4.2 Five-spot problem

In this example we discuss the computational efficiency of the proposed SG-XFEM-LS model and the effect of the capillary pressure on the fluid flow pattern.

The five-spot benchmark problem is utilized for this purpose. This problem addresses conceptual fluid flow in a reservoir filled by a non-wetting phase and displaced by a wetting phase with an injection well at the center and four production wells at the corners, Figure 4.5, (see also Helmig (1997)). Due to symmetry, a 2D plane square domain of length, $L = 100$ m, with injection and production wells at opposite corners of one of the diagonals is modeled.

Figure 4.5 shows the geometry and the boundary conditions, and Table 4.4 gives the involved geometrical and material parameters. The capillary pressure-saturation relationships for the porous matrix and the fracture continuum follow that of Brooks-Corey, Eq. (4.25). The relative permeability-saturation relationship for the fracture continuum is assumed linear, and for the porous matrix follows that of Brooks-Corey, Eqs. (4.26)-(4.27). The injected wetting phase fluid volume rate is equal to the non-wetting production volume rate.

The finite element domain is discretized using 4-node isoparametric quadrilateral elements with varying mesh sizes, shown in the first column of Table 4.5. Figure 4.6 shows the computed non-wetting phase saturation profiles in the porous matrix and the fracture continuum at different times. Obviously fluid flow in the fractured continuum is faster due to its higher permeability. This analysis is conducted using
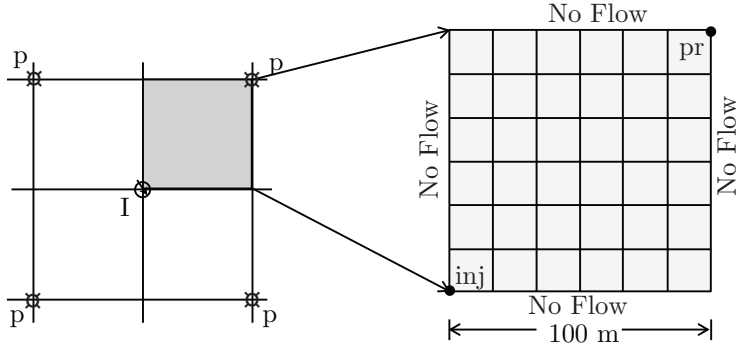
Figure 4.5: Domain and boundary conditions of the five-spot injection example
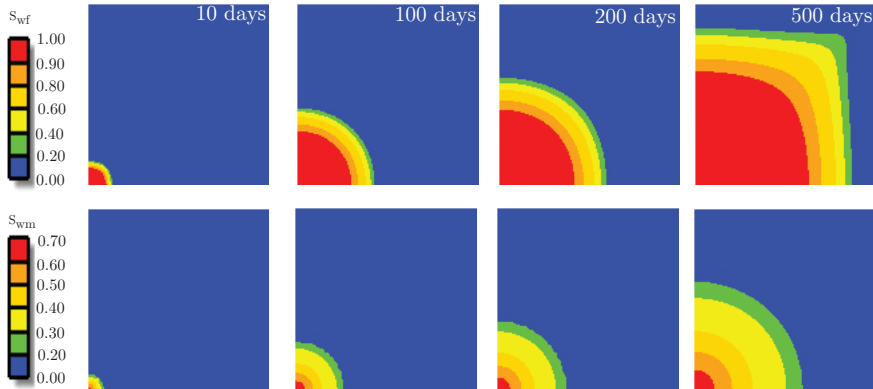
Figure 4.6: Fracture and matrix saturation contours at different times

a mesh size of 1225 elements.

Computational efficiency

To examine the computational efficiency of the proposed model, finite element analysis using meshes of different sizes are examined. Since there is no analytical solution to this problem, the accuracy is examined relative to a "converged" Galerkin solution using a very fine mesh of 1600 elements. This simulation resulted in a breakthrough time of 512.4 days for the wetting phase to reach to the production well. A threshold value of 0.01% was chosen.

Table 4.5 shows the breakthrough times calculated by the proposed SG-XFEM-LS model and the standard Galerkin finite element method for different mesh sizes.

Table 4.4: Simulation parameters of the five-spot problem.

Parameter	Value	Unit
Domain length, L	100	m
Matrix permeability, k_m	1×10^{-11}	m^2
Fracture permeability, k_f	2×10^{-10}	m^2
Matrix porosity, ϕ_m	0.25	
Fracture porosity, ϕ_f	0.15	
Fracture spacing, d	0.18	
Wetting phase viscosity, μ_w	1×10^{-3}	Pa.s
Non-wetting phase viscosity, $\mu_n w$	1×10^{-3}	Pa.s
Residual saturation in matrix, S_{wrm}	0.0	
Residual saturation in fracture, S_{wrf}	0.0	
Matrix Brooks and Corey parameter, λ_m	2.5	
Fracture Brooks and Corey parameter, λ_f	4.5	
matrix Entry pressure, P_{bm}	10000	Pa
Fracture Entry pressure, P_{bf}	50	Pa
Injection and production rate, q	1.3×10^{-5}	m$^2/s$

Table 4.5: Standard Galerkin model vs. SG-XFEM-LS model

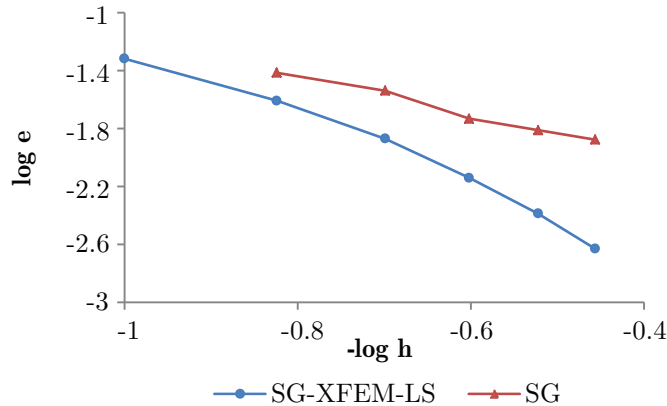| Element size (m)	Numbers of elements	Breakthrough time (Standard Galerkin)	Breakthrough time (SG-XFEM method)
10.0	10×10	not converged	537.0
6.67	15×15	532.1	525.0
5.0	20×20	527.2	519.3
4.0	25×25	521.9	516.1
3.33	30×30	520.3	514.5
2.86	35×35	519.2	513.4
2.5	40×40	512.4	—

Figure 4.7: Relative error in breakthrough time for different mesh sizes

Figure 4.7 shows the corresponding relative errors, calculated using the l^2-norm on the breakthrough times compared to a reference solution. The figure shows that the proposed model converges faster.

Capillary pressure effect

Appropriate description of transport parameters, such as relative permeability and capillary pressure, is essential for predicting the flow process in fractured porous media. Difference in the capillary pressure between the fractured zone and the porous matrix might have a substantial effect on the fluid flow in reservoirs (Firoozabadi, 2000). The most commonly used assumption for modeling fluid flow in fractured reservoirs is a linear relative permeability-saturation relationship with zero capillary pressure in the fractures (de la Porte et al., 2005). Romm and Blake (1972) found that the capillary pressure is zero in the aperture between two parallel glass plates, and the relative permeability and saturation were linearly dependent. In the contrary, Firoozabadi and Thomas (1990) utilizing different capillary pressure-saturation relationships, found that the capillary pressure in the fractures is non-zero and can have a significant effect on the non-wetting phase flow. Firoozabadi and Hauge (1990) proposed a capillary pressure-saturation relationship in the fracture continuum similar to that in the porous matrix continuum.

To study the effect of fracture capillary pressure on two phase flow in a fractured porous medium, this numerical example is re-conducted using different capillary pressure parameters. Figure 4.8 shows the saturation profile after 200 days of injection for low (left) and high (right) fracture capillary pressures. The figure clearly

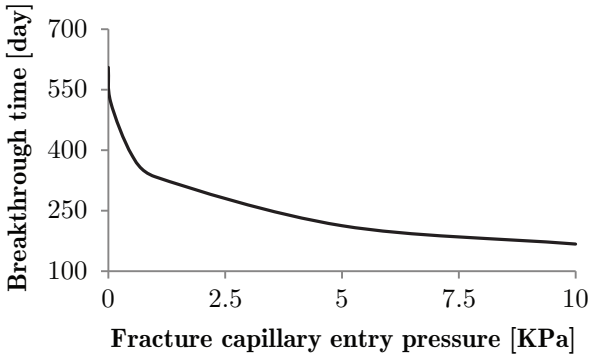Figure 4.8: Effect of fracture capillary pressure on CO_2 saturation contours

Figure 4.9: Breakthrough times for different capillary entry pressures

shows that for the low capillary pressure, the CO2 plume exhibits a relatively sharp front, while that of the high capillary pressure exhibits a smeared front.

Figure 4.9 shows the breakthrough times for different capillary entry pressures, Eq.(4.25). The Figure shows that by increasing the capillary pressure, the breakthrough time decreases. With a low entry pressure (low capillary pressure), the process is advection dominant, and there is a sharp saturation front. On the contrary, with a high entry pressure, the process is diffusive, and hence it takes less time for the injected fluid to reach to the production well. This phenomena is apparent in Figure 4.8, where it can be seen that the high capillary pressure case exhibits a wide spread saturation front.

4.4.3 CO_2 Leakage problem

In this example we utilize the SG–XFEM–LS model to compute CO_2 flow under its buoyancy in a deformable fractured reservoir. We simulate coupled hydromechanical processes in a likely leaky environment. For this, the CO_2 leakage benchmark problem introduced by (Ebigbo et al., 2007) is modeled.

The geometry consists of a CO_2 injection well, two aquifers, one aquitard and a leaky well, Figure 4.10. The lower aquifer is assumed fractured. The physical domain extends horizontally 1000 m, and the upper aquifer is located 2840 m below the ground surface. The thickness of the aquifers is 30 m each, and the aquitard is 100 m. The leaky well is located 100 m from the injection well.

This problem is modeled using a finite element mesh size of 1875, 4-node isoparametric quadrilateral elements. The simulation parameters are given in Table 4.6. Brooks and Corey relative permeability– saturation relationships are used for the porous matrix, and a linear relative permeability–saturation curve is used for the fractured zone.

Initially, the domain is fully saturated with brine water under a hydrostatic pressure condition. The no-flow condition is prescribed on the horizontal boundaries, and a constant hydrostatic pressure is imposed on the vertical boundaries. CO_2 is injected for 600 days and the analysis was conducted using a time step size of 0.1 day.

Figure 4.11 shows the computed CO_2 saturation profile at different time intervals for the porous matrix and the fractured zone. It can be seen that the CO_2 plume extends radially under buoyancy forces, and upon reaching the leakage well, rises to the upper aquifer.

Figure 4.12 shows the vertical displacement profile at the top of the aquitard vs. distance for different time intervals. As a result of CO_2 injection, the pore pressure

Table 4.6: Simulation parameters of the leakage problem

| Parameter	Value	Unit
Lateral dimension, L	1000	m
Aquifers thickness, w_1	30	m
Aquitard thickness, w_2	100	m
Distance between wells, d	100	m
Aquifers matrix permeability, k_{1m}	1.0×10^{-14}	m^2
Aquifers fracture permeability, k_{1f}	1.0×10^{-14}	m^2
Leaky well permeability, k_2	1×10^{-13}	m^2
matrix Porosity, ϕ_m	0.2	
fracture Porosity, ϕ_m	0.15	
Brine viscosity, μ_w	2.535×10^{-4}	Pa.s
CO$_2$ viscosity, μ_g	3.95×10^{-5}	Pa.s
Brine density, ρ_w	1045	kg/m^3
CO$_2$ density, ρ_g	479	kg/m^3
Injection rate, q_{inj}	1.04×10^{-4}	m^2/s
Residual water saturation, S_{wr}	0.0	
Residual CO$_2$ saturation, S_{gr}	0.0	
fracture spacing, d	3	m
Biot's constant, α	1.0	
Young's modulus, E	6.0	MPa
Poisson's ratio, ν	0.4	
Water bulk modulus, K_w	0.43×10^7	MPa
Bulk modulus of CO$_2$, K_g	0.1	MPa
Solid phase density, ρ_s	2400	kg/m^3
Bulk modulus of solid, K_s	0.14×10^4	MPa

Figure 4.10: CO$_2$ leakage problem.
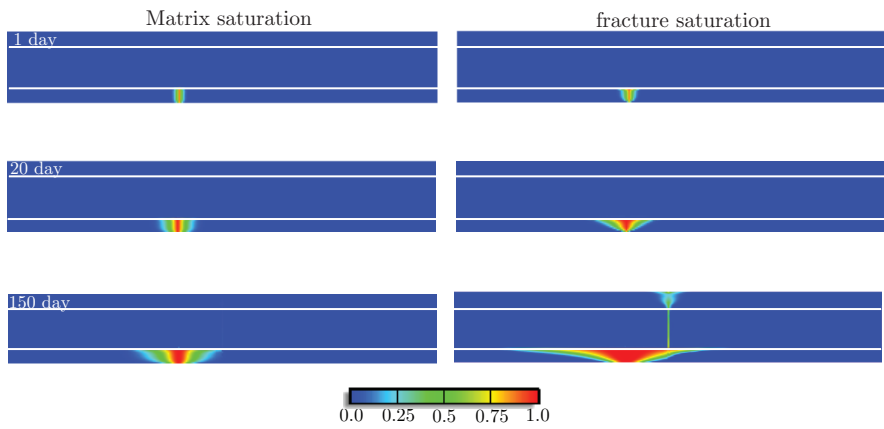
Figure 4.11: CO_2 saturation profiles in the porous matrix (left) and the fractured zone (right).
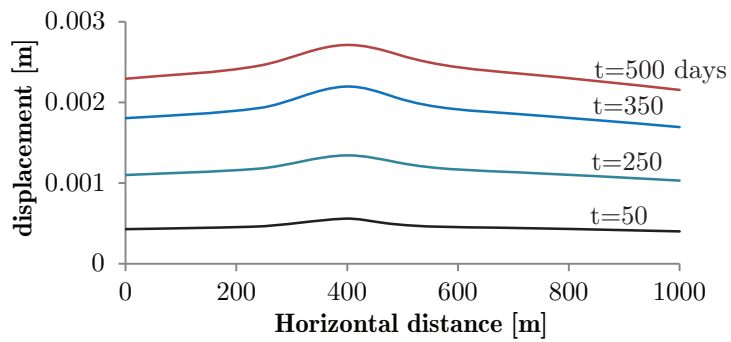

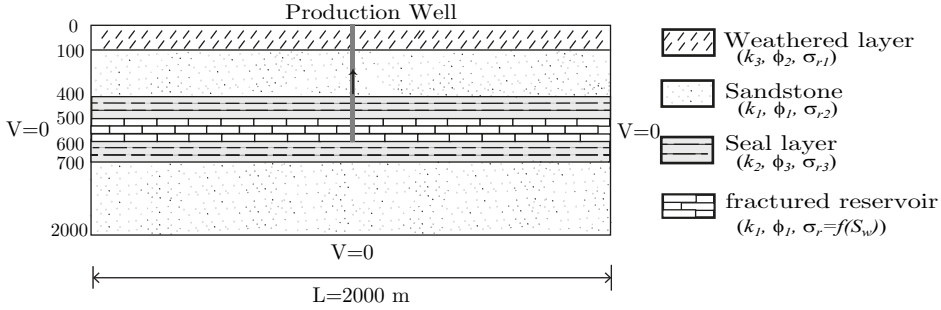Figure 4.12: Vertical displacement at the top of the aquitard.

Figure 4.13: Geometry of the electrokinetic simulation example.

increases near the injection well causing uplifting of the cap rock.

4.4.4 Front tracking of electrokinetic potential

In this example we illustrate the capability of the proposed model to simulate coupled hydromechanical–electrokinetic flow in fractured media. We study the effects of fracture spacing and salinity on the streaming potential. We also discuss several constitutive models describing the relative SP coupling coefficient, C_r.

Electrokinetic measurement has proven to be an efficient technique for monitoring fluid motion in underground formations in response to pumping or injection of fluids or contaminants. To gain insight into the physics of this phenomena, a numerical example simulating water encroachment during oil production, based on the work of Saunders et al. (2008), is examined. Saunders et al. (2008) original example is modified to include the effect of fractures on the electrokinetic flow.

A 2D reservoir domain, consisting of six layers is modeled (Figure 4.13). It consists of a 100 m fractured reservoir bounded by conductive, low permeability layers, representing reservoir seals. The seal layers are located between two highly permeable sandstone layers. At the top of the geometry, a highly resistive weathered layer exists. At the left boundary of the reservoir, a water aquifer exists. As oil is pumped out, the water in the aquifer expands and moves into the reservoir, displacing oil. The material and other simulation parameters are given in Table 4.7.

A large finite element domain (2000 m × 2000 m) is simulated to allow for setting zero potential at the boundaries, used as a reference for the electrokinetic measurements. No electrical potential flux is applied on the domain surface. The gravitational force is neglected.

The water is considered the wetting phase and the oil is the non-wetting phase.

Table 4.7: Simulation parameters of the electrokinetic simulation example.

Parameter	Value	Unit
Lateral dimension, L	2000	m
Reservoir thickness, w_1	100	m
Reservoir matrix permeability, k_{1m}	4.0×10^{-14}	m^2
Reservoir fracture permeability, k_{1f}	3.0×10^{-13}	m^2
Confining rock permeability, k_2	1×10^{-15}	m^2
Upper layer permeability, k_3	3.0×10^{-13}	m^2
Reservoir matrix porosity, ϕ_{1m}	0.25	
Reservoir fracture porosity, ϕ_{1f}	0.15	
Confining rock Porosity, ϕ_2	0.01	
Upper layer porosity, ϕ_3	0.3	
Upper layer conductivity, σ_{r1}	3.0×10^{-5}	Sm^{-1}
Sandstone conductivity, σ_{r2}	0.0097	Sm^{-1}
Confining rock conductivity, σ_{r3}	0.0135	Sm^{-1}
Brine viscosity, μ_w	1.0×10^{-3}	Pa.s
Oil viscosity, μ_o	1.0×10^{-3}	Pa.s
Oil density, ρ_o	900	kg/m^3
oil conductivity, σ_{nw}	1.0×10^{-5}	Sm^{-1}
Production rate, q	1.8×10^{-3}	kg/ms
Residual water saturation, S_{wr}	0.2	
Residual oil saturation, S_{nr}	0.2	
Fracture spacing, d	5	
Initial pressure, P_i	10.0	MPa

The phase's relative permeability–saturation relationships in the porous matrix are given by quadratic functions of the form:

$k_{rwm} = k'_{wm} S_{em}^2$

$k_{rom} = k'_{om} (1 - S_{em})^2$

where k'_{wm} and k'_{om} are the maximum relative permeability, equal to 0.3 and 0.8 respectively. For the fractured continuum, a linear relative permeability–saturation function is utilized.

As water encroaches towards the well, the water front in the fracture continuum is always ahead of that of the porous matrix. This entails having at each time interval two saturation fronts and two corresponding SP peaks. Figure 4.14 shows streaming potentials calculated along the center of the fractured reservoir, oriented parallel to the horizontal axis of the model and passing through the well, for different time intervals. The figure shows that at each time interval there are two SP peaks: a slow one in the porous matrix, and an advanced one in the fractured zone. At early time intervals (not shown in the figure), the SP peak in the fractured zone dominates, giving rise to effectively one peak.

Figure 4.15 and 4.16 show the corresponding water saturation fronts in the fractured zone and the porous matrix, respectively, calculated along the centerline of the reservoir. Comparing these figures to Figure 4.14, reveals that, for any specific time interval, the two streaming potential peaks coincide with their corresponding saturation fronts. This correspondence might be vital for using the electrokinetic potential for monitoring fluids displacement in fractured underground formations.

Fracture spacing effect

Figure 4.17 shows the effect of fracture spacing on the spatial distribution of SP. Three domains are examined: a single porosity, high fracture spacing and low fracture spacing. The figure shows that for the single porosity domain and the high fracture spacing domain, the SP exhibits a single peak, while for the low spacing fractures, SP exhibits clear double peaks. This exhibits the merit of the double porosity model which is capable of modeling a wide range of fractured formations. It shows clearly that for a highly fractured domain, two distinct saturation fronts, and thus SP fronts, can be identified.

Constitutive equations

As mentioned in Section section 4.2.4, in literature there are several models describing the relative SP coupling coefficient, C_r. For an unsaturated porous medium, the relative SP coupling coefficient is a function of a number of parameters, including the wettability of the rock and the distribution of fluids in the porous

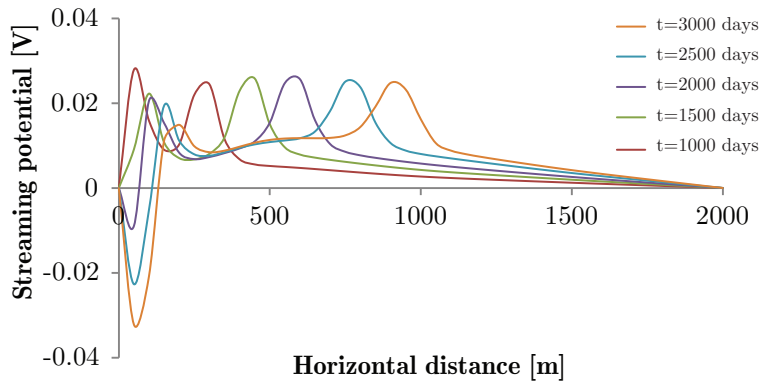Figure 4.14: Streaming potential along a section in the center of the reservoir at different time intervals.
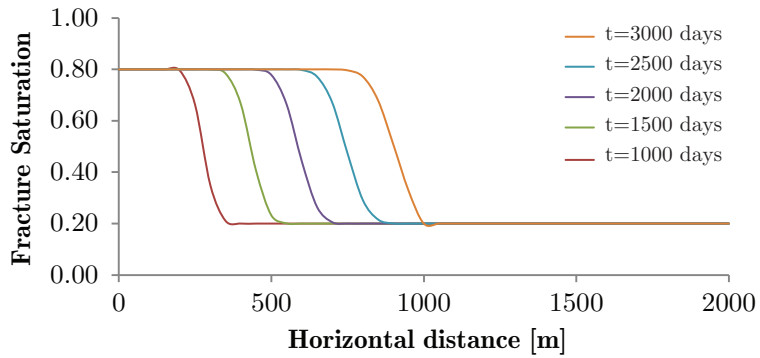

Figure 4.15: Water saturation profile in the fracture continuum along a section in the center of the reservoir.
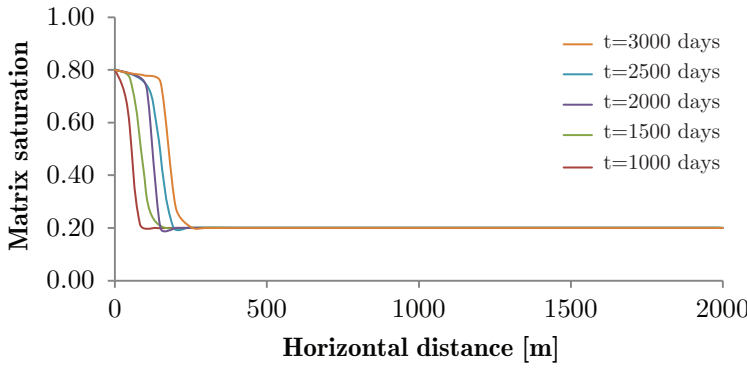
Figure 4.16: Water saturation profile in the matrix continuum along a section in the center of the reservoir.
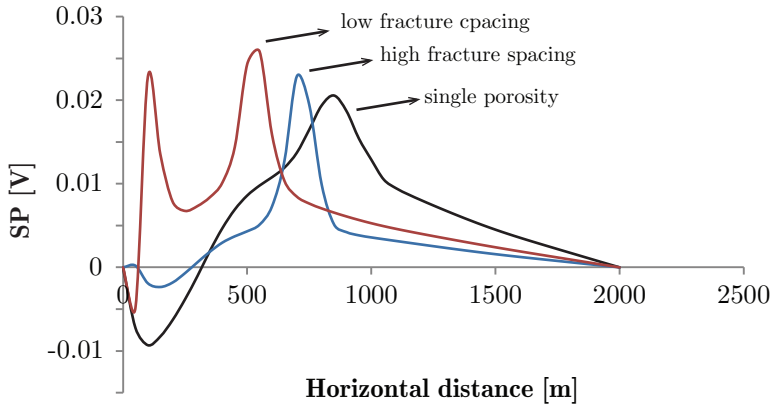

Figure 4.17: Streaming potential profile for different degrees of fracturing.

medium. Here, this numerical example is re-calculated using constitutive models presented in section 4.2.4.

Figure 4.18 shows the relationship between the relative coupling coefficient and water saturation for different models. Figure 4.19 shows the calculated cross coupling coefficient, L, and Figure 4.20 shows the streaming potential profiles, after 2500 days, obtained from these constitutive models. Apparently, the calculated streaming potentials due to different C_r are not very much different from each other, though Jackson's model shows some divergence.

Salinity effect

The salinity of the formation brine affects its electrical conductivity, and hence the electrokinetic coupling coefficient. Electrical conductivity increases with increasing brine salinity. Salinity also affects the zeta potential, permittivity and viscosity, see Eq. (4.29). The effect of salinity on permittivity and viscosity is ignored in this study. According to Worthington et al. (2002), salt concentration, C_f, is related to the brine electrical conductivity, σ_w by

$$\log(\sigma_w) = 9.42203 \times 10^{-1} + 8.88900 \times 10^{-1} [\log(C_f)]$$
$$-2.72398 \times 10^{-2} [\log(C_f)]^2 - 2.25682 \times 10^{-3} [\log(C_f)]^3 \qquad (4.143)$$
$$+1.46605 \times 10^{-5} [\log(C_f)]^4$$

Following Saunders et al. (2008), the salinity is related to the zeta potential by

$$\zeta = 16.175 \times \log(C_f) - 16.606 \qquad (4.144)$$

To study this effect, several numerical simulations were conducted for different salinity values. Figure 4.21 shows SP peak values vs. salinity. It shows that the maximum electrical potential at the saturation fronts decreases significantly as the salinity increases. This indicates that electrokinetic monitoring of fluid movement can give more accurate results in low salinity reservoirs, compared to high salinity ones.
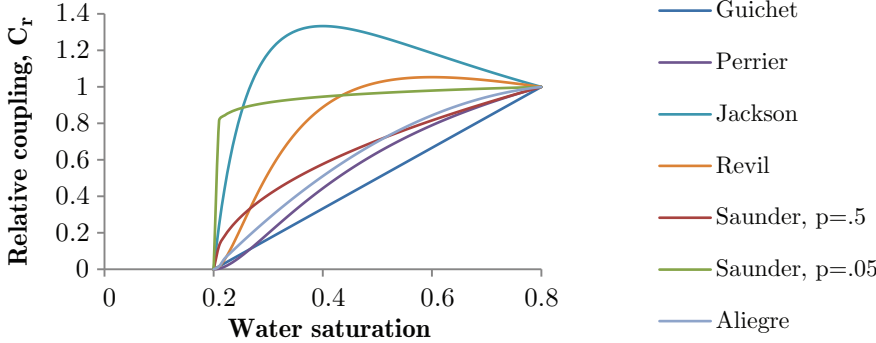
Figure 4.18: Relative coupling coefficient vs. water saturation for different models.
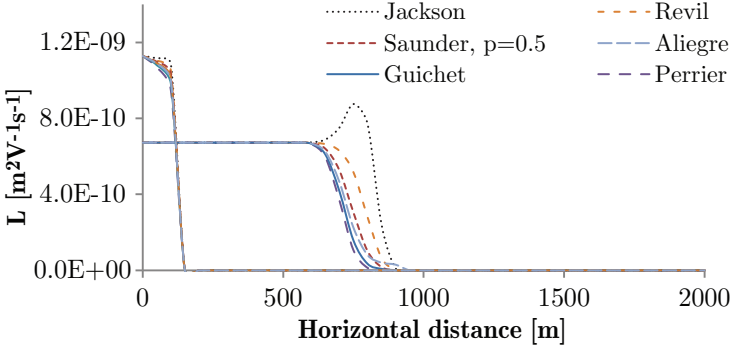

Figure 4.19: Cross coupling coefficient, L for different relative SP coupling models.
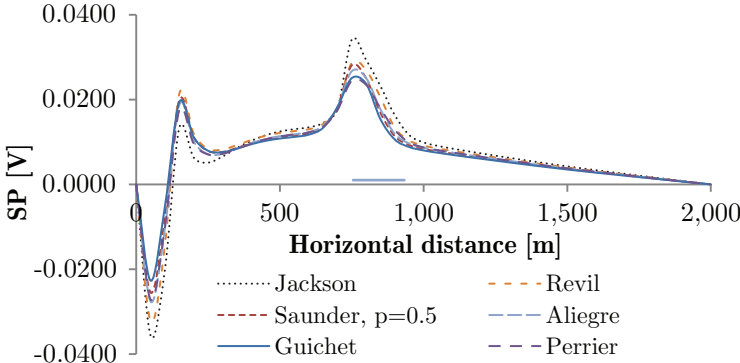

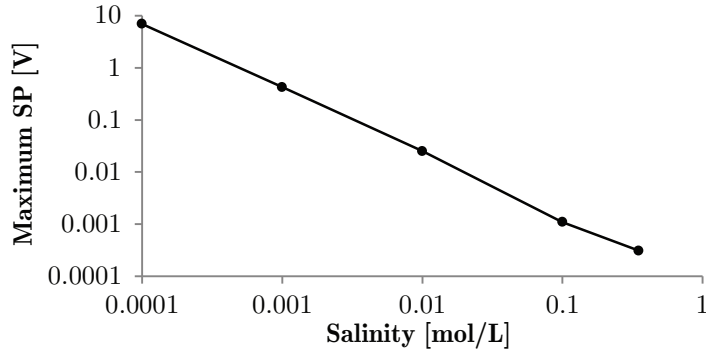Figure 4.20: Electrokinetic response due to different models.

Figure 4.21: Maximum potential at the front vs. brine salinity.

4.5   Conclusions

In this chapter, a new coupled electrokinetic–hydromechanical computational model is introduced to simulate CO_2 sequestration in fractured geological formations. The governing equations are formulated based on the averaging theory and the double porosity model; and solved using a mixed discretization scheme. A coupled standard Galerkin finite element method, extended finite element method, level-set method, and Petrov–Galerkin method are formulated. The standard Galerkin method is utilized to discretize the deformation and the diffusive dominant field equations. The extended finite element method, together with the level-set method and the Petrov-Galerkin method are utilized to discretize the advective dominant field equations. The level set method is utilized to trace the moving saturation front and the extended finite element method to model the front. Utilization of the extended finite element method and the level-set method produces a locally conservative discretization scheme, giving a stable and convergent model. However, this entails introducing an extra degrees of freedom in the fracture saturation field. Nevertheless, utilization of standard Galerkin method to discretize other quantities limits this increase to the minimum, yielding a computationally efficient numerical scheme.

Several verification and numerical examples with parametric analyzes are presented. The examples demonstrate the capability of the proposed SG-XFEM-LS model to simulate challenging problems describing coupled solid deformation, multiphase flow and electrokinetic flow in unsaturated fractured porous media. It has been shown that the proposed model is capable of solving these kinds of problems, which typically involve several state variables with different transient nature, using relatively coarse meshes.

Conclusions and Future
Works

5

5.1   Conclusion

The main objective of this work is to develop a computational model capable of simulating the complicated nature of CO_2 geo-sequestration using relatively coarse meshes, making it thus suitable for engineering practice.

Modeling the geoenvironmental impact of CO_2 sequestration involves theoretical and numerical challenges. It involves strong coupling between physical phenomena and hydro-mechanical processes occurring in complicated geometries, ranging from micro-scale to mega-scale. Due to this complicated combination of geometry and processes, it is vital to obtain a good combination between the mathematical model and the numerical model. The mathematical model should be able to simulate flow processes at the microscopic level and scale them up to the macroscopic level. The numerical model, on the other hand, should be consistent, stable and computationally efficient.

In this work, a coupled multi-physical computational model, based on the averaging theory, for formulating the governing field equations; and a mixed discretization scheme, based on coupling between the standard Galerkin finite element method (SG), the extended finite element method (XFEM), and the level-set method (LS); has been introduced to simulate CO_2 sequestration in geologic formations. SG has been utilized to discretize the deformation and the diffusive dominant field equations, and XFEM, together with LS, have been utilized to discretize the advective dominant field equations. Utilization of XFEM and LS produces a locally conservative discretization scheme, giving a stable and computationally efficient model. However, an extra degree of freedom must be added to describe the discontinuity in the advective field. Nevertheless, utilization of SG limits this increase to the minimum, yielding a

computationally efficient numerical scheme.

Chapter 2 of this thesis deals with the simulation of the isothermal two-phase flow in an unsaturated rigid porous medium. Four numerical examples illustrating the accuracy, stability, mesh insensitivity and convergence of the model are given. The Buckley-Leverett example, which is an advective-dominate process, demonstrates that the standard Galerkin method exhibits spurious oscillations, obviously due to advection; the result of the upwind method is rather smooth, but highly dissipative; but the proposed model produces a monotonic profile, and is less dissipative. Unlike the Buckley-Leverett problem, the McWhorter problem exhibits diffusion due to the capillary effect, and hence no sharp front exists. In this example, the three discretization procedures are in good agreement with the quasi-analytical solution. The CO_2 leakage example shows the efficiency of the model and indicates that the proposed model is stable and perturbation in the model parameters result in a physically realistic perturbation in the flow behavior, even for relatively coarse meshes.

Chapter 3 extends the previous model with coupling the electrokinetic process and mechanical deformation with two-phase flow in an unsaturated porous medium. The standard Galerkin method has been utilized to discretize the deformation and the diffusive dominant field equations, and XFEM, together with LS, have been utilized to discretize the advective dominant field equations. The capability of the mixed SG-XFEM-LS numerical scheme has been examined to simulate coupled solid deformation, multiphase flow, and electrokinetic flow in unsaturated porous media. The coupled deformation-multiphase flow example reveals that the formation deformation, which is a function of stiffness, has minor influence on the CO_2 flow. On the other hand, the coupled electrokinetic-multiphase flow example reveals that the salinity of the formation brine can play a major role in the electrokinetic flow, and hence, measuring the streaming potential can be a useful tool for monitoring CO_2 flow remotely.

In Chapter 4, the model is extended for simulation of coupled multiphysics processes of CO_2 sequestration in fractured porous media. The governing equations are formulated based on the averaging theory and the double porosity model; and solved using a mixed discretization scheme. The examples in this chapter demonstrate the capability of the proposed SG–XFEM–LS model to simulate challenging problems describing coupled solid deformation, multiphase flow and electrokinetic flow in unsaturated fractured porous media.

So, in conclusion, it has been shown that the proposed model is capable of solving these kinds of problems, which typically involve several state variables of different transient nature, using relatively coarse meshes. To facilitate the formulation of the

computational model and its computer implementation, several assumption were made. The thermodynamic parameters, such as the density and viscosity are made constant. The material behavior under the mechanical forces is assumed to be linear elastic. Also, it is assumed that there is no dissolution or chemical reaction in the reservoir. Though, many other physical and modeling aspects, including the type of balance equations, unsaturated multiphase flow, buoyancy effect, capillary effect, deformation and electrokinetic flow in a CO_2 environment, are carefully considered. The focus of this thesis was the development of a new computational technique tailored to the nature of the involved processes and phenomena. The pressure dependency of fluid properties will not degrade the computational efficiency of the proposed model.

5.2 Recommendations for future work

The following recommendations are proposed for future study. They have been organized into 3 categories, each having its own relevance for future research: the *required steps* have to be taken to continue with this model; the *improvements* will increase the robustness over the model; and the *extensions* will produce additional potentially relevant results that are not presented in this work.

Required steps

- *code optimization* - The implemented algorithm and the C++ code is needed to be optimized to improve computation time of the model.

- *3D level set model* - The developed reinitialization algorithm for the level-set method works for 2D examples. Modification is needed to include 3D problems.

Improvements

- *Non-linear solver* - The Newton-Raphson solver can be tuned to improve numerical performance and stability.

- *Time integration* - A finite difference scheme in time is utilized to solve the semi-discrete system of equations. More advanced time integration should be considered to increase the stability of the model.

- *Enrichment function* - In this work the extended finite element spatial discretization is conducted by adding an enhanced function necessary to capture a high

gradient field which exists within the element. Different enhancement functions are utilized and made suitable for different applications. Here, the level-set function is utilized to enhance the water saturation field. Other enhancement functions can be considered and examined for further improvement.

Extensions

- *3D model* - Our focus mainly lied on developing an efficient computational model. The 2D numerical examples are presented to show the capability of the model. A more realistic behavior of multiphysics processes in CGS should be demonstrated by means of 3D examples. Extension to 3D is in principle straightforward, once the 2D extension is understood. The main focus should be placed in implementation of front tracking in 3D (level set method).The theory and formulation of the 3D XFEM does not differ much from the 2D XFEM. The same enrichment function can be used in 3D XFEM.

- *Other physical processes* - The physical model is focused on the simulation of the involved processes during the injection and in the early time after the injection when the dominant process is two-phase flow. For the long term simulation other mechanisms like dissolution of CO_2 into water and geochemical reaction should be considered.

- *Pressure, volume and temperature (PVT) model* - Simple thermodynamic properties of CO_2 and water are used in the simulations. A more elaborated PVT model is needed to be developed.

- *Non-linear elasticity* - The current model uses a linear elastic material model, which is not valid for large deformations, if occurring. Implementation of a non-linear constitutive model will increase the physical relevance of the results.

- *Deformable fractures* - In the double porosity model, deformation is assumed to occur only in the porous matrix; however, due to a coupling between the two subdomains, the deformation of the whole domain is affected by the gradients in the pressure field between the porous matrix and fractured zone and the fractures might play a dominant role in the coupled hydromechanical processes in fractured reservoirs. The current model can be applied for a fractured porous medium with a low stiffness porous matrix rock. For a hard rock, where stress-induced changes in hydraulic properties of fractures are high, a new model, considering fracture deformation, should be developed.

Bibliography

S. Abbas, A. Alizada, and T.-P. Fries. The xfem for high-gradient solutions in convection-dominated problems. *International journal for numerical methods in engineering*, 82(8):1044–1072, 2010.

E. Aifantis. Introducing a multi-porous medium. *Development in Mechanics*, 8: 209–211, 1977.

R. Al-Khoury and L. Sluys. A computational model for fracturing porous media. *International Journal for Numerical Methods in Engineering*, 70(4):423–444, 2007.

V. Allègre, L. Jouniaux, F. Lehmann, and P. Sailhac. Streaming potential dependence on water-content in fontainebleau sand. *Geophysical Journal International*, 182 (3):1248–1266, 2010.

V. Allègre, F. Lehmann, P. Ackerer, L. Jouniaux, and P. Sailhac. A 1-d modelling of streaming potential dependence on water content during drainage experiment in sand. *Geophysical Journal International*, 189(1):285–295, 2012.

J. Andersson and B. Dverstorp. Conditional simulations of fluid flow in three-dimensional networks of discrete fractures. *Water Resources Research*, 23(10): 1876–1886, 1987.

T. Arbogast and I. Yotov. A non-mortar mixed finite element method for elliptic problems on non-matching multiblock grids. *Computer methods in applied mechanics and engineering*, 149(1):255–265, 1997.

ASME. Asme general position statement on technology and policy recommendations and goals for reducing carbon dioxide emission in the energy sector. Technical report, ASME, 2009.

K. Aziz and A. Settari. *Petroleum reservoir simulation*. Applied Science Publishers, 1979.

Y. Bachmat and J. Bear. Macroscopic modelling of transport phenomena in porous media. 1: The continuum approach. *Transport in Porous Media*, 1(3):213–240, 1986.

S. Bachu. Sequestration of CO_2 in geological media in response to climate change: road map for site selection using the transform of the geological space into the CO_2 phase space. *Energy Conversion and Management*, 43(1):87–102, 2002.

S. Bachu, W. Gunter, and E. Perkins. Aquifer disposal of CO_2: Hydrodynamic and mineral trapping. *Energy Conversion and Management*, 35(4):269–279, 1994.

M. Bai, D. Elsworth, and J. C. Roegiers. Modeling of naturally fractured reservoirs using deformation dependent flow mechanism. *International Journal of Rock Mechanics and Mining Sciences and*, 30(7):1185–1191, 1993.

M. Bai, F. Meng, J. Roegiers, and Y. Abousleiman. Modeling two-phase fluid flow and rock deformation in fractured porous media. *Poromechanics, edited by JF Thimus et al*, pages 333–338, 1998.

G. I. Barenblatt, I. P. Zheltov, and I. N. Kochina. Basic concepts in the theory of seepage of homogeneous liquids in fissured rocks [strata]. *Journal of Applied Mathematics and Mechanics*, 24(5):1286–1303, 1960.

P. Bastian. *Higher Order Discontinuous Galerkin Methods for Flow and Transport in Porous Media Challenges in Scientific Computing - CISC 2002*, volume 35 of *Lecture Notes in Computational Science and Engineering*, pages 1–22. Springer, 2003.

J. Bear. *Hydraulics of groundwater*. Courier Dover Publications, 2012.

J. Bear and A. H.-D. Cheng. *Modeling groundwater flow and contaminant transport*, volume 23. Springer Dordrecht, Heidelberg, London, New York, 2010.

J. Bear, C. Tsang, and G. de Marsily. *Flow and contaminant transport in fractured rock*. Academic Press, 1993.

T. Belytschko and T. Black. Elastic crack growth in finite elements with minimal remeshing. *International Journal for Numerical Methods in Engineering*, 45(5): 601–620, 1999.

S. Benson and L. Myer. Monitoring to ensure safe and effective geologic sequestration of carbon dioxide. In *IPCC workshop on carbon dioxide capture and storage*, pages 137–151. Citeseer, 2000.

B. Berkowitz. Characterizing flow and transport in fractured geological media: A review. *Advances in Water Resources*, 25(8–12):861–884, 2002.

R. Boer. *Theory of porous media: highlights in historical development and current state.* Springer New York, 2000.

R. Boer, I. P. P. Techniki, and P. A. Nauk. *Porous media: a survey of different approaches.* Universität-GH-Essen, Fachbereich 10-Bauwesen, 1991.

A. Boleve, A. Revil, F. Janod, J. Mattiuzzo, and A. Jardani. A new formulation to compute self-potential signals associated with ground water flow. *Hydrology and Earth System Sciences Discussions*, 4(3):1429–1463, 2007.

A. Bolève, A. Revil, F. Janod, J. L. Mattiuzzo, and A. Jardani. Forward modeling and validation of a new formulation to compute self-potential signals associated with ground water flow. *Hydrology and Earth System Sciences*, 11(5):1661–1671, 2007. HESS.

F. Brezzi, T. J. Hughes, L. D. Marini, and A. Masud. Mixed discontinuous galerkin methods for darcy flow. *Journal of Scientific Computing*, 22(1-3):119–145, 2005.

A. N. Brooks and T. J. R. Hughes. Streamline upwind/petrov-galerkin formulations for convection dominated flows with particular emphasis on the incompressible navier-stokes equations. *Computer Methods in Applied Mechanics and Engineering*, pages 199–259, 1982.

R. H. Brooks and A. T. Corey. Hydraulic properties of porous media. *Hydrology Papers, Colorado State University*, (March), 1964.

S. E. Buckley and M. C. Leverett. Mechanism of fluid displacements in sands. *Petroleum Transactions, AIME*, 146:107 – 116, 1942.

H.-Y. Chen and L. Teufel. Coupling fluid-flow and geomechanics in dual-porosity modeling of naturally fractured reservoirs. In *SPE annual technical conference and exhibition*, 1997.

Z. Chen, G. Huan, and B. Li. An improved impes method for two-phase flow in porous media. *Transport in Porous Media*, 54(3):361–376, 2004.

Z. Chen, G. Huan, and Y. Ma. *Computational methods for multiphase flows in porous media*. Society for Industrial and Applied Mathematics, 2006.

J. Chessa and T. Belytschko. An extended finite element method for two-phase fluids. *Journal of Applied Mechanics*, 70(1):10–17, 2003a.

J. Chessa and T. Belytschko. An enriched finite element method and level sets for axisymmetric two-phase flow with surface tension. *International Journal for Numerical Methods in Engineering*, 58(13):2041–2064, 2003b.

L. Chin, L. Thomas, J. Sylte, and R. Pierson. Iterative coupled analysis of geomechanics and fluid flow for rock compaction in reservoir simulation. *Oil & Gas Science and Technology*, 57(5):485–497, 2002.

M. H. Cho, H. G. Choi, and J. Y. Yoo. A direct reinitialization approach of level-set/splitting finite element method for simulating incompressible two-phase flows. *International Journal for Numerical Methods in Fluids*, 67(11):1637–1654, 2011.

T. F. Cho, M. E. Plesha, and B. C. Haimson. Continuum modelling of jointed porous rock. *International Journal for Numerical and Analytical Methods in Geomechanics*, 15(5):333–353, 1991.

H. G. Choi. A least-square weighted residual method for level set formulation. *International Journal for Numerical Methods in Fluids*, pages n/a–n/a, 2011.

H. Class, A. Ebigbo, R. Helmig, H. Dahle, J. Nordbotten, M. Celia, P. Audigane, M. Darcis, J. Ennis-King, Y. Fan, B. Flemisch, S. Gasda, M. Jin, S. Krug, D. Labregere, A. Naderi Beni, R. Pawar, A. Sbai, S. Thomas, L. Trenty, and L. Wei. A benchmark study on problems related to CO_2 storage in geologic formations. *Computational Geosciences*, 13(4):409–434, 2009.

K. Coats. A note on impes and some impes-based simulation models. *SPE Journal*, 5(3):245–251, 2000.

J. Cordazzo, C. R. Maliska, and F. S. V. da Silva, A. F. C.and Hurtado. The negative transmissibility issue when using cvfem in petroleum reservoir simulation, 29–Dec 2004 2004.

J. H. Cushman. Proofs of the volume averaging theorems for multiphase flow. *Advances in Water Resources*, 5(4):248 – 253, 1982.

J. de la Porte, C. Kossack, and R. Zimmerman. The effect of fracture relative permeabilities and capillary pressures on the numerical simulation of naturally fractured reservoirs. In *SPE Annual Technical Conference and Exhibition*, 2005.

G. De Marsily. Quantitative hydrogeology, groundwater hydrology for engineers, 1986.

M. Dentz and D. Tartakovsky. Abrupt-interface solution for carbon dioxide injection into porous media. *Transport in Porous Media*, 79(1):15–27, 2009.

DOE. Carbon sequestration atlas of the united states and canada, 2007.

J. Dolbow and T. Belytschko. A finite element method for crack growth without remeshing. *Int. J. Numer. Meth. Engng*, 46(1):131–150, 1999.

J. Dolbow, N. Moës, and T. Belytschko. Discontinuous enrichment in finite elements with a partition of unity method. *Finite elements in analysis and design*, 36(3): 235–260, 2000.

J. Douglas, R. Ewing, and M. Wheeler. A time-discretization procedure for a mixed finite element approximation of miscible displacement in porous media. *RAIRO Anal.*, numer 17:pp. 249–265, 1983.

F. A. Dullien. *Porous media: fluid transport and pore structure*. Academic press, 1991.

L. J. Durlofsky. A triangle based mixed finite element—finite volume technique for modeling two phase flow through porous media. *Journal of Computational Physics*, 105(2):252–266, 1993.

A. Ebigbo, H. Class, and R. Helmig. CO_2 leakage through an abandoned well: problem-oriented benchmarks. *Computational Geosciences*, 11(2):103–115, 2007.

R. Ehrlich. Viscous coupling in two-phase flow in porous media and its effect on relative permeabilities. *Transport in Porous Media*, 11(3):201–218, 1993.

Y. Epshteyn and B. Riviere. Fully implicit discontinuous finite element methods for two-phase flow. *Applied Numerical Mathematics*, 57(4):383–401, 2007.

M. J. Esrig. Pore pressures, consolidation, and electro-kinetics. *J. Soil Mech. Fdns Div. Am. SOC. civ. Engrs*, 4(94):899–921, 1967.

R. E. Ewing, B. A. Boyett, D. K. Babu, and R. F. Heinemann. Efficient use of locally refined grids for multiphase reservoir simulation, 1989.

R. W. Falta, K. Pruess, I. Javandel, and P. A. Witherspoon. Numerical modeling of steam injection for the removal of nonaqueous phase liquids from the subsurface: 1. numerical formulation. *Water Resources Research*, 28(2):433–449, 1992.

A. Firoozabadi. Recovery mechanisms in fractured reservoirs and field performance. *Journal of Canadian Petroleum Technology*, 39(11), 2000.

A. Firoozabadi and J. Hauge. Capillary pressure in fractured porous media (includes associated papers 21892 and 22212). *Journal of Petroleum Technology*, 42(6): 784–791, 1990.

A. Firoozabadi and L. Thomas. Sixth spe comparative solution project: Dual-porosity simulators. *Journal of Petroleum Technology*, 42(6):710–715, 762–763, 1990.

P. Forsyth. A control-volume, finite-element method for local mesh refinement in thermal reservoir simulation. *SPE Reservoir Engineering*, 5(4):561–566, 1990.

T.-P. Fries and T. Belytschko. The extended/generalized finite element method: an overview of the method and its applications. *International Journal for Numerical Methods in Engineering*, 84(3):253–304, 2010.

D. Gawin and B. A. Schrefler. Thermo-hydro-mechanical analysis of partially saturated porous materials. *Engineering Computations*, 13(7):113–143, 1996.

D. Gawin, P. Baggio, and B. A. Schrefler. Coupled heat, water and gas flow in deformable porous media. *International Journal for Numerical Methods in Fluids*, 20(8-9):969–987, 1995.

H. R. Ghafouri and R. W. Lewis. A finite element double porosity model for heterogeneous deformable porous media. *International Journal for Numerical and Analytical Methods in Geomechanics*, 20(11):831–844, 1996.

P. W. J. Glover, M. J. Hole, and J. Pous. A modified archie's law for two conducting phases. *Earth and Planetary Science Letters*, 180(3–4):369–383, 2000.

S. K. Godunov. A difference method for numerical calculation of discontinuous solutions of the equations of hydrodynamics. *Matematicheskii Sbornik*, 89(3): 271–306, 1959.

W. G. Gray. Local volume averaging of multiphase systems using a non-constant averaging volume. *International Journal of Multiphase Flow*, 9(6):755 – 761, 1983.

W. G. Gray and C. T. Miller. Thermodynamically constrained averaging theory approach for modeling flow and transport phenomena in porous medium systems: 1. motivation and overview. *Advances in Water Resources*, 28(2):161–180, 2005.

X. Guichet, L. Jouniaux, and J.-P. Pozzi. Streaming potential of a sand column in partial saturation conditions. *J. Geophys. Res.*, 108(B3):2141, 2003.

M. Hassanizadeh and W. G. Gray. General conservation equations for multi-phase systems: 1. averaging procedure. *Advances in Water Resources*, 2(0):131–144, 1979a.

M. Hassanizadeh and W. G. Gray. General conservation equations for multi-phase systems: 3. constitutive theory for porous media flow. *Advances in Water Resources*, 3(1):25–40, 1980.

S. Hassanizadeh and W. G. Gray. General conservation equations for multiphase systems: 2. mass, momenta, energy, and entropy equations. *Adv. Water Resour*, 2 (4):191–203, 1979b.

Z. Heinemann, G. Gerken, and G. von Hantelmann. Using local grid refinement in a multiple-application reservoir simulator, 15-18 November 1983 1983.

Z. Heinemann, C. Brand, and Y. Munka, M.and Chen. Modeling reservoir geometry with irregular grids. *SPE Reservoir Engineering*, 5(2):225–232, 1991.

R. Helmig. *Multiphase flow and transport processes in the subsurface: a contribution to the modeling of hydrosystems.* Springer, 1997.

H. J. Herzog. Peer reviewed: What future for carbon capture and sequestration? *Environmental Science & Technology*, 35(7):148A–153A, 2001.

R. Hinkelmann. *Efficient numerical methods and information-processing techniques for modeling hydro-and environmental systems*, volume 21. Springer, 2005.

S. Holloway. An overview of the underground disposal of carbon dioxide. *Energy Conversion and Management*, 38:S193–S198, 1997.

S. Holloway and D. Savage. The potential for aquifer disposal of carbon dioxide in the uk. *Energy Conversion and Management*, 34(9):925–932, 1993.

U. Hornung. *Homogenization and porous media*, volume 6. Springer, 1997.

T. J. Hughes, L. P. Franca, and G. M. Hulbert. A new finite element formulation for computational fluid dynamics: Viii. the galerkin/least-squares method for advective-diffusive equations. *Computer Methods in Applied Mechanics and Engineering*, 73(2):173–189, 1989.

T. J. Hughes, G. Engel, L. Mazzei, and M. G. Larson. The continuous galerkin method is locally conservative. *Journal of Computational Physics*, 163(2):467–488, 2000.

P. S. Huyakorn. *Computational methods in subsurface flow.* Academic Press, 1983.

IPCC. Carbon dioxide capture and storage, tech. rep. Technical report, Intergovernmental Panel on Climate Change,, 2005.

T. Ishido and J. W. Pritchett. Numerical simulation of electrokinetic potentials associated with subsurface fluid flow. *Journal of Geophysical Research*, 104(B7): 15247–15259, 1999.

T. Ishido and J. W. Pritchett. Characterization of fractured reservoirs using continuous self-potential measurements. In *Proc. 28th Stanford Workshop on Geothermal Reservoir Engineering*, pages 158–165, 2003.

T. Ishido, Y. Nishi, and J. W. Pritchett. Application of self-potential measurements to geothermal reservoir engineering: characterization of fractured reservoirs. In *Thirty-Fifth Workshop on Geothermal Reservoir Engineering*, 2010.

M. D. Jackson. Characterization of multiphase electrokinetic coupling using a bundle of capillary tubes model. *Journal of Geophysical Research: Solid Earth*, 113(B4): n/a–n/a, 2008.

M. D. Jackson. Multiphase electrokinetic coupling: Insights into the impact of fluid and charge distribution at the pore scale from a bundle of capillary tubes model. *Journal of Geophysical Research*, 115(B7):B07206, 2010.

J. W. Johnson and J. Nitao. Enhanced caprock integrity and selfsealing of the immiscible plume through mineral trapping during prograde and retrograde CO_2 sequestration in saline aquifers. *AAPG Bull*, 86:161–162, 2002.

J. W. Johnson, J. J. Nitao, and K. G. Knauss. Reactive transport modeling of CO_2 storage in saline aquifers to elucidate fundamental processes, trapping mechanisms and sequestration partitioning. *Geological storage of carbon dioxide*, 233:107–128, 2004.

J. W. Johnson, J. J. Nitao, and J. P. Morris. Reactive transport modeling of cap rock integrity during natural and engineered CO_2 storage. *Carbon dioxide capture for storage in deep geologic formations*, 2:787–813, 2005.

M. Y. Khaled, D. E. Beskos, and E. C. Aifantis. On the theory of consolidation with double porosity—iii a finite element formulation. *International Journal for Numerical and Analytical Methods in Geomechanics*, 8(2):101–123, 1984.

A. R. Khoei and T. Mohammadnejad. Numerical modeling of multiphase fluid flow in deforming porous media: A comparison between two- and three-phase models for seismic analysis of earth and rockfill dams. *Computers and Geotechnics*, 38(2): 142–166, 2011.

R. A. Klausen and T. Russell. Relationships among some locally conservative discretization methods which handle discontinuous coefficients. *Computational Geosciences*, 8(4):341–377, 2004.

P. D. Lax. Weak solutions of nonlinear hyperbolic equations and their numerical computation. *Communications on pure and applied mathematics*, 7(1):159–193, 1954.

A. Legay, J. Chessa, and T. Belytschko. An eulerian–lagrangian method for fluid–structure interaction based on level sets. *Computer Methods in Applied Mechanics and Engineering*, 195(17):2070–2087, 2006.

P. A. Lemonnier et al. Improvement of reservoir simulation by a triangular discontinuous finite element method. In *SPE Annual Technical Conference and Exhibition*. Society of Petroleum Engineers, 1979.

R. J. LeVeque. *Finite volume methods for hyperbolic problems*, volume 31. Cambridge university press, 2002.

R. Lewis and W. Pao. Numerical simulation of three-phase flow in deforming fractured reservoirs. *Oil & Gas Science and Technology*, 57(5):499–514, 2002.

R. Lewis and Y. Sukirman. Finite element modelling of three-phase flow in deforming saturated oil reservoirs. *International Journal for Numerical and Analytical Methods in Geomechanics*, 17(8):577–598, 1993.

R. W. Lewis and H. R. Ghafouri. A novel finite element double porosity model for multiphase flow through deformable fractured porous media. *International Journal for Numerical and Analytical Methods in Geomechanics*, 21(11):789–816, 1997.

R. W. Lewis and B. A. Schrefler. *The Finite Element Method in the Static and Dynamic Deformation and Consolidation of Porous Media, 2nd Edition*. John Wiley and Sons, 1998.

R. W. Lewis, P. J. Roberts, and B. A. Schrefler. Finite element modelling of two-phase heat and fluid flow in deforming porous media. *Transport in Porous Media*, 4(4):319–334, 1989.

N. Linde, D. Jougnot, A. Revil, S. K. Matthäi, T. Arora, D. Renard, and C. Doussan. Streaming current generation in two-phase flow conditions. *Geophysical Research Letters*, 34(3):L03306, 2007.

H.-H. Liu, J. Rutqvist, and J. G. Berryman. On the relationship between stress and elastic strain for porous and fractured rock. *International Journal of Rock Mechanics and Mining Sciences*, 46(2):289–296, 2009.

Y. Liu, L. Wang, and B. Yu. Sharp front capturing method for carbon dioxide plume propagation during injection into a deep confined aquifer. *Energy and Fuels*, 24 (2):1431–1440, 2010. doi: 10.1021/ef9010498.

A. Masud and T. J. Hughes. A stabilized mixed finite element method for darcy flow. *Computer Methods in Applied Mechanics and Engineering*, 191(39):4341–4370, 2002.

U. M. Mayer, A. Gerstenberger, and W. A. Wall. Interface handling for three-dimensional higher-order xfem-computations in fluid–structure interaction. *International journal for numerical methods in engineering*, 79(7):846–869, 2009.

D. B. McWhorter and D. K. Sunada. Exact integral solutions for two-phase flow. *Water Resour. Res.*, 26(3):399–413, 1990.

J. Meek. A brief history of the beginning of the finite element method. *International journal for numerical methods in engineering*, 39:3761–3774, 1996.

A. Michel. A finite volume scheme for two-phase immiscible flow in porous media. *SIAM Journal on Numerical Analysis*, 41(4):1301–1317, 2003.

J. Mitchell. *Fundamentals of Soil Behavior*. John Wiley and Sons, 1993.

J. Monteagudo and A. Firoozabadi. Comparison of fully implicit and impes formulations for simulation of water injection in fractured and unfractured media. *International Journal for Numerical Methods in Engineering*, 69(4):698–728, 2007.

J. Moore, S. Glaser, F. Morrison, and G. M. Hoversten. The streaming potential of liquid carbon dioxide in brea sandstone, 2004.

J. R. Moore and S. D. Glaser. Self-potential observations during hydraulic fracturing. *Journal of Geophysical Research: Solid Earth*, 112(B2):B02204, 2007.

P. K. Moore. Interpolation error-based a posteriori error estimation for two-point boundary value problems and parabolic equations in one space dimension. *Numerische Mathematik*, 90(1):149–177, 2001.

M. Musivand and R. Al-Khoury. On the theory of co2 geo-sequestration. In R. Al-Khoury and J. Bundschuh, editors, *Computational Models for CO2 Geo-sequestration & Compressed Air Energy Storage*, Sustainable Energy Developments, chapter 2, pages 11–77. Taylor & Francis Group/CRC Press, 2014.

J. Noorishad, M. Ayatollahi, and P. Witherspoon. A finite-element method for coupled stress and fluid flow analysis in fractured rock masses. In *International Journal of Rock Mechanics and Mining Sciences & Geomechanics Abstracts*, volume 19, pages 185–193. Elsevier, 1982.

J. M. Nordbotten. *Sequestration of Carbon in Saline Aquifers Mathematical and Numerical Analysis.* PhD thesis, 2004.

J. M. Nordbotten, M. A. Celia, S. Bachu, and H. K. Dahle. Semianalytical solution for CO_2 leakage through an abandoned well. *Environmental Science and Technology*, 39(2):602–611, 2004.

J. M. Nordbotten, M. A. Celia, and S. Bachu. Injection and storage of co2 in deep saline aquifers: Analytical solution for co2 plume evolution during injection. *Transport in Porous media*, 58(3):339–360, 2005.

L. Onsager. Reciprocal relations in irreversible processes. i. *Physical Review*, 37(4): 405–426, 1931. PR.

S. Osher and R. P. Fedkiw. Level set methods: an overview and some recent results. *Journal of Computational physics*, 169(2):463–502, 2001.

S. Osher and J. Sethian. Fronts propagating with curvature-dependent speed: Algorithms based on hamilton-jacobi formulations. *Journal of Computational Physics*, 79(1):12–49, 1988.

D. Peaceman. *Fundamentals of numerical reservoir simulation.* Elsevier Scientific Pub. Co. : distributors for the U.S. and Canada, Elsevier North-Holland, 1977.

F. Perrier and P. Morat. Characterization of electrical daily variations induced by capillary flow in the non-saturated zone. *pure and applied geophysics*, 157(5): 785–810, 2000.

G. F. Pinder and W. G. Gray. *Finite element simulation in surface and subsurface hydrology*, volume 295. Academic Press New York, 1977.

K. Pruess. Tough2: A general-purpose numerical simulator for multiphase fluid and heat flow. Technical report, Lawrence Berkeley Lab., CA (United States), 1991.

K. Pruess. Numerical simulation experiments on the long-term evolution of a CO_2 plume under a sloping caprock, 2010.

K. Pruess and J. García. Multiphase flow dynamics during CO_2 disposal into saline aquifers. *Environmental Geology*, 42(2):282–295, 2002.

K. Pruess, J. Garcia, T. Kovscek, C. Oldenburg, J. Rutqvist, C. Steefel, and T. Xu. Intercomparison of numerical simulation codes for geologic disposal of CO_2. Technical Report LBNL-51813, 2002. Other Information: PBD: 27 Nov 2002.

N. A. Rahman and R. W. Lewis. Finite element modelling of multiphase immiscible flow in deforming porous media for subsurface systems. *Computers and Geotechnics*, 24(1):41–63, 1999.

P. M. Reppert and F. D. Morgan. Temperature-dependent streaming potentials: 1. theory. *Journal of Geophysical Research*, 108(B11):2546, 2003.

A. Revil and N. Linde. Chemico-electromechanical coupling in microporous media. *Journal of colloid and interface science*, 302(2):682–694, 2006.

A. Revil, H. Schwaeger, I. Cathles, L. M., and P. D. Manhardt. Streaming potential in porous media 2. theory and application to geothermal systems. *J. Geophys. Res.*, 104(B9):20033–20048, 1999.

A. Revil, N. Linde, A. Cerepi, D. Jougnot, S. Matthäi, and S. Finsterle. Electrokinetic coupling in unsaturated porous media. *Journal of Colloid and Interface Science*, 313(1):315–327, 2007.

A. Riaz, M. Hesse, H. Tchelepi, and F. Orr. Onset of convection in a gravitationally unstable diffusive boundary layer in porous media. *Journal of Fluid Mechanics*, 548:87–111, 2006.

B. Riviere. Numerical study of a discontinuous galerkin method for incompressible two-phase flow. In *ECCOMAS Proceedings*, 2004.

E. S. Romm and W. R. Blake. *Fluid flow in fractured rocks*. Phillips Petroleum Company, 1972.

P. Royer, J. L. Auriault, J. Lewandowska, and C. Serres. Continuum modelling of contaminant transport in fractured porous media. *Transport in Porous Media*, 49 (3):333–359, 2002.

B. J. Rozon. A generalized finite volume discretization method for reservoir simulation, 6-8 February 1989 1989.

J. Rutqvist and C.-F. Tsang. A study of caprock hydromechanical changes associated with CO_2 injection into a brine formation. *Environmental Geology*, 42(2):296–305, 2002.

J. Rutqvist, Y.-S. Wu, C.-F. Tsang, and G. Bodvarsson. A modeling approach for analysis of coupled multiphase fluid flow, heat transfer, and deformation in fractured porous rock. *International Journal of Rock Mechanics and Mining Sciences*, 39(4):429–442, 2002.

J. Rutqvist, J. Birkholzer, F. Cappa, and C. F. Tsang. Estimating maximum sustainable injection pressure during geological sequestration of CO_2 using coupled fluid flow and geomechanical fault-slip analysis. *Energy Conversion and Management*, 48(6):1798–1807, 2007.

J. Rutqvist, D. W. Vasco, and L. Myer. Coupled reservoir-geomechanical analysis of CO_2 injection at in salah, algeria. *Energy Procedia*, 1(1):1847–1854, 2009.

P. Sailhac, M. Darnet, and G. Marquis. Electrical streaming potential measured at the ground surface: Forward modeling and inversion issues for monitoring infiltration and characterizing the vadose zone. *Vadose Zone Journal*, 3(4):1200–1206, 2004.

E. Sánchez-Palencia. Non-homogeneous media and vibration theory. In *Non-homogeneous media and vibration theory*, volume 127, 1980.

P. Saripalli and P. McGrail. Semi-analytical approaches to modeling deep well injection of CO_2 for geological sequestration. *Energy Conversion and Management*, 43(2):185–198, 2002.

J. H. Saunders, M. D. Jackson, and C. C. Pain. A new numerical model of electrokinetic potential response during hydrocarbon recovery. *Geophys. Res. Lett.*, 33(15):L15316, 2006.

J. H. Saunders, M. D. Jackson, and C. C. Pain. Fluid flow monitoring in oil fields using downhole measurements of electrokinetic potential. *Geophysics*, 73(5): E165–E180, 2008.

J. H. Saunders, M. D. Jackson, M. gulamali, J. Vinogradov, and C. C. Pain. Streaming potential at hydrocarbon reservoir conditions. *Geophysics*, 77(1):E77–E90, 2012.

B. A. Schrefler. Computer modelling in environmental geomechanics. *Computers & Structures*, 79(22-25):2209–2223, 2001. doi: DOI: 10.1016/S0045-7949(01)00076-1.

W. R. Sill. Self-potential modeling from primary flows. *Geophysics*, 48(1):76–86, 1983.

N. Sukumar and T. Belytschko. Arbitrary branched and intersecting cracks with the extended finite element method. *Int. J. Numer. Meth. Engng*, 48:1741–1760, 2000.

N. Sukumar, D. L. Chopp, N. Moës, and T. Belytschko. Modeling holes and inclusions by level sets in the extended finite-element method. *Computer methods in applied mechanics and engineering*, 190(46):6183–6200, 2001.

S. Sun and M. F. Wheeler. Symmetric and nonsymmetric discontinuous galerkin methods for reactive transport in porous media. *SIAM Journal on Numerical Analysis*, 43(1):195–219, 2005.

M. Talebian, R. Al-Khoury, and L. Sluys. An extended finite element model for CO_2 sequestration. *International Journal of Numerical Methods for Heat & Fluid Flow*, 23(8):1421–1448, 2013a.

M. Talebian, R. Al-Khoury, and L. Sluys. Coupled electrokinetic–hydromechanic model for CO_2 sequestration in porous media. *Transport in Porous Media*, 98(2): 287–321, 2013b.

M. Talebian, R. Al-Khoury, and L. Sluys. A computational model for coupled multiphysics processes of CO_2 sequestration in fractured porous media. *Advances in Water Resources*, 59:238–255, 2013c.

S. Valliappan and N. Khalili. Flow through fissured porous media with deformable matrix. *International Journal for Numerical Methods in Engineering*, 29(5): 1079–1094, 1990.

M. T. van Genuchten. A closed-form equation for predicting the hydraulic conductivity of unsaturated soils. *Soil Sci. Soc. Am. J.*, 44(5):892–898, 1980.

G. Wagner, N. Moës, W. Liu, and T. Belytschko. The extended finite element method for rigid particles in stokes flow. *International Journal for Numerical Methods in Engineering*, 51(3):293–313, 2001.

H. Wang. *Theory of Linear Poroelasticity with Applications to Geomechanics and Hydrogeology*. Princeton University Press, 2000.

H. Wang, J. Chessa, W. K. Liu, and T. Belytschko. The immersed/fictitious element method for fluid–structure interaction: volumetric consistency, compressibility and thin members. *International journal for numerical methods in engineering*, 74(1): 32–55, 2008.

J. E. Warren and P. J. Root. The behavior of naturally fractured reservoirs. *Old SPE Journal*, 3(3):245–255, 1963.

G. Weir, S. White, and W. Kissling. Reservoir storage and containment of greenhouse gases. *Energy Conversion and Management*, 36(6):531–534, 1995.

G. Wells and L. Sluys. A new method for modelling cohesive cracks using finite elements. *International Journal for Numerical Methods in Engineering*, 50(12): 2667–2682, 2001.

M. F. Wheeler and I. Yotov. Multigrid on the interface for mortar mixed finite element methods for elliptic problems. *Computer methods in applied mechanics and engineering*, 184(2):287–302, 2000.

M. F. Wheeler and I. Yotov. A multipoint flux mixed finite element method. *SIAM Journal on Numerical Analysis*, 44(5):2082–2106, 2006.

S. Whitaker. Flow in porous media i: A theoretical derivation of darcy's law. *Transport in Porous Media*, 1(1):3–25, 1986.

S. Whitaker. *The method of volume averaging*, volume 13. Springer, 1999.

R. Wilson and E. C. Aifantis. On the theory of consolidation with double porosity. *International Journal of Engineering Science*, 20(9):1009–1035, 1982.

M. Worthington, J. Saunders, C. Pain, and M. Jackson. Electrokinetic and vsp monitoring of fluid flow in petroleum reservoirs, 2002.

Y.-S. Wu and K. Pruess. Numerical simulation of non-isothermal multiphase tracer transport in heterogeneous fractured porous media. *Advances in Water Resources*, 23(7):699–723, 2000.

B. Wurmstich and F. D. Morgan. Modeling of streaming potential responses caused by oil well pumping. *Geophysics*, 59(1):46–56, 1994.

T. Xu and K. Pruess. Modeling multiphase non-isothermal fluid flow and reactive geochemical transport in variably saturated fractured rocks: 1. methodology. *American Journal of Science*, 301(1):16–33, 2001.

T. Xu, J. A. Apps, and K. Pruess. Numerical simulation of CO_2 disposal by mineral trapping in deep aquifers. *Applied geochemistry*, 19(6):917–936, 2004.

T. Xu, E. Sonnenthal, N. Spycher, and K. Pruess. Toughreact—a simulation program for non-isothermal multiphase reactive geochemical transport in variably saturated geologic media: Applications to geothermal injectivity and CO_2 geological sequestration. *Computers & Geosciences*, 32(2):145–165, 2006.

T. Xu, J. A. Apps, K. Pruess, and H. Yamamoto. Numerical modeling of injection and mineral trapping of CO_2 with h¡ sub¿ 2¡/sub¿ s and so¡ sub¿ 2¡/sub¿ in a sandstone formation. *Chemical Geology*, 242(3):319–346, 2007.

O. Zienkiewicz, R. Taylor, and P. Nithiarasu. *The Finite Element Method for Fluid Dynamics*, volume 3. Butterworth-Heinemann, 2005.

Nomenclature

<div style="text-align: right">A</div>

Alphabets

a_J	XFEM new degree of freedom
$\mathbf{b}_\pi$	external supply of a thermodynamic property for the phase π
$\mathbf{C}$	electrokinetic coupling coefficient, VPa^{-1}
$\mathbf{C}_f$	salt concentration, mole/m^3
$\mathbf{C}_r$	relative coupling coefficient
$\mathbf{D}_e$	stiffness matrix of the solid
E	Young's modulus of elasticity, Pa
f_π	fractional flow function of phase π
$\mathbf{G}_\pi$	net production of a thermodynamic property for the phase π
g	gravitational acceleration, ms^{-2}
$\mathbf{g}$	gravity acceleration vector, ms^{-2}
h_e	characteristic length of the element, m
I	Identity tensor
$\mathbf{J}_\pi$	flux vector of a thermodynamic property for the phase π
$\mathbf{j}$	total electric current density, Am^{-2}
$\mathbf{k}$	intrinsic permeability tensor, m^2
k_e	electro-osmotic permeability, $m^2s^{-1}V^{-1}$
$k_{r\pi\alpha}$	relative permeability of π phase in α continuum
K_π	bulk modulus of the phase π, Pa^{-1}
K_s	bulk modulus of the grain material, Pa^{-1}
$\mathbf{L}$	cross coupling coefficients, $m^2V^{-1}s^{-1}$
$\hat{\mathbf{L}}$	displacement-strain operator
l	characteristic length of a matrix block, m
$\mathbf{m}$	a vector equal to $\mathbf{m} = [1,1,1,0,0,0]^T$

m	cementation exponent
n	Archie's saturation exponent. Otherwise defined in the text.
n_e	number of nodes in the element
p_c	capillary pressure, Pa
$p_{\pi\alpha}$	π phase pressure in α continuum, Pa
P_b	entry pressure, Pa
Q_π	source or sink terms
q_π	imposed volumetric flux of phase π normal to the boundary
$S_{\pi\alpha}$	π phase saturation in α continuum
$S_{r\pi\alpha}$	residual saturation of phase π in α continuum
S_e	effective saturation
$\breve{\mathbf{t}}_\pi$	intra-phase stress tensor, $N\,m^{-2}$
$\mathbf{u}$	displacement vector of solid phase, m
$\mathbf{v}_\Gamma$	interface velocity, $m\,s^{-1}$
$\mathbf{v}_\pi$	mass averaged velocity of phase π, $m\,s^{-1}$
V	electrical potential, V

Greek

α	Biot's constant
$\bar{\alpha}$	shape factor of fractured domain, m^{-2}
$\boldsymbol{\epsilon}$	total strain of the solid
$\boldsymbol{\epsilon}_0$	initial strain
ϵ_w	brine permittivity, $F\,m^{-1}$
Φ	level set function
ϕ	porosity
$\boldsymbol{\lambda}$	pore size distribution index
μ_π	dynamic viscosity of phase π, Pa s
υ	Poisson's ratio
θ	time integration parameter
$\bar{\rho}$	effective density in multiphase domain, $kg\,m^{-3}$
ρ_π	intrinsic phase averaged density of phase π , $kg\,m^{-3}$
$\boldsymbol{\sigma}$	total stress, $N\,m^{-2}$
$\boldsymbol{\sigma}'$	effective stress, $N\,m^{-2}$
$\boldsymbol{\sigma}''$	effective stress with Biot's constant included, $N\,m^{-2}$
σ_e	electrical conductivity, Sm^{-1}
σ_π	electrical conductivity of phase π , Sm^{-1}
σ_r	relative electric conductivity

τ	stabilization parameter
Ψ	a thermodynamic property
ψ	fractional volume of the fractures
ζ	Zeta potential, V

Subscripts and Superscripts

eff	effective
f	fracture continuum
g	gas phase
m	matrix continuum
π	phase π
r	residual saturation
s	solid phase
sat	saturated porous media
w	water phase

Publications

<div style="text-align: right">B</div>

This research activity has led to several publications in the international journals and conferences. These are summarized below.

International Journals

1. M. Talebian, R. Al-Khoury, and L. Sluys. An extended finite element model for CO_2 sequestration. International Journal of Numerical Methods for Heat Fluid Flow, *International Journal of Numerical Methods for Heat Fluid Flow*, vol. 23, iss. 8, pp. 1421-1448, 2013. [DOI: 10.1108/HFF-12-2011-0256]

2. M. Talebian, R. Al-Khoury, and L. Sluys. Coupled electrokinetic- hydromechanic model for CO_2 sequestration in porous media., *Trans- port in Porous Media*, vol. 98, iss. 2, pp. 287-321, 2013. [DOI: 10.1007/s11242-013-0145-y]

3. M. Talebian, R. Al-Khoury, and L. Sluys. A computational model for coupled multiphysics processes of CO_2 sequestration in fractured porous media, *Advances in Water Resources*, vol. 59, pp. 238-255, 2013. [DOI: 10.1016/j.adv watres.2013.06.012]

Book Chapter

1. R. Al-Khoury and M. Talebian. Coupled partition of unity-level set finite element formulation for CO_2 geo-sequestration., In R. Al-Khoury and J. Bundschuh, editors, Computational Models for CO_2 Geo-sequestration and Compressed Air Energy Storage, Sustainable Energy Developments, chapter 10. Taylor & Francis Group/CRC Press/CRC Press, 2014.

International Conferences and Workshops

1. R. Al-Khoury, M. Talebian and L. Sluys. A Hydromechanic-Electrokinetic Model for CO_2 Sequestration in Geological Formations, in *Proc. of Fifth Biot Conference*

on Poromechanics , Vienna, Austria, pp. 2042-2048, Publisher: American Society of Civil Engineers, ISBN: 978-0-7844-1299-2, 2013.

2. M. Talebian, R. Al-Khoury and L. Sluys. Hydro-mechanical modeling of CO_2 Sequestration, in *Euromech Colloquium 539, Mechanics of Unsaturated Porous Media*, Utrecht, The Netherlands, 2013.

3. R. Al-Khoury, M. Talebian and L. Sluys. Computational Advances in Modeling CO_2 Sequestration in Porous Media, in *Porous media research in the Netherlands, Dutch Interpore*, Shell, Rijswijk, The Netherlands, September 2012.

4. M. Talebian, R. Al-Khoury and L. Sluys. XFEM-Level set model for CO_2 sequestration, in *4th International Conference on Porous Media*, Purdue University, West Lafayette, USA, May 2012.

5. M. Talebian, R. Al-Khoury and L. Sluys. An Efficient Computational Model for CO_2 Flow in Porous Media, in *Fourteenth Engineering Mechanics Symposium*, Lunteren, Netherlands, October 2011.

6. M. Talebian, R. Al-Khoury and L. Sluys. An Efficient Computational Model for CO_2 Flow In Porous Media, in *IV International Conference On Computational Methods For Coupled Problems In Science and Engineering*, Kos Iceland, Paper P18, ISBN: 978-84-87867-59-0, June 2011.

Acknowledgements

And then suddenly it has gotten this far: you are writing the acknowledgments section for your PhD thesis. It's a special feeling to bring a huge story to the end. This thesis is the result of four years of research at the Computational Mechanics group in the Faculty of Civil Engineering and Geosciences of Delft University of Technology. However, a PhD thesis is not written by itself, but is the result of the cooperation between a lot of people. I greatly appreciate all who have contributed directly or indirectly to the content of the thesis, to the underlying work, and to my personal life during this period. I gratefully acknowledge the financial support by Agentschap NL (Dutch Ministry of Economic Affairs)

First and foremost, I would like to thank Rafid Al-Khoury for giving me the opportunity to work with him and under his supervision. He has taught me, both consciously and unconsciously, how to be a good researcher. I appreciate all his contributions of time, ideas, and supporting to make my PhD experience productive and stimulating. The joy and enthusiasm he has for his research was contagious and motivational for me, even during tough times in the PhD pursuit. I am sure that I could not have finished this thesis without his help and support. Rafid was not only a supervisor, but a mentor and a dear friend who had always a kind word and smile.

I also would like to thank my promoter Prof. Bert Sluys for giving me the opportunity to join his group in order to obtain a PhD and for the ideas and views he expressed during the regular meetings. Bert, thank you for the gentleness, support, trust, thoughts, feedback and freedom you gave me.

I like to express my great appreciation for the members of the doctoral committee for taking on the task of reviewing my manuscript and giving constructive remarks that helped to improve the manuscript. Thanks to Erik Jan Lingen and Martijn Stroeven for their help in the implementation of the model in Jem/Jive C++ library.

My special thanks to Amin Karamnejad and Mehdi Musivand Arzanfudi. Mehdi,

who I was fortunate to share office with and share ideas, inspired me with his calm and structured way of working. Amin, a truly kind colleague and friend, who is always prepared to help others.

The members of the CM group have contributed immensely to my personal and professional time at Delft. The group has been a source of friendships as well as good advice and collaboration. I would like to thank my colleagues Adriaan Sillem, Aliyeh Alipour, Angelo Simone, Anneke Meijer, Awais Ahmed, Edlira Kondo, Frank Everdij, Frans van der Meer, Jaap Weerheijm, Jitang Fan, Kristian Ølgaard, Luis Magalhaes Pereira, Marcello Malagu, Marjon van der Perk, Mehdi Nikbakht, Mohammad Latifi, Mahdi Banatehrani, Nghi Le, Oriol Lloberas Valls, Prithvi Mandapalli, Roberta Bellodi, Salar Mostofizadeh, Vinh Phu Nguyen, Xuming Shan and Zahid Shabir for their friendship, support and help during my PhD. My sincere gratitude also goes to our loving secretaries, Anneke and Marjon for always being supportive. Thanks to Merijn and Barend for helping me to translate my thesis summary and propositions to Dutch.

Finally, I would like to thank some people around me that is not in any way linked to this thesis but is rooted much deeper, all my family and friends. A very special word of thanks goes to my parents for their unconditional help and love and for supporting all my steps in the academic world. I cannot imagine myself doing much without having them around.

Mahnoush, the final words are for you. Thank you for your patience, unconditional support, endurance, enthusiasm and love, which were essential ingredients for finishing this thesis. I am glad to have you on my side in our new adventure.

Mojtaba Talebian
Delft, 2014

Curriculum Vitae

December 16$^{\text{th}}$, 1979   Born in Iran, as Mojtaba Talebian.

1994 - 1998   Diploma in Mathematics, Dr. Hessabi High School, Iran.

1998 - 2002   Bachelor of Science in Reservoir Engineering, Petroleum University of Technology, Abadan, Iran.

2002 - 2004   Master of Engineering in Reservoir Engineering, University of Calgary, Calgary, Canada.

2005 - 2007   Reservoir Engineering training coordinator and instructor, National Iranian Oil Company Trade and Technology Training Center, Ahwaz, Iran.

2007 - 2009   Reservoir Engineer, NIOC Improved Oil Recovery Research Institute, Tehran, Iran.

2009 - 20013   PhD candidate in the Computational Mechanics group at the Faculty of Civil Engineering and Geosciences, Delft University of Technology, Netherlands.

Since 2013   Reservoir Engineer, SGS Horizon, Voorburg, Netherlands.